

Università degli studi di Perugia  
Dottorato di ricerca in Fisica  
XXIII Ciclo

---



Search for  
**SUperSYmmetry**  
in the  
**Same Sign DiLepton Final State**  
with the  
**CMS Experiment at LHC**

*Candidato:*  
Roberta Volpe

---

A.A. 2009/10

---

*Relatori:*  
Dott. Michele Pioppi  
Dott. Attilio Santocchia

---

*Coordinatore del corso di Dottorato:*  
Prof. Maurizio Busso



*to a couple of people  
who preferred the non-existence*



# Contents

<b>Contents</b>	<b>iii</b>
<b>Introduction</b>	<b>ix</b>
<b>1 Supersymmetry</b>	<b>1</b>
1.1 SM and its limitations . . . . .	2
1.1.1 Bases of the Standard Model . . . . .	2
1.1.2 Quadratic divergences of Higgs mass . . . . .	6
1.1.3 Dark matter . . . . .	7
1.1.4 Asymmetry between matter and antimatter . . . . .	8
1.2 Supersymmetry . . . . .	8
1.2.1 Basis of supersymmetric models . . . . .	9
1.2.2 Spontaneous supersymmetry breaking . . . . .	12
1.2.3 Minimal Supersymmetric Standard Model . . . . .	14
1.2.4 Mass spectrum in MSSM . . . . .	17
1.2.5 The link between two different scales . . . . .	21
1.2.6 The Constrained Minimal Supersymmetric Standard Models	22
1.2.7 SUSY answers to the SM problems . . . . .	27
1.3 Experimental Bounds on SUSY Models . . . . .	29
1.3.1 Bounds from Flavor Physics . . . . .	30
1.3.2 Muon anomalous magnetic momentum . . . . .	31
1.3.3 Direct Searches of SUSY at Colliders . . . . .	32
1.4 Direct Searches of SUSY at LHC . . . . .	33
1.4.1 Production of Sparticles . . . . .	33
1.4.2 Decays of Sparticles . . . . .	34
1.4.3 SUSY Topologies . . . . .	37
1.4.4 Same Sign Di Leptonic topology . . . . .	38

<b>2 The CMS Detector at the LHC</b>	<b>43</b>
2.1 The Large Hadron Collider . . . . .	43
2.2 The Compact Muon Solenoid Experiment . . . . .	48
2.2.1 Inner Tracking System . . . . .	51
2.2.2 Electromagnetic Calorimeter . . . . .	54
2.2.3 Hadronic Calorimeter . . . . .	56
2.2.4 Superconducting magnet . . . . .	58
2.2.5 Muon System . . . . .	58
2.2.6 The Trigger System . . . . .	61
<b>3 Same Sign Dilepton SUSY Analysis</b>	<b>67</b>
3.1 Monte Carlo Samples . . . . .	68
3.1.1 Background samples . . . . .	68
3.1.2 Signal samples . . . . .	69
3.2 Analysis strategy . . . . .	70
3.3 Physics objects reconstruction . . . . .	73
3.3.1 Generalities of the Particle Flow technique . . . . .	74
3.3.2 Muons . . . . .	75
3.3.3 Electrons . . . . .	76
3.3.4 Jets . . . . .	77
3.3.5 Tau Jets . . . . .	79
3.3.6 Missing Transverse Energy . . . . .	80
3.3.7 $H_T$ and $MH_T$ . . . . .	81
3.4 Hadronic High Level Trigger . . . . .	81
3.5 Physics objects Identification . . . . .	83
3.5.1 Electrons and Muons . . . . .	83
3.5.2 Hadronic Tau Identification . . . . .	92
3.6 Selection results . . . . .	96
3.7 Background Estimation Methods . . . . .	99
3.7.1 Main Background Sources . . . . .	101
3.7.2 Method of the Estimation of Background from Non-Prompt Leptons . . . . .	102
3.7.3 Determination of $\epsilon_{T/L}$ for Non-Prompt Leptons . . . . .	104
3.7.4 Number of selected events with two opposite sign leptons . .	106
3.7.5 Estimation of Background Yield . . . . .	111
3.7.6 Closure Test with Monte Carlo . . . . .	112

3.7.7	Possible sources of systematic uncertainties . . . . .	114
3.7.8	Background estimation in real data . . . . .	115
3.8	Sensitivity studies . . . . .	117
3.8.1	Sensitivity evaluation . . . . .	118
3.8.2	Upper Limits . . . . .	123
<b>4</b>	<b>Same Sign W pair production</b>	<b>131</b>
4.1	Same Sign Ws production from Single Parton Scattering . . . . .	132
4.2	Same Sign Ws production from Double Parton Scattering . . . . .	132
4.2.1	Features determining the DPS cross section . . . . .	133
4.2.2	Existing calculations of the DPS cross section . . . . .	135
4.3	Strategy to estimate the SSW contribution from the SM . . . . .	139
4.4	MC Samples Used . . . . .	141
4.4.1	Same sign W from Single Parton Scattering . . . . .	141
4.4.2	DPS in Pythia8 . . . . .	142
4.5	DPS Same Sign W yield estimation . . . . .	142
4.5.1	Selection . . . . .	142
4.5.2	Strategy for an inclusive DPS SSW cross section measurement	147
4.5.3	Selection Results . . . . .	149
4.6	Extrapolation of SSW DPS contribution at high HT . . . . .	150
4.6.1	Strategy . . . . .	151
4.6.2	Validation with real data . . . . .	152
4.6.3	Contribution to SSDL SUSY Background . . . . .	154
<b>Conclusions</b>		<b>157</b>
<b>Acronyms</b>		<b>163</b>
<b>Bibliography</b>		<b>165</b>
<b>Acknowledgment</b>		<b>171</b>
<b>List of Figures</b>		<b>179</b>
<b>List of Tables</b>		<b>182</b>



# Introduction

The Standard Model (SM) describes in a satisfactory way several features of Nature which have been observed in particle physics experiments.

The most characteristic feature of the SM, the one needed to explain the origin of the masses of all the detected particles, is the spontaneous symmetry breaking of the group on which the SM is based. Such feature cannot be derived from the mathematical basis of the SM, instead it is put by hand in order to explain the experimental evidence. Moreover, issues arising in astrophysics, lead to think of the existence of a kind of physical matter not described in the contest of the SM. These and other limitations of the SM lead to think of it as an asymptotic theory to which a more general one tends for energies explored so far. Indeed this is the way the fundamental science advanced in the past and will go on in advancing.

One of the most accredited theories built up to now is the SuperSymmetry, a symmetry which contains the symmetries which represent the pillars of the SM. It forecasts a correspondence between fermions and bosons, for every SM particle there exists a superpartner with different spin statistics, named sparticles.

The success of this theory, is that if it exists, much likely would manifest itself at the LHC energies. Such topic makes the SUSY currently an interesting theory not only for its beauty and elegance, but also for a pragmatic reason: it is possible to test its existence in the next few years, indeed this is also one of the reasons of the choice of the energy range in the LHC project.

The SUSY framework can be developed in several ways, depending on different matters, especially on speculations on the way the supersymmetry is spontaneously broken. There exist many SUSY models differing for different mechanisms, which in turn can be divided to infinite submodels, which correspond in the infinite values of the parameters not fixed by the theory, namely sparticle masses and couplings. This makes the focusing on a single model useless and ineffectual. Although basis of SUSY are well defined, the way it can manifest itself is not known. The most convenient way to proceed is to consider the general features shared by every

SUSY model, these are the presence of sparticles not interacting with the standard matter, giving rise to a large energy not detected and large jet activity.

In this thesis the signature with two same sign leptons (*SSDL*) is considered; such final state is possible in SUSY and is strongly suppressed in the SM, this makes the SSDL topology the cleanest one. It is almost background free and, despite the lower efficiency compared to the other topologies, it is one of the most promising one, especially in the early stages of LHC, when detectors and the high density environment is not completely under control.

An aggressive approach has been chosen, developing a strategy as inclusive as possible: taking into account also for the final states with tau leptons hadronically decaying and by considering a lepton  $p_T$  threshold as low as possible.

A feasibility study of this search with an integrated luminosity of  $100\text{pb}^{-1}$  is presented, along with the statistical significance which is possible to obtain with such statistics. Furthermore, the distributions of variables used in the selection, have been checked and validated by comparisons between simulation and data using the integrated luminosity collected since March till September 2010, corresponding to  $3\text{ pb}^{-1}$ . A careful study has been performed on the background contributions coming from physical processes with final states different from the signal and selected because of instrumental mis-measurements. Data driven methods to estimate background from these sources have been developed and validated with the collected data.

The Standard Model physics processes with the signal final state are few and with low cross section, but they need to be investigated. A study has been performed on the production in the SM context of two  $W$  bosons with the same sign and the impact they can give to the SSDL SUSY search.

The production of same sign  $W$  pairs in a single parton interaction can occur only at higher orders in perturbative expansion of the SM compared to the opposite sign diboson production. Therefore it is suppressed and its cross section is calculable perturbatively within the electroweak theory. Another source of same sign  $Ws$  is the occurrence of two different hard parton interactions within the same proton-proton collision, known as Double Parton Scattering (DPS). A part the role as background in many searches, the DPS has also an autonomous importance, indeed its yield depends on the internal structure of the colliding hadrons and a measurement of DPS cross section could provide indications about the way the

partons arrange inside the proton at LHC energy scale. The production of same sign  $W$  bosons, despite its low yield, is considered in literature a golden channel for the study of DPS, indeed two same sign leptons is a channel much cleaner compared to the more copious final states including jets.

A strategy to measure the DPS  $WW$  production has been planned. The DPS  $WW$  production, with both the  $W$ s decaying in leptons, is expected to have low hadronic activity, since the  $W$  production cross section is sharply falling with the jet multiplicity. On the contrary, the selection aimed to the SUSY search select events with energetic jets. One method to estimate the contribution of same sign  $W$  bosons coming from DPS is described.

The Chapter 1 is dedicated to a brief introduction to the theoretical framework of the SUSY with a focus on the possible solution it can give to the SM issues and on the phenomenological implications at the LHC energies. The experimental apparatus, the LHC along with the CMS detector, is described in Chapter 2. The Chapter 3 is dedicated to the description of the analysis searching for SUSY in the SSDL channel, the feasibility study with  $L = 100\text{pb}^{-1}$  and the first validations with the real data available. The study on the same sign  $W$  production within the SM is described in Chapter 4. Finally an overview of the full work is in the conclusion.



# Chapter 1

## Supersymmetry

*Tiger, tiger, burning bright  
In the forests of the night,  
What immortal hand or eye  
Dare frame thy fearful  
symmetry?*

William Blake – The Tiger

*I believe that, if a triangle could  
speak, it would say, in like  
manner, that God is eminently  
triangular*

Baruch Spinoza

---

The Large Hadron Collider (LHC) will explore for the first time the region of energies of Tera electronVolt (TeV). The importance to investigate the physics at such energies relies mostly on the forecast that new physics likely will manifest itself just at few TeV energies.

The Standard Model (SM) is the theory which describes in a satisfying way the known physics at the energies explored up to now, but some of its properties are not justified by the model itself and some problems arising in the whole fundamental physics indicate that some physics beyond the SM should exist.

## 1.1 SM and its limitations

The SM describes successfully the fundamental interactions, as several precision experiments have demonstrated.

The bases of the Standard Model are briefly described in the following section; given the wide range of the subject, the focus on the following is on the features of the model which are extended to the supersymmetry.

### 1.1.1 Bases of the Standard Model

The SM is a non-Abelian Yang-Mills [1] type gauge theory based on the group  $SU(3)_C \times SU(2)_L \times U(1)_Y$ , the coupling constants will be referred to as  $g_1$  for  $U(1)_Y$ ,  $g_2$  for  $SU(2)_L$  and  $g_3$  for  $SU(3)_c$ .

The  $SU(3)_C$  group is the base of the Quantum Chromo Dynamic (QCD) which describes the strong interactions. The quarks are assigned to the **3** representation, the antiquarks to its conjugate **3\*** and the gluons are the gauge bosons.

The group  $SU(2)_L \times U(1)_Y$  represents the ElectroWeak (EW) interactions. The left and right handed components of the quark and lepton fields are assigned to different representations of the group because of the chiral structure of the weak interactions.

The gauge bosons needed to the invariance under  $SU(2)_L \times U(1)_Y$  transformations, are named  $B_\mu$  and  $W_\mu^i$  with  $i = 1, 2, 3$ .

A symmetry of the vacuum is a symmetry for the Hamiltonian (namely if  $G|0\rangle = 0$ , then  $[G, H] = 0$ , where  $G$  is the generator of the transformation); but there can exist a symmetry for the Hamiltonian ( $[G, H] = 0$ ) that transform a state in another with different energy, namely the states are not degenerate under such transformation, therefore the vacuum can be not unique. In this case the symmetry is not manifest in the energy spectrum and is called *spontaneously broken*. The Goldstone theorem [2] states that when this happens, a massless excitation must exist.

A transformation under which the Hamiltonian is invariant can be a *global* (the transformation does not depend on the space-time) or a *local* (in every point of the space-time the fields undergo a different transformation) symmetry. In the latter case further degrees of freedom appear besides the Goldstone excitation.

The QCD  $SU(3)_C$  is assumed to be unbroken; instead, in order to describe the

particle phenomenology, the EW  $SU(2)_L \times U(1)_Y$  group needs to be spontaneously broken to the  $U(1)_{em}$  group.

The massless excitation is a boson field, named the *Goldstone boson*, and since the symmetry is local, a vector field ( $A_\mu$ ), originally massless, gains mass. Nevertheless, thanks to the gauge invariance, the so called *Higgs mechanism* [3] allows for the massless scalar to be eliminated, leaving a massive real vector, in such a way the number of degrees of freedom in the model remains the same as in the unbroken case.

Every field introduced so far is massless until the  $SU(2) \times U(1)$  is kept unbroken; it can be spontaneously broken if a new sector is added at the Lagrangian density; it consists of a complex  $SU(2)_L$  doublet  $\Phi$  of zero spin fields and has to be of the form:

$$[D^\mu \Phi(x)]^\dagger [D_\mu \Phi(x)] - \mu^2 \Phi^\dagger(x) \Phi(x) - \lambda [\Phi^\dagger(x) \Phi(x)]^2 \quad (1.1)$$

where  $\lambda > 0$ , in order for energy to be bounded from below, and  $\mu^2 < 0$ , otherwise no symmetry breaking would occur. In order to break the gauge symmetry, such doublet must acquire a Vacuum Expectation Value (VEV) different from zero. The minimum value of the classical energy density occurs for  $\Phi_0$  such that  $\Phi_0^\dagger \Phi_0 = \frac{-\mu^2}{2\lambda}$ . There are infinite values of the  $\Phi$  components which satisfy such relation and by choosing one of them, the symmetry  $SU(2)_L \times U(1)_Y$  is broken, while the  $U(1)_{em}$  remains unbroken. The chosen value is:

$$\langle \Phi_0 \rangle = \begin{pmatrix} 0 \\ \frac{v}{\sqrt{2}} \end{pmatrix} \quad (1.2)$$

where  $v = \sqrt{-\mu^2/\lambda}$ . A generic  $\Phi$  field can be expressed by the deviations from  $\Phi_0$  and in the *unitary gauge* [4] it reads:

$$\langle \Phi(x) \rangle = \frac{1}{\sqrt{2}} \begin{pmatrix} 0 \\ v + \sigma(x) \end{pmatrix}. \quad (1.3)$$

By expressing the Lagrangian as a function of it, it is easy to see that the bosons  $Z$  and  $W^\pm$  acquire mass, while the photon remains massless. Furthermore, the generalization of the Higgs mechanism in  $SU(2)$ , makes possible that the Goldstone bosons disappear, while the  $\sigma(x)$  field outlasts, and on quantization it gives rise to the so called *Higgs scalars*, which are massive, electrically neutral, and spin 0 particles.

The gauge bosons of the  $SU(2) \times U(1)$ , mass eigenstates of the model, are two charged vector bosons  $W_\mu^\pm$  and two neutral vector bosons,  $Z_\mu$  and a  $A_\mu$ ; they are related one each other and with the gauge field  $B_\mu$ , by the mixing:

$$Z_\mu = \cos\theta_W W_\mu^3 - \sin\theta_W B_\mu \quad (1.4)$$

$$A_\mu = \sin\theta_W W_\mu^3 + \cos\theta_W B_\mu \quad (1.5)$$

where the the Weinberg angle  $\theta_W$  is introduced by

$$\sin\theta_W = \frac{g_1}{\sqrt{g_2^2 + g_1^2}}, \cos\theta_W = \frac{g_2}{\sqrt{g_2^2 + g_1^2}}, \quad \text{and} \quad \tan\theta_W = \frac{g_1}{g_2} \quad (1.6)$$

The Standard Model observed particles are summarized in Tab. 1.1.

particle	simbol	spin	charge
neutrinos	$\nu_e \quad \nu_\mu \quad \nu_\tau$	1/2	0
charged leptons	$e \quad \mu \quad \tau$	1/2	$\pm 1$
up quarks	$u \quad c \quad t$	1/2	+ 2/3
down quarks	$d \quad s \quad b$	1/2	- 1/3
EW	$\gamma$	-	0
gauge	$W^\pm$	1	$\pm 1$
bosons	$Z$	1	0
gluons	$g$	1	0

field	$(SU(3)_C, SU(2)_L, U(1)_Y)$
$\begin{pmatrix} \nu_L \\ e_L \end{pmatrix}$	$(\mathbf{1}, \quad \mathbf{2}, \quad -\frac{1}{2})_L$
$e_R$	$(\mathbf{1}, \quad \mathbf{1}, \quad -1)_R$
$\begin{pmatrix} u_L \\ d_L \end{pmatrix}$	$(\mathbf{3}, \quad \mathbf{2}, \quad \frac{1}{6})_L$
$u_R$	$(\mathbf{3}, \quad \mathbf{1}, \quad \frac{2}{3})_R$
$d_R$	$(\mathbf{3}, \quad \mathbf{1}, \quad -\frac{1}{3})_R$

Table 1.1: Observed elementary particles in Standard Model.

The gauge interactions do not take into account the different flavors of the particles, the dependence of physics from flavor is described by the so called *Yukawa interactions*, which involve several further free parameters in the SM.

The SM Lagrangian is the most general renormalizable Lagrangian consistent with the features described so far and can be expressed as the sum  $\mathcal{L}_{SM} = \mathcal{L}_{kin+gauge} + \mathcal{L}_{Higgs} + \mathcal{L}_{Yukawa}$ .

Besides the mass of the Higgs boson, which has not been observed yet, the other parameters of the SM are: the  $SU(2)$  gauge coupling ( $g_2$ ), the hypercharge  $U(1)$  gauge coupling ( $g_1/2$ ) and the Higgs VEV  $v/\sqrt{2}$ . They are estimated by measuring the observables related to them: the  $Z$  boson mass ( $M_Z$ ), the Fermi constant ( $G_F$ ) and the fine structure constant ( $\alpha$ ).

The electroweak theory was developed by Glashow, Salam and Weinberg in '60s, in '70s the first experiments at CERN which measured the Weinberg angle started and in early '80 the measurements of the  $W$  and  $Z$  masses confirmed the forecast of the model. Since then the Standard Model has been proved to work well by several precision measurements which allowed to test it also beyond the tree level. In particular the LEP experiments have measured the masses of the gauge bosons  $W$  and  $Z$  confirming the relation between them through the Weinberg angle, with the value obtained from weak neutral currents measurements. Another success of the SM was the prediction of the interval where the top quark mass lies, indeed it was foreseen by calculating the quantum fluctuations in the framework of the SM before it was directly discovered at Tevatron.

The SM achieved many successes also from a theoretical point of view. It is renormalizable and preserves unitarity at every order of perturbation theory, thus observable quantities can be calculated in terms of the parameters of the theory. A characteristic property is that the conservation of the Baryon and Lepton numbers, experimentally observed, are features appearing naturally in the SM; indeed the most general SM lagrangian which is gauge invariant implies the  $B$  and  $L$  invariance. Therefore the Standard Model has many properties which make it a beautiful theory, nevertheless in its framework many limitations of different origin arise.

Before providing some theoretical details on SM limitations (in the next sections), we could here just note that the SM can not describe the nature in a complete way because: (i) it does not include gravity and (ii) it provides three different kind of interactions, each one with its coupling, while a theory unifying all the known interactions would be preferred.

Already only these limitations lead to speculate on other possible theories, and in order to explain the good agreement between the SM predictions and the experi-

mental results, such theories should have the SM as limit at energies explored so far.

### 1.1.2 Quadratic divergences of Higgs mass

From the conceptual point of view, the first limitation of the SM as fundamental theory is that its most important feature, namely the spontaneous breaking of the Electro-Weak symmetry, can not be deduced by first principles. Indeed the potential of the Higgs field,

$$V = \mu^2 |\phi|^2 + \lambda |\phi|^4 \quad (1.7)$$

can provide the symmetry breaking only if the parameter  $\mu^2$  is negative and its sign is chosen just in order to explain the needed mass generation. Therefore it is natural to think of the SM as an effective theory which represents the low energy limit of a fundamental theory which is able to explain the symmetry breaking, i.e. able to foresee the right sign of the  $\mu^2$  parameter.

Furthermore the  $\mu^2$  parameter is a renormalizable quantity and receives large additive radiative corrections from loop diagrams and some of them are UltraViolet (UV) divergent. From Eq.(1.7) we see that the Higgs mass is  $m_H^2 = -2\mu^2$ . The corrections to the Higgs mass given by the coupling with fermions and scalars (both self-couplings and with other scalar fields) can be expressed respectively as [5]:

$$\Delta m_H^2 = -\frac{|y_f|^2}{8\pi^2} \Lambda_{UV}^2 + \dots \quad (1.8)$$

$$\Delta m_H^2 = -\frac{|y_S|^2}{16\pi^2} [\Lambda_{UV}^2 - 2m_S^2 \ln(\Lambda_{UV}/m_S) + \dots]. \quad (1.9)$$

The cut off  $\Lambda_{UV}$  used to regulate the theory can be considered the upper limit of the scale in which the SM works. Such scale should be of the order of Plank scale if not any new physics exists, since the gravity is the only known interaction not included in SM.

$v$  and  $m_H$  are related by the relation  $v = \sqrt{-2m_H^2/\lambda}$ , and electroweak measurements fix the vacuum expectation value of the Higgs to be  $v/\sqrt{2} \sim 174$  GeV while the Plank mass is  $M_{Pl} \sim 2.4 \times 10^{18}$  GeV.

By assuming  $\Lambda \gg v$ , the corrections are  $\Delta m_H^2 \gg v^2$ . In order for such divergences to cancel there should be a very precise fine-tuning,  $\mathcal{O}(10^{26})$ , between the fermionic and bosonic terms; it does not violate any principle, but it likely indicates that the SM is just an effective theory working only at the energies explored

so far. This is what is known as the *gauge hierarchy problem*.

Instead, if we consider  $\Lambda < \mathcal{O}(TeV)$ , the fine tuning is not needed and physics beyond Standard Model is expected at energies  $\mathcal{O}(TeV)$ .

### 1.1.3 Dark matter

Besides particle physics, the other main field of the modern fundamental physics is the astrophysics. Also the astrophysics research met some troubles to explain some experimental evidences and this is another issue which leads to believe to the existence of new physics. Measurements of the cosmic microwave background, supernova luminosities versus distance, and structure formation [6], lead to consider an Universe with a large fraction of a matter not understood up to now, called *dark matter*.

It is supposed to be constituted by non-relativistic particle species, which interact only very feebly with the Standard Model ones [7], named Weak Interacting Massive Particles (WIMPs). They must be massive, electrical and color neutral, and stable at least at cosmic time scale, since no one of the SM particles is an appropriate candidate, some physics beyond SM should exist.

The mechanism that has been supposed to explain the dark matter density is the following. In the early universe the temperature is supposed to be very high, such particles are in thermodynamic equilibrium with SM particles. When the universe cooled the particle density decreased very fast, because the annihilation became more likely than the creation. At a certain time the density get a such low value that the annihilation stopped, leaving their number unchanged up to now. However the density decreased because of the expansion of the universe and reached the current value. Such a mechanism is referred to as *thermal freeze out* [8].

The resulting relic particle energy density is ([9]):

$$\Omega_{DM} h^2 \equiv \frac{\rho_{DM}}{\rho_{tot}} h^2 \sim \frac{3 \times 10^{-27} cm^3 s^{-1}}{\langle \sigma v \rangle} \quad (1.10)$$

where  $h$  is the current Hubble constant [8] and  $v$  is the velocity of the particle, so that  $\langle \sigma v \rangle$  is the thermal average of the annihilation cross section during the freeze-out.  $\Omega_{DM} h^2$  has been measured to be  $0.1099 \pm 0.0062$  [9] therefore the dark matter should be constituted by particles which had  $\langle \sigma v \rangle \simeq 2.7 \times 10^{-26} cm^3 s^{-1}$ .

This value is in agreement with an annihilation cross section for a generic weak-scale interaction, in particular since the annihilation cross section for a particle with mass  $M$  and coupling  $\alpha$  can be roughly expressed by  $\langle \sigma v \rangle \sim (\alpha/M)^2$ , this

cross section value can be obtained for non Standard Model particles with coupling and mass required to solve the hierarchy problem mentioned in Sec.1.1.2. This is a such good matter that it is referred to as the *WIMP miracle* [10].

### 1.1.4 Asymmetry between matter and antimatter

Another issue not explained by the SM is the dominance of the matter over the antimatter. Most of the ordinary matter in the universe consists of protons and neutrons; since they are baryons, the asymmetry between matter and antimatter results in a violation of baryonic number ( $B$ ). The process of creating an excess of baryons over anti-baryons in the early universe, starting from a Universe with equal numbers of both, is called *baryogenesis* and a mechanism responsible for it is needed. The baryogenesis can be occurred only if the three so called *Sakharov conditions* [11] are satisfied: (1) there should exist some interactions with violation of  $B$ , (2) violation of  $C$  and  $CP$  should be possible and (3) such  $B$ ,  $C$ , and  $CP$  violating interaction should have been occurred in a period in which the universe was not in thermodynamic equilibrium. The SM could satisfy such conditions, but the  $CP$  violation foreseen by it is not enough to explain the observed matter-antimatter asymmetry. One of the mechanism explaining the baryogenesis is the *Electroweak Baryogenesis* [8]. It is particularly interesting because it can be tested also at the current hadron colliders (LHC and Tevatron). There should have been a period when the  $SU(2)_L \times U(1)_Y$  symmetry was exact (the unbroken phase) and at some time it transited to the phase where such symmetry is spontaneously broken, namely at a certain point there was the *electroweak phase transition*. The baryon asymmetry holds also after this transition, only if the critical temperature  $T_C$  in which the minimum of the potential occurs for a  $\langle\phi\rangle \neq 0$  is such that  $\langle\phi(T_C)\rangle > T_C$ , namely if the electroweak transition have been *strongly first order*. This condition is related to the Higgs mass and in the SM it can not be satisfied [8], therefore new physics is expected.

## 1.2 Supersymmetry

From the previous sections is evident that new theories are needed to explain some experimental evidences.

Many hypotheses have been investigated in the past years and one of the most accredited one is the existence of a symmetry bigger than the one supposed by

the SM, the theory which assumes such new symmetry is named SUperSYmmetry (SUSY).

A brief description of the general properties of such theories is given in the next sections, furthermore a list of possible answers given by SUSY to the SM problems (hinted in Sec. 1.1) is reported.

### 1.2.1 Basis of supersymmetric models

The hierarchy problem leads to think of the new symmetry as something which relates particles with different spin. On such grounds the supersymmetric models have been developed.

The basis of supersymmetric models is a transformation which converts a fermionic field  $\psi$  to a bosonic one  $\phi$  and vice-versa:

$$\delta\phi = \epsilon \cdot \psi \quad \text{and} \quad \delta\phi^* = \epsilon^\dagger \psi^\dagger \quad (1.11)$$

where  $\epsilon^\alpha$  is an infinitesimal, anticommuting two-component Weyl fermion. Such symmetry is generated by the conserved charge  $Q$ , which respects:

$$\{Q, Q\} = 0, \quad \{Q, Q^\dagger\} = 2\sigma^\mu P_\mu \quad (1.12)$$

so that:

$$Q|boson\rangle \sim |fermion\rangle, \quad Q|fermion\rangle \sim |boson\rangle \quad (1.13)$$

The models in which only one supersymmetric generator  $Q$  (and  $Q^\dagger$ ) exists are called  $\mathcal{N} = 1$  supersymmetric theories.

The irreducible representations of the supersymmetry algebra are called *supermultiplet* and contain an equal number of bosonic and fermionic fields. The Lagrangian density for a simple model describing only one bosonic and one fermionic non interacting fields (the Wess-Zumino model [12]) reads:

$$\mathcal{L}_{free} = -\partial^\mu \phi^{*i} \partial_\mu \phi_i + i\psi^{\dagger i} \bar{\sigma}^\mu \partial_\mu \psi_i + F^{*i} F_i, \quad (1.14)$$

where four  $2 \times 2$  matrices  $\sigma^\mu$  are the three Pauli matrices for  $\mu = 1, 2, 3$ , and the unity matrix for  $\mu = 0$ . The first two terms describe the non-interacting scalar and fermion fields; the last term contains the auxiliary fields  $F^i$  needed to make the supersymmetry algebra closing also off-shell, as the quantum mechanics requires. The lagrangian in Eq. 1.14 is invariant under the supersymmetric transformations:

$$\delta\phi_i = \epsilon\psi_i \quad (1.15)$$

$$\delta(\psi_i)_\alpha = -i(\sigma^\mu \epsilon^\dagger)_\alpha \partial_\mu \phi_i + \epsilon_\alpha F_i \quad (1.16)$$

$$\delta F_i = -i\epsilon^\dagger \bar{\sigma}^\mu \partial_\mu \psi_i \quad (1.17)$$

and their complex conjugates.

The most general renormalizable interactions terms, invariant under supersymmetric transformations, are of the form:

$$\mathcal{L}_{int} = \left( -\frac{1}{2}W^{ij}\psi_i\psi_j + W^iF_i \right) + c.c. \quad (1.18)$$

where  $W^{ij}$  is analytic in  $\phi_k$ . So it must be of the form  $W^{ij} = M^{ij} + y^{ijk}\phi_k$ , and can be written as:

$$W^{ij} = \frac{\delta^2}{\delta\phi_i\delta\phi_j}W, \quad \text{provided that} \quad W = L^i\phi_i + \frac{1}{2}M^{ij}\phi_i\phi_j + \frac{1}{6}y^{ijk}\phi_i\phi_j\phi_k. \quad (1.19)$$

$W^i$  can be defined as  $W^i = \delta W / \delta\phi_i$  as well, so this explains the notation.

The so called *superpotential*  $W$  (1.19) (analytic function of the complex scalar fields) embodies the most general non-gauge interactions for chiral multiplets.

By using the equation of motion, the auxiliary fields  $F_i$  and  $F^{*i}$  can be expressed in terms of the scalar fields, in such a way the lagrangian density for the matter fields, including both free and interaction terms, reads:

$$\mathcal{L}_{chiral} = -\partial^\mu\phi^{*i}\partial_\mu\phi_i + i\psi^{\dagger i}\bar{\sigma}^\mu\partial_\mu\psi_i - \frac{1}{2}\left(W^{ij}\psi_i\psi_j + W_{ij}^*\psi^{\dagger i}\psi^{\dagger j}\right) - W^iW_i^* \quad (1.20)$$

The last term is defined as the *scalar potential*  $V(\phi, \phi^*) \equiv W^kW_k^*$ , so that the lagrangian density can be expressed explicitly as a function of the only fields:

$$\begin{aligned} \mathcal{L}_{chiral} = & -\partial^\mu\phi^{*i}\partial_\mu\phi_i - V(\phi, \phi^*) + i\psi^{\dagger i}\bar{\sigma}^\mu\partial_\mu\psi_i \\ & - \frac{1}{2}M^{ij}\psi_i\psi_j - \frac{1}{2}M_{ij}^*\psi^{\dagger i}\psi^{\dagger j} - \frac{1}{2}y^{ijk}\phi_i\psi_j\psi_k - \frac{1}{2}y_{ijk}^*\phi^{*i}\psi^{\dagger j}\psi^{\dagger k}. \end{aligned} \quad (1.21)$$

By linearizing the equation of motion, it is possible to realize that both bosons and fermions have the same squared-mass matrix  $(M^2)_i^j = M_{ik}^*M^{kj}$ . This leads to a collection of chiral supermultiplets. Each supermultiplet contains a mass-degenerate complex scalar and Weyl fermion. The introduction of these new fields, besides the SM ones, solve the problem reported in Sec.1.1.2, because the quadratic divergences lying in the SM, here cancel in a systematic way.

The other ingredients needed to construct a supersymmetry gauge theory are the gauge fields. They are defined as the gauge boson field  $A_\mu^a$  and a two-component Weyl fermion *gaugino*  $\lambda^a$  ( $a$  runs over the dimension of the gauge group).

The gauge transformations for such massless gauge fields are:

$$\delta_{gauge}A_\mu^a = \partial_\mu\Lambda^a + gf^{abc}A_\mu^b\Lambda^c \quad \text{and} \quad \delta_{gauge}\lambda_\mu^a = gf^{abc}\lambda_\mu^b\Lambda^c \quad (1.22)$$

where  $g$  is the gauge coupling,  $f^{abc}$  are the totally antisymmetric structure constants defining the gauge group and  $\Lambda^a$  is an infinitesimal gauge transformation parameter. Also in this case the introduction of auxiliary fields is necessary in order for the algebra to close off-shell, these new fields are called  $D^a$ . Therefore the lagrangian density part which describes the gauge fields reads:

$$\mathcal{L}_{gauge} = -\frac{1}{4}F_{\mu\nu}^a F^{\mu\nu a} + i\lambda^{\dagger a}\bar{\sigma}^\mu D_\mu \lambda^a + \frac{1}{2}D^a D_a, \quad (1.23)$$

$$\text{with } F_{\mu\nu}^a = \partial_\mu A_\nu^a - \partial_\nu A_\mu^a + g f^{abc} A_\mu^b A_\nu^c \text{ and } D_\mu \lambda^a = \partial_\mu \lambda^a + g f^{abc} A_\mu^b \lambda^c. \quad (1.24)$$

The final step needed to obtain a full Lagrangian for a supersymmetric model is the introduction of the gauge interactions between the fields defined so far.

As usual in gauge field theory [13], the possible renormalizable interaction terms (with field mass dimension at most 4) are added with unknown coefficients to the field Lagrangian  $\mathcal{L}_{chiral} + \mathcal{L}_{gauge}$  and invariance of the total Lagrangian under gauge supersymmetry transformations is required. As it is known from the SM, such demand can be satisfied provided the ordinary derivatives in  $\mathcal{L}_{chiral} + \mathcal{L}_{gauge}$  are replaced by the *covariant derivatives*.

In order to define the covariant derivatives, the gauge transformation for the fields has to be introduced. The supersymmetry and the gauge transformations commute, therefore  $\phi_i$ ,  $\psi_i$  and  $F_i$  are in the same representation of the gauge group. By calling  $(T^a)_i{}^j$  the hermitian matrices of the representation, they have to satisfy  $[T^a, T^b] = if^{abc}T^c$ , with  $f^{abc}$  defined by Eq.(1.22).

The gauge transformation for the fields is  $\delta_{gauge}X_i = ig\Lambda^a(T^a X)_i$   $X_i = \phi_i, \psi_i, F_i$ , and the derivatives are changed as in the following:

$$\partial_\mu \phi_i \rightarrow D_\mu \phi_i = \partial_\mu \phi_i - igA_\mu^a(T^a \phi)_a \quad (1.25)$$

$$\partial_\mu \psi_i \rightarrow D_\mu \psi_i = \partial_\mu \psi_i - igA_\mu^a(T^a \psi)_a \quad (1.26)$$

Provided such replacement in  $\mathcal{L}_{chiral} + \mathcal{L}_{gauge}$  the full Lagrangian density for a renormalizable supersymmetric theory is:

$$\mathcal{L}_{full} = \mathcal{L}_{chiral} + \mathcal{L}_{gauge} - \sqrt{2}g(\phi^* T^a \psi)\lambda^a - \sqrt{2}g\lambda^{\dagger a}(\psi^\dagger T^a \phi) + g(\phi^* T^a \phi)D^a \quad (1.27)$$

Where the coefficients of the last three terms are found by imposing the supersymmetry invariance. The third and fourth terms represent the interactions between the gauginos with the matter fields. By taking into account the last term of Eq.(1.23) and the last term of Eq.(1.27), in the full Lagrangian there is the contribution  $\frac{1}{2}D^a D_a + g(\phi^* T^a \phi)D^a$  which imply for the  $D^a$  field the equation of motion

$D^a = -g(\phi^* T^a \phi)$ ; since now we have an explicit expression of  $D^a$  as a function of  $\phi$ , the last term of Eq.(1.27) can be considered as supplementary term for the scalar potential  $V(\phi, \phi^*)$ , which now reads:

$$V(\phi, \phi^*) = F^{*i} F_i + \frac{1}{2} \sum_a D^a D^a = W_i^* W^i + \frac{1}{2} \sum_a g_a^2 (\phi^* T^a \phi)^2. \quad (1.28)$$

It is worth noting that the scalar potential is never negative, regardless of the fields values.

### 1.2.2 Spontaneous supersymmetry breaking

The superpartners (partners with different spin) of the SM particles are named *sparticles* and have not been observed yet, this means that they can not have the same masses of their SM partners.

From what we learned from the SM physics, we expect that supersymmetry should be broken in order to allow particles to gain different masses, although the supersymmetry would make the spectrum degenerate.

As it is known (and hinted in Sec.1.1) a spontaneous breaking of a symmetry can be realized if the lagrangian is invariant under such symmetry but the vacuum is not. An operator whose VEV is different from zero must exist and it would represent the order parameter of the symmetry breaking.

If the  $\psi$  field acquires a nonzero VEV the Lorentz invariance would be broken and, since the 4-momentum of the vacuum should be zero,  $\langle \partial_\mu \phi \rangle = \langle \partial_\mu \psi \rangle = 0$ . A non null  $\langle D \rangle$  leads to complications, since it is not possible to have a supersymmetry breaking conserving gauge invariance for a non abelian group, therefore a non zero  $F$  VEV is expected.

As in every spontaneously symmetry breaking, there must exist a Nambu-Goldstone mode with the same quantum numbers of the generator of the broken symmetry, so it should be a massless neutral Weyl fermion, called *goldstino* (which is not the Godstone boson super-partner, though the terminology would suggest it).

However the mechanism which makes the F-term VEV not vanishing requires the introduction of a parameter which gives the required values of the generated masses. The value of such parameter can be artificially chosen, nevertheless we would like a theory which implies in a natural way the scale of the parameter. In other words: VEV for F is different from zero but we could ask which is the

dynamical mechanism responsible for this. Furthermore, the way how the  $F$ -term VEV couples to the other fields is another important question. It is proved that such couplings can not be tree level renormalizable interactions [14], therefore it is thought that Spontaneous Symmetry Braking (SSB) occurs in a *hidden sector* of particles that has no direct couplings to the *visible sector* and some interactions should link such hidden sector with the visible one. It has been argued that the supersymmetry is broken at a scale  $M_{SUSY}^2 (>> M_W^2)$  in the hidden sector where the goldstino resides and a messenger sector makes the interaction between the two sectors possible [5].

The exact mechanism by which the supersymmetry is broken, although of great scientific interest, is not a main scope for the time being: since it occurs in a sector weakly interacting with the observable one, it has not immediate consequences on phenomenology. On the contrary, the way how the supersymmetry breaking is transmitted from the hidden to the observable sector, implies some restrictions on the sparticle spectrum, therefore it is of great interest from the current experimental point of view. The scenario in which these interactions are electroweak and QCD is called *Gauge Mediated Supersymmetry Breaking (GMSB)*, while the scenario in which the messenger interactions are gravitational is named *Plank Mediated Supersymmetry Breaking (PMSB)*. Disregarding the dynamical mechanism responsible for the supersymmetry breaking, some assumptions can be made in order to construct models which can be thought as an effective low energy ( $\sim TeV$ ) theory. To this aim, the supersymmetry breaking terms are added explicitly to the Lagrangian.

In order for the difference between the EW and Plank scale to be stable under quantum corrections, it is necessary that the mass gap between the SM particles and their superpartners is small enough, namely  $|m_f^2 - m_{\tilde{f}}^2| < \sim 1 \text{ TeV}^2$  and the supersymmetry breaking is named *soft*. The soft supersymmetry breaking terms are summed up in  $\mathcal{L}_{soft}$ , so that the total Lagrangian density can be written as  $\mathcal{L} = \mathcal{L}_{SUSY} + \mathcal{L}_{soft}$  and the most general gauge invariant form for  $\mathcal{L}_{soft}$  is:

$$\mathcal{L}_{soft} = -\phi_i^*(m)_{ij}\phi_j + \left( \frac{1}{3!} \mathcal{A}_{ijk}\phi_i\phi_j\phi_k - \mathcal{B}_{ij}\phi_i\phi_j + \mathcal{C}_i\phi_i + h.c. \right) - \frac{1}{2}(M\lambda^a\lambda^a + h.c) \quad (1.29)$$

The coefficients  $\mathcal{A}_{ijk}$ ,  $\mathcal{B}_{ij}$  and  $\mathcal{C}$  are referred to as the trilinear, bilinear and linear coefficients in the following. Such parameterization of the supersymmetry breaking can be made in range of the minimal extension of the Standard Model called

Minimal Supersymmetric Standard Model (MSSM) and described in the next section. The parameters in the general form (1.29) are explicitly studied in the range of any specific model of supersymmetry breaking transmission from the hidden to the visible sector.

### 1.2.3 Minimal Supersymmetric Standard Model

Given the components in the previous sections it is possible to construct the supersymmetric generalization of the standard model, the so called Minimal Supersymmetric Standard Model (MSSM). The supersymmetry changes the 1/2 spin fermionic matter fields, in bosonic superpartners which have 0 spin in order to be matter fields (1 spin fields would be gauge bosons); they are the *sleptons* and *squarks*. For the first generation:

$$\tilde{l}_{1L} = \begin{pmatrix} \tilde{\nu} \\ \tilde{e}^- \end{pmatrix}_L, \tilde{e}_{1R} = \tilde{e}_R, \tilde{q}_{1L} = \begin{pmatrix} \tilde{u} \\ \tilde{d} \end{pmatrix}_L, \tilde{u}_{1R} = \tilde{u}_R, \tilde{d}_{1R} = \tilde{d}_R. \quad (1.30)$$

The so called *superfield formalism* is often introduced in order to make more compact the formulas and perform calculations in quantum field theory. A *superfield*  $\Phi$  is defined by three components:  $\Phi = (\phi, \psi, F)$ .

By calling  $L_i$  the left chiral lepton doublet superfield and  $\bar{E}_i$  the antilepton singlet chiral superfield, for every  $i$ -th generation, they can be written as:

$$L_i = \begin{pmatrix} L_{\nu_i} \\ L_i \end{pmatrix}_L, \bar{E}_j, Q_i = \begin{pmatrix} Q_k \\ Q_l \end{pmatrix}, \bar{U}_j, \bar{D}_j. \quad (1.31)$$

where  $i = e, \mu, \tau$ ,  $j = 1, 2, 3$ ,  $k = u, c, t$  and  $l = d, s, b$ .

As regards the gauge fields, besides the boson SM gauge fields  $(B_\mu, W_\mu, g_\mu)$ , in the model the fermionic spin 1/2 fields are present:  $\tilde{\lambda}_0$  belonging to  $U(1)_Y$ ,  $\tilde{\lambda}$  belonging to  $SU(2)_L$  and  $\tilde{g}^a$  belonging to  $SU(3)_c$ .

Since the superpotential does not depends on  $\phi^\dagger$ , in order to allow for interactions with the lower component of the left chiral fermions field, the supersymmetric extension of the SM Higgs sector needs to be constituted by two Higgs doublets. They are indicated as:

$$H_u = \begin{pmatrix} H_u^1 \\ H_u^2 \end{pmatrix} = \begin{pmatrix} H_u^0 \\ H_u^- \end{pmatrix}; H_d = \begin{pmatrix} H_d^1 \\ H_d^2 \end{pmatrix} = \begin{pmatrix} H_d^+ \\ H_d^0 \end{pmatrix}; \quad (1.32)$$

With the electroweak symmetry breaking three of these eight real degrees of freedom become the longitudinal modes of the vector bosons  $W^\pm$  and  $Z^0$ , while the other five become the scalar mass eigenstates named:  $h_0$  and  $H_0$  (CP-even),  $A^0$  (CP-odd),  $H^+$  and  $H^-$ . In the MSSM the superpotential (Eq. 1.19), which is the source of nonlinear fermion-scalar interactions reads:

$$W_{MSSM} = \mu H_u \cdot H_d - f_{ij}^e H_u \cdot L_i \bar{E}_j - f_{ij}^d H_u \cdot Q_i \bar{D}_j - f_{ij}^u Q_i \cdot H_d \bar{U}_j \quad (1.33)$$

where the  $f_{ij}^{e,u,d}$  are the Yukawa coupling parameters for each generation pair  $ij$ . The first term is what determines the symmetry breaking and is called  $\mu$ -term.

Near the minimum, by using the gauge  $SU(2)_L$  invariance, the charged components can be assumed null and the potential term for the neutral components is:

$$V_{scalar} = (m_{H_u}^2 + \mu^2)|H_u^0|^2 + (m_{H_d}^2 + \mu^2)|H_d^0|^2 \quad (1.34)$$

$$-B\mu(H_u^0 H_d^0 + h.c.) + \frac{1}{8}(g_1^2 + g_2^2)(|H_u^0|^2 + |H_d^0|^2)^2. \quad (1.35)$$

where  $B$  is a coefficient with dimension of mass, proportional to the bilinear coefficient introduced in 1.29 for the fields  $H_u^0$  and  $H_d^0$ .

The scalar field potential at the weak scale should have a minimum for non-zero field values of  $H_u^0$  or  $H_d^0$  and zero values for other fields.

In order to assure stability, the potential has to be bounded from below, it implies the requirement:

$$m_{H_u}^2 + m_{H_d}^2 + 2\mu^2 > 2B\mu. \quad (1.36)$$

In order to make the supersymmetry breaking possible, the origin should be a maximum, by imposing that the second derivative is negative, the condition

$$(B\mu)^2 > (m_{H_u}^2 + \mu^2)(m_{H_d}^2 + \mu^2) \quad (1.37)$$

is obtained.

By introducing the parameter  $\tan\beta \equiv \langle H_u^0 \rangle / \langle H_d^0 \rangle$  such conditions can be written as:

$$\sin(2\beta) = \frac{2B\mu}{m_{H_u}^2 + m_{H_d}^2 + 2|\mu|^2} \quad (1.38)$$

$$m_Z^2 = \frac{|m_{H_d}^2 - m_{H_u}^2|}{\sqrt{1 - \sin^2(2\beta)}} - m_{H_u}^2 - m_{H_d}^2 - 2|\mu|^2 \quad (1.39)$$

	spin 0	spin 1/2	$(SU(3)_C, SU(2)_L, U(1)_Y)$
$Q$	$(\tilde{u}_L \tilde{d}_L)$	$(u_L d_L)$	$(\mathbf{3}, \mathbf{3}, \frac{1}{6})$
$\bar{U}$	$\tilde{u}_R^*$	$u_R^\dagger$	$(\bar{\mathbf{3}}, \mathbf{1}, -\frac{2}{3})$
$\bar{D}$	$\tilde{d}_R^*$	$d_R^\dagger$	$(\bar{\mathbf{3}}, \mathbf{1}, \frac{1}{3})$
$L$	$(\tilde{\nu} \tilde{e}_L)$	$(\nu e_L)$	$(\bar{\mathbf{1}}, \mathbf{2}, -\frac{1}{2})$
$\bar{E}$	$\tilde{e}_R^*$	$e_R^\dagger$	$(\bar{\mathbf{1}}, \mathbf{1}, 1)$
$H_u$	$(H_u^+ H_u^0)$	$(\tilde{H}_u^+ \tilde{H}_u^0)$	$(\bar{\mathbf{1}}, \mathbf{2}, +\frac{1}{2})$
$H_d$	$(H_d^0 H_d^-)$	$(\tilde{H}_d^0 \tilde{H}_d^-)$	$(\bar{\mathbf{1}}, \mathbf{2}, -\frac{1}{2})$
<i>gluon, gluino</i>	$g$	$\tilde{g}$	$(\mathbf{8}, \mathbf{1}, 0)$
$W, Winos$	$W^\pm, W^0$	$\tilde{W}^\pm, \tilde{W}^0$	$(\mathbf{1}, \mathbf{3}, 0)$
$B, bino$	$B^0$	$\tilde{B}^0$	$(\mathbf{1}, \mathbf{1}, 0)$

Table 1.2: Higgs bosons and sparticles in the MSSM with their partners.

Eq. 1.33 is not the most general form of the gauge invariant superpotential  $W$ ; the additional possible terms violate the  $B$  and  $L$  leptonic numbers and, since the experiments do not show such violations, we would like such terms are absent from the lagrangian. In order to obtain a lagrangian without such terms a new symmetry has been introduced.

The R-parity is defined as

$$P_R = (-1)^{3(B-L)+2s} \quad (1.40)$$

It is a discrete symmetry which allows to divide the SM particles from their supersymmetric partners. All SM particles have  $P_R = +1$ , while the sparticles have  $P_R = -1$ . An exact  $R$  parity symmetry makes the mixing between particle and sparticles impossible; this has two important consequences regarding the phenomenology of the model in collider experiments: (i) since the initial state is  $P_R = +1$ , the sparticles must be produced in pairs and (ii) the Lightest Supersymmetric Particle (LSP) must be stable. The latter property makes the SUSY models able to solve a cosmological issue, as reported in Sec. 1.1.3.

The electroweak symmetry breaking makes the gauge eigenstates (higgsinos and gauginos) to mix in order to form mass eigenstates. Their neutral components form the four so called *neutralinos*, indicated with  $\tilde{\chi}_i^0$ , and their charged components mix to form the two so called *charginos*, indicated with  $\tilde{\chi}_j^\pm$ , each one with charge  $\pm 1$ .

### 1.2.4 Mass spectrum in MSSM

#### Gauginos and Higgsinos

As already mentioned, the electroweak symmetry breaking  $SU(2) \times U(1) \rightarrow U(1)_{em}$ , leads to a mixing between the gauginos and the higgsinos.

The charged  $\psi^\pm$  components resulting from the mixing have the Lagrangian mass terms:

$$-\mathcal{L}_{MASS}^c = (\psi^-)^T \mathbf{X} \psi^+ + h.c \text{ with } \mathbf{X} = \begin{pmatrix} M_2 & \sqrt{2}M_W \sin\beta \\ \sqrt{2}M_W \cos\beta & \mu \end{pmatrix} \quad (1.41)$$

By diagonalizing such matrix, the lagrangian can be written in terms of the mass eigenstates,  $\chi^\pm$ , and the diagonal mass matrix  $M_c$ :

$$-\mathcal{L}_{MASS}^c = (\chi_k^-)^T (\mathbf{M}^c)_{km} \chi_m^+ + h.c \text{ with } \mathbf{M}^c = \begin{pmatrix} \tilde{M}_1 & 0 \\ 0 & \tilde{M}_2 \end{pmatrix} \quad (1.42)$$

So that:

$$-\mathcal{L}_{MASS}^c = \tilde{M}_1 \overline{\tilde{\chi}_1^+} \tilde{\chi}_1^+ + \tilde{M}_2 \overline{\tilde{\chi}_2^+} \tilde{\chi}_2^+ \quad (1.43)$$

The neutralinos mass term of the lagrangian can be obtained in an analogous way, leading to:

$$-\mathcal{L}_{MASS}^n = -\frac{1}{2} \sum_l \tilde{M}_l^n \overline{\tilde{\chi}_l^0} \tilde{\chi}_l^0 \quad (1.44)$$

where the  $\tilde{\chi}_l^0$  are the mass eigenstates and are ordered such that  $\tilde{M}_{\tilde{\chi}_1^0} < \tilde{M}_{\tilde{\chi}_2^0} < \tilde{M}_{\tilde{\chi}_3^0} < \tilde{M}_{\tilde{\chi}_4^0}$ . If a grand unified theory is assumed,  $M_1 = M_2$  at the GUT scale, while at weak scale they are related by:

$$M_1(M_Z) = \frac{5}{3} \tan^2 \theta_W M_2(M_Z) \sim \frac{1}{2} M_2(M_Z) \quad (1.45)$$

Some general features of the mass spectrum can be deduced, depending from the following cases:

- $|\mu| \gg |M_{1,2}| \gg M_Z$ : the  $\tilde{\chi}_1^0$  and  $\tilde{\chi}_2^0$  are mostly the neutral  $U(1)_Y$  and  $SU(2)_L$  gauginos (*bino* and *wino*),  $\tilde{\chi}_1^+$  is mostly the charged *winos*, while the heavier neutralinos and charginos are mostly respectively the neutral and charged higgsinos. From Eq.(1.45), the following rough relations between the masses can be derived:  $M_{\tilde{\chi}_1^\pm} \simeq M_{\tilde{\chi}_2^0} \simeq 2M_{\tilde{\chi}_1^0}$  and  $|\mu| \simeq M_{\tilde{\chi}_3^0} \simeq M_{\tilde{\chi}_4^0} \simeq M_{\tilde{\chi}_2^\pm} \gg M_{\tilde{\chi}_1^\pm}$ .

- $|\mu| \simeq M_2$  or  $|\mu| \simeq M_1$ : the strong mixing between the gauginos and the higgsinos makes the forecast on the masses difficult, nevertheless if  $|\mu|, |M_2| >> M_Z$  the relation  $M_{\tilde{\chi}_1^\pm} \simeq M_{\tilde{\chi}_2^0}$  is still valid.
- $\mu \ll |M_{1,2}|$ : the lighter neutralinos and lighter charginos are predominantly higgsinos and their masses are  $\sim |\mu|$ , while the heavier chargino is mostly the charged wino.

### Sfermions

The sfermion masses can arise from the three different contributions. Some coming from the soft part of the scalar potential, others arising from the F-terms and D-terms. The terms arising from the higgsinos in  $W$  and the ones coming from trilinear scalar couplings mix the left and right sfermions.

By writing the lagrangian density after the breaking of the electroweak symmetry, it is possible to realize that besides the L-R mixing, also the flavor mixing is allowed. The sfermion mass terms of the lagrangian can be written in a compact form by defining the vector  $\tilde{\mathbf{f}}$  and the matrix  $\mathcal{M}_{\tilde{\mathbf{f}}}^2$ :

$$\tilde{\mathbf{f}} = \begin{pmatrix} \tilde{f}_L \\ \tilde{f}_R \end{pmatrix}, \mathcal{M}_{\tilde{\mathbf{f}}}^2 = \begin{pmatrix} \mathcal{M}_{\tilde{f}_{LL}}^2 & \mathcal{M}_{\tilde{f}_{LR}}^2 \\ \mathcal{M}_{\tilde{f}_{RL}}^2 & \mathcal{M}_{\tilde{f}_{RR}}^2 \end{pmatrix}, \quad (1.46)$$

$\tilde{\mathbf{f}}$  is a six component vector since  $\tilde{f}_R$  can be  $\tilde{u}_R, \tilde{d}_R, \tilde{e}_R$  and  $\tilde{f}_L$  can be  $\tilde{u}_L, \tilde{d}_L, \tilde{e}_L$  and  $\tilde{\nu}_L$  and the matrix  $\mathcal{M}_{\tilde{\mathbf{f}}}^2$  is a  $2 \times 2$  Hermitian matrix of  $3 \times 3$  blocks. In such a way the lagrangian term associated to the sfermions masses reads:

$$-\mathcal{L}_{\tilde{f}_{mass}} = \sum_{\tilde{\mathbf{f}}} \tilde{\mathbf{f}}^\dagger \mathcal{M}_{\tilde{\mathbf{f}}}^2 \tilde{\mathbf{f}} \quad (1.47)$$

The mass eigenstates  $\tilde{\mathbf{f}}^m$  can be obtained through a the unitary matrices which diagonalize the  $\mathcal{M}_{\tilde{\mathbf{f}}}^2$ :

$$\tilde{\mathbf{f}}^m = \mathbf{W}^{\tilde{\mathbf{f}}^\dagger} \tilde{\mathbf{f}}, \quad \mathcal{M}_{\tilde{\mathbf{f}}}^{2(diag)} = \mathbf{W}^{\tilde{\mathbf{f}}^\dagger} \mathcal{M}_{\tilde{\mathbf{f}}}^2 \mathbf{W}^{\tilde{\mathbf{f}}} \quad (1.48)$$

It is useful considering the lightest sfermions of the three generations, namely  $\tilde{\tau}$ ,  $\tilde{b}$  and  $\tilde{t}$ . The MFV hypothesis leads to make the assumption that they are not coupled to the other generation sfermions. Therefore the flavor mixing terms can be supposed absent, on the contrary the L-R mixing gives rise to two mass eigenstates for each of them:  $\tilde{\tau}_1, \tilde{\tau}_2$ ,  $\tilde{b}_1, \tilde{b}_2$  and  $\tilde{t}_1, \tilde{t}_2$ . Since the  $\tilde{t}$  is supposed to be the lightest sfermion, it is worth looking at the explicit form of its mass matrix:

$$\mathcal{M}_{\tilde{t}}^2 = \begin{pmatrix} m_{\tilde{q}_3}^2 + (1/2 - 2/3 \sin^2 \theta_W) M_Z^2 \cos 2\beta + m_t^2 & -m_t(A^{t*} + \mu \cot \beta) \\ -m_t(A^t + \mu^* \cot \beta) & m_{\tilde{t}}^2 + 2/3 M_Z^2 \cos 2\beta \sin^2 \theta_W + m_t^2 \end{pmatrix} \quad (1.49)$$

Given the proportionality of the off diagonal terms to the top mass, the L-R mixing is larger compared to the other quark mixing.

### Higgs bosons

In the MSSM, there are two Higgs doublets and the mass eigenstates are:  $m_h < m_A |\cos 2\beta| < m_H$ . The Eq.1.38, for large  $\tan \beta$  reads:

$$m_Z^2 = -2(m_{H_u}^2 + |\mu|^2) + \frac{2}{\tan^2 \beta} (m_{H_d}^2 - m_{H_u}^2) + \mathcal{O}(1/\tan^4 \beta) \quad (1.50)$$

At tree level the relation  $m_{h^0} < m_Z |\cos(2\beta)|$  should be valid and the lightest Higgs boson would be in a mass range already explored at LEP. Nevertheless  $m_{h^0}$  undergoes large corrections, the main ones coming from top and stop loops, they are illustrated in Fig. 1.1.

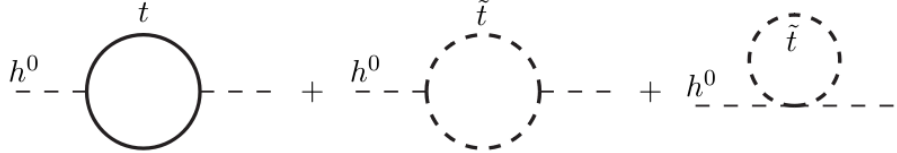


Figure 1.1: Top and stop loops corrections to the lightest Higgs mass.

If the squark masses are positive at the scale where  $M_{H_u} = M_{H_d}$ , they remain positive also at electroweak scale. At tree level  $m_t = y_t v \sin \beta$ ,  $m_b = y_b v \cos \beta$  and  $m_\tau = y_\tau v \cos \beta$ . Some models assume the unification of the three couplings at the GUT scale, so that  $\tan \beta \sim m_t/m_b$ . Radiative electroweak symmetry breaking is possible only if

$$\tan \beta \equiv \frac{\langle H_u^0 \rangle}{\langle H_d^0 \rangle} < \frac{m_t(m_t) S_t^{1/2}}{m_b(m_t) S_b^{1/2}} \sim 60 \sqrt{\frac{S_t}{S_b}} \quad (1.51)$$

where  $S_t \equiv m_{H_u}^2 + m_{\tilde{Q}_3}^2 + m_{\tilde{t}_R}^2 + |A^t|^2$  and  $S_b \equiv m_{H_d}^2 + m_{\tilde{Q}_3}^2 + m_{\tilde{b}_R}^2 + |A^t|^2$ .

In many models of broken symmetry,  $S_t \sim S_b$ , so that  $\tan \beta < 60$ .

The  $\mathcal{L}_{soft}$  in Eq.(1.29) in MSSM is a function of the following parameters.

- The complex gauginos masses  $M_{1,2,3}$ , of the gaugino  $\lambda_0$  associated to the  $U(1)_Y$ ,  $\lambda$  associated to  $SU(2)_L$  and the gluinos  $\tilde{g}^a$  associated to the  $SU(3)_C$ . The real Higgs scalar mass parameters  $m_{1,2}$  (related by the bilinear coefficients  $\mathcal{B}_{ij}$  in Eq.(1.29)).

	spin	$P_R$	gauge eigenstates	mass eigenstates
<i>Higgs Bosons</i>	0	+1	$H_u^0 \ H_d^0 \ H_u^+ \ H_d^-$	$h^0 \ H^0 \ A^0 \ H^\pm$
<i>squarks</i>	0	-1	$\tilde{u}_L \ \tilde{u}_R \ \tilde{d}_L \ \tilde{d}_R$ $\tilde{s}_L \ \tilde{s}_R \ \tilde{c}_L \ \tilde{c}_R$ $\tilde{t}_L \ \tilde{t}_R \ \tilde{b}_L \ \tilde{b}_R$	$\tilde{t}_1 \ \tilde{t}_2 \ \tilde{b}_1 \ \tilde{b}_2$
<i>sleptons</i>	0	-1	$\tilde{e}_L \ \tilde{e}_R \ \tilde{\nu}_e$ $\tilde{\mu}_L \ \tilde{\mu}_R \ \tilde{\nu}_\mu$ $\tilde{\tau}_L \ \tilde{\tau}_R \ \tilde{\nu}_\tau$	$\tilde{\tau}_1 \ \tilde{\tau}_2 \ \tilde{\nu}_\tau$
<i>Neutralinos</i>	$\frac{1}{2}$	-1	$\tilde{B}^0 \ \tilde{W}^0 \ \tilde{H}_u^0 \ \tilde{H}_d^0$	$\tilde{\chi}_1^0 \ \tilde{\chi}_2^0 \ \tilde{\chi}_3^0 \ \tilde{\chi}_4^0$
<i>Charginos</i>	$\frac{1}{2}$	-1	$\tilde{W}^\pm \ \tilde{H}_u^+ \ \tilde{H}_d^-$	$\tilde{\chi}_1^\pm \ \tilde{\chi}_2^\pm$
<i>Gluino</i>	$\frac{1}{2}$	-1	$\tilde{g}$	
<i>Goldstino</i>	1/2	-1	$\tilde{G}_{1/2}$	
<i>Gravitino</i>	3/2	-1	$\tilde{G}_{3/2}$	

Table 1.3: Sparticles in MSSM, both gauge eigenstates and mass eigenstates (when different from the gauge eigenstates) are reported.

- Furthermore there are  $3 \times 3$  matrices in the generations space, the hermitian  $\mathcal{M}_{\tilde{q}}^2$  (left squark masses)  $\mathcal{M}_{\tilde{u}}^2, \mathcal{M}_{\tilde{d}}^2$  (right squark masses),  $\mathcal{M}_{\tilde{l}}^2$  (left sleptons) and  $\mathcal{M}_{\tilde{e}}^2$  (right sleptons).
- The coefficients of the trilinear terms, which are the complex  $3 \times 3$  matrices  $f^e A^e, f^d A^d, f^e A^e$  ( $f A \equiv \mathcal{A}$  in Eq.(1.29)).
- The linear term is absent because in MSSM there is not a  $\phi$  field invariant under  $SU(3)_c \times SU(2)_L \times U(1)_Y$ , so  $\mathcal{C} = 0$ .

If every one of such parameters is complex, after subtracting some non physical ones, we are left with 124 degrees of freedom, so besides the 19 parameters of the SM, there would be other new 105 ones.

Despite the MSSM is useful to give an idea of the sparticle phenomenology, it is just an effective theory. Indeed it can not account for the dynamical supersymmetry breaking and the explicit soft supersymmetry breaking makes the number of parameters of the model very large to be considered a fundamental theory.

The dimension of the parameter space can be considerably reduced by making theoretical assumptions. Furthermore, as already mentioned in Sec.1.2.2, an hidden sector, where the SSB occurs, should be connected to the observable sector.

These and other issues lead to think that another scale, different from the EW scale, is involved in the theory and it should be much larger than  $\mathcal{O}(\text{TeV})$  scale. The connection between the two very different scales is possible through the Renormalization Group Evolution (RGE) and described in the next section.

### 1.2.5 The link between two different scales

The values of every parameter of the Lagrangian density at one scale, in example the Plank scale, can be related to the values at another scale, as the TeV scale probed by the actual colliders, by using the RGE. The renormalization conditions are imposed at some arbitrarily chosen scale  $Q$  (renormalization scale) and the dependence of each parameter quoted in the previous section from  $Q$  is given by the Callan-Symanzik equations [15] which depend on the particular gauge group of the theory. By making assumptions on the breaking terms it is possible to estimate the values of some parameters by following the RGE to the scale which can be explored by the current experiments and verify that the assumptions are compatible with the experimental results.

Therefore the experimental research at low energies allows to restrict the possible models and, hopefully, by finding some general principle, to reduce the many free parameters in the Lagrangian. The most important contributions from the low energy physics to the construction of the supersymmetric models come from the following issues.

- Flavor Changing Neutral Current (FCNC) processes are forbidden in SM tree level, at higher orders they are possible but strongly suppressed; this is in agreement with the experimental results, while the general SUSY models do not contain such property, this is called the *SUSY flavor problem*; therefore a requirement that this property maintains also in SUSY models, should be introduced.
- In SM the CP violation is suppressed in agreement with precise measurements, while in MSSM many phases could be the sources of CP violation. This is referred to as the *SUSY CP problem*.

The source of FCNC and CP violation in SUSY is due to the soft mass terms and the trilinear couplings. Both SUSY flavor and CP problems can be solved by making an assumption (*universality*) on the soft SUSY breaking masses. Indeed,

by assuming that both the mass matrices  $\mathcal{M}_Q^2$  and the Yukawa couplings matrices  $f_{ij}A_{ij}$  are diagonal, the FCNC contributions are within the experimental bounds and the only sources of CP violation are due to the Yukawa couplings, like in the SM.

Moreover given the amount of the third family Yukawa couplings compared to the first two families ones, it can be assumed that only the matrix elements concerning the third generation fermions are not negligible ( $A_{\tilde{t}}$ ,  $A_{\tilde{b}}$  and  $A_{\tilde{\tau}}$ ), while all the others are assumed null.

The scenario in which the breaking of flavor universality (the symmetry which would exist in SM without the Yukawa sector) is induced only by the Yukawa interaction, is named Minimal Flavor Violation (MFV) [16].

The rigorous definition of MFV is in [16], its physical meaning is that the dynamics of Flavor Violation is completely determined by the structure of the ordinary Yukawa couplings.

By making such assumptions, the RGE for the coupling constants is:

$$\frac{1}{g_i(Q)^2} - \frac{1}{g_i(Q_0)^2} = -\frac{b_i}{2\pi^2 \ln\left(\frac{Q}{Q_0}\right)} \quad (1.52)$$

With  $\alpha_i = g_i^2/4\pi$  and imposing the initial values  $\alpha_1$ ,  $\alpha_2$  and  $\alpha_3$  at  $Q = M_Z$ , the trend obtained is shown in Fig.1.2.

Unlike for the Standard Model, in which there is no match between the three couplings (even taking into account the experimental uncertainties of the input values at EW scale), in the MSSM the three gauge coupling constants match at  $Q \simeq 2 \times 10^{16}$ GeV. Such feature maintain for every value of the sparticles mass in the range between  $M_Z$  and  $\mathcal{O}(1)$ TeV. Therefore the MSSM can be some remnant of a Grand unified supersymmetric theory with superpartners around the TeV scale; for this reason the common value of couplings at the matching scale is indicated with  $g_{GUT}$ .

### 1.2.6 The Constrained Minimal Supersymmetric Standard Models

In the so called Constrained Minimal Supersymmetric Standard Model (CMSSM) all the soft SUSY-breaking scalar masses, gauginos masses and the trilinear term are assumed to be universal at the GUT scale, namely:

$$g_1 = g_2 = g_3 \equiv g_{GUT} \quad (1.53)$$

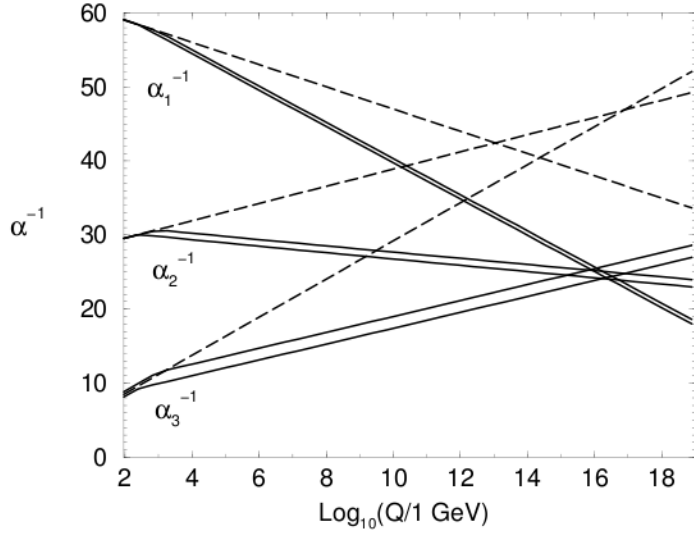


Figure 1.2: RG evolution of the  $\alpha^{-1}(Q)$  in the Standard Model (dashed lines) and the MSSM (solid lines). In the MSSM case, the sparticle mass thresholds are varied between 250 GeV and 1 TeV, and  $\alpha^3(m_Z)$  between 0.113 and 0.123. Two-loop effects are included. [5].

$$M_1 = M_2 = M_3 \equiv m_{1/2} \quad (1.54)$$

$$m_{Q_i}^2 = m_{U_i}^2 = m_{D_i}^2 = m_{L_i}^2 = m_{E_i}^2 = m_{H_u}^2 = m_{H_d}^2 \equiv m_0^2 \quad (1.55)$$

$$A_t = A_b = A_\tau \equiv A_0 \quad (1.56)$$

By using the Renormalization Group Evolution (RGE) is possible to obtain every parameter of the theory at the EW scale. In such scenario the number of free parameters is strongly reduced, allowing for the study of supersymmetry phenomenology. In the range of the PMSB, this is what is called **minimal SUper-GRAvity (mSUGRA)** and is one of the most used models by experiments to make simulations of susy signals.

If the gravity is included in the model the parameters  $\epsilon_\alpha$  (see Sec. 1.2.1) should vary in the space-time leading in a natural way to a local gauge symmetry (*super-gravity*).

In order to cancel the new terms due to the local transformation a new field is introduced: it must be fermionic, with a  $\mu$  space time index and spin 3/2. It is the gauge fermion of the local gauge supersymmetry which eats the Goldstino.

It is called *gravitino*, its mass is indicated by  $m_{3/2}$  and is the superpartner of the *graviton*.

Besides the  $m_0$ ,  $m_{1/2}$  and  $A_0$ , the other parameters of the model are the universal bilinear coupling  $B$  introduced in Sec. 1.2.3 and the  $\mu$  parameter introduced in Sec. 1.1. Since the  $M_Z$  value is fixed by the experiments results,  $|\mu|$  can be expressed as a function of the others parameters and the electroweak symmetry breaking imposes its magnitude, so only its sign remains a free parameter. By introducing the parameter  $\tan\beta \equiv \langle H_u^0 \rangle / \langle H_d^0 \rangle$ , the  $B$  can be expressed as a function of  $\tan\beta$  and  $\mu$ , therefore the free parameters of the mSUGRA model are:

$$m_0, \quad m_{1/2}, \quad A_0, \quad \tan\beta, \quad \text{sign}(\mu) \quad (1.57)$$

In such a model the mass spectrum is determined by choosing only four parameters and a sign, instead of 124 parameters, as in MSSM with soft supersymmetry breaking.

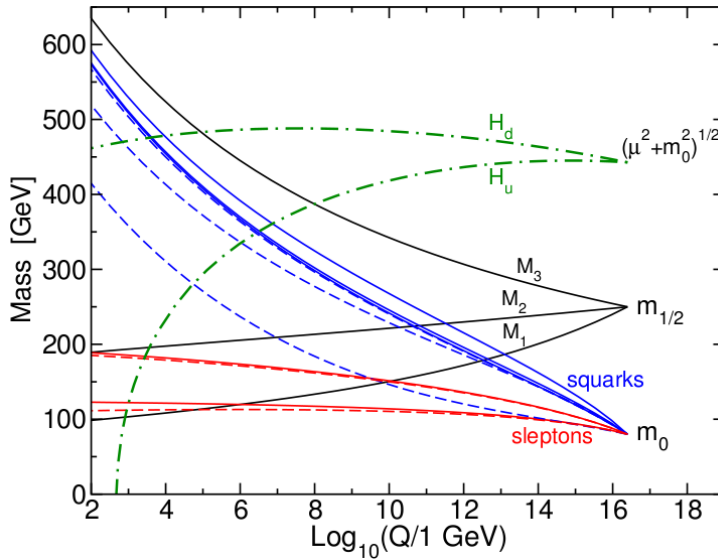


Figure 1.3: Example of the running of a specific model parameters [5].

The mass spectrum of the sparticles is determined by choosing the value of these five parameters, by imposing the absence of extra CP violation and electroweak symmetry breaking.

Also in the GMSB scenario a minimal version has been developed, the so called **mGMSB** model. In GMSB models the messenger superfields are vector like representations of  $SU(3)_C \times SU(2)_L \times U(1)_Y$ , they are representations of  $5 \oplus \bar{5}$  and their number is named  $n_5$ . Sfermion masses and gauginos masses are of the same

order, on the contrary the trilinear A-parameters are smaller and they are often assumed to be null. In this model, since scalar masses receive contributions only by two loops terms, also the Higgs masses are lower than the sfermions ones. This gives rise to a messenger mass  $M_M \sim m_{soft} \sim \mathcal{O}(50 \text{ TeV})$ .

The soft supersymmetry breaking parameters have gravity mediated contributions in every supersymmetric theory including gravity [14], therefore also in the mGMSB model there must exist terms  $\propto \langle F_S \rangle / M_{Pl}$  and they are assumed to be  $<\sim 0.1\%$  of the contributions from gauge interactions. The gravitino mass is

$$m_{3/2} \simeq \frac{1}{M_{Pl}} \sqrt{\frac{1}{3} \sum_i |\langle F_i \rangle|^2} \quad (1.58)$$

in this scenario it is preferred to be very light and in many models it is the LSP. The free parameters used to describe this scenario are:

$$m_{soft}, \quad M_M, \quad n_5, \quad \tan\beta, \quad \text{sign}\mu \quad (1.59)$$

It is not useful considering only one model in order to perform a SUSY search, and often the models are not driven by physical motivation, but only by simplicity. Nevertheless, focusing on a specific model can be useful to perform complete simulation in order to get an idea of the possible signature arising from the detected final states.

Therefore, although keeping in mind that a specific simplified model is not indicative of the reality, the developing of the analysis described in the next chapters has been performed considering as signal some particular points of the *mSUGRA* scenario. For such reason the next section describes the main features of this model.

### Mass spectrum in mSUGRA

The equations of the Renormalization Group are differential coupled equations and it is not possible to analytically solve them, therefore numerical methods are used in order to obtain the mass spectrum, namely the masses of the sparticles at the weak scale, of a specific model. The condition that every gaugino masses match at the unification scale and the fact that  $M_\alpha$  and  $g_\alpha^2$  running are related by  $d(M_\alpha/g_\alpha^2)/d(\ln(Q/Q_0)) = 0$  [14], imply that at every point of the RGE, from the unification scale to the EW scale they are related by  $M_3 : M_2 : M_1 = g_3^2 : g_2^2 : 5/3g_1^2$  and at the EW scale  $M_1 : M_2 : M_3 \sim 1 : 2 : 7$ . Despite complications due to the mixing, these relations show that there is a considerable mass splitting between the gluino and the lighter charginos and neutralinos. Some other general properties

which hold in most of space parameters of the mSUGRA models are the following. The lightest stop, sbottom and stau are lighter than their counterparts of the first two generations. Squarks are heavier than sleptons, Right-handed sfermions are lighter than left-handed sfermions.

If  $m_0$  increases, all masses rise considerably except the lightest Higgs and the gauginos, which are nearly constant and all the masses increase with increasing  $m_{1/2}$ . The masses of the gauginos and the first two generations of sfermions hardly depend on  $\tan\beta$ . The mass of the lightest Higgs is constant for large  $\tan\beta$ , but drops considerably if  $\tan\beta$  becomes small.

By changing the values of the 5 parameters, a different mass spectrum is obtained. The simulation of the entire procedure, from the physical process generation till the full simulation of the detector is an expensive task, in term of time and space, therefore it is not possible to check the final detected products of every one of the infinite points of the 5-dimensional parameters space. In order to have an idea of the typical signatures which SUSY can lead at LHC, the experiments chose a little number of points, named benchmark points, and perform the entire simulation for them. In CMS collaboration, the benchmark points for mSUGRA are called LMX (Low Mass X). Every one gives rise to a different mass spectrum and a different SUSY production cross section. With LHC running at  $\sqrt{s} = 7$  TeV, the benchmark point of the mSUGRA model with the largest cross section is the so called LM0. It is defined by the following values for the parameters:  $m_0 = 200$ ,  $m_{1/2} = 160$ ,  $\tan\beta = 10$ ,  $\text{sign}\mu = +$ ,  $A_0 = -400$ . The cross section of a sparticle pair production is 39 pb and the resulting mass spectrum is indicatively shown in Fig.1.4.

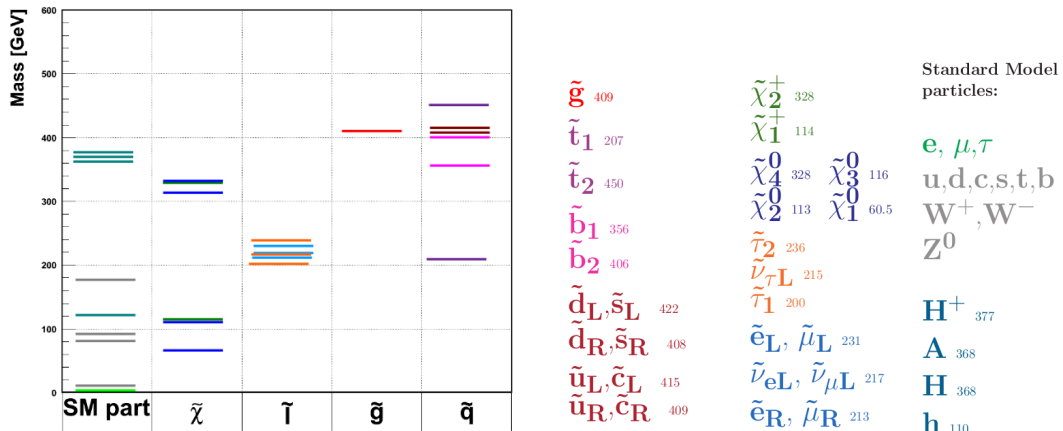


Figure 1.4: Indicative mass spectrum for the LM0 point in mSUGRA model.

### 1.2.7 SUSY answers to the SM problems

In Sec.1.1 some limitations of the Standard Model were reported. In the introduction of the supersymmetry of the previous sections, some hints of the answers which susy can provide to such SM issues, were given. A review of the way SUSY could solve the SM problems is given more explicitly in the following.

- **The Hierarchy problem**

As reported in Sec. 1.1.2, the quadratic corrections to  $m_H^2$  are:

$$\Delta m_H^2 = \frac{1}{8\pi^2} \left( \frac{1}{2} \lambda_S - |\lambda_f|^2 \right) \Lambda_{UV}^2 + \dots \quad (1.60)$$

The introduction of a new bosonic (fermionic) field for every fermionic (bosonic) SM field, means adding a new term for every term in Eq. 1.2.7. Because of the relations between the Yukawa couplings, the new terms have the same module and opposite sign of the SM terms; as illustrated in Fig. 1.5 the supersymmetric vertices  $-\frac{1}{2} y^{ijk} \phi_i \psi_j \psi_k$  and its conjugate appear on the fermion loop diagram, while the  $-\frac{1}{4} y^{ijm} y_{klm} \phi_i \phi_j \phi^{*k} \phi^{*l}$  is in the scalar loop, therefore in this way a systematic cancellation of the divergences is obtained.

This explains the large difference between the electroweak and the new

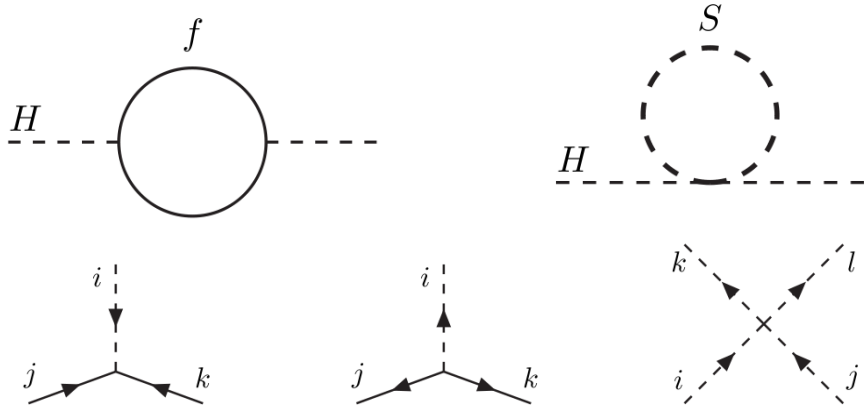


Figure 1.5: Up: the fermionic and scalar loops to the Higgs field. Down: the vertices of the Yukawa interactions of the scalar-fermion-fermion vertex, its conjugate, and the quartic scalar interactions.

physics scales without fine tuning at tree level. The stability of this hierarchy, namely the holding also at upper orders (*naturalness*), is obtained in SUSY models provided the mass gap between the sparticles and their SM

partners is less than  $\mathcal{O}(TeV)$ . In this range of mass, the naturalness is assured by the fact that in Supersymmetry gauge theory superpotential (1.19) does not receive any renormalization to any order of in perturbation theory, therefore no counterterms associated to the superpotential are needed [5].

- **EW spontaneous symmetry breaking** The scalar potential for the Higgs scalar fields, after imposing that the electroweak symmetry is broken, is reported in Eq. 1.34.

The RGE makes possible that the  $m_{H_u}^2$  parameter is negative at the EW scale, and this is what is needed to explain the SM  $SU(2) \times U(1)$  Electro Weak symmetry breaking.  $m_{H_u}^2$  can be negative at weak scale, thought other mass terms remain positive; The mechanism which make  $m_{H_u}^2$  negative at weak scale, thought other mass terms remain positive, is named *Radiative Electro Weak Symmetry Breaking* (REWSB), it can be considered as a dynamical explanation of the negative sign of the squared Higgs mass in the SM (solving one of the SM problems which is reported in Sec.1.1.2), and it relates the supersymmetry breaking to the electroweak symmetry breaking. The large difference between the value of the physical Higgs mass, leading to a positive  $m_{H_u}^2(\text{phys})$  parameter, and the bare one, is mainly due to the top and stop loop corrections mentioned in Sec.1.2.6.

- **candidate for dark matter**

As reported in Sec.1.2.3, the R parity is needed in order to get rid of the terms which violate B and L and such symmetry implies that the lightest supersymmetric particle is stable. On the cosmological side, it is known that the most of the matter in the universe is unknown and characterized by neutral particles. Therefore the LSP can be a Dark Matter candidate provided that it is neutral, thus by inferring the only missing feature to the LSP, it becomes a suitable way to solve the cosmological problem. For this reason the favorite candidates for the LSP are electrically neutral and colorless sparticles: gravitino, the lightest sneutrino and neutralino. Which the particular sparticle embodying the LPS is, depends on the specific model, and general arguments can be derived by distinguishing between the two scenarios of the communication of the supersymmetry breaking. In the PMSB the lightest neutralino is the most favorite candidate to be the LSP the possibility that sneutrinos are lighter than neutralinos is not excluded but less likely. On the contrary in GMSB, given the large range of possible values

of the messenger scale, the gravitino can be very light and it is very likely that it is the LSP. If it is the case the second lightest sparticle is called Next to Lightest Supersymmetric Particle (NLSP). As reported in Sec.1.1.3, from the measured value of  $\Omega_{DM} h$  the value  $\langle \sigma v \rangle$  of the particles can be extracted so that constraints can be derived on the supersymmetric models in order to make the LSP candidate suitable to embody the WIMPs.

- **Asymmetry matter-antimatter** The electroweak baryogenesis according to SUSY models occurred in the following way. At temperatures well above the electroweak scale in the early universe the full  $SU(2)_L \times U(1)_Y$  electroweak gauge symmetry is unbroken. As the universe cools, this symmetry is broken spontaneously down to the  $U(1)_{em}$  gauge symmetry of electromagnetism. This electroweak phase transition is strongly first order and is able to generate a chiral asymmetry which is transformed into a net baryon number density [8].

## 1.3 Experimental Bounds on SUSY Models

The study of the SUSY can be performed by following two different approaches [17]. In the *bottom-up* approach, the SM Lagrangian is the renormalizable part of a more general local Lagrangian, which includes higher-dimensional operators. These operators are constructed in terms of SM fields and suppressed by inverse powers of an effective scale  $\Lambda_{NP} > M_W$ .

Instead the *top-down* approach tries to guess the structure of the new physics in the ultraviolet region, specifying the new fields. It is more predictive but also more model dependent.

For the time being the *bottom-up* approach is preferred, it is used to derive some general principles from experimental results, by analyzing models beyond SM with few parameters. If new physics will manifest at TeV region, because of the arguments in Sec.1.1.2, the new theory should have a non generic structure and some constraints can be imposed to its form by considering the experimental information.

In principle if the number of observables is greater than the number of free parameters of the model, the latter can be tested. A list of some observables sensitive to susy, and the way they can be useful to claim or to set limits to susy signals, is given in the following.

### 1.3.1 Bounds from Flavor Physics

$b \rightarrow s\gamma$

In the SM the decay  $b \rightarrow s\gamma$  is suppressed and occurs through the  $tW^-$  loop. The experimental value obtained by The Heavy Flavor Averaging Group (HFAG) is  $BR(B \rightarrow X_s\gamma) = (352 \pm 23 \pm 9) \times 10^{-6}$  [18].

In Supersymmetry scenario this decay can occur via several other loops, the leading order contributions are shown in Fig. 1.6. The  $b \rightarrow s\gamma$  decay rate is to be calculated

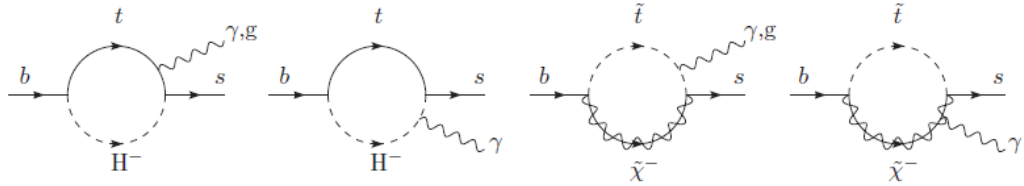


Figure 1.6: Leading order loops contribution to  $b \rightarrow s\gamma$  in susy.

at  $m_b$  scale, where the QCD coupling is large and leads to divergences therefore the use of the RGE is needed. At scale  $Q < m_W$  an effective Hamiltonian is used, and the assumption that the two theories match at the  $Q = m_W$  scale is imposed. The full calculation procedure is very complicated and suffers from several uncertainties (QCD corrections, the choice of the scale, next to leading contributions,..), moreover it depends on the parameters of the SUSY model.

### $B_s \rightarrow \mu^+\mu^-$ decay

In the framework of the SM the decay  $B_s \rightarrow \mu^+\mu^-$  and  $B_d \rightarrow \tau^+\tau^-$  are suppressed because they are FCNC. The latter can be studied especially at B Factories, in the following only the former is dealt with. In Fig. 1.7 the SM diagram of  $B_s \rightarrow \mu^+\mu^-$  is shown. Its branching ratio has been calculated to be  $BR(B_s \rightarrow$

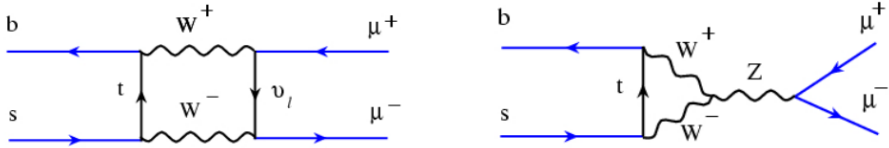


Figure 1.7: Contribution diagrams to  $B_d \rightarrow \tau^+\tau^-$  in the Standard Model contest

$\mu^+\mu^-) = (3.4 \pm 0.4) \times 10^{-9}$  [19]. The latest experimental result has been obtained

at Tevatron by the CDF collaboration with an integrated luminosity of  $3.7 \text{ fb}^{-1}$  and the result is  $BR(B_s \rightarrow \mu^+ \mu^-) < 3.6 \times 10^{-8}$  at 90 % C.L [20]. In MSSM the matter multiplets with weak isospin  $T_3 = 1/2$  couple only to  $\hat{H}_u$  and  $T_3 = -1/2$  only with  $\hat{H}_d$  in MSSM a tree level, this leads to the suppression of FCNC processes. Nevertheless, there are one loop contributions, which allow for the coupling between  $H_u$  and  $T = -1/2$  fermions and, as a consequence, flavor-violating couplings of the neutral Higgs scalars can occur. Such couplings can become manifest by the study of the processes  $B_s \rightarrow \mu^+ \mu^-$  and  $B_d \rightarrow \tau^+ \tau^-$  because such decays occur through the neutral Higgs bosons. In the framework of mSUGRA model, the branching fractions for such decays are very sensitive to  $\tan\beta$  and  $A_0$  values, in particular they can be also  $\mathcal{O}(10^3)$  greater than the SM values.

Fig. 1.8 shows the contours of  $BR(B_s \rightarrow \mu\mu) = 10^{-7}$  in the  $m_0-m_{1/2}$  plane of the mSUGRA model for  $\mu > 0$  and  $\mu < 0$  and for several values of  $\tan\beta$ .

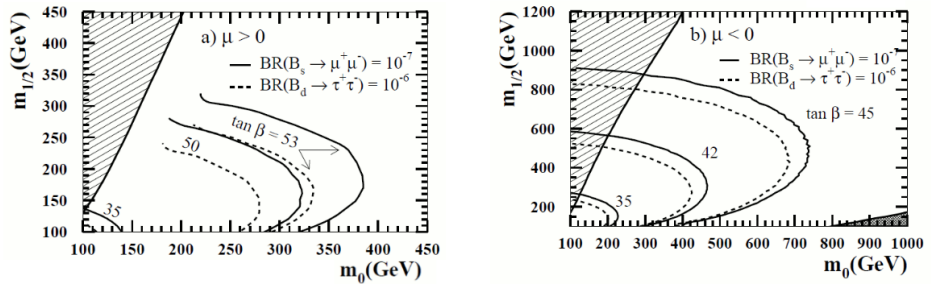


Figure 1.8: [21]Contours in the  $m_0$ - $m_{1/2}$  plane of the mSUGRA model with  $A_0 = 0$  where the branching fraction for  $B_s \rightarrow \mu^+ \mu^-$  ( $B_s \rightarrow \tau^+ \tau^-$ ) is  $10^{-7}$  ( $10^{-6}$ ) for several values of  $\tan\beta$ . In the striped region the  $\chi_1^0$  is not the LSP and the dark-shaded region in the b) figure is excluded by theoretical constraints on EWSB.

### 1.3.2 Muon anomalous magnetic momentum

The parameter  $a_\mu = (g - 2)_\mu/2$ , the muon magnetic momentum, has been measured with a precision better than  $10^{-6}$  by the  $(g - 2)_\mu$  collaboration of the BNL experiment [22]. The measured value is  $a_\mu^{exp} = (11659208.0 \pm 6.3) \times 10^{-10}$ .

The calculated value in the SM including the one loop and two loop EW contributions have been calculated and are  $a_\mu^{EW} = (15.4 \pm 0.02) \times 10^{-10}$ ; therefore the discrepancy between the experimental value and the theoretical value including QED and EW is  $\Delta(exp, theo_{QED+EW}) = (720.8 \pm 6.3) \times 10^{-10}$ . It is clear that the calculation of the hadronic contribution is needed. The  $a_\mu^{hadLO}$  depends mainly on

the cross section of  $e^+e^- \rightarrow \gamma^* \rightarrow \text{hadrons}$  which is measured by several experiments working at  $e^+e^-$  colliders (CMD-2 [23], SND [24], KLOE [25], BABAR [26]) and a 0.6 % of accuracy has been obtained. By using them the hadronic contribution calculated is  $a_\mu^{\text{hadronic}} = (689.8 \pm 5) \times 10^{-10}$  [27] leading to a resulting SM value:

$$a_\mu^{SM} = (11659177.0 \pm 5.0) \times 10^{-10} \quad (1.61)$$

Therefore  $a_\mu^{\text{exp}} - a_\mu^{SM} = (31.0 \pm 8.1) \times 10^{-10}$  which corresponds to  $3.8\sigma(a_\mu)$ . In Supersymmetric models other contributions to  $a_\mu$  exist, they are given by the  $\tilde{W}_i$ - $\tilde{\nu}_\mu$  and  $\tilde{Z}_i$ - $\tilde{\mu}_j$  loops and are:

$$\Delta a_\mu^{\text{SUSY}} \propto \frac{m_\mu^2 \mu M_i \tan\beta}{M_{\text{SUSY}}^4} \quad (1.62)$$

where  $M_{\text{SUSY}}$  is the characteristic mass of the sparticle in the loop and  $M_i$  is the gaugino mass. This relation states that  $\Delta a_\mu^{\text{SUSY}}$  grows with  $\tan\beta$  and has the same sign of  $\mu$ . The latter has implications in the dealing with SUSY models; in mSUGRA the  $\text{sign}(\mu)$  is one of the five free parameters, therefore, if the experimental value of the  $a_\mu$  is taken into account to constrain the model,  $\text{sign}(\mu)$  should be positive.

### 1.3.3 Direct Searches of SUSY at Colliders

In the previous sections the experimental bounds on SUSY models available for the time being, were reported. They relies on measurements performed at low energy physics and that provide limitations on parameters existing in several models. Therefore they represent an indirect way to probe SUSY.

Although such measurements are important and useful to invalidate or setting limits in the space parameters of some models, the only way to claim that the supersymmetry exists is through a direct observation of superparticles.

Furthermore, the several constructed models relies strongly on the masses and couplings of the new particles, therefore only their observation can really discriminate among the many models.

The search for supersymmetry started in the early '80 with  $e^+e^-$  collision experiments, then continued with  $Spp\bar{S}$  collider at CERN, where the last limit was set by the UA2 experiment. It collected data at a center of mass energy of  $\sqrt{s} = 630$  GeV and measured the limits:  $m_{\tilde{q}} > 74$  GeV and  $m_{\tilde{g}} > 79$  GeV, leaving the possibility for the existence of a light gluino  $m_{\tilde{g}} < 4$  GeV [28]. Since 1989 to 2000

SUSY searches were performed at LEP and LEP2 where several limits to the sparticles masses were set, in the range of many models in addition to the Higgs boson search [29]. The last collider were SUSY has been looked for, and where the data analysis are still on going, is Tevatron. D0 and CDF experiments have performed many searches setting lower limits to sparticles masses and upper limits to cross sections of SUSY processes. Up to now no evidence of SUSY has been observed.

## 1.4 Direct Searches of SUSY at LHC

The LHC will reach center of mass energy never explored so far and, in case SUSY exists, the CMS detector is suitable for detect it. In the following some hints about the SUSY phenomenology which is possible to observe at LHC are given.

### 1.4.1 Production of Sparticles

At LHC the sparticle production occurs via the collisions between the constituents of the protons and the production cross sections are calculated in the framework of the parton model. Every cross section of the partonic processes  $\hat{\sigma}(ab \rightarrow cd)$  can be computed by using the MSSM; by calling  $A$  the hadron containing  $a$  and  $B$  the hadron containing  $b$  the the cross section of the hadronic process is, like every SM process at hadron collider:

$$d\sigma(AB \rightarrow c + d + X) = \sum_{a,b} \int_0^1 dx_a \int_0^1 dx_b f_{a/A}(x_a, Q^2) f_{b/B}(x_b, Q^2) d\hat{\sigma}(ab \rightarrow cd) \quad (1.63)$$

where  $X$  represents eventual additional hadronic production,  $f_{a/A}(x_a, Q^2)$  and  $f_{b/B}(x_b, Q^2)$  are the Parton Distribution Functions (PDFs). From the discussion in Sec. 1.2.3 on the implications of the R-parity, is clear that at LHC the sparticles can be produced only in pairs. In the following some possible sparticle productions directly from the proton proton collisions are listed, some their features and the way they can be detected is reported.

**Sleptons and sneutrinos.**  $\tilde{l}\tilde{\nu}_l$  They can be produced only by electro-weak interactions so their rates are very low compared to Standard Model processes. Therefore, despite their clean signature, especially in the final state with no jets, the disentanglement from background would be difficult. Unless there exist the GMSB scenario with a short lived  $\tilde{\chi}_1^0$  NLSP such to give rise to the characteristic signature  $ll\gamma\gamma\cancel{E}_T$ .

**Charginos and Neutralinos.** Charginos pair production, Chargino-Neutralino production and Neutralinos pair production are not large at LHC. Their rates are smaller than the Tevatron ones because the valence partons in a proton proton collision are only quarks.

**The gluinos and squarks.** At hadron colliders the largest sparticles production cross sections are for gluinos and squark production, as shown in Fig.1.9, since they are produced via strong interactions. In order to be produced at LHC, gluinos and squarks must be lighter of  $\mathcal{O}(TeV)$ , nevertheless, if the kinematic allows for it, their production is the most promising mechanism for detecting SUSY signals.

Gluinos and the first generation of squarks are among the heaviest sparticles in many susy models, therefore once produced, they will decay in lighter (s)particles which in turn will decay again. Given they are the heaviest sparticles a long chain of many decays, *cascade decays*, will occur. Such a cascade stops when the LSP is produced, since it can not decay to any other heavier sparticle and, because of the R-parity, it can not decay in SM particles.

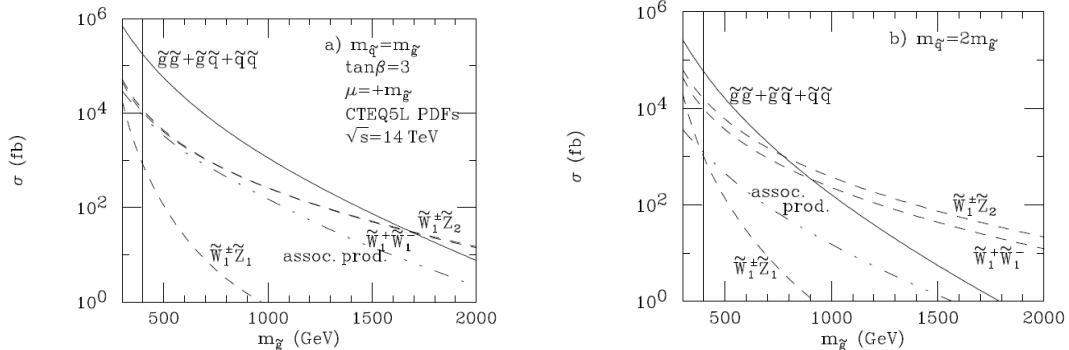


Figure 1.9: Comparison among several sparticles production at LHC assuming a particular model [30].

### 1.4.2 Decays of Sparticles

In most of models all the MSSM sparticles can decay at tree level via two or three-body decays mediated by SM gauge interactions. Here the decays of sparticle are reported. In the following  $\tilde{\chi}_j$  can mean  $\tilde{\chi}_j^+$  or  $\tilde{\chi}_j^-$ .

### Decays of gluinos and squarks

Here some decay modes are listed:

- $\tilde{g} \rightarrow q\bar{q}'\tilde{\chi}_j^\pm$ ,  $\tilde{g} \rightarrow q\bar{q}\tilde{\chi}_i^0$  where  $i = 1, \dots, 4$  and  $j = 1, 2$ .
- $\tilde{g} \rightarrow q\bar{q}$  if the gluon is enough massive, furthermore if the kinematics allows for it, it is the dominant gluon decay.

Squark mainly decay through two bodies decays, some are here listed.

- Since for the first generation the Yukawa couplings can be neglected:  $\tilde{u}_L \rightarrow u\tilde{\chi}_i^0$ ,  $d\tilde{\chi}_j^+$ ,  $u\tilde{g}$  and  $\tilde{d}_L \rightarrow d\tilde{\chi}_i^0$ ,  $u\tilde{\chi}_j^-$ ,  $d\tilde{g}$ ;  $\tilde{u}_R \rightarrow u\tilde{\chi}_i^0$ ,  $u\tilde{g}$  and  $\tilde{d}_R \rightarrow d\tilde{\chi}_i^0$ ,  $d\tilde{g}$  the decays into a gluino are dominant (if the kinematic allows for them).
- the decays of the squarks of the third generation are complicated by the Yukawa couplings and the mixing effects, some examples for the sbottom are:  $\tilde{b}_{1,2} \rightarrow b\tilde{g}, b\tilde{\chi}_i^0, t\tilde{\chi}_j, \chi_j\tilde{t}_{1,2}, H^-\tilde{t}_{1,2}$ .  $\tilde{b}_2 \rightarrow Z\tilde{b}_1, h\tilde{b}_1, H\tilde{b}_1, A\tilde{b}_1$ . The stop decays are analog to them.

The possible decay chains depend on which inequality is true between  $m_{\tilde{q}} < m_{\tilde{g}}$  and  $m_{\tilde{q}} > m_{\tilde{g}}$ .

- $\mathbf{m}_{\tilde{q}} < \mathbf{m}_{\tilde{g}}$  :

$$\begin{aligned} \tilde{g} \rightarrow & \bar{q}\tilde{q}_{L,R} + \text{c.c}; \\ \tilde{q}_{L,R} \rightarrow & q\tilde{\chi}_l^0, l = 1, \dots, 4; \\ \tilde{q}_L \rightarrow & q'\tilde{\chi}_k^\pm, k = 1, 2; \\ \tilde{q} \rightarrow & q\bar{b}\tilde{b}_1 \text{ if } m_{\tilde{q}} > m_b + m_{\tilde{b}_1}. \end{aligned}$$

- $\mathbf{m}_{\tilde{q}} > \mathbf{m}_{\tilde{g}}$  :

$$\begin{aligned} \tilde{q}_L \rightarrow & q'\tilde{\chi}_k^\pm, k = 1, 2; \\ \tilde{q}_{L,R} \rightarrow & q\tilde{g}, q\tilde{\chi}_l^0, l = 1, \dots, 4; \\ \tilde{g} \rightarrow & q\bar{q}\tilde{\chi}_l^0, \\ & q\bar{q}'\tilde{\chi}_k^\pm, \\ & \tilde{t}\tilde{t}_1 + t\tilde{\bar{t}}_1 \text{ if } m_{\tilde{g}} > m_{\tilde{t}_1} + m_t, \\ & \tilde{b}\tilde{b}_1 + \tilde{t}\tilde{\bar{b}}_1 \text{ if } m_{\tilde{g}} > m_{\tilde{b}_1} + m_b. \end{aligned}$$

### Decays of sleptons

In the following the possible decays of sleptons are listed.

- $\tilde{e}_L \rightarrow e\tilde{\chi}_i^0, \nu_e\tilde{\chi}_j^-$ .  $\tilde{\nu}_e \rightarrow \nu_e\tilde{\chi}_i^0, e\tilde{\chi}_j^+$ .  $\tilde{e}_R \rightarrow e\tilde{\chi}_i^0$ .

- $\tilde{\tau}_1 \rightarrow \tau\tilde{\chi}_i^0, \nu_\tau\tilde{\chi}_j^-$ .  $\tilde{\tau}_2 \rightarrow \tau\tilde{\chi}_i^0, \nu_\tau\tilde{\chi}_j^-, \chi\tilde{\nu}_\tau, H^-\tilde{\nu}_\tau$ .  $\tilde{\tau}_2 \rightarrow Z\tilde{\tau}_1, h\tilde{\tau}_1, H\tilde{\tau}_1, A\tilde{\tau}_1$ .  
 $\tilde{\nu}_\tau \rightarrow \nu_\tau\tilde{\chi}_i^0, \tau\tilde{\chi}_i, W\tilde{\tau}_{1,2}, H^+\tilde{\tau}_{1,2}$ .

### Chargino and neutralino decays

We saw that the gluinos and squarks produced by p-p interactions can decay in charginos and neutralinos, so the next step of the decay chain is the decays of such particles. Chargino decays only via electroweak interactions; if the kinematics allows, the dominant processes are the following two-bodies decays:

- $\tilde{\chi}_j^- \rightarrow W\tilde{\chi}_i^0, H^-\tilde{\chi}_i^0, \rightarrow \tilde{q}_L\bar{q}', \tilde{q}_Lq', \rightarrow \tilde{\nu}_l\bar{l}, \tilde{l}_L\nu_l$  and  $\tilde{\chi}_2^- \rightarrow Z_i\tilde{\chi}_1^-, \rightarrow h\tilde{\chi}_1^-, \rightarrow H\tilde{W}_1^-, A\tilde{W}_1^-$ ;
- $\tilde{\chi}_i^0 \rightarrow WW_j, H^+\tilde{\chi}_j^-, Z\tilde{\chi}_{i'}^0, h\tilde{\chi}_{i'}^0, H\tilde{\chi}_{i'}^0, A\tilde{\chi}_{i'}^0$  and  $\tilde{\chi}_i^0 \rightarrow \tilde{q}_{R,L}\bar{q}, \tilde{q}_{R,L}q, \tilde{l}_{R,L}\bar{l}, \tilde{l}_{R,L}q, \tilde{\nu}_l\bar{\nu}_l, \tilde{\nu}_l\nu_l$ .

where  $i, i' = 1, \dots, 4$  and  $i > i'$  Several other decays are possible and would be dominant if the ones listed above are suppressed or kinematically forbidden.

### Decays of the Higgs bosons

The Higgs bosons decay mostly via two body modes to SM particles and to sparticles only if the lightest ones are light enough.

- The decays of the light scalar Higgs boson  $h$  at tree level are:  $h \rightarrow l\bar{l}, h \rightarrow q\bar{q}$  is possible for every quark but top because of the limit  $m_h < 135$  GeV and  $h \rightarrow \tilde{\chi}_i^0\tilde{\chi}_{i'}^0, \tilde{\chi}_j^-\tilde{\chi}_{j'}^-, \tilde{f}\bar{\tilde{f}}, AA$ , with  $i, i' = 1, \dots, 4$  and  $j, j' = 1, 2$ . The dominant decay is  $h \rightarrow b\bar{b}$  for the most of the space parameters.
- The heavy scalar Higgs boson  $H$  can decay essentially in the same modes listed for the light  $h$ , with the difference which also  $H \rightarrow t\bar{t}, WW, ZZ$  are possible as well other decays which for  $h$  are forbidden because it is not enough massive.
- The pseudoscalar  $A$  possible decays are:  $A \rightarrow q\bar{q}, l\bar{l}, \rightarrow \tilde{Z}_i\tilde{Z}_{i'}, \tilde{\chi}_j^+\tilde{\chi}_{j'}, \tilde{f}\bar{\tilde{f}}$  and  $A \rightarrow hZ, gg, \gamma\gamma$ .
- The charged scalar Higgs boson  $H^\pm$  mostly decay via:  $H^+ \rightarrow q\bar{q}', \nu_l\bar{l}, \rightarrow \tilde{Z}_i\tilde{\chi}_j^+, \tilde{f}\bar{\tilde{f}}', hW$ . The dominant one is the decay  $H^+ \rightarrow t\bar{b}$  or, if the latter is forbidden,  $H^+ \rightarrow \tau^+\nu_\tau$ .

### 1.4.3 SUSY Topologies

In the previous sections only a brief review of the supersymmetric general features and some hints to how the models are built were given. Despite the description was very simplified and short, an idea of the great deal of unexplained issues was given. Many questions have no answers and they are destined to remain unsolved until some SUSY signals will be observed. Trying to develop an analysis aimed to the search for a particular observable foreseen by a specific model is unthinkable. In order to maximize the probability to find some signals, the susy searches are based on the categorization in experimental signatures. Furthermore, in a field so uncertain the approach should be as model-independent as possible and should relies on general properties shared by every SUSY model.

Since gluinos and squarks production gives rise to many and very energetic jets in the final state, a feature of the SUSY signals is a large hadronic activity, furthermore the existence of a stable LSP gives rise to a general feature of SUSY signatures. Indeed, by assuming that the LSP is neutral, as required in order to solve cosmological issues (Sec.1.1.3), it can not be detected and it manifests through large missing transverse energy ( $\cancel{E}_T$ ). Even if there exist many possible decay cascades, and despite they can be very complicate and can not be foreseen by the current knowledge of the SUSY physics, every decay chain must stop with the production of the LSP.

Therefore the common feature of all the possible cascades is the production of large  $\cancel{E}_T$  and several energetic jets, while the leptons can be soft because they usually are produced in the last steps of the chain.

The categorization in different topologies, usually used, is the following:

- **Hadronic:** it is characterized by large  $\cancel{E}_T$  and high jet multiplicity; the vantage of this channel is the large efficiency, while the difficulty to probe such signature arises because of the large QCD background, indeed it can give rise to missing energy due to mis-measurement. Some appropriate variables, such as  $\alpha_T$  [31] can help to disentangle SUSY signal from QCD. In many GMSB scenarios the gravitino is the LPS, while the NLSP particle is embodied by  $\tilde{\tau}_1$  and its lifetime and mass measurements can provide information about the  $m_{3/2}$  parameter, giving indications on the supersymmetry breaking mechanism.
- **Single Lepton (SL) channel:** Compared to the hadronic channel, this is much more clear because the requirement of a lepton suppresses the QCD

background. Nevertheless there are several SM background which have a signature similar to the SUSY one, they are especially  $W + jets$  and  $t\bar{t}$ , since they can have a final state with missing energy, a lepton and hard jets.

- **Opposite Sign Di-Lepton (OSDL) channel:** This channel is particularly useful to estimate sparticle masses. Indeed the decay  $\tilde{\chi}_l^0 \rightarrow \tilde{\chi}_{n(<l)}^0 l^+ l^-$  gives rise to an edge in the distribution of the invariant mass of the pair  $l^+ l^-$  and its position can give indications on some sparticle masses [32].
- **Same Sign Di-Lepton (SSDL) channel:** A final state with two same sign leptons is a feature of SUSY signal with the production of at least a gluino, given its nature and its decay modes. In this channel it is easy to get rid of most of the SM background.
- **Tri Leptonic:** Another channel with reduced SM contribution is the one with three leptons in the final state. Indeed three leptons can arise from SM processes with small cross section as dibosons production.

Since the yield and the shape of SUSY signals for every channel depend on the models, the comparison of the several analysis is useful to reduce the dependence from the models in the interpretation of the results.

One of the most promising signature is the SSDL channel, indeed it has the vantage that the SM background can be considerably reduced by the same sign lepton requirement, since the few SM processes with such signature have low cross sections. A focus on the SSDL topology is given in the following.

#### 1.4.4 Same Sign Di Leptonic topology

The final state with two same sign leptons, which is a rare signature in SM physics, is possible and not suppressed in SUSY models because of the existence of Majorana particles. In MSSM the gluino (as the other gauginos) is a Majorana fermion, one important feature of this kind of particles is that they can decay in either sign particles with the same probability. Therefore both  $\tilde{g}\tilde{g}$  and  $\tilde{g}\tilde{q}$  can lead to final state with two same sign leptons. In the following the stages which can lead to SSDL final signature are described.

### Production of at least one gluino

As mentioned in the previous section, the production of  $\tilde{g}\tilde{g}$  and  $\tilde{g}\tilde{q}$  are among the preferred sparticles productions.

$$gg \rightarrow \tilde{g}\tilde{g}, gq \rightarrow \tilde{g}\tilde{q}_i, q\bar{q} \rightarrow \tilde{g}\tilde{g} \quad (1.64)$$

Some diagrams describing such productions are shown in Fig. 1.10 and Fig. 1.11

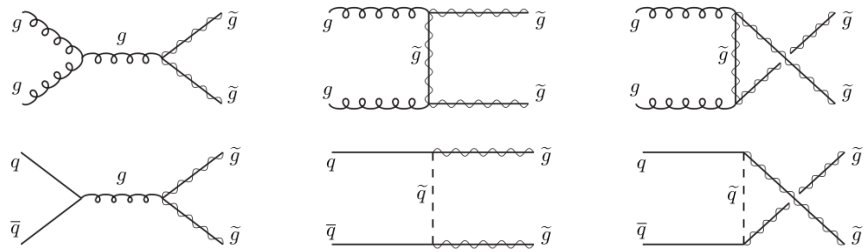


Figure 1.10: Gluino pairs production at LHC from strong gluon-gluon fusion (up) and quark-antiquark (down) interactions [5].

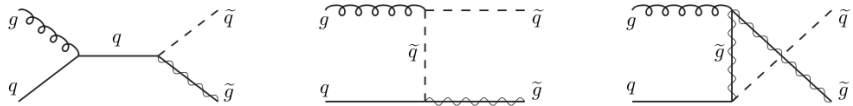


Figure 1.11: Squark Gluino production at LHC from strong gluon-quark fusion [5].

If  $m_{\tilde{q}}, m_{\tilde{g}} < \sim TeV$ , the  $gg$  fusion contribution to squarks and gluinos production, is the largest one at LHC. The largest rate of inclusive strong interacting sparticle production occurs if  $m_{\tilde{q}} \sim m_{\tilde{g}}$ .

As already mentioned, the gluino has a characteristic way to decay; unlike the other (s)particle it can decay in positive or negative final state with the same probability. In example:

$$\Gamma(\tilde{g} \rightarrow u\bar{d}\tilde{W}_j^-) = \Gamma(\tilde{g} \rightarrow d\bar{u}\tilde{W}_j^+) \quad (1.65)$$

Since in colliders the sparticle must be produced in pairs, this is the feature which can lead to the very typical signature of two same sign leptons in the final state. Once  $\tilde{g}\tilde{q}$  or  $\tilde{g}\tilde{g}$  are produced, they can decay in several modes, depending from the mass spectrum, the couplings, and in general from all the parameters of the model. In particular for these productions, the same sign dilepton final state can

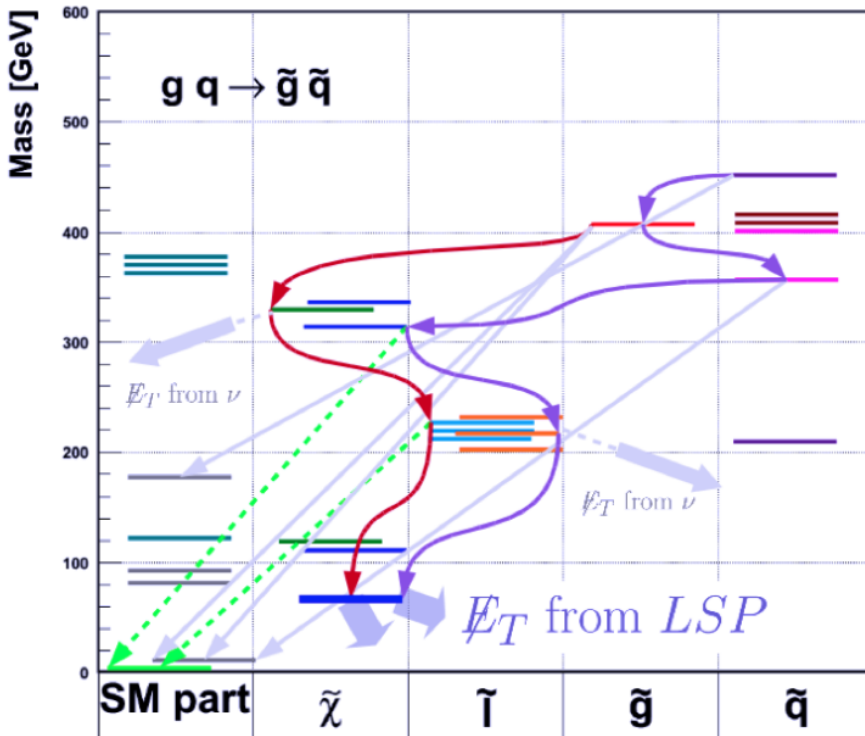


Figure 1.12: Example of decay chain which can origin from  $\tilde{g}\tilde{q}$  production in the contest of LM0 point in mSUGRA scenario. The red (violet) arrows indicate a possible decay chain starting from a gluino (squark). The green dashed arrows represent the lepton emissions. The light violet thick arrows illustrate the produced missing energy and the light violet thin arrows illustrate all the other SM particles emission

arise from different decay chains. One of these chains is illustrated as an example in Fig.1.12 for the benchmark point LM0 in the mSUGRA contest.

In the following the decay illustrated in fig.1.12 is explicitly described in terms of every particle decay and the experimental signature deriving from each one of them.

decays of sparticles	experimental signatures
$\tilde{g} \rightarrow u\bar{d}\tilde{\chi}_2^+$	2 jets
$\tilde{\chi}_2^+ \rightarrow \tilde{e}_L \nu_e$	$\cancel{E}_T$
$\tilde{e}_L \rightarrow e \chi_1^0$	$e^+, \cancel{E}_T$
$\tilde{t}_2 \rightarrow \tilde{g} t$	$t \rightarrow W b \rightarrow q\bar{q}'b$
$\tilde{g} \rightarrow \tilde{b}\tilde{b}_1$	1 b-jet
$\tilde{b}_1 \rightarrow b \chi_3^0$	1 b-jet
$\chi_3^0 \rightarrow \tilde{\nu}_\tau \tau$	$\tau^+ \rightarrow \nu \nu \mu$
$\tilde{\nu}_\tau \rightarrow \nu_\tau \chi_1^0$	$1 \mu^+, \cancel{E}_T$
	$\cancel{E}_T$
	4 jets, 3 b-jets, $e^+, \mu^+$ , large $\cancel{E}_T$

This is only one example, but the final signature deriving from this decay chain, namely large jet multiplicity, two same sign leptons and large missing transverse energy, is common in several other cases.



# Chapter 2

## The CMS Detector at the LHC

*We do not learn by experience,  
but by our capacity for  
experience*  
Buddha

---

### 2.1 The Large Hadron Collider

The Large Hadron Collider (LHC) is a proton-proton ( $p\text{-}p$ ) collider situated at CERN laboratories near Geneva. It was designed to reach the centre of mass energy of 14 TeV and the luminosity of  $10^{34}\text{cm}^{-2}\text{s}^{-1}$ . Also, the LHC will collide heavy ions in dedicated runs, the high-energy heavy-ion beams will reach energies of 2.75 TeV per nucleon, that is over 30 times higher than at the previous accelerators, allowing us to further extend the study of QCD matter under extreme conditions of temperature, density, and parton momentum fraction.

Four main experiments will benefit of the high energy collisions delivered by the LHC. Atlas (A Toroidal LHC Apparatus) and CMS (Compact Muon Solenoid) are large multi-purpose experiments which will collect data from  $p\text{-}p$  collisions; LHCb (LHC beauty) is an experiment dedicated to the study of CP violation and rare decays in the range of b-quark physics arising from  $p\text{-}p$  collisions; Alice (A large Ion Collider Experiment) will analyze data produced by heavy ions collisions.

The LHC was built in the tunnel which lodged LEP collider [33] therefore several already existing structures were exploited. Some new structures have been added

as the Fig.2.1 illustrates. The ring-shaped tunnel lies between 45m and 170m below the surface and it is 26.7 km long. The LHC ring [34] is constituted by eight arcs spaced out by eight long straight sections where detectors, Radio Frequency (RF) cavities, and other facilities are situated. Such eight octants division gives rise to the eight positions called *Point X*. The high luminosity Interaction Points are Point 1 (P1) and Point 5 (P5) where the Atlas and CMS experiments are respectively situated.

The beam energy and the design luminosity of the LHC have been chosen in order to study physics at the TeV energy scale, which is the energy range where the possibly existing physics not observed yet, both within and beyond the Standard Model, is expected to appear. Indeed, as the Chapter 1 describes, there are reliable motivation to believe that SUSY, one of the most investigated new physics scenarios, will be detectable at TeV scale.

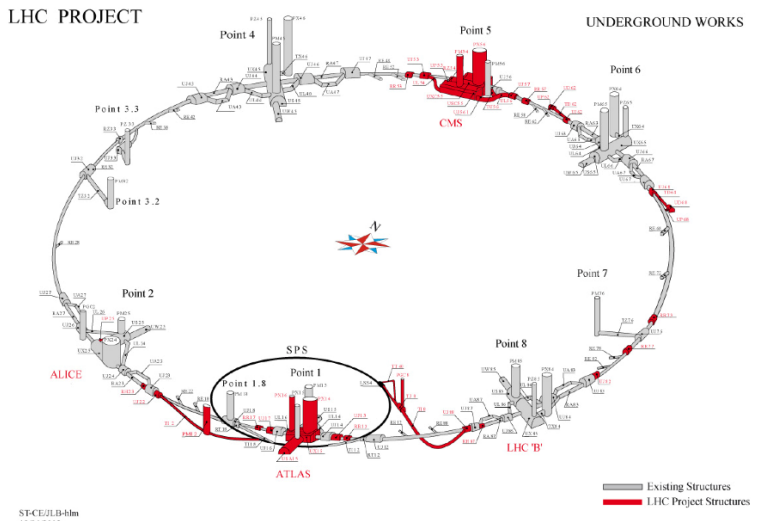


Figure 2.1: The LHC ring with the already existing LEP structures (in grey) and the new structures appositely built for LHC (in red).

### The Acceleration Path

The LHC ring is the last stage of the path the protons follow before colliding. The acceleration compound committed to the several acceleration stages to prepare the protons bunches to the admittance to the LHC is illustrated in Fig.2.2 and described in detail in [35]. The protons are produced in a duoplasmatron, where hydrogen is ionized, and injected in the LINear ACcelerator 2 (LINAC2)

which enhances their energy up to 50 MeV. The protons exiting from the LINAC2, grouped in bunches of  $30\ \mu\text{s}$ , start a stage where they go through several circular-shaped accelerators which lead them to the LHC ring. The first one is the Proton Synchrotron Booster (PSB) a four rings accelerator, leading the protons to an energy of 1.4 GeV and to 190 ns bunches. After that the protons end in the Proton Synchrotron (PS) which accelerates them up to 25 GeV and further divides them in more compressed bunches: the separation time is 24.95 ns and the time extension is less than 4 ns. The proton bunches are injected in the Super Proton Synchrotron (SPS) where undergo an acceleration up to 450 GeV. The proton bunches are now ready (many high intensity bunches with small transverse and well defined longitudinal emittance) to be injected in the LHC pipes.

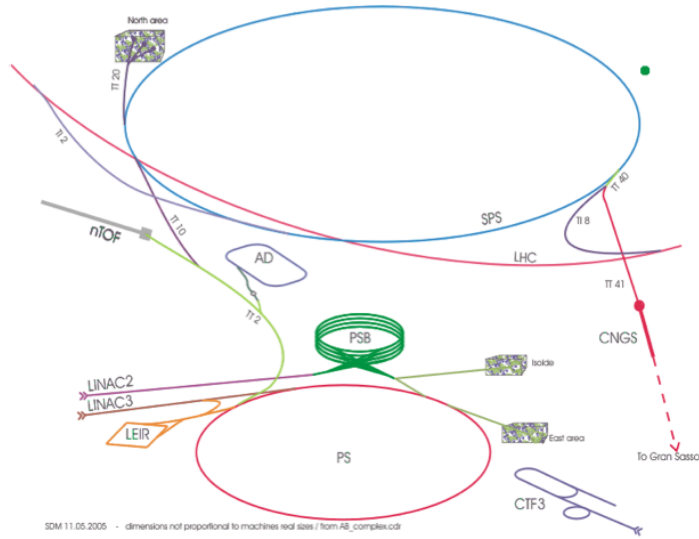


Figure 2.2: The acceleration compound committed to the several acceleration stages to prepare the protons bunches to the admittance to the LHC [35].

In the LHC the two beams circulating in opposite directions are accelerated in separated vacuum chambers spaced by 194 mm in the horizontal plane and at about 100 m far from the interaction point the two pipes join into one. Since the installation space in the LEP tunnel is limited a twin-bore (two-in-one) design has been adopted for almost all of the LHC superconducting magnets. Fig.2.3 shows the division of LHC in eight regions, giving rise to the eight octants, sectors and Impact Points (IP).

Two Radio Frequency (RF) cavities are hosted in the 4<sup>th</sup> octant, each one is dedicated to one beam. At IP6 the dump insertion is situated. It is a combination of

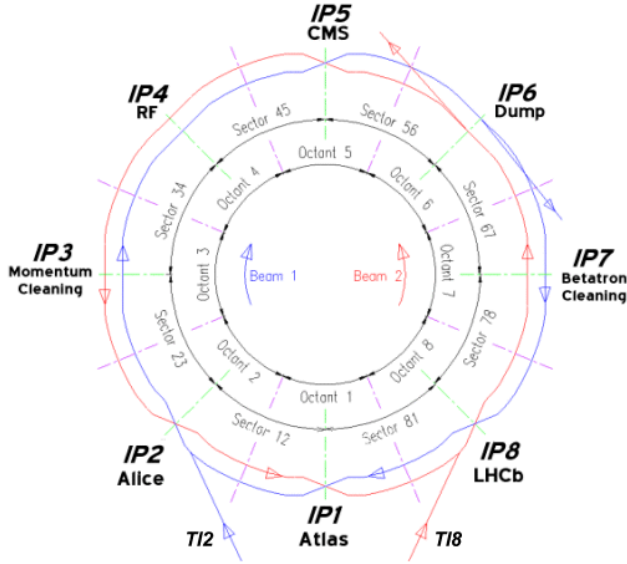


Figure 2.3: The way LHC ring is divided in sectors and octants. The position of the four main experiments is also shown [34].

horizontally deflecting fast-pulsed magnets and vertically-deflecting magnets which serve to vertically extract the beams from the machine. The 3<sup>rd</sup> and 7<sup>th</sup> octants house collimators needed to remove halo particles with large transverse and longitudinal oscillation amplitudes respectively.

The four remaining octants correspond to IP1, IP2, IP5 and IP8, where the two beams cross and interact one each other and which lodge the four main experimental apparatuses ATLAS, LHCb, CMS and ALICE respectively. Section 2.2 is dedicated to the description of the CMS experiment, situated at one of the two position where the  $p$ - $p$  beams interact with the highest luminosity. How the luminosity depends on the machine parameters is described in the following.

### Luminosity Delivered by LHC

Given a physical collision process with cross section  $\sigma$ , the number of events produced in a given time interval,  $n$ , is proportional to the instantaneous luminosity delivered by the collider machine  $\mathcal{L}$ :

$$n = \mathcal{L}\sigma, \quad \text{with} \quad \mathcal{L} = \frac{N_b^2 n_b f_{rev} \gamma_r}{4\pi \epsilon_n \beta^*} F \quad (2.1)$$

All the parameters which  $\mathcal{L}$  depends on are features of the machine:  $N_b$  is the number of particles per bunch,  $n_b$  is the number of bunches per beam,  $f_{rev}$  is the

revolution frequency,  $\gamma_r$  is the Lorentz-boost factor,  $\epsilon_n$  is the normalized transverse beam emittance,  $\beta^*$  is the beta-function at the collision point and  $F$  is the geometric luminosity reduction factor due to the crossing angle at the interaction point. From the above expression for the rate  $n$ , is clear that, in order to study rare/not copious processes, besides a high center of mass energy, a high intensity beam is needed.

The geometrical factor  $F$  depends on the crossing angle at the interaction point  $\theta_c$ , the longitudinal and transverse RMS size of a bunch  $\sigma_z$  and  $\sigma_*$  respectively, in the following form:

$$F^2 = \frac{1}{1 + \left(\frac{\theta_c \sigma_z}{2\sigma_*}\right)^2} \quad (2.2)$$

The compromise between an as high as possible  $\mathcal{L}$  and the technical restrictions required to the above listed parameters, resulted in the chosen values of the beam parameters reported in Tab.2.1 and parameters related to the peak luminosity reported in Tab.2.2.

	Injection	Collision: Nominal Design
Beam Energy	450 GeV	7 TeV
CoM Energy	-	14 TeV
$\gamma_r$	480	7461
$N_b$		$1.15 \times 10^{11}$ p/b
$n_b$		2808
min. bunch spacing		24.95 ns

Table 2.1: Beam parameters for the nominal LHC design.

Although the design Center of Mass (CoM) Energy and luminosity have been chosen as 14 TeV and  $10^{34} \text{ cm}^{-2} \text{ s}^{-1}$ , respectively, the values reached in the start-up runs, called Collision2010, are CoM energy of 7 TeV and peak luminosity of  $2 \cdot 10^{32} \text{ cm}^{-2} \text{ s}^{-1}$ .

In order to compute the integrated luminosity which is possible to collected in a given time period, it is necessary to consider that  $\mathcal{L}$  is not constant, since it is degraded by several effects with respect to the nominal conditions. The more important ones are: the beam loss from collisions, which gives rise to a decay time of the bunch intensity  $\tau_{nuclear}$ ; the beam loss due to beam-beam interactions, called

	Injection	Nominal Design Collision
Peak luminosity	-	$10^4 \times 10^{30} \text{ cm}^{-2}\text{s}^{-1}$
$\epsilon_n$	$3.5 \mu\text{m}$	$3.75 \mu\text{m}$
$\beta^*$	18	0.55
$\sigma_z$	11.24 cm	7.55 cm
$\sigma_*$	$375.2 \mu\text{m}$	$16.7 \mu\text{m}$
$\theta_c$	$320 \mu\text{rad}$	$285 \mu\text{rad}$
$F$	1.0	0.84

Table 2.2: Luminosity parameters for the nominal LHC design.

Intra Beam Scattering (IBS) which leads to a lifetime  $\tau_{IBS}$ ; the interactions of the beam with the residual gas corresponding to a time  $\tau_{resgas}$ . By taking into account for these main sources, the luminosity lifetime can be expressed as:

$$\tau_L = \left( \frac{1}{\tau_{nuclear}} + \frac{1}{\tau_{IBS}} + \frac{1}{\tau_{resgas}} \right)^{-1} \sim 20h \quad (2.3)$$

Therefore, given an initial luminosity  $\mathcal{L}_0$ , the integrated luminosity in one run which lasts a time  $T_{run}$  is given by:

$$\mathcal{L}_{int} = \int_0^{T_{run}} \mathcal{L}_0 e^{-\frac{t}{\tau_L}} dt = \mathcal{L}_0 \tau_L \left( 1 - e^{-\frac{T_{run}}{\tau_L}} \right) \quad (2.4)$$

The LHC started to operate at the end of 2008, after an incident to the sector 34 (see Fig.2.3), underwent a long stop for about one year. At the end of 2009 some runs at  $\sqrt{s} = 0.9 \text{ GeV}$  and  $\sqrt{s} = 2.36 \text{ GeV}$  were performed and in March 2010 the center of mass energy of 7 TeV was reached.

Fig.2.4 shows the peak luminosity and the integrated luminosity per day, in the whole period of  $p$ - $p$  collisions in 2010. Fig.2.5 shows the integrated luminosity in the whole period. Additionally the luminosity recorded by CMS, one of the two large purpose experiments at LHC, is indicated. The CMS detector is described in the next section.

## 2.2 The Compact Muon Solenoid Experiment

The Compact Muon Solenoid (CMS) Experiment [36] is one of the two experiments aimed to a wide range of physics results. Their main scope is to observe new phenomena, since the LHC will provide an environment with physics conditions which

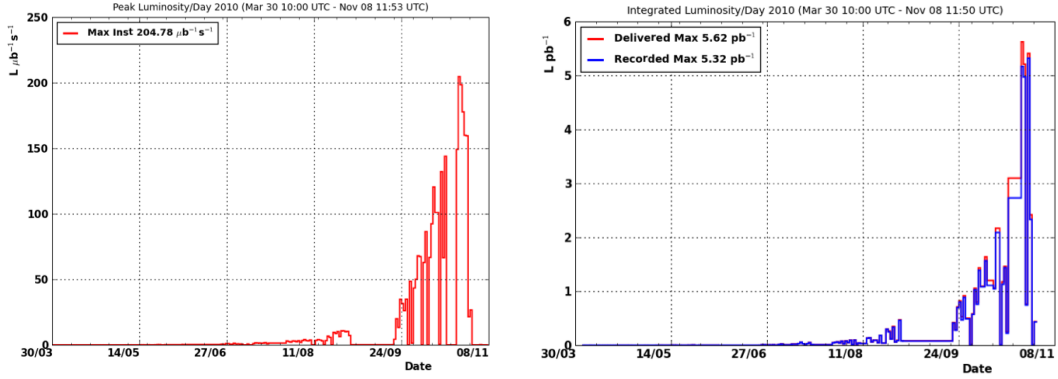


Figure 2.4: Left: maximum value of the instantaneous luminosity reached per day. Right: integrated luminosity per day.

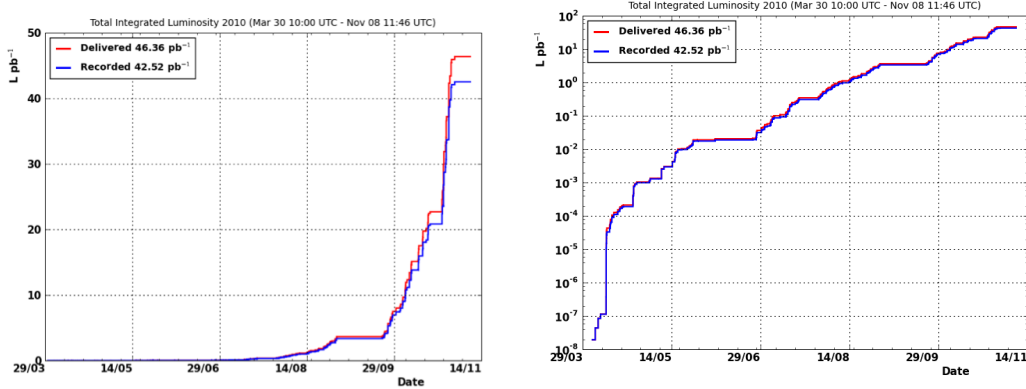


Figure 2.5: Integrated Luminosity collected since March till November 2010 in linear (left) and logarithmic (right) scale.

have never been explored before. The experiments at LHC can also be exploited to perform measurements in specific physics topic, as precision measurements and non perturbative QCD physics.

The very extensive plan of the multi-purpose experimental apparatuses at P1 and P5, requires several conditions to be satisfied.

The requirements due to the LHC environment are summarized in the following.

- The high cross sections and luminosity which are being reached by LHC, require the experiments there installed to have high trigger efficiency and radiation hard detectors.
- The short time between collisions (25 ns) requires fast readout of the high granularity detectors and good synchronization with the accelerator machine.

- The inelastic cross section determines the severe GHz rate of input data for the detectors which must effectively be brought down almost 4 (6) orders of magnitude by the first (last) level of a trigger system.

The detectors features required to obtain the aimed physics results have been considered in the CMS design, and the main ones are here summarized.

- Good muon identification and momentum resolution over a wide range of momenta and angles, good dimuon mass resolution ( $\sim 1\%$  at 100 GeV/c $^2$ ), and the ability to determine unambiguously the charge of muons with  $p < 1$  TeV/c;
- Good charged-particle momentum resolution and reconstruction efficiency in the inner tracker. Efficient triggering and offline tagging of  $\tau$ 's and  $b$ -jets, requiring pixel detectors close to the interaction region;
- Good electromagnetic energy resolution, good diphoton and dielectron mass resolution ( $\sim 1\%$  at 100GeV/c $^2$ ), wide geometric coverage,  $\pi^0$  rejection, and efficient photon and lepton isolation at high luminosities;
- Good missing-transverse-energy and dijet-mass resolution, requiring hadron calorimeters with a large hermetic geometric coverage and with fine lateral segmentation.

The CMS apparatus has the usual cylindrical structure with the different subsystems installed in a concentric shape around the LHC beam pipe at P5 .

The coordinate system adopted by the CMS Collaboration is as described in the following. The origin is centered at the nominal collision point, the  $y$ -axis points vertically upward and the  $x$ -axis point horizontally toward the centre of the LHC ring. The  $z$ -axis lies along the beam and points toward the anti-clockwise direction. The azimuthal  $\phi$  angle is measured in the  $x$ - $y$  plane starting from the  $x$  axis, while the polar  $\theta$  angle is measured from the  $z$ -axis toward the  $x$ - $y$  plane .

Unlike the  $p$ - $p$  collision center of mass energy, which is known from the beam energy, the center of mass energy of the colliding partons is unknown, since it also depends on the Particle Distribution Functions (PDFs) of the single partons. Since the longitudinal component of the partons momenta and so also of the collisions center of mass is not known, it is not possible to reconstruct completely the initial state, but only the transverse component of it. For this reason, the  $x$

and  $y$  variables are fully used to compute the transverse component of every variable, while the  $z$  component is not used. Instead of  $z$  another variable is usually considered in hadron colliders which is additive under Lorentz boosts, the *rapidity* defined as:

$$y = \frac{1}{2} \ln \left( \frac{E + p_z}{E - p_z} \right) \quad (2.5)$$

Such variable, can be approximated in the high energy limit by another one, the *pseudorapidity*  $\eta$ , which depends only on  $\theta$  and is defined as:

$$\eta = -\ln \left( \tan \frac{\theta}{2} \right) \quad (2.6)$$

In the high energy regime of LHC the approximation is fully satisfied and the  $\eta$  variable can be considered as invariant along Lorentz boosts up to an additive constant.

The cylindrical structure is defined by the superconductor central magnet which has a diameter of 5.9 m and length of 13 m.

At its interior, in the order starting from centre toward the extern, the inner tracking system, the Electromagnetic CALorimeter (ECAL) and the Hadronic CALorimeter (HCAL) are arranged. Outside the central solenoid the Muon System layers are spaced out with the layers of the magnet return yoke.

Since the analysis presented in this thesis exploit every element of the CMS experimental apparatus, a short review of all the subsystems is given in this section, a more detailed description is in [36]. The complete CMS apparatus is shown in Fig.2.6, where is clear the same cylindrical shape for every subsystem, with the barrel and two disks (End Caps) at its extremities which close the structure.

### 2.2.1 Inner Tracking System

The CMS tracking system is the largest silicon tracker ever built. It has been designed to reconstruct trajectories of charged particles (tracks) with a transverse momentum  $p_T$  as low as 1 GeV/c and a  $|\eta|$  as large as 2.5. The CMS tracking system has been constructed keeping in mind the high density of tracks in the region surrounding the LHC collision pipe and the required low occupancy necessary to measure a low resolution impact parameter and to reconstruct secondary vertexes. The expected density  $dN_{ch}/d\eta$  of the charged particles arising from a  $p$ - $p$  collisions at 7 TeV in the  $|\eta| < 2.5$  region, is between 5.5 and 7 leading to a charged particle multiplicity of about 30 [38], while at energy and full luminosity design the charged

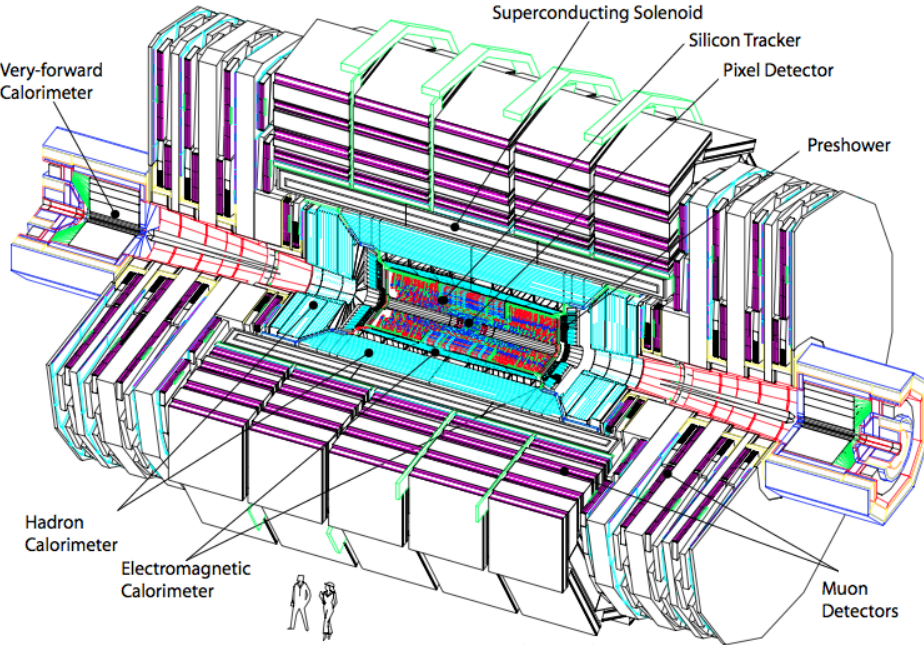


Figure 2.6: A perspective view of the CMS detector [37].

particles multiplicities can reach  $10^3$  every 25 ns . The requirements to operate with these high multiplicities led to compose the system with two kind of detectors since in the inner region the granularity has to be greater than the outer. The most internal subsystem are the Pixel detectors which occupy the region till a radius of 20 cm. At radii between 20 and 115 cm the tracking subsystem is constituted by the Silicon Strips detectors. The whole length is 5.8 m, the diameter is 2.5 m and consists of  $200m^2$  of active silicon region covering the central area with  $|\eta| < 2.5$ . A  $z-y$  section of the whole tracking system is shown in Fig.2.7 (left), where the different  $\eta$  regions are visible. All the tracking system is in a uniform magnetic field of 3.8 T provided by the superconducting solenoid.

### Pixel detector

The Silicon Pixel detectors consist of 66 millions of channels extending till a radius of 20 cm. Due to the high track multiplicity the pitch in  $r-\phi \times z =$  is  $100 \times 150\mu\text{m}^2$ , which allows for an occupancy as low as  $10^{-4}$  per pixel and per bunch crossing. The Pixel detector is composed by 3 cylindrical layers with 768 modules and 2 forward disks with 672 modules, the whole structure is shown in Fig.2.8 (left). Every module is linked to a read out radiation hard chip which is able to perform automatic zero suppression after the amplification of the charge signal.

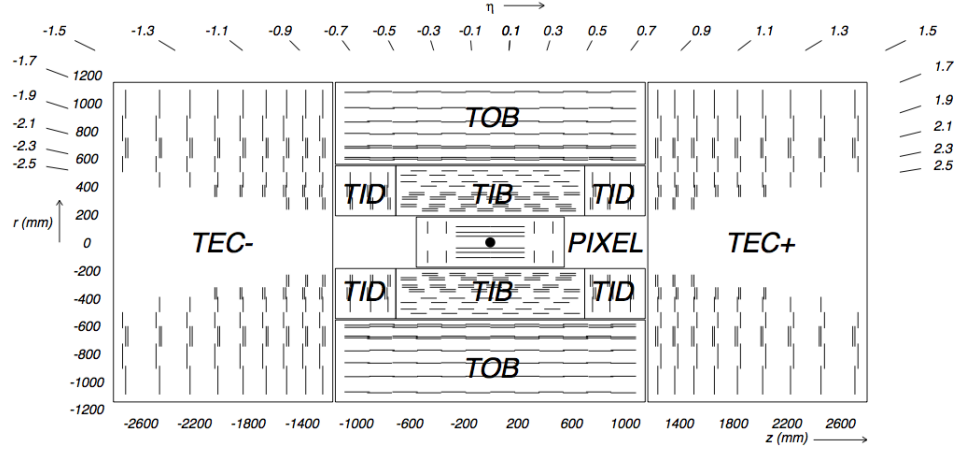


Figure 2.7:  $z$ - $r$  section of the inner tracking system [37].

The position of the layers and the  $\eta$  region they cover are illustrated in Fig.2.8 (right).

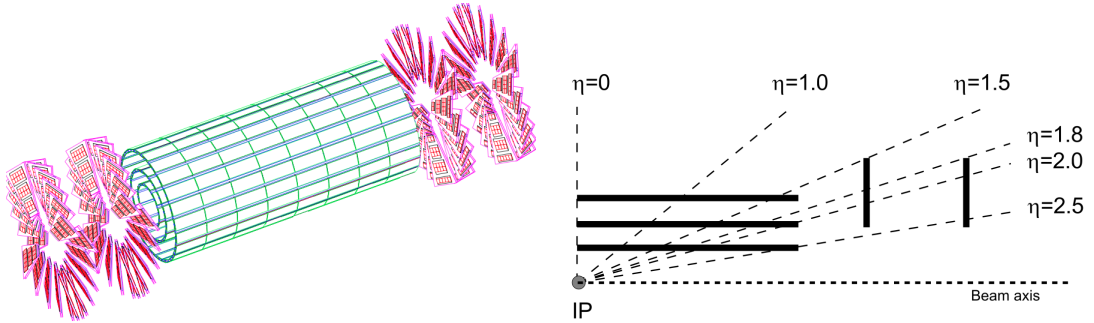


Figure 2.8: Left: a perspective of the Pixel subdetector structure. Right: a quarter of the  $r$ - $z$  section, showing the position of the Pixels layers.

### Silicon Strips Detector

At radii greater than 20 cm the lower multiplicity compared to the inner one, allows the use of the Silicon Strip detector. This subsystem has 2.8 millions channels and it is divided in four components. The Tracker Inner Barrel (TIB) and the Tracker Inner Disks (TID) occupy the region with radii between 20 cm and 55 cm and are constituted by  $320\mu\text{m}$  thick micro-strip sensors. The TIB is composed by 4 layers with the sensor strips oriented in the beam direction and a pitch of  $80\mu\text{m}$  ( $120\mu\text{m}$ ) on layers 1 and 2 (3 and 4) allowing for a single point resolution of  $23\mu\text{m}$  ( $35\mu\text{m}$ ). The TID is composed by 3 disks with the sensor strips radially oriented and

has a pitch varying between 100 and 141  $\mu\text{m}$ . They provide up to 4 measurements of  $\phi$  and  $r$  of a trajectory. Fig.2.9 (left) shows the TIB and TIB structure as long as the disks apparatus, which houses services as the cooling fluid supply line, the electrical and optical fibers panels, named *margherita*.

The third constituent of the inner tracking system is the Tracker Outer Barrel (TOB) which surrounds the TIB and TID. The TOB extends to a radius of 116 cm and between  $-118$  and  $+118$  in the  $z$  coordinate. It is formed by 6 layers of  $500\mu\text{m}$  thick micro-strip sensors leading to other 6 measurements in  $r\text{-}\phi$ . The 1-4 layers have a pitch of  $183\mu\text{m}$  leading to a resolution of  $53\mu\text{m}$ , while the 5-6 layers pitch is  $122\mu\text{m}$ , leading to a resolution of  $35\mu\text{m}$ .

The two silicon strip disks which close the extremities of the TOB are called Tracker End Caps (TEC  $+$ / $-$  depending on their  $z$  position) and each one is composed by 9 layers which extend in the radii between 22.5 cm and 113.5 cm and in the longitudinal direction occupy  $124\text{cm} < |z| < 282\text{ cm}$ , a schematic drawing of one end cap is shown in Fig.2.9 (right). Each disk has several rings, up to 7, the thickness of the strips in the inner 4 rings is  $320\mu\text{m}$ , while the others are  $500\mu\text{m}$  thick. The average pitch of the radial strips is between  $97\mu\text{m}$  and  $184\mu\text{m}$ .

Some of the moduls (those in the first two layers of the TIB and TOB, the first two rings of the TID and the rings 1,2,5 of the TEC $\pm$ ) of the Silicon Strip detector allow for the measurement of a second coordinate. Two micro-strip detector modules are mounted back to back with a stereo angle of 100 mrad providing a single point resolution of  $230\mu\text{m}$  in TIB,  $530\mu\text{m}$  in TOB, while in the endcaps it is variable with the pitch.

## 2.2.2 Electromagnetic Calorimeter

The features required to the CMS electromagnetic calorimeter, namely fine granularity, endurance to radiation, and velocity have led to the choice of material used. The CMS Electromagnetic Calorimeter (ECAL) is a homogeneous lead tungstate ( $\text{PbWO}_4$ ) crystals calorimeter. It benefits from a high density ( $8.28\text{ g}/\text{cm}^3$ ), short radiation length ( $X_0=0.89\text{ cm}$ ) and a small Moliere radius ( $2.2\text{ cm}$ ). The  $\text{PbWO}_4$  scintillation decay time is comparable to the LHC bunch crossing time, as a result in 25 ns about the 80 % of the light is emitted. It is composed by a barrel (EB) made of 661200 crystals and two endcaps (EE) with 7324 crystals. Moreover a pre-shower detector (PS) is situated in front of the endcap disks. A schematic view of the ECAL is provided by Fig.2.10 (left). The EB covers the region with

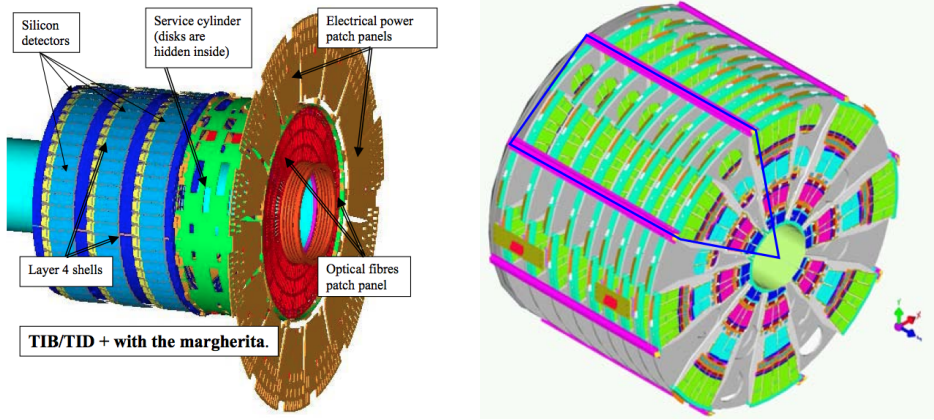


Figure 2.9: Views of the four silicon strip tracker system. Left: schematic drawing of TIB and TID with the margherita disk. Right: a schematic drawing of the TEC system [37] .

$|\eta| < 1.479$  with a granularity of  $\Delta\eta \times \Delta\phi = 0.0174 \times 0.0174$ .

A thin-walled alveolar structure contains the crystals, constituting a submodule. The crystals have the centre of the front face at a radius of 1.29 and are 230 mm long, corresponding to  $25.8 X_0$ . The submodules are collected in modules (each one containing 400 or 500 crystals depending on  $\eta$ ) which, in turn are collected, in groups of 4, in supermodules which hold 1700 crystals. Such structure is visible in Fig.2.10 (left) and the EB mechanism is shown in Fig.2.10 (right).

The region with pseudorapidity values  $1.479 < |\eta| < 3.0$  is covered by the EE. Each End Cap is divided in two halves, or *Dees*, which contain 3662 crystals each, and is placed at about 315 cm far from the interaction point. Identically shaped crystals are grouped in SuperCrystals (SCs) through a carbon-fibre alveol structures. In each Dee there are 138 SCs and 18 special partial super-crystals in the inner and outer circumference.

The crystals are arranged in a  $x$ - $y$  grid and head toward a point slightly shifted from the interaction point resulting in angles which range between 2 and 8 degrees.

The Pre Shower detector (PS) is aimed to identify neutral pions via the photon detection, detected in the endcaps in the pseudorapidity region  $1.653 < |\eta| < 2.6$ . Furthermore it is useful to also improve the position measurements of electrons and photons and to help to the discrimination of electrons and minimum ionizing particles. The PS is a two layers sampling calorimeter 20 cm thick. The absorber material is lead radiators, while the signal is collected by silicon sensors. The

incident electrons or photons make electromagnetic showers to initiate in the lead radiators, which are then absorbed by the silicon strip sensors which determine the deposited energy and the transverse shower profiles. The lead planes are arranged in two Dees, one on each side of the beam pipe and are completely covered by the silicon sensors.

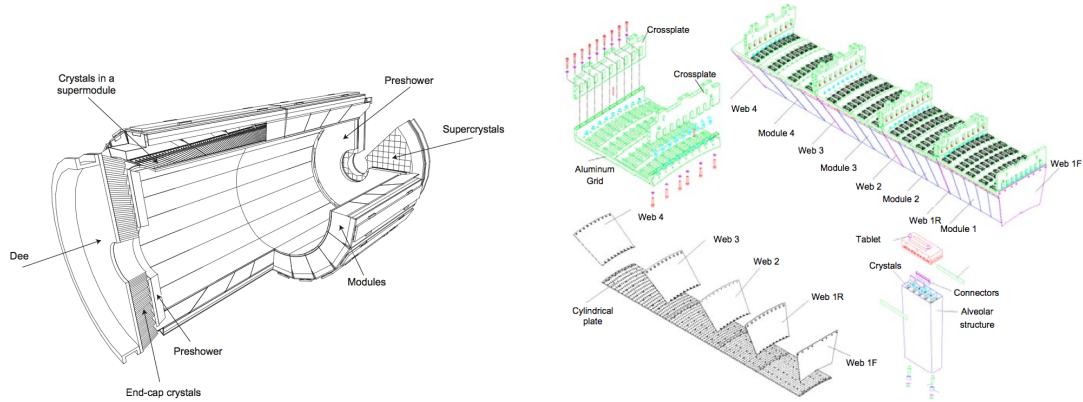


Figure 2.10: Left: Layout of the CMS electromagnetic calorimeter showing the arrangement of the crystal modules, supermoduls and end caps. Right: layout drawing of the EB mechanism [37] .

### 2.2.3 Hadronic Calorimeter

The CMS Hadronic Calorimeter (HCAL) is constituted by the HCAL Barrel (HB), the HCAL EndCaps (HE), the HCAL Outer (HO) and the forward HCAL (HF). HB and HE are sampling calorimeter with brass as the absorber material and scintillators as active material. They are placed inside the central magnet, the HB covers the region  $0 < |\eta| < 1.4$ , the HE the region  $1.3 < |\eta| < 3$ , so that they share a region of pseudorapidity ( $1.3 < |\eta| < 1.4$ ) in order to maximize the hermetic coverage of the subsystem. At  $\theta \sim 57$  degrees a gap divides the HB and HE. The HB is divided in 18 azimuthal wedges (this division is shown in Fig.2.11 (right)), each one has  $4\phi$  sectors of 5 degrees.

The HE has a single brass unit for each layer, while the scintillators are separated in  $\phi$  wedges, each one with 4 sectors. The HE position is shown in Fig.2.11 (middle and right). The presence of the magnet at radius 2.95 m forces the HB dimensions, its thickness is only 5 (10) radiation lengths at  $\eta = 0$  ( $\eta = 1.2$ ). For this reason an additional component of the hadron calorimeter is placed outside the solenoid cryostat in order to recuperate the energy escaped from the HB. This further

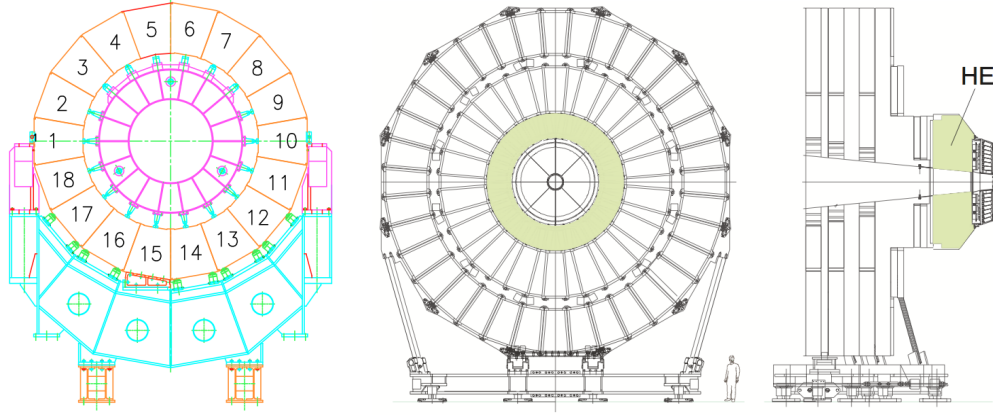


Figure 2.11: Drawing of the  $r\phi$  section illustrating the division in wedges of the HB (left). drawing showing the HE position in the CMS apparatus in the  $r\phi$  section (middle) and  $rz$  section (right). [37]

member is called Hadron Outer (HO) and is made of 5 rings, each one divided in  $12\phi$  sectors. Since the most central part of the apparatus, the EB and HB have the minimal number of radiation lengths, the ring centered at  $\eta = 0$  has two layers, unlike the other rings which have only one layer as shown in Fig.2.12 (left) . HB, HE and HO have a calorimeter towers segmentation in  $\eta$  and  $\phi$  of  $0.087 \times 0.087$ , except the HO in the region  $|\eta| > 2.5$  in which the segmentation is  $0.175 \times 0.175$ . The layout of the HCAL towers for all the subdetectors is shown in Fig.2.12 (right).

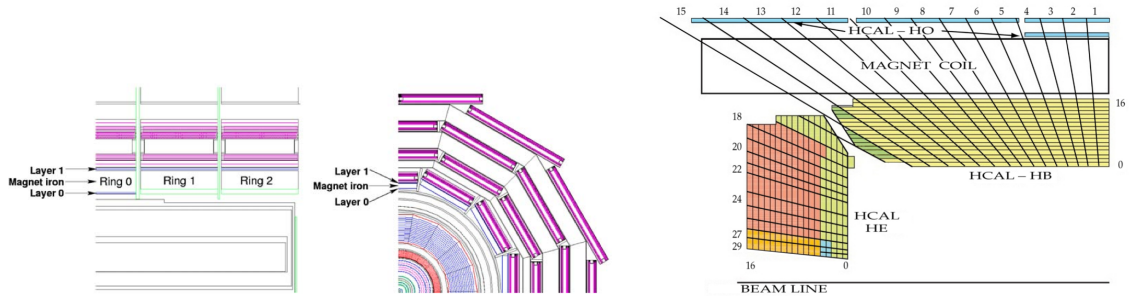


Figure 2.12: Left: a schematic drawing showing the HO modules positions and their layered structure. Right: the tower structure of the HB, HE and HO subsystems [37] .

The two elements of a forward hadronic calorimeter (HF) are two cylindrical steels with an outer radius of 130 cm and are placed 11.2 m far from the interaction point. The HF is in charge of detect particles in the pseudorapidity range  $3 < |\eta| < 5.2$ . The very forward region it covers, forced its design, since the active medium

should be enough radiation hard to endure the high density environment, where the energy density is about 7 times greater than the central region. The active material chosen is quartz fibres (fused-silica core and polymer hard-cladding). The HF structures is similar to other subsystems, it is divided in 12  $\phi$  wedges of 20 degrees and each wedge has two 10 degrees sectors. The fibers are arranged parallel to the beam line and the towers granularity is  $\delta\eta \times \delta\phi = 0.175 \times 0.035$  for  $|\eta| > 4.7$  and  $\delta\eta \times \delta\phi = 0.175 \times 0.175$  for lower  $|\eta|$ . In order to distinguish showers generated by electrons and photons from the ones generated by hadrons, half of the fibers run over all the full length, while the other half are present only in the region starting 22 cm from the front of HF. When the Cherenkov light is generated by charged shower particles which overcome the threshold, a small fraction of the light is captured.

#### 2.2.4 Superconducting magnet

The central superconducting solenoid is designed to provide a uniform magnetic field of  $B = 3.8T$  at its interior. It is constituted of 4 layers of NbTi superconductor, the coil is lying in a vacuum chamber and a cryogenic system keeps it at a temperature of 4.45 K. A return yoke ring, which surrounds and supports the central magnet, conducts the magnetic flux lines and at the same time is part of the muon system subdetector. The yoke is constituted of five iron rings, each one 1.8 m thick, in the barrel and six disks in the end caps. The yoke layers are spaced out by the muon chambers as is shown n Fig.2.6.

#### 2.2.5 Muon System

The muons are the easiest particles to detect in hadron colliders experiments, therefore they play a crucial role in the early stage of LHC. The muon system is deputed to muon identification, momentum measurement and triggering. The great deal of material in the flux-return yoke provides a hadron absorber needed to the identification of muons. The requirements to provide good muon momentum resolution and trigger capability are fulfilled thank to the high field provided by the solenoidal magnet. The muon system structure is the same as the other CMS subsystems, namely it is constituted by a cylindrical barrel closed at the two extremities by two end caps. The barrel is divided in 5 wheels, each one separated in 12 sectors and each sector is composed of 4 detector stations integrated in the magnet return yoke. Each EndCap is constituted by 4 disks, three of which are in turn divided

in two concentric rings, and one has three rings. The entire muon system covers the region  $|\eta| < 2.4$ . Three types of gaseous particle detectors are used, depending on the region. Drift tube (DT) chambers with standard rectangular drift cells are used in the barrel, since in this area the neutron-induced background is small, the muon rate is low and the magnetic field is uniform and mostly contained in the steel yoke. They are arranged in four stations spaced out by the layers of the flux return yoke and cover the region  $|\eta| < 2.4$ . The muon rates and the background levels are enhanced in the endcaps region, for this reason Cathode Strip Chambers (CSC) more resistant to radiation, are used for the EndCaps muon system. In order to improve the estimation of background rate and the correct beam crossing time at LHC full luminosity regime, an additional muon system, is placed in both the barrel and endcap regions. Such subsystem, dedicated to muon triggering, consists of Resistive Plate Chambers (RPC).

### The Barrel Drift Tube System

The 4 DT stations in every wheel sector, form concentric cylinders around the beam line. The drift tube cells, with a transversal dimension of 21 mm, are arranged in groups of 4 layers staggered of half a cell, named SuperLayers (SL). This Muon Barrel assemblage is shown in Fig.2.13. The SL are arranged to form the 4 muon chambers labeled MB1, MB2, MB3, MB4; the outermost chamber (MB4) is made of two SLs measuring the hits in  $r\text{-}\phi$  plane, while the other three, besides the two SL deputed to the  $r\text{-}\phi$  hits, have also a central SL measuring the hits in the  $r\text{-}z$  plane. By measuring 8 track points, in the  $r\text{-}\phi$  plane a resolution of 100  $\mu\text{m}$  is obtained.

The inner three wheels have 60 chambers, while the outer ones have 70. On the whole, considering the 130 chambers of the muon system, there are 172000 sensitive wires.

### The EndCap CSC System

The EndCaps Muon CSC chambers are multi-wire proportional chambers constituted by 6 anode wire planes interleaved among 7 cathode panels. The wires run in the azimuthal direction so to define the radial coordinate. The chambers have a trapezoidal shape and are arranged in groups of 72 labeled ME1/1, ME1/2, ME1/3, ME2/2, ME3/2, and groups of 32 named ME2/1, ME3/1 ME4/1. Other

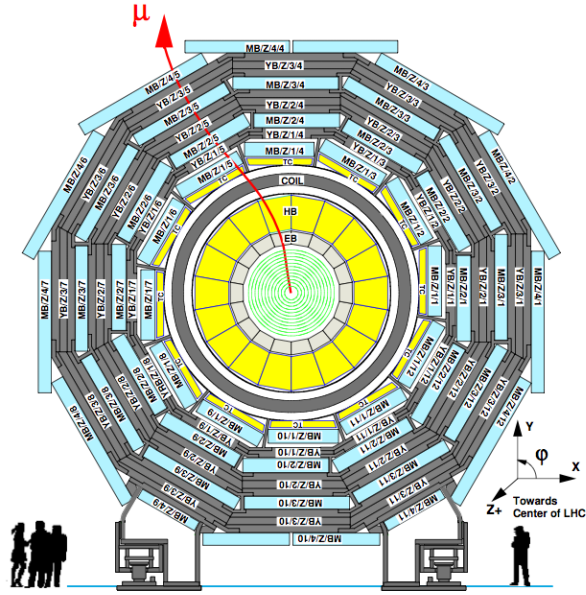


Figure 2.13: Layout of the CMS barrel muon DT chambers in one of the 5 wheels [37].

72 chambers are named ME4/2 and are not available during the first CMS data taking stage.

Some chambers cover 10 deg others 20 deg and, except for the ME1/3 ring, all the chambers overlap providing a contiguous  $\phi$  coverage.

In the  $0.9 < |\eta| < 1.2$  region, the barrel and endcap overlap, thus both DT and CSC provide the muon detection. In the  $1.2 < |\eta| < 2.4$  region the muon detection is provided by 3 or 4 CSC stations.

### The Resistive Plate Chambers system

The RPC are gaseous parallel-plate detectors with the feature to provide, besides a discrete spatial resolution, also a time resolution comparable to the scintillators one. The RPC is able to measure the time of an ionising event with a much shorter time than the interval (25 ns) between two consecutive LHC bunch crossing (BX). For this reason a muon trigger based on RPC has been developed. It is capable, even in high rate and background, to associate a BX to a muon track and to measure the muon transverse momentum with a high accuracy in a very high rate environment (to  $10^3 \text{ Hz/cm}^2$ ). The CMS RPC chambers are constituted by 2 or 3 moduls which are double-gap type, operated in avalanche mode with common read-out strips in between. The total induced signal is the sum of two single-gap

signals. This provides an efficiency higher than the single-gap ones, but allowing the single-gaps to operate at lower gas gain corresponding to a lower high voltage. In the barrel, the 6 RPC layers are placed in the muon stations interleaved by the iron yoke. The two outer station have one RPC layer each, while the inner ones have two RPC layers each. This is aimed to always provide at least four layers information to the trigger, even for low- $p_T$  muons which do not reach the outer barrel layers.

The RPC positioned on the end cap muon stations are mounted on both the faces of the disks. They cover, in the original design, the  $|\eta| < 2.1$  region.

The arrangement of the muon system modules are shown in Fig.2.14, where is visible also the position of every other subdetector described above.

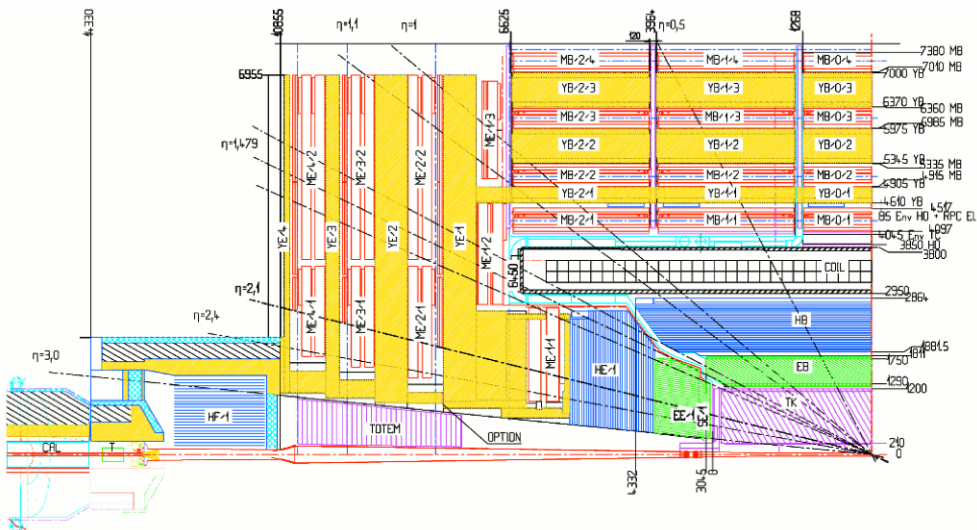


Figure 2.14: A quarter of the  $r$ - $z$  section of the CMS detector, with the position of every subdetector, in particular the CSC muon chambers are visible [37] .

## 2.2.6 The Trigger System

The LHC provides very high interaction rates of  $p$ - $p$  collisions leading to an interval between two BX of 25 ns. Moreover several collisions can occur in each BX, the number depending on the LHC luminosity. This leads to a high number of events corresponding to a great deal of data. On the contrary the interesting events, for the analysis described in this thesis and for many others, have a much (several magnitude orders) lower rate. At full luminosity design, the event rate, given by the number of bunch crossing per second times the number of collisions in one

bunch crossing, is about 800 MHz. Since the storage of the whole data collected by CMS is a prohibitive task, a first stage of the selection is performed on line and divided in two steps.

The trigger system, deputed to this on line selection, should reduce drastically the event rate, the nominal rate reduction factor of the whole trigger system is  $10^6$  leading to a event rate of  $\mathcal{O}(100)$  which is possible to store and analyzing offline. It is composed by two systems, the Level-1 (L1) Trigger and the High Level Trigger (HLT) each one in charge of one step of the selection.

### **Level 1 Trigger**

The L1 trigger consists of custom designed largely programmable electronics. It has a synchronous pipelined structure of processing elements which has to analyze every LHC event. The nominal event rate reduction of the L1 trigger at full luminosity leads to an event rate of 100kHz. At every BX, each element passes its result to another one, and the whole amount of data which the pipeline memories can hold corresponds to 192 BX. Therefore the L1 decision has to be taken in only  $3.2 \mu\text{s}$ .

This time must include also, for the DT the electron drift time (400 ns), and for all the detectors the time needed to the data transmission. Indeed part of the L1 electronics is placed on the detectors, part is housed in a underground control room about 90 m far from the CMS cavern. Therefore the L1 electronics spend only  $1\mu\text{s}$  to perform the decision calculation.

The L1 trigger is composed by three subsystems: the Calorimeter Trigger, the Muon Trigger and the Global Trigger. The first two, also called Trigger Primitive Generators (TPG) are based on energy deposits in the calorimeters and track segments or hit patterns in muon chambers. The TPG have the task of identify physics objects and choose the best four trigger candidates for each physics object type, without taking any decision. The information related to the selected physics objects are sent to the Global Trigger, which performs the selection.

### **Calorimeter Trigger**

The calorimeters, besides their own granularity, are also divided in trigger towers only for trigger purposes. The division in trigger towers has a granularity of  $\eta \times \phi =$

$0.087 \times 0.087$  up to  $|\eta| = 1.74$ , for larger  $|\eta|$  it is coarser. This subdivision is illustrated in Fig.2.15 for a quarter of the  $r$ - $z$  section. The TPG electronics for the Calorimeter Trigger is integrated with the calorimeter read out. The calorimeter TPGs sum the transverse energies measured in ECAL crystals or in HCAL read-out towers to obtain the trigger tower  $E_T$ . They also associate this sum to a bunch crossing number and in addition, only for the ECAL, a bit indicating the transverse extent of the electromagnetic deposit is saved. The division in trigger towers has a granularity of  $\eta \times \phi = 0.087 \times 0.087$  up to  $|\eta| = 1.74$ , for larger  $|\eta|$  it is coarser. A high speed copper link transmit the TPG information from the detectors to the Regional Calorimeter Trigger (RCT), which find candidate electrons, photons, taus and jets and separates the electrons and photons in isolated and non isolated ones. The information about such candidates and the  $E_T$  sum, are then transmitted to the Global Calorimeter Trigger (GCT) which sort all the candidates, calculate the total transverse energy and missing transverse energy, then send these information to the Global L1 Trigger. The RCT transmit also some information to the Muon Trigger, needed to muon isolation determination.

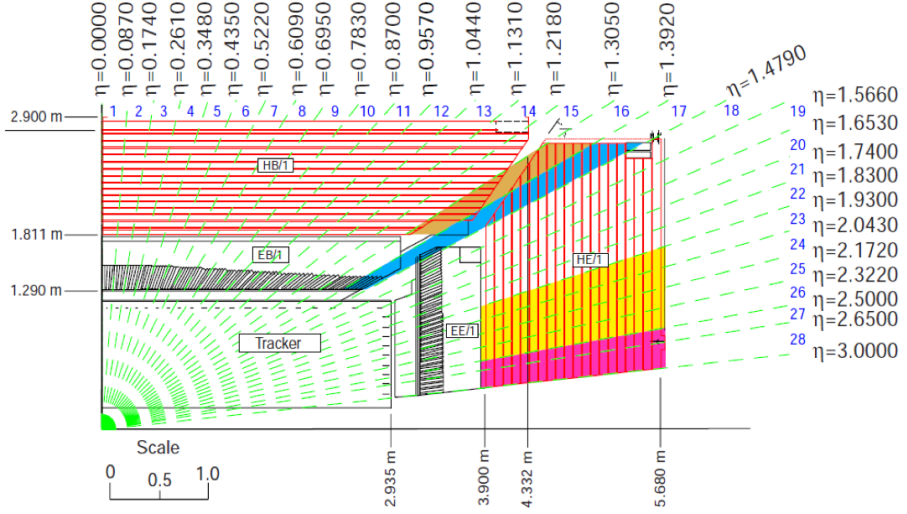


Figure 2.15: Drawing of a quarter of the  $r$ - $z$  CMS section showing the division in trigger towers of the calorimeters.

### Muon Trigger

Each one of the muon subdetector system has a L1 muon trigger system with own trigger logic. Only the CSC station ME1/1 currently is not equipped with trigger electronics, therefore the muon trigger acceptance is  $|\eta| < 2.1$ , instead of its design

acceptance of  $|\eta| < 2.4$ . The DT chambers provide local trigger information in the form of track segments in the  $\phi$  projection and hit patterns in  $\eta$  projection, while CSCs provide 3-dimensional track segments. Both DT and CSC determine the BX which originated the event.

The regional muon trigger consists of the DT and CSC Track Finders, which join segments to the complete tracks and assign physical parameters to them.

The RPCs, with their excellent timing resolution, provide an independent source of track candidates and send its hits information to the CSC in order to improve the resolution and possible ambiguities.

The Global Muon Trigger (GMT) sorts the DT, CSC, RPC candidates, validates the muon sign and try to match the RPC candidates with the CSC or DT ones. Moreover it uses the information given by the Regional Calorimeter Trigger in order to decide if the candidate muons are isolated. At most 4 muons are sent to the L1 Global Trigger.

## L1 Global Trigger

The physics objects arriving to the L1 Global Trigger from GMT and GCT can be the candidate muons, hadronic jets from partons, tau lepton jets, electrons and photons, the latter two have also the information regarding the isolation. Each object type has at most 4 candidates which are ranked in  $p_T$  and every candidate is characterized by its  $p_T$  or  $E_T$ ,  $(\eta, \phi)$  and a quality word. Furthermore global quantities regarding the whole event arrive to the L1 Global Trigger as well: the total and missing transverse energy, the scalar sum of the transverse energies of jets above a programmable threshold and jet multiplicity for several  $E_T$  threshold. The L1 Trigger uses all these information to decide if at least a one of the thresholds in the L1 table is passed.

After the decision by the L1, the event is processed and filtered by the High Level Trigger (HLT), which is part of the Data Acquisition system, briefly described in the next section.

## Data Acquisition and High Level Trigger

Once the Level-1 Trigger decides to accept an event, the accepted signal is distributed to the Front-End Driver (FED), which copy the data from the buffer into the Data Acquisition (DAQ) system.

The so called Event Builder subsystem is dedicated to assemble the event which

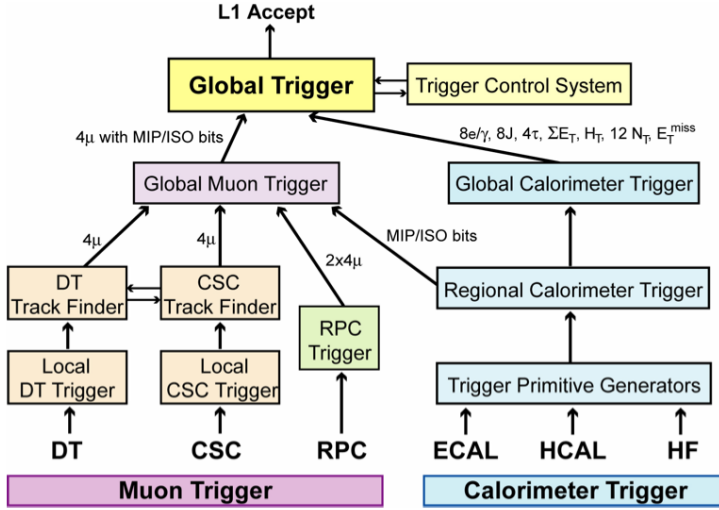


Figure 2.16: Schematic view of the L1 Trigger system.

are stored on over 600 FED and distributes them to the HLT processing nodes. The DAQ system also allows the execution of additional analysis modules that perform quality and integrity checks on the processed data, called Data Quality Monitoring (DQM). These provide quick feedback and allow detection of various detector problems without waiting for the process of offline reconstruction.

The HLT [39] is in charge to reduce the event rate 100 kHz of a factor  $10^3$ . It is a software system implemented in a filter farm of about one thousand commercial processors. This allows for full flexibility and optimization of the algorithms. Data read from subdetectors are assembled by a builder unit and then assigned to a switching network that dispatches events to the processor farm. The algorithm implementation is fully software, therefore it could be modified and improved without any hardware intervention.

It is organized in three virtual layers: the so called Level2 considers only muon and calorimetry information, the Level 2.5 uses also information coming from the Pixel detector, and Level3 takes information also from the whole tracking system. Each step selects the number of events which are processed by the successive level. The track reconstruction makes the Level3 very time expensive, and since the measurement precision is not required to the trigger, it is performed on a limited number of hits and only in the interesting regions. This layered structure provides reliable algorithms needed to perform the last step of the online selection. Event by event, the HLT code runs on a single processor and has to make a decision in 300 ms, and in order to be efficient it has to manage to reject not interesting events as soon as

possible.

## Computing

The central concept of the CMS data model is the so called *Event*. It provides access to the recorded data from a single triggered bunch crossing, and to data derived from it. Events are physically stored as persistent ROOT files. The users of the system, and the physical computer centres it comprises, are distributed worldwide, interconnected by high-speed international networks. Since the data samples will typically be very large, downloading data for analysis would be wasteful; instead, since the analysis software has small size, it can be hosted in the computer farm where the data are stored. Once the code is run, the results are downloaded in the analyst site. This mechanism is provided by the worldwide LHC Computing Grid (LCG) [40] and can be used in CMS through the tool CMS Remote Analysis Builder (CRAB) [41] which facilitates the access to the data in a user friendly way.

CMS makes use of several event formats with differing levels of detail and precision.

*RAW* events contain the full recorded information from the detector, plus a record of the trigger decision and other metadata. *RAW* data is accepted into the offline system at the HLT output rate (nominally 300 Hz for pp collisions). The *RAW* data will be classified by the online system into several distinct primary datasets, based upon the trigger signature.

Reconstructed (*RECO*) data is produced by applying several levels of pattern recognition and compression algorithms to the *RAW* data. These algorithms include: detector-specific filtering and correction of the digitised data; cluster- and track-finding; primary and secondary vertex reconstruction; particle ID, using a variety of algorithms operating on cross-detector information.

*AOD* data is produced by filtering of *RECO* data, either in bulk production, or in a skimming process which may also filter a primary dataset into several analysis datasets. *AOD* events contain the parameters of high-level physics objects, plus sufficient additional information to allow kinematic refitting.

# Chapter 3

## Same Sign Dilepton SUSY Analysis

*The analytical power should not  
be confounded with simple  
ingenuity*

Edgar Allan Poe – The Murders  
in the Rue Morgue

---

The theoretical background to the existence of SUSY signal with two same sign leptons in the final state has been described in Chapter 1. The main advantage of this signature is that the yield from SM processes is very low. Since in the early period of data taking at 7 TeV both the hadronic physics processes and the detector are not expected to be known accurately, the selection should be as simple and robust as possible. The aim is to observe an excess of events over the Standard Model background after such selection, if no deviation is observed some SUSY models will be excluded. The Standard Model background yield after the same sign selection, will be very small, but, in order to be able to claim a new physics contribution, the standard model processes need to be known very accurately. Therefore this search relies in a crucial way on the estimation of the background contributions, the accuracy of which depends on the knowledge of the standard model physics processes and the response of the detector to them.

## 3.1 Monte Carlo Samples

### 3.1.1 Background samples

The signal topology is essentially characterized by two isolated leptons with the same charge sign, moreover the two features of general SUSY events are present: high missing transverse energy and high jet multiplicity. Relying on these features the following background sources can arise.

- **QCD:** With *QCD* events is meant the processes with only hadronic jets in the final state. Even if the generic *QCD* processes do not contain prompt leptons neither missing energy from neutrinos, these physics objects can origin from mismeasurements, furthermore leptons can arise from decays of hadrons produced in the hadronization of heavy flavor quarks. These events can be an important background source because of their enormous cross section.
- **$W+jets$ :** when the  $W$  decays in leptons, the charged lepton is isolated and with high  $p_T$  and the neutrino gives rise to missing energy. Even if there is not a second prompt lepton, this process can pass the selection because of a second lepton arising from instrumental background or from a heavy flavor quark produced in association with the  $W$ . Its large cross section makes it an important background source in many analysis in multi-leptonic channels.
- **$Z+jets$ :** This process can have the signal topology if the  $Z$  decays in charged leptons, with charge mismeasurement and the missing transverse measurement arises from jets mis-measurement or if the  $Z$  decays in neutrinos. In both cases the signature with two same sign leptons comes from instrumental background. This process has a cross section smaller than the  $W$  production.
- **$t\bar{t}+jets$ :** the semileptonic decay of the top pair production gives rise to final states which can mimic the signal. Indeed, besides the lepton coming from the  $W$ , the certain presence of two  $b$ -jets makes it likely that leptons coming from heavy flavors are considered isolated.
- **$VV+jets$ :** The diboson processes have a much lower cross section compared to the background above quoted. Nevertheless they have to be accurately studied because they are the only background sources which can give rise to the same physics final state of the signal. It happens if it is  $WZ$  with

$W \rightarrow l^\pm \nu$  and  $Z \rightarrow l^+ l^-$ . Also, the other possibilities ( $ZZ, W^+ W^-$ ), can pass the selection because of mismeasurements.

- **Same Sign W bosons** There exist two kinds of processes leading to same sign  $W$ , with a cross section much lower than the diboson already cited, but which need attention: (i) the production of two same sign  $W$ s from a single parton interaction, which is possible at orders  $\alpha_{EW}^4$  and  $\alpha_{EW}^4 \alpha_{QCD}^2$  (with the additional production of two partons for the charge conservation); (ii) two parton interactions in the same proton proton collision, each one with the production of a  $W$ . To the same sign  $W$  production is dedicated the Chapter 4.

The hard scattering of the background processes was simulated with different generators: MadGraph [42], Pythia [43], Tauola [44] were used. For every MC sample the parton shower was performed by Pythia6 generator.

Tab.3.1 reports the main features of each sample used.

### 3.1.2 Signal samples

The great deal of possible SUSY scenarios makes focusing on a single model not useful.

Nevertheless, in order to have a feeling of the performance of the analysis, samples of specific models are useful. To this aim, in CMS the LMX benchmark points, introduced in Sec.1.2.6, are used. The one with the large cross section is LM0 and is taken as the signal prototype 3.2. Also by considering only the mSugra scenario, the LMX points are just a little part of the whole and continuum set of possible models. Samples which scan a wide range of  $m_0$  and  $m_{1/2}$  values are used in order to have a broader perspective of the sensitivity of the analysis to mSugra signals. Two samples were available in CMS, with the same values of the parameters  $A_0 = 0$  and  $sign(\mu) = +$ . One sample has the  $\tan\beta$  parameter  $\tan\beta = 3$  and the other one  $\tan\beta = 10$ . Both are constituted of about 10000 events for each considered point in the  $(m_0, m_{1/2})$  plane. Values of  $m_0$  parameter are separated by  $50 GeV/c^2$  and the scanned range is  $m_0 = [0, 4000] GeV/c^2$ ; values of  $m_{1/2}$  parameter are separated by  $20 GeV/c^2$  and the scanned range is  $m_{1/2} = [100, 600] GeV/c^2$ .

For both the LMX and the mSugra scan points, the mass spectrum was generated using SoftSUSY v2.0.17 [45] and several points are successfully processed by SOFTSUSY spectrum calculator. Then SUSY-Hit v1.3 [46] is applied for radiative

symbol	physics process	generator	$\sigma \times BR$ [pb]	gen. $N_{ev}$
<b>Wjets</b>	<b>W(<math>\rightarrow e, \mu, \tau</math>)+jets</b>	MadGraph	28049	10M
<b>Zjets</b>	<b>Z(<math>\rightarrow ll</math>)+jets <math>m(ll) &gt; 50\text{GeV}</math></b>	MadGraph	3040	100k
<b>Zee</b>	<b>Z(<math>\rightarrow ee</math>)+jets <math>m(ee) &gt; 20\text{GeV}</math></b>	Pythia6	1482	100k
<b>Z<math>\mu\mu</math></b>	<b>Z(<math>\rightarrow \mu\mu</math>)+jets <math>m(\mu\mu) &gt; 20\text{GeV}</math></b>	Pythia6	1482	100k
<b>Z<math>\tau\tau</math></b>	<b>Z(<math>\rightarrow \tau\tau</math>)+jets, <math>m(\tau\tau) &gt; 20\text{GeV}</math></b>	Pythia6	1482	100k
<b>t<math>\bar{t}</math></b>	<b>t<math>\bar{t}</math>+jets</b>	MadGraph	150.3	1M
<b>tW</b>	<b>tW</b>	MadGraph	10.6	466437
<b>WW</b>	<b>WW+jets</b>	Pythia6	43	122980
<b>ZZ</b>	<b>ZZ+jets</b>	Pythia6	5.9	145368
<b>WZ</b>	<b>WZ+jets</b>	Pythia6	18.2	118120
<b>q15</b>	<b>QCD, <math>\hat{p}_T &gt; 15\text{ GeV}</math></b>	Pythia6	$8.762 \times 10^8$	6295857
<b>q30</b>	<b>QCD, <math>\hat{p}_T &gt; 30\text{ GeV}</math></b>	Pythia6	$6.041 \times 10^7$	5069664
<b>q80</b>	<b>QCD, <math>\hat{p}_T &gt; 80\text{ GeV}</math></b>	Pythia6	$9.238 \times 10^5$	2065792
<b>q170</b>	<b>QCD, <math>\hat{p}_T &gt; 170\text{ GeV}</math></b>	Pythia6	$2.547 \times 10^4$	3171950
<b>q300</b>	<b>QCD, <math>\hat{p}_T &gt; 300\text{ GeV}</math></b>	Pythia6	$1.256 \times 10^3$	3130363
<b>q470</b>	<b>QCD, <math>\hat{p}_T &gt; 470\text{ GeV}</math></b>	Pythia6	$8.798 \times 10^1$	2159497
<b>q800</b>	<b>QCD, <math>\hat{p}_T &gt; 800\text{ GeV}</math></b>	Pythia6	2.186	2181700
<b>q1400</b>	<b>QCD, <math>\hat{p}_T &gt; 1400\text{ GeV}</math></b>	Pythia6	$1.122 \times 10^{-2}$	1185024

Table 3.1: List of the MC background samples used in this analysis. The cross sections listed are those used in this work.

correction to mass spectra and branching ratios. The hadronization and decay of SM particles are handled by PYTHIA. A summary of these sample features is in Tab.3.2. In the figures in the following of the chapter, the grey boxes indicate some mSugra scan points, which for any technical issues were missing in one of the steps leading to the final sample used.

## 3.2 Analysis strategy

In order to increase the sensitivity, two main features have been introduced in this analysis with respect to typical analyses for the search of susy in leptonic final states [48], [49], [50]. (*i*) the introduction of every lepton flavor (including  $\tau$ ) channel in the final states:  $\mu\mu$ ,  $\mu e$ ,  $\mu\tau$ ,  $ee$ ,  $e\tau$ ,  $\tau\tau$ . (*ii*) The reduction of the

physics process	$\sigma$ [pb]	generator	generated $N_{ev}$
LM0	54.5	SoftSUSY	207533
	mSugra parameters	generator	generated $N_{ev}$
<b><math>\tan\beta=3</math></b>	$A_0 = 0$ , $\text{sign}(\mu) = +$ , $\tan\beta=3$	SoftSUSY	20M
<b><math>\tan\beta=10</math></b>	$A_0 = 0$ , $\text{sign}(\mu) = +$ , $\tan\beta=10$	SoftSUSY	20M

Table 3.2: List of the MC signal samples used in this analysis. The LM0 cross section is at NLO with a k-factor as calculated by Prospino [47].

transverse momentum threshold of the considered leptons.

The choice of these two features is discussed in the following.

## Inclusion of $\tau$ s in the final state

Taus decaying into hadrons are generally excluded from the searches because of the high QCD jet mis-identification. By excluding the taus, not only the available statistics will be lowered, but also the analysis could get a dependence from the model. Instead, a common approach to all the six possible final states improves the sensitivity to every SUSY model, especially those with large  $\tan\beta$ , where the decay of charginos to tau leptons is favoured with respect the other two lepton families, since the Yukawa coupling get larger for the fermions of the third family and their masses get lower [51]. Moreover the comparison of the results among the several lepton channels can be useful to check the reliability of the analysis and in case estimate systematics uncertainties.

A look at the presence of taus compared to the other leptons, can be given using the mSugra Scan samples; though they are not large  $\tan\beta$  models, where the dominance of tau would be more evident, an effect of the taus enhancement compared to the electrons and muons is visible.

Fig.3.1 and 3.2 show the generator level ratio of the number of events with a chargino decaying, directly or with an intermediate state, to  $\tau$ , to the number of events where the chargino decays in electron (muon), indicated as  $B(\chi^\pm \rightarrow \tau)/B(\chi^\pm \rightarrow e(\mu))$ . In the most of the  $(m_0, m_{1/2})$  plane  $B(\chi^\pm \rightarrow \tau)/B(\chi^\pm \rightarrow e(\mu))$  is about 1, with shifts due to statistical fluctuations, while there exists an area where such ratio reaches  $\mathcal{O}(100)$  values.

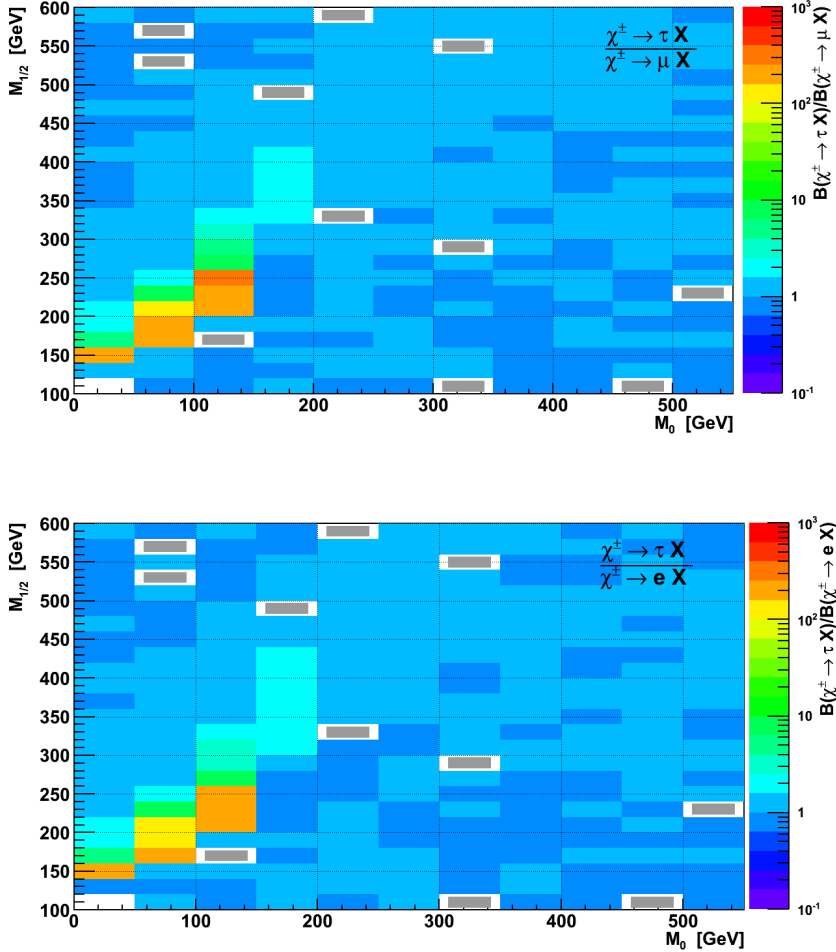


Figure 3.1: Top (Bottom)  $B(\chi^\pm \rightarrow \tau)/B(\chi^\pm \rightarrow e(\mu))$  at generator level for the sample with  $\tan\beta=3$ . The grey boxes indicate some technical failure.

## Inclusion of low $p_T$ leptons

The typical analyses for SUSY searches use lepton  $p_T$  thresholds similar to those used by analyses aimed to measurements of SM physics. In SM analyses the signal leptons are the products of SM vector bosons decays, therefore, even in the case the bosons are produced at rest, the constraint of their invariant mass sets a minimum in the lepton  $p_T$  originating from a two-body decays. The threshold usually used is about  $p_T > 20\text{-}30$  GeV. There exist some models where the Chargino and the Neutralino are almost degenerate. In this case the leptons produced in the decay of  $\chi^\pm \rightarrow l^\pm \chi^0$  can be very soft. In order for the analysis to be sensitive also to such scenarios, the minimum  $p_T$  required for the two leptons is lowered to 5 GeV. Since

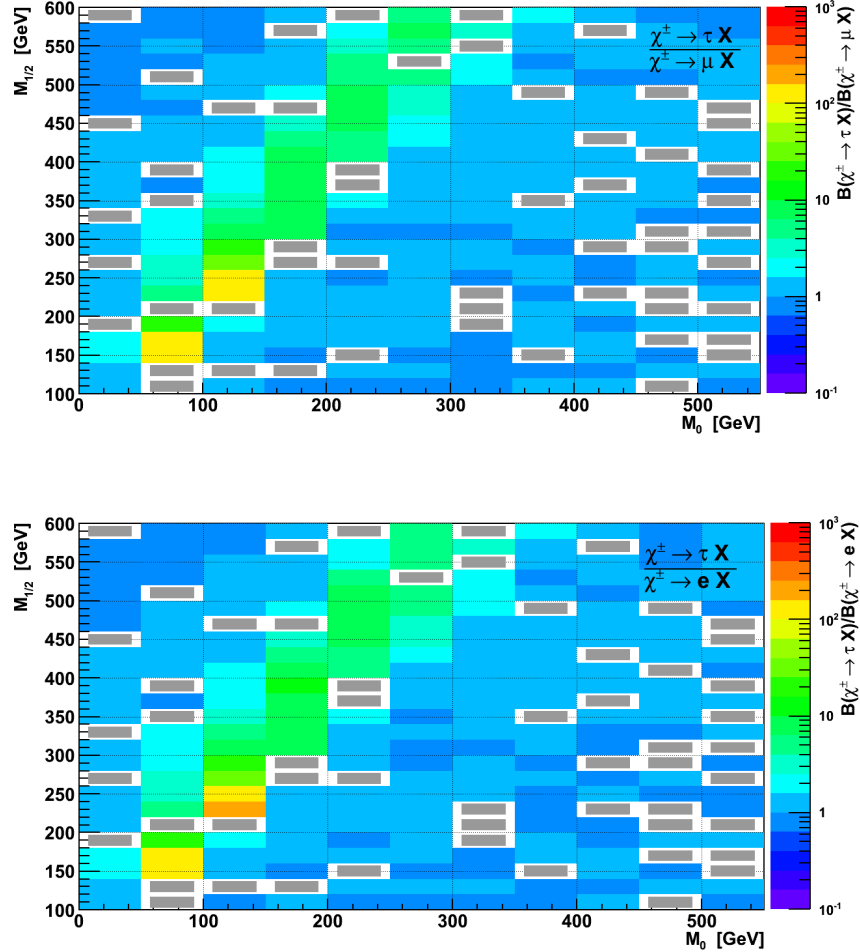


Figure 3.2: Top (Bottom):  $B(\chi^\pm \rightarrow \tau)/B(\chi^\pm \rightarrow e(\mu))$  at generator level for the sample with  $\tan\beta=10$ . The grey boxes indicate some technical failure.

the leptons with low  $p_T$  (order of few GeV) have different properties with respect to the more energetic ones, a dedicated study on these properties, especially the isolation, has been performed in order to understand the behavior of these soft leptons. Furthermore the inclusion of low  $p_T$  leptons requires that no leptonic triggers are used, therefore the use of hadronic triggers is considered.

### 3.3 Physics objects reconstruction

In high energy physics analyses, the physics objects reconstruction is the starting point to derive the event which originates from the collisions. In hadron colliders, it

is a hard task especially because of the large QCD events contribution which is a background for the most of the analyses. In new physics search it is very important to be able to determine the nature of the events and disentangle among different kinds. An accurate reconstruction of the event can be performed with the Particle Flow technique [52] [53] [54], which is described in the next sections.

### 3.3.1 Generalities of the Particle Flow technique

The aim of the Particle Flow (PF) event reconstruction is to reconstruct and identify all the stable particles in the event by using the information coming from each subdetector. These information are combined in order to obtain as better as possible the determination of the direction and energy of every stable particle. This technique aims to reconstruct the whole event after the investigation of every part of it. The main feature needed to reconstruct as many as possible stable particles is a high granularity of the detector. The CMS subdetectors, especially the silicon tracker and the electromagnetic calorimeter, fit with this requirement. Even in collisions with large momentum transfer, each final state particle which is often a constituent of a jet, brings only a small fraction of the full collision energy, this gives rise to a final state with several particles with  $p_T$  and energy of only few GeV. The detection of these less energetic particles is difficult but it is crucial in the particle flow reconstruction.

The stages of the particle flow reconstruction are here summarized.

1. The first step is collecting the so called ***elements*** of the PF reconstruction, namely calorimeter clusters, tracks, muon tracks. Their detection needs to have high efficiency and low fake rate, for this reason dedicated tracking and clustering algorithms have been developed in CMS.
  - **Iterative tracking.** Tracks are seeded and reconstructed with very tight criteria, so that the fake rate is negligible; the hits assigned to the tracks are kept and excluded from the next step where the track seeding criteria are loosened in order to increase the efficiency, while the fake rate remains low because the combinatorics is reduced [55].
  - **Clustering.** *Cluster seeds* are the cells with a energy over a given threshold; by aggregating with specific criteria the seeds, the *topological clusters* are constructed and for each component seed a *particle flow*

*cluster* is defined. This applies for the ECAL, HCAL, PS (first and second layers).

2. A **link algorithm** defines a distance for each pair of elements. It serves to quantify the goodness of the link in order to build sets of elements called **blocks**; an example is illustrated in Fig.3.3. Since the blocks are often constituted only of few elements (because of the fine granularity of the detector), the algorithm performance is independent of the event complexity.
3. The Particle reconstruction algorithm, by using the information in the blocks, identifies the stable particles which gave rise to each block. Starting from such particles, the **PF objects** are reconstructed. The way a specific kind of particle is assigned to one block and the PF object is defined is explained in the following.

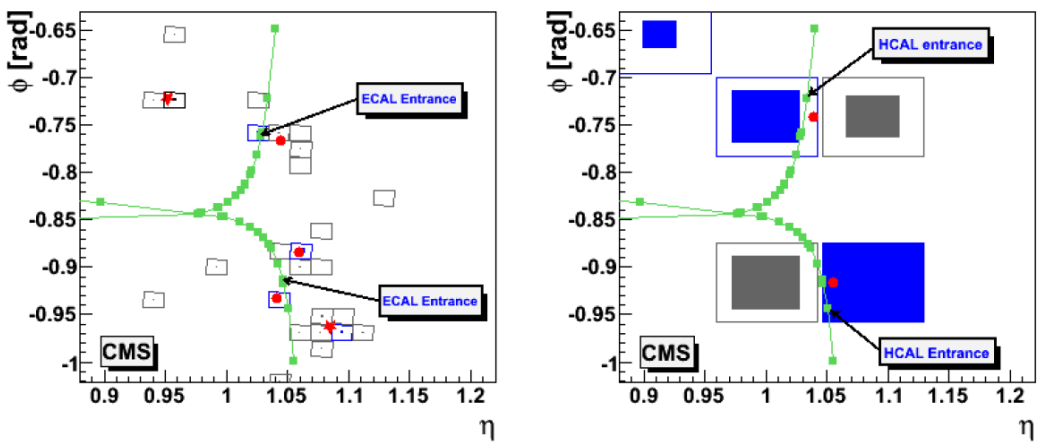


Figure 3.3: Charged-hadron tracks (lines with squares, representing the hits measured in the tracker and the various extrapolation positions to the ECAL and HCAL) each linked to one or two ECAL clusters (left) and an HCAL cluster (right) which are indicated with dots. Each square represents a calorimeter cell. The grey area is proportional to the logarithm of the energy measured in each cell. The clusters represented by a star are linked to neither of the two tracks, and are therefore photon candidates.

### 3.3.2 Muons

The muons are the particles reconstructed at first by the PF procedure. In CMS the muons can be reconstructed with two algorithms. One uses only the muon

chambers information and gives rise to the so called *Stand alone muons* [56], the other algorithm combines the muon chambers measurement with the information from the tracker.

The Stand-Alone muon reconstruction uses a Kalman Filter technique [57] [58], while the Global Muon reconstruction performs a combined fit of on the charged track in the tracker and a muon track in the muon system. A link between these two tracks is established when such global fit returns an acceptable  $\chi^2$ , the latter is considered as the distance between the two elements.

If the momentum given by the combined fit is compatible with the one measured by the tracker only, then the global muon is considered a Particle Flow muon.

### 3.3.3 Electrons

The electron reconstruction starts after the possible assignment of elements to muons is complete. The large amount of tracker material induces the electrons to undergo a significant Bremsstrahlung photon emission. Therefore the original energy of the electron can be spread in a wide range of  $\phi$  in the form of deposits of energy in the electromagnetic calorimeter. Moreover the electron curvature radius is not constant and its trajectory results to be different from a helix. Therefore, a satisfactory tracking procedure for the electron reconstruction aims to consider the energy of every emitted photon in order to go back to the electron trajectory. Furthermore it aims to reconstruct with a good efficiency also electrons with low  $p_T$  and non isolated. In the usual tracking procedure the tracks are reconstructed with a Kalman Filter (KF) approach under the assumption that the charged particle is a muon. Unlike for the muons, during the material crossing, the electrons are affected by energy losses with non-Gaussian fluctuations. The algorithm which takes into account this issue (caused by the Bremsstrahlung emission), uses a Gaussian Sum Filter (GSF) [59], which allows for precise reconstruction. Its drawback is a large CPU-time consumption, so a pre-selection of the seeds in the tracks is needed. [60]

#### Seeding strategy

The usual seeding strategy, called ECAL-driven, identifies the barycentre of the ECAL energy deposits and from it the possible position of the hits in the pixels or in the inner strips is obtained. This strategy works properly if the energy deposits of the emitted photons is matched in a “super-cluster” with the one from the electron. This approach is highly efficient for isolated and high  $p_T$  electrons.

On the contrary, for low  $p_T$  electrons a seeding starting from tracks, called Tracker-driven, is preferred. First a KF is performed leading to a  $\chi^2_{KF}$ , a first selection is applied based on the number of hits  $n_{hit}$  and  $\chi^2_{KF}$ , then a light GSF refit is performed by using five variables and a  $\chi^2_{GSF}$  is obtained. A Boost Decision Trees (BDT) [61] estimator is used to further select the tracks and define the pre-selected electrons. The variable used in the BDT are the following:  $\chi^2_{GSF}$ ,  $\chi^2_{KF}/\chi^2_{GSF}, n_{hit}$ , energy loss as measured by the tracking, the quality of the matching between the ECAL-cluster and the track.

The ECAL-driven and the Tracker-driven seeds are merged in a single collection and the full GSF algorithm, using eleven variables, is applied to it. The Bremsstrahlung photons can convert and generate additional seeds, in this case more tracks than the real electrons can be reconstructed. In order to cope with this issue a cleaning procedure is applied and the result is a GSF track collection.

### Linking

The optimal granularity of the CMS ECAL allows for the clustering of the energy deposit due to the electron and separately those due to the emitted photons. The elements of the electron are: KF and GSF tracks, ECAL, HCAL and preshower clusters. If the outermost tracker measurement, extrapolated to the calorimeters (both ECAL and HCAL and preshower), is inside a cell of a cluster, the track-cluster link is obtained. The Bremsstrahlung recovery strategy starts from a GSF track, in each layer of the tracking detector a tangent to the track is traced till the calorimeters; a cluster is looked for by the linking algorithm and if it is the case, a cluster-Bremsstrahlung photon association is defined. In order to determine the link between a cluster and the electron track, all the clusters not linked to a KF track and which fulfil the requirement  $|\Delta\eta(\text{cluster-track})| < 0.05$ , are considered as connected to the GSF track. The closest one to the track extrapolation is considered as the electron cluster.

The  $p_T$  of the particle flow electron is obtained from a weighted average of the electron cluster energy and the momentum coming from the GSF track.

### 3.3.4 Jets

The jets are composed for the 60% by charged particles, for the 25 % by photons and for the 10 % by neutral hadrons. Since both the tracker and the ECAL in

CMS provide accurate measurements, the 90% of the jet energy is determined with high precision. The jet clustering used is a *sequential clustering* type, named Anti- $\kappa_T$  [62]. The jet algorithms require in input a set of 4-vectors; in PF reconstruction the 4-momentum of the particles reconstructed with the PF procedure are used, unlike the calorimeter based approaches which use calorimetric energy deposits. By reconstructing the particle content of the jets their position and energy will be determined with better performances compared to the measurements obtained by the only calorimeter.

Data-MC comparison of some variables is shown in Fig.3.4. The used sample, referred to as *di-jet*, is obtained requiring events passing the minimum bias trigger, one well defined primary vertex and two jets with the following features:  $|\eta| < 3$ ,  $\Delta\phi(jet1, jet2) > \pi - 0.5$  and  $p_T > 25 \text{ GeV}/c$ .

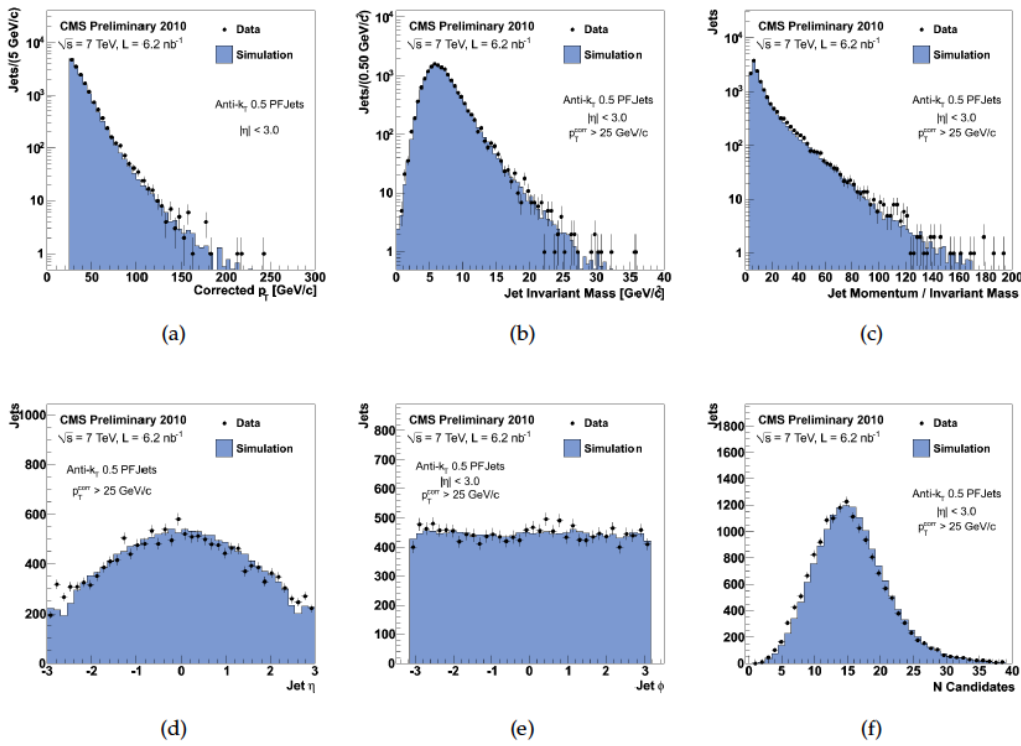


Figure 3.4: Basic jet properties in di-jet events: Distributions of (a) jet transverse momentum; (b) jet invariant mass; (c) the ratio of jet momentum to jet invariant mass; (d) jet pseudorapidity; (e) jet azimuth; and (f) number of particle constituents in a jet [53].

### 3.3.5 Tau Jets

About 2/3 of the taus decay hadronically, such decays are mainly composed by one or three charged pions and by zero and one or two neutral pions, the latter decaying almost immediately in a pair of photons. Only 1 % of the tau decays contain neutral hadrons, therefore the HCAL, the CMS subdetector with the weakest performances, is only marginally used in tau particle flow reconstruction. This makes the PF an ideal technique to reconstruct taus.

In the PF reconstruction, the tau four-momentum is the sum of the four-momenta of all the particles in a small cone of radius  $\Delta R = 0.15$  around the direction of the leading particle in the jet with  $p_T > 0.5$  GeV/c. The leading particle should be within a cone of radius  $\Delta R = 0.1$  around the jet direction and is required to have  $p_T$  above 5 GeV/c .

An *isolation annulus* is defined as the region between a narrow signal cone and a wider cone as is shown in Fig.3.5. It is required that no charged hadrons with  $p_T > 1$  GeV and no photons with  $p_T > 1.5$  GeV are contained in such annulus.

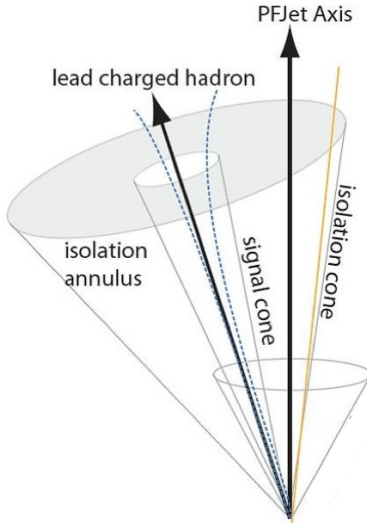


Figure 3.5: Definition of the Tau isolation annulus [63].

The isolation annulus is defined by dedicated algorithms, in this analysis the so called *shrinking cone* algorithm is used [63]. It provides a fixed external cone of radius  $\Delta R = 0.5$ . The internal signal cone is fixed at  $\Delta R = 0.15$  for photons, while for the charged hadrons it has a size changing with the tau-jet  $E_T$ :  $\Delta R = 0.5/E_T$  and anyhow it must be  $0.07 < \Delta R < 0.15$

Since the directions of the particles which define the cone are measured at the

primary vertex of the particle flow event, this reconstruction allows for the reconstructed tau momentum to be not biased by the presence of the underlying event particles. Furthermore the reconstructed tau direction also has a better resolution compared to the standard reconstruction, and, more importantly, the  $\phi$  obtained by PF technique does not undergo to the magnetic field bias which affects the tau  $\phi$  in standard reconstruction.

### 3.3.6 Missing Transverse Energy

After the particle flow event reconstruction, the missing transverse energy is computed by considering the sum of the transverse momentum vector over all the reconstructed particles in the events. This two-dimensional vector is changed in the opposite in the azimuthal direction and named  $\vec{E}_T$ :

$$\vec{E}_T = - \sum_{i=0}^N (\vec{p}_T)_i \quad (3.1)$$

where the sum runs on the PF reconstructed particles.

Its module is indicated with  $E_T = |\vec{E}_T|$ . The better resolution of the PF  $E_T$  with respect to the one based on the calorimetric deposits, is clear from Fig.3.6. Furthermore this figure shows the good agreement between data and simulation, both in minimum bias and in di-jet events.

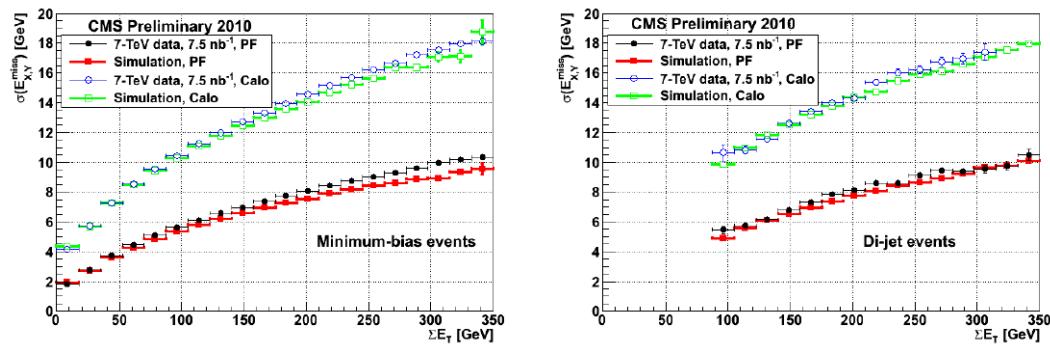


Figure 3.6: Resolution of  $E_T$  for particle based (solid symbols) and calorimeter based (hollow symbols) reconstruction in data (circles) and simulation (squares) as a function of  $\sum E_T$ .

### 3.3.7 $H_T$ and $MH_T$

$H_T$  is the scalar sum of the transverse energies of jets with corrected  $E_T$  greater than 50 GeV. By expressing such jets with  $jet50$   $H_T$  is defined as:

$$H_T = \sum_{jet50}^{N_{jet50}} \sqrt{p_x^2(jet50) + p_y^2(jet50)}. \quad (3.2)$$

The missing  $H_T$ , referred to as  $MH_T$ , is defined as:

$$MH_T = \sqrt{\left( \sum_{jet50}^{N_{jet50}} p_x(jet50) \right)^2 + \left( \sum_{jet50}^{N_{jet50}} p_y(jet50) \right)^2} \quad (3.3)$$

where the sum is over the reconstructed jets with  $E_T > 50$  GeV.

## 3.4 Hadronic High Level Trigger

The HLT trigger to be used in this analysis should not rely on leptonic requirements, since also low  $p_T$  leptons are to be considered. The hadronic HLT paths available in CMS can rely on: (*i*) missing transverse energy, (*ii*) the scalar sum of the physics objects transverse energy and (*iii*) the requirement of two jets with an average transverse energy greater than a given value. In the early stages of LHC the performances of the calorimeters are not well understood, furthermore in hadronic colliders the QCD is responsible of most of energy deposits and it is not accurately known, due to its non-perturbative nature. For such reasons the trigger paths relying on missing transverse energy should not be used until the detectors are accurately known and the QCD physics at this energy range is under control.

The efficiency of the HLT trigger should not be different from a final state to another. A dependence on the leptons flavor could lead the analysis to a dependence on a specific model. Another important feature required to a trigger for this analysis, is an efficiency less dependent on lepton  $p_T$  as possible. This is a desired feature for many analysis, and it is mandatory for searches of new physics, since the signal spectrum is not known.

The efficiency of several trigger paths have been checked for each lepton flavor final state and as a function of the  $p_T$  of the second lepton. In Fig.3.7 this trend is shown for two trigger paths one belonging to the (*ii*) category, using  $H_T$ , and the other to the (*iii*) category. The most inclusive not pre-scaled paths are chosen in each category.

- HLT<sub>HT200</sub> : It requires a  $H_T^{HT} > 200$  GeV computed at HLT by using jets with  $p_T > 30$  GeV.
- HLT<sub>DiJetAve70</sub> : it is seeded by the L1 path L1\_SingleJet70 and requires at least one pair of jets with average scalar  $p_T$  greater than 70 GeV.

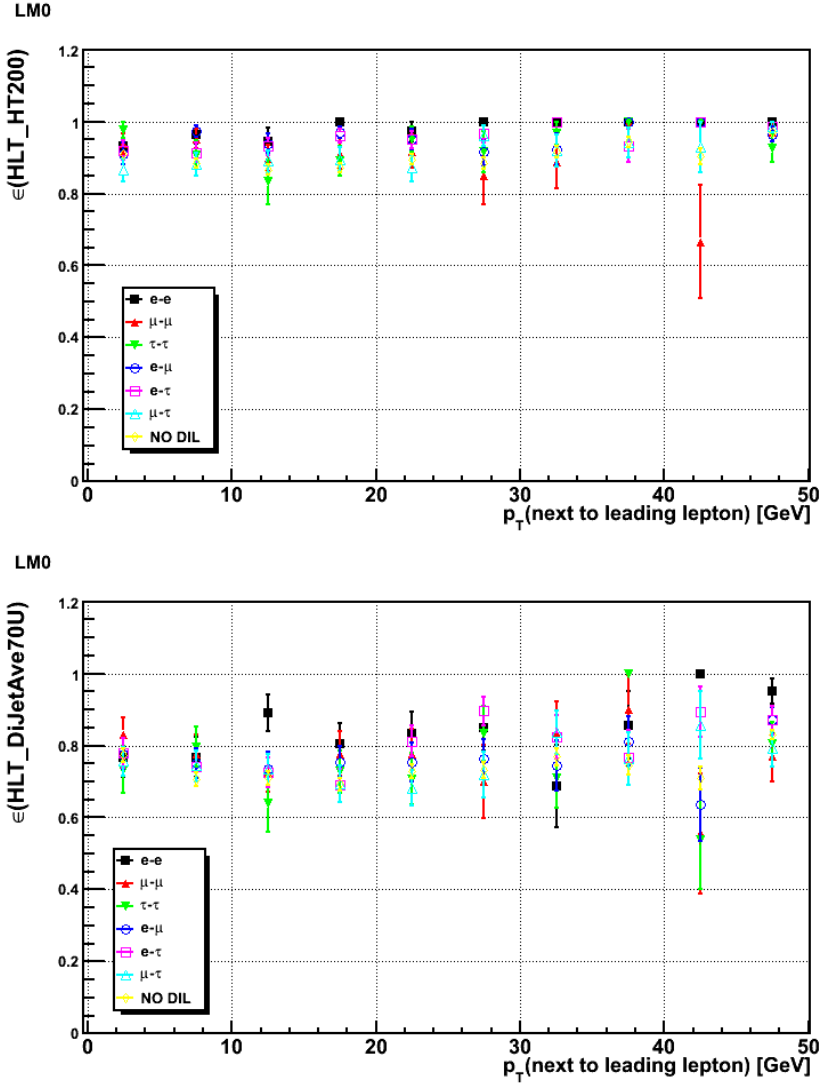


Figure 3.7: HLT efficiency of the paths  $HLT\_HT200$  (top) and  $HLT\_DiJetAve70$  (bottom) as a function of the transverse  $p_T$  of the less energetic lepton, for different final states.

Both such HLT paths show an efficiency independent on the lepton  $p_T$  and lepton flavor of the final states. From Fig.3.7 is evident that the HLT<sub>HT200</sub> trigger

is more efficient than the HLT\_DiJetAve70, therefore the former has been used in this analysis.

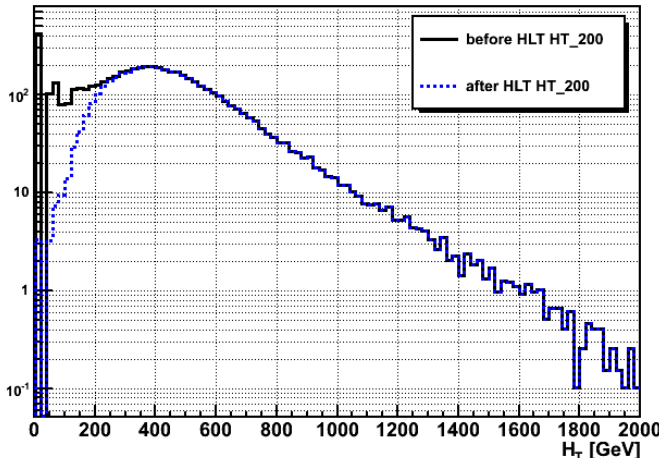


Figure 3.8: Offline reconstructed  $H_T$  variable before and after applying the  $HLT\_HT200$  trigger (based on  $H_T^{HLT}$ ).

## 3.5 Physics objects Identification

This section describes how the origin of the reconstructed leptons is determined. In Sec.3.5.1 the identification of muons and electrons is described. The leptonic tau decay leads the production of a muon or an electron and neutrinos, therefore the final state manifests itself as a charged lepton (muon or electron) and missing transverse energy. In this case the tau lepton identification is brought back to muon or electron identification. The hadronic tau decays need another kind of identification which is described in Sec.3.5.2.

For every lepton flavor the transverse momentum cut is  $p_T > 5$  GeV and a cut on the pseudorapidity  $\eta$  is applied depending on the acceptance of the specific subdetector used.

### 3.5.1 Electrons and Muons

The reconstructed leptons can have been originated from several sources. A selection is needed to disentangle leptons coming from decays of SM vector bosons or new physics particles, from the leptons coming from hadrons resulting from

the hadronization of partons in QCD events or fake leptons due to instrumental background.

The fake leptons are reduced by applying a set of cuts which exploit some features of the true electrons and muons and is referred to as lepton *identification*. The muon identification chosen is the one used by the analysis of Standard Model processes. The electron identification used in SM analyses is less efficient for low  $p_T$  electrons. For this reason for electrons with  $p_T < 20$  GeV a different identification was applied.

In order to distinguish leptons coming from decays of  $b$  and  $c$  coming from Heavy flavor particles from signal muons and electrons, the exploited feature is the *isolation*. Indeed a muon or an electron in pure QCD events, being a jet constituent, is surrounded by other charged particles and photons. On the contrary the leptons which are considered signal leptons are expected to have limited activity around them.

The isolation studies for Standard Model analyses are performed for leptons with  $p_T > 20$  GeV. In this analysis also lower  $p_T$  leptons are considered, and since the surrounding activity depends also on the  $p_T$  range, a different isolation cut was applied for leptons with  $p_T < 20$  GeV.

A generator level categorization has been performed in order to classify the type of reconstructed muons and electrons, so that the source of background leptons can be determined from MC studies and their identification and selection can be optimized. For each reconstructed lepton, the generated leptons were looked for within a cone in  $(\eta, \phi)$  plane delimited by  $\Delta R \equiv \sqrt{(\Delta\eta)^2 + (\Delta\phi)^2} < 0.5$ . The closest generated lepton found was associated to the considered reconstructed candidate and depending from its nature the reconstructed lepton is defined to be in one of the following categories:

- **Prompt:** if it is matched to a generated lepton which come from decays of SUSY particles, a  $W$ , a  $Z$ , or a  $\tau$ ;
- **Heavy-Flavor:** if the generated lepton origins from decays of  $b$  and  $c$  coming from Heavy flavor particles (these are referred to as  $HF$  in the following);
- **Fake:** if no generated leptons are found within a cone with  $\Delta R = 0.5$ . This category can arise from several sources, which can be different if the lepton is a muon or a electron.

### Muons identification

The muon variables used to select signal muons are listed in the following. The muon should be reconstructed both by the silicon tracker and the muon chambers, therefore it must be in the region covered by such subdetectors. Cuts on number of tracker hits and on the  $\chi^2$  of the global fit are applied. There must be at least a muon hit and a requirement on the impact parameter  $d_0$  of the track. The cut values are here reported:

- $|\eta| < 2.4$  ;
- *Tracker Muon and Global Muon*;
- $N_{trkHits} > 10$ ,  $\chi^2/n.d.f. < 10$ ,  $N_{validMuonHits} > 0$ ;
- $d_0 < 0.02$  cm.

### Electron identification

The electron identification is challenging due to the several sources of background. One of the major source of mismeasurements of electrons is the photon conversion. It can lead to charge mismeasurement in real electrons as well to reconstructed fake electrons.

Since the photon conversions often occur far from the primary vertex, usually in the tracker material or the beam pipe, a first requirement which reduces this issue is to reject the electron candidates having an **impact parameter**  $d_0$  respect to the primary vertex greater than some chosen value.

When a track has its first hit far from the beamline, its trajectory can be extrapolated till to the innermost tracker layer; if it meets some active detector layer but there is no hits on it, the track is said to have *missing hits* and is likely originated from an electron from photon conversions. Therefore the requirement that the electron track has **no missing hits** further reduces the photon conversion background.

The electron candidates from photon conversions surviving to the above described requirements can be rejected by exploiting the fact that the two tracks from a photon conversion are parallel to each other in the point where they origin from. Two quantities are defined for each track within a cone with  $\Delta R < 0.3$  around the GSF electron track and opposite charge with respect to the candidate track:

$\Delta \cot(\theta) = \cot(\theta_{\text{track}}) - \cot(\theta_{\text{GSFtrack}})$  and **Dist** described indicate in Fig.3.9 and more accurately in [64].

If among these tracks there exists any with  $\Delta \cot(\theta) < 0.02$  and  $Dist < 0.02$ , then the candidate GSF electron is considered as a fake from photon conversion and rejected.

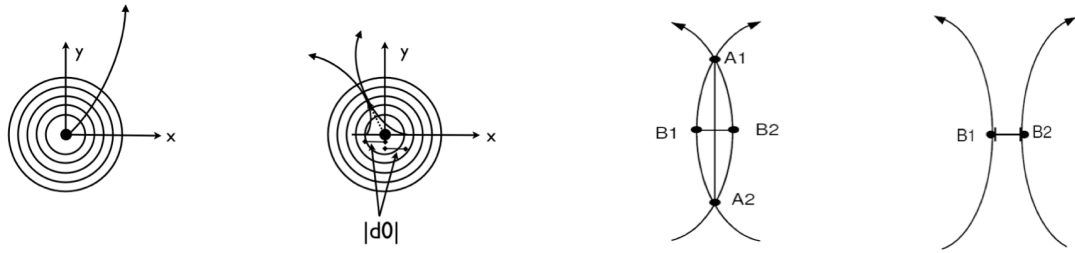


Figure 3.9: From left to right: track of an electron originating from the primary vertex; tracks from photon conversion; definition of the *Dist* variable: the distance between the *B1* and *B2* points in the *x-y* plane, when the two tracks overlap *Dist* is defined to be negative.

When the conversions occur early in the detector material, rejecting them can be more difficult and it can affect the charge measurement. Since in this analysis the correct determination of the leptons charge is crucial, a method to reduce as much as possible the charge mismeasurement is necessary. In CMS the electron charge can be determined in three different ways described in [65], it can be taken equal to: (i) the GSF track charge  $Q_{\text{GSF}}$ ; (ii) to the charge of the general track  $Q_{\text{gen}}$  which shares at least one hit in the pixel detector with the GSF track; (iii) the supercluster charge  $Q_{\text{SC}}$ , which is determined by computing the sign of the  $\phi$  difference between the vector joining the beam spot and the supercluster position and the one joining the beam spot and the first hit of the electron track.

In this analysis all these three methods are exploited by requiring that  $Q_{\text{GSF}} = Q_{\text{gen}} = Q_{\text{SC}}$ , otherwise the candidate electron is rejected.

Besides the requirements described above dedicated mainly to the conversion rejection, a further selection is applied aimed to reduce other background sources. These further requirements are different depending on the  $p_T$  range of the electron candidate. In the following *high* (*low*)  $p_T$  refers to  $p_T > 20$  GeV ( $5 < p_T < 20$  GeV).

### High $p_T$ electrons identification

Signal electrons can be distinguished from other particles due to their unique characteristics that are primarily measured in the ECAL and tracker. Ideally, the electron track would match well with the cluster of energy found in ECAL, both in position and momentum. The track would also emanate directly from the event vertex and be isolated from other tracks and calorimeter energy deposits.

In CMS several electron identification methods have been developed. In early periods of data taking at 7 TeV the most simple and robust identification is preferred. In such a method simple cuts with fixed threshold are applied to variables with a high power to discriminate between prompt and fake electrons.

These variables are:

- $\Delta\phi$  and  $\Delta\eta$ : Geometrical matching between the electron track parameters at the vertex extrapolated to the super cluster and the measured super cluster position.
- $\sigma_{inj\eta}$ : the width of the ECAL cluster along the  $\eta$  direction computed for all the crystals in the  $5 \times 5$  block of crystals centered on the highest energy crystal of the seed cluster.
- $H/E$ : Ratio of the hadronic to the electromagnetic energy deposits of the calorimeters clusters matched to the electron track.

The chosen cuts are the results of an optimization performed by the CMS collaboration.

	Barrel	End Caps
$\sigma_{inj\eta}$	0.01	0.03
$\Delta\Phi$	0.06	0.03
$\Delta\eta$	0.004	0.007
$H/E$	0.04	0.025

Table 3.3: Electron identification cuts.

### Low $p_T$ electron identification

In order to identify signal electrons with  $p_T$  lower than 20 GeV the output of a multivariate analysis is used. Such analysis relies on discriminant variables

which are constructed with information contained by each PF electron supercluster: ECAL cluster associated to the GSF track and ECAL clusters associated to the Bremsstrahlung tracks tangents. Such variables are listed in the following:  $E_e/p_{out}$ , where  $E_e$  is the electron cluster energy and  $p_{out}$  is the track outer-momentum;  $\sum E_\gamma/(p_{in} - p_{out})$  which is the ratio between the Bremsstrahlung energy as measured by the ECAL and the one as measured by the tracker;  $(E_e + \sum E_\gamma)/p_{in}$  which represents the agreement between the total energy measured by the ECAL and the inner track momentum;  $|\eta_{GSF} - \eta_{cluster}|$  which represents the matching between the pseudorapidity measured by the track and the one measured by the ECAL. Furthermore, this multivariate analysis takes into account also the possibility that the Bremsstrahlung emission occurs early in the tracker so that the  $p_{in}$  should be underestimated. On the other hand if the Bremsstrahlung emission occurs too late, the presence of several showers makes difficult to disentangle the ECAL clusters. Such two cases are identified from PF reconstruction and dedicated variables are used instead of the ones above reported.

In order to discriminate electron from charged hadrons, additional tracking (both from GSF and KF tracks) variables are used.

All such variables are used as input to a Boosted Decision Trees (BDT) method. It has been trained with a signal sample constituted by both isolated and non isolated electrons  $Z \rightarrow ee$  and  $bjets$  samples respectively, while the background electrons sample consists of pions.

The discriminant variable on which a cut is performed in this analysis is shown in Fig.3.10 for signal, not isolated and fake electrons. The chosen cut is  $Mva > 0.6$ . Besides on cutting on the  $Mva$  variable, a cut on  $H/E > 0.02$  is performed. The  $H/E$  variable for electron with  $p_T < 20$  GeV is shown in Fig.3.11.

### High $p_T$ lepton isolation

The isolation for leptons with  $p_T > 20$  GeV has been studied by many working groups, since they are the signal for many SM analyses.

The used variables are here defined:

$$Iso_{abs}^{track} \equiv \sum_{\Delta R < 0.3} p_T^{track}; \quad (3.4)$$

$$Iso_{abs}^{ECAL} \equiv \sum_{\Delta R < 0.3} E_T^{ECAL}; \quad Iso_{abs}^{HCAL} \equiv \sum_{\Delta R < 0.3} E_T^{HCAL}; \quad (3.5)$$

$$Iso_{rel}^{comb} \equiv \frac{\sum_{\Delta R < 0.3} (p_T^{track} + E_T^{ECAL+HCAL})}{p_T^{lep}} \quad (3.6)$$

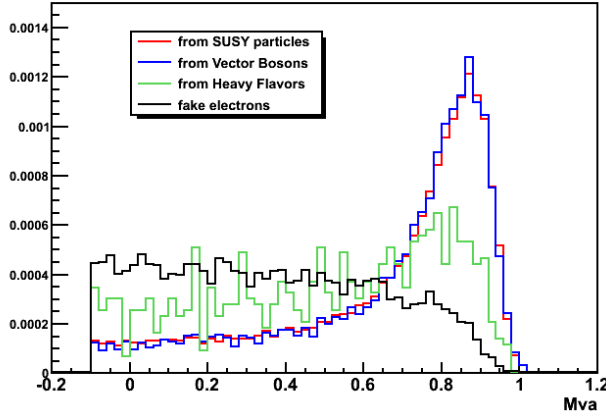
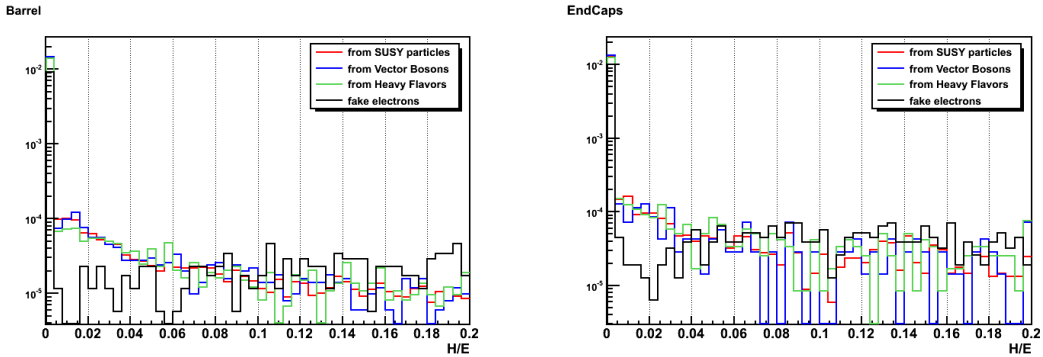


Figure 3.10: Mva output variable

Figure 3.11:  $H/E$  in the barrel (left) and in the End Caps (right).

where the sums run over the objects inside a cone with  $\Delta R = 0.3$  around the candidate lepton.

The SM analyses in which the signal leptons come from vector boson decays apply an isolation requirement by cutting on the  $Iso_{rel}^{comb}$  variables, and the cut values are 0.1 for electrons and 0.15 for muons.

### Low $p_T$ lepton isolation

The variables introduced in Eq.(3.4) and used to select isolated leptons in SM analysis are shown in Fig.3.12, for the electrons and 3.13, for the muons, as a function of the reconstructed lepton  $p_T$  separately for prompt, Heavy-Flavor and fake leptons.

Looking at such scatter plots it is possible to gather that at low  $p_T$  values, the cut rejects a significant fraction of signal events, therefore, additional optimization

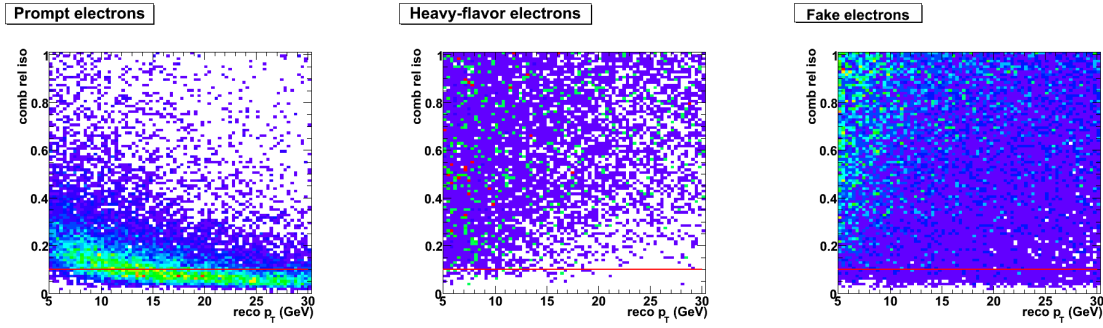


Figure 3.12:  $Iso_{rel}^{comb}$  variable for prompt (left), heavy flavor (middle) and fake (right) electrons

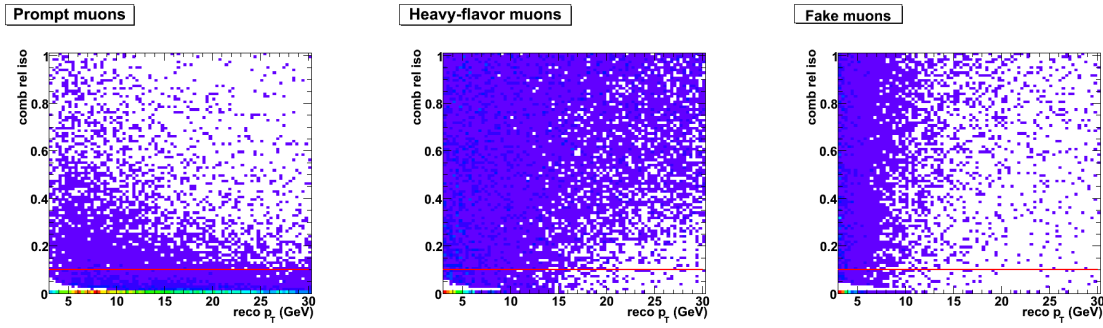


Figure 3.13:  $Iso_{rel}^{comb}$  variable for prompt (left), heavy flavor (middle) and fake (right) muons.

of the isolation procedure is needed; it is detailed in [66] and here summarized.

The isolation variables used for low  $p_T$  leptons are computed with particle flow quantities. They are sums on  $p_T$  of particles reconstructed with the PF technique.

$$Iso_{abs}^{chHad} \equiv \sum_{\Delta R < 0.3} p_T^{chargedHad}; \quad Iso_{abs}^{neuHad} \equiv \sum_{\Delta R < 0.3} p_T^{neutralHad}; \quad (3.7)$$

$$Iso_{abs}^{ph} \equiv \sum_{\Delta R < 0.3} p_T^{photons} \quad (3.8)$$

$$Iso_{abs}^{PFcomb} \equiv Iso_{abs}^{chHad} + \frac{1}{3} Iso_{abs}^{neuHad} + Iso_{abs}^{ph} \quad (3.9)$$

where the sums are on the  $p_T$  of the particles reconstructed inside a cone of  $R = 0.3$  around the considered lepton. The lepton isolation was investigated after the low  $p_T$  lepton identification described above. In order to resemble the large

multiplicity high- $E_T$  jet environment characteristic of SUSY particles production an additional cut,  $H_T > 300$  GeV, was applied.

The following figures, Fig.3.14 and Fig.3.15, show the combined relative isolation  $Iso_{abs}^{PFcomb}/p_T(\text{lep})$  as a function of  $p_T(\text{lep})$  for prompt and heavy flavor electrons and muons.

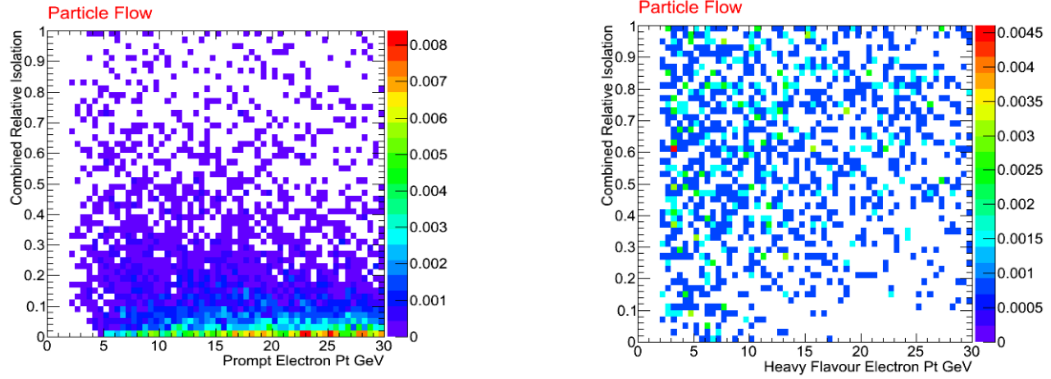


Figure 3.14: Particle Flow Combined Relative Isolation as a function of  $p_T$  for prompt (left) and Heavy Flavor (right) electrons.

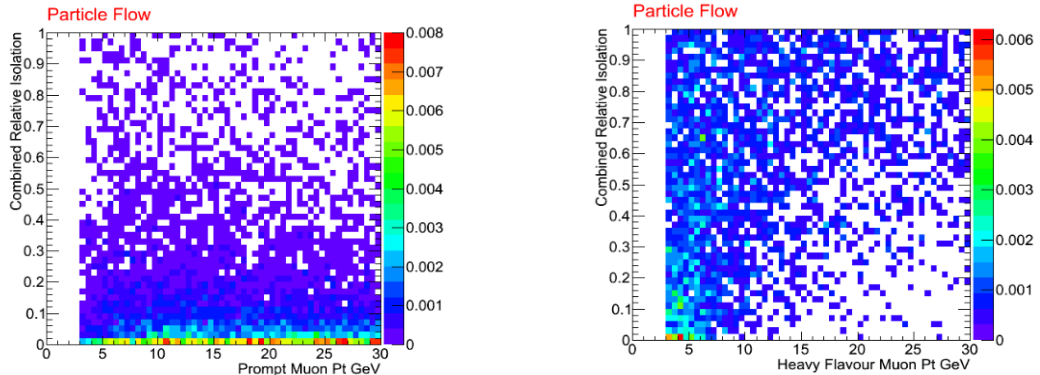


Figure 3.15: Particle Flow Combined Relative Isolation as a function of  $p_T$  for prompt (left) and Heavy Flavor (right) muons.

The optimization procedure was based on a comparison of signal efficiency and background rejection. Efficiency as a function of isolation cut,  $\epsilon(x)$ , was defined as the ratio of reconstructed leptons with isolation  $< x$  to all reconstructed leptons. Rejection as a function of isolation cut,  $rej(x)$ , was defined as the ratio of reconstructed leptons with isolation  $> x$  to all reconstructed leptons, namely for all cut values  $x$ ,  $rej(x) = 1 - \epsilon(x)$ .

The reconstructed leptons are separated in intervals of  $p_T$ , each one 3 GeV wide. The isolation selection is chosen to be based on cutting on the combined isolation variable  $Iso_{abs}^{PFcomb}$  because it is performing better than cutting on one of the separated isolation variables.

The choice of the working point is made by considering the small signal yield in the same sign dilepton search. Between the efficiency and the purity, the former in this case is preferred, therefore the working point is chosen as the lowest cut on isolation at which  $\epsilon_{prompt}$  is greater than 0.9. The cut resulting from this optimization is referred to as  $Cut_{PF}^{eff09}$ . Fig.3.16 shows the  $Cut_{PF}^{eff09}$  as a function of the  $p_T$  bins of the reconstructed muons and electrons.

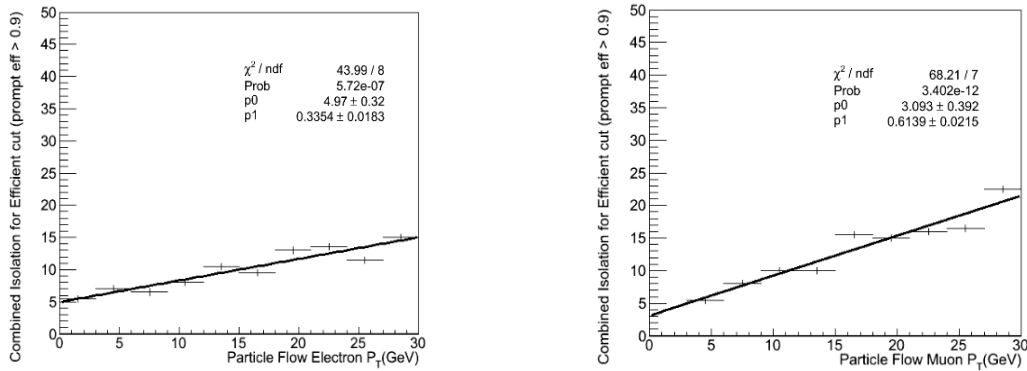


Figure 3.16:  $Cut_{PF}^{eff09}$  as a function of the lepton  $p_T$ , for the electrons (left) and the muons (right).

The result of this optimization for both muons and electrons, is that the optimal cut values enhances with the lepton  $p_T$  and the trend can be well approximated to be linear. Therefore a linear fit was performed and the cut values are taken considering the fit parameters shown in Fig.3.16. Hence the isolation cut is:

$$Iso_{abs}^{PFcomb} < p_0 + p_1 \cdot p_T^{lep} \quad (3.10)$$

where

- $p_0 = 5.0$  [GeV] and  $p_1 = 0.34$  for electrons;
- $p_0 = 3.1$  [GeV] and  $p_1 = 0.17$  for muons;

### 3.5.2 Hadronic Tau Identification

The taus are the only leptons which have a mass large enough to decay in hadrons. The hadronic tau decays are 65% of the total tau decays, so it is important to

manage to identify these decays and disentangle them from the quarks and gluons jets, which are much more abundant, given the high cross section of QCD dijets processes.

After the tau reconstruction described in Sec.3.3.5, the QCD jets faking taus is considerably reduced. A further selection on the reconstructed taus is performed in order to disentangle taus from the fake ones due to isolated electrons and muons which can emit bremsstrahlung photons, named *against e* and *against μ* respectively.

After these pre-identification requirements a tighter identification is needed. In CMS a tau identification based on a neural network has been developed and is called Tau Neural Classifier (TaNC) [67]. It can be applied to the taus reconstructed with the particle flow technique and it is briefly described in the following.

In most of the tau decays a resonance is produced, so the tau identification can be performed by looking for such resonances.

Visible Decay Products	Resonance	Mass [MeV/c <sup>2</sup> ]	Fraction [68]
$\pi^-$	-	135	10.9 %
$\pi^-\pi^0$	$\rho$	770	25.5 %
$\pi^-\pi^0\pi^0$	$a_1$	1200	9.3 %
$\pi^-\pi^-\pi^+$	$a_1$	1200	9.03 %
$\pi^-\pi^-\pi^+\pi^0$	$a_1$	1200	4.5 %
total			59.2 %
others had			5.59 %

Table 3.4: Details of the five hadronic tau decays considered by the TaNC algorithm.

A discriminant is defined for each of the five decay modes listed in Tab.3.4. For each tau candidate, first the decay mode is reconstructed and then the neural network classifiers establish if such final states particles are products of a quark or gluon jet or if it is compatible with an intermediate resonance which is typical of the tau decays.

**Tau lepton reconstruction:** The number of produced  $\pi^0$  is the main feature of each decay mode and in order to determine it, the photons produced in each  $\pi^0$  decay have to be reconstructed. The photons are reconstructed with PF technique and a set of them is selected by the *shrinking-cone* algorithm (Sec.3.3.5) and some

energy requirement. The invariant mass for each of the selected photons pairs is computed and the best pairs, namely with invariant mass closest to the  $\pi^0$  mass, are considered as  $\pi^0$  candidates. The efficiency of this reconstruction depends on  $|\eta|$  and  $p_T$  of the tau candidate.

**Neural network classifiers:** In the TaNC the neural network used have two hidden layers and a single node in the output layers.

The training of the network was performed using simulated  $Z \rightarrow \tau\tau$  events as the signal-like sample and simulated QCD dijet events as the background training sample. These two samples are divided in five subsamples, one for each reconstructed decay mode.

Also the set of variables used in constructing the discriminant is different for each decay mode, although several of them are in more than one discriminant. The performances of this technique as a function of  $\eta$  and  $p_T$  of the tau candidate would allow to use it in different contests. On the other hand the most of the variables are dependent from  $\eta$  and  $p_T$  of the tau candidate and such variables depend on the specific process occurred in the event. For this reason the training process should be as much as possible independent of the  $\tau$  ( $\eta, p_T$ ) spectrum. To this aim a weighting procedure is applied to the training samples in order to obtain the same  $(\eta, p_T)$  spectrum for the tau candidates in both the signal and background samples. In such a way for each point in  $(\eta, p_T)$  the training is performed on signal and background with the same number of events. Since five neural networks are used, a working point, namely the signal efficiency and the fake rate, is defined by five cut values on the discriminants. The working point used in this analysis provides an expected QCD di-jet fake rate of 0.50 % for tau candidates with  $20 < p_T < 50$  GeV, which is referred to as TaNC 0.50%. Fig.3.17 shows the performances of TaNC 0.50% with respect to the other algorithms [63]. The probabilities for quark/gluon jets to pass the tau candidate selection criteria, *fake rate*, are measured from data, while the efficiencies are obtained with simulated  $Z \rightarrow \tau^+\tau^-$  events.

Fig.3.18 shows the probabilities for quark/gluon jets to pass the tau candidate selection criteria of the TaNC tau identification algorithm, for the working point used in this work (in orange) and the others working points.

### Summary of lepton selection

In Tab.3.5, 3.6, the summaries of the electron and muon selections are reported.

Further requirements are needed to avoid possible double counting of physics objects. Indeed two reconstructed objects can origin from the same physics object,

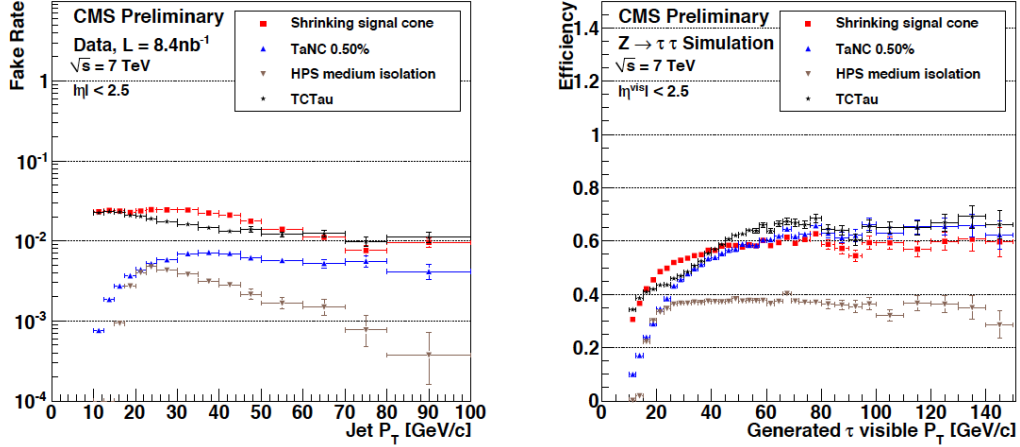


Figure 3.17: Left: Probabilities for quark/gluon jets to pass the tau candidate selection criteria for several tau identification algorithms as function of  $p_T$  as measured from data. Right: efficiencies of several algorithms to reconstruct the hadronic decays of tau lepton in simulated  $Z \rightarrow \tau^+\tau^-$  events. [63].

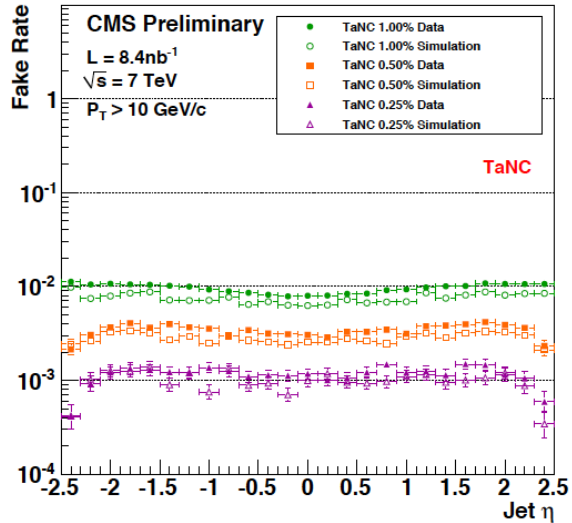


Figure 3.18: Data-MC comparison of probabilities for quark/gluon jets to pass the tau candidate selection criteria of the TaNC tau identification algorithms as function of  $\eta$  [63].

a lepton or a jet. In order to get rid of such overlap a separation in  $\eta$  and  $\phi$  is required between the reconstructed physics objects. Which object is rejected and the order of the requirements are described in the following:

1.  $\mu$ ,  $e$  and  $\tau$  identification;

Electrons	$5 < p_T < 20 \text{ GeV}$	$p_T > 20 \text{ GeV}$
isolation	$Iso_{abs}^{PFcomb} < 5.0 \text{ [GeV]} + 0.34 \cdot p_T^{lep}$	$Iso_{rel}^{comb} < 0.1$
identification	$Mva > 0.6 \text{ AND } H/E < 0.2$	VBF80 (see Tab.3.3)
acceptance		$ \eta  < 2.5$
conversion rejection		$d_0 < 0.02 \text{ cm}$ $N_{missingHits} = 0$ $\Delta cot(\theta) < 0.02$ and $Dist < 0.02 \text{ cm}$
charge compatibility		$Q_{GSF} = Q_{gen} = Q_{SC}$

Table 3.5: Summary of the electron selection.

Muons	$5 < p_T < 20 \text{ GeV}$	$p_T > 20 \text{ GeV}$
isolation	$Iso_{abs}^{PFcomb} < 3.1 \text{ [GeV]} + 0.17 \cdot p_T^{lep}$	$Iso_{rel}^{comb} < 0.15$
acceptance		$ \eta  < 2.4$
identification		$d_0 < 0.02 \text{ cm}$ $N_{trkHits} > 10$ $\chi^2/n.d.f. < 10$ $N_{validMuonHits} > 0$

Table 3.6: Summary of the muon selection.

2. If  $\Delta R(\mu, e) < 0.1$ , then reject the electron;
3. If  $\Delta R(\mu, \tau) < 0.1$  or  $\Delta R(e, \tau) < 0.1$ , then reject the tau;
4. If  $\Delta R(\tau, jet) < 0.1$ , then reject the jet;

Fig.3.20 shows the  $p_T$  of the identified leptons after the trigger requirement.

## 3.6 Selection results

The selection, based on the variables detailed above, is here summarized.

- HLT trigger requirement: HLT\\_HT200 ;
- $H_T > 350 \text{ GeV} ;$

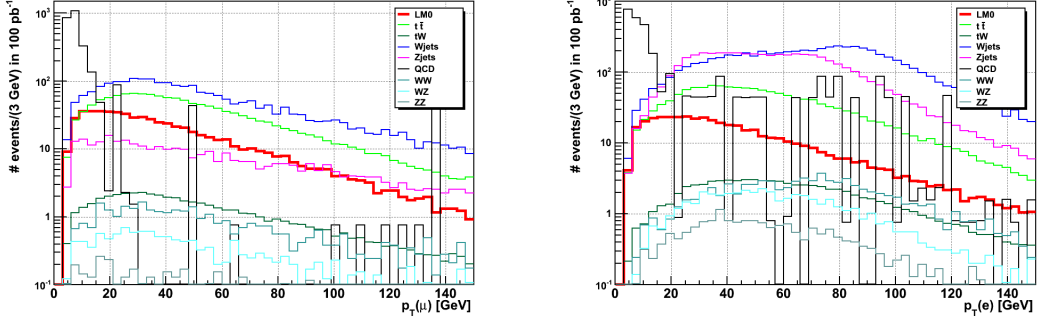


Figure 3.19: Reconstructed  $p_T$  of the identified muons(left) and electrons (right).

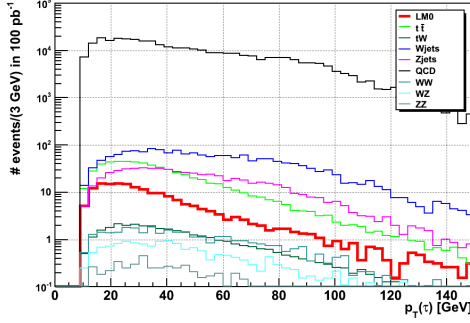


Figure 3.20: Reconstructed  $p_T$  of the identified taus (right).

- $MH_T > 50 \text{ GeV}$ ;
- At least two identified isolated leptons;
- the two leptons with highest  $p_T$  must have the same charge

Some variables used in the selection are shown in the next figures for the considered samples assuming an integrated luminosity of  $100 \text{ pb}^{-1}$ . The cross sections used in order to get the number of selected events expected with an integrated luminosity of  $100 \text{ pb}^{-1}$ , are the ones at the highest order provided in literature and reported in Tab.3.1.

Some first comparisons between data collected since March to September and Monte Carlo simulations have been possible. Fig.3.24-3.25 show the distributions of the number of leptons, for each flavor and all the flavors together obtained after the requirements on the  $H_T$  and  $MH_T$ . A good data-MC agreement is evident, this gives confidence on the reliability of the Monte Carlo simulation results regarding the number of selected events.

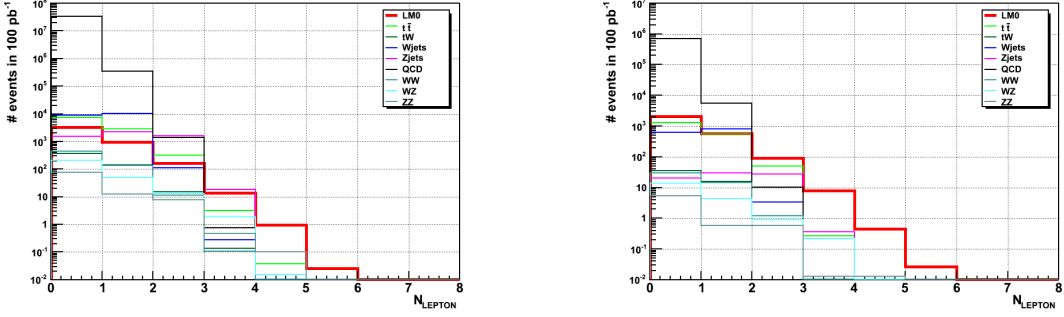


Figure 3.21: Number of reconstructed and identified leptons after only the HLT requirement (left) and after the  $H_T$  and  $MH_T$  (right).

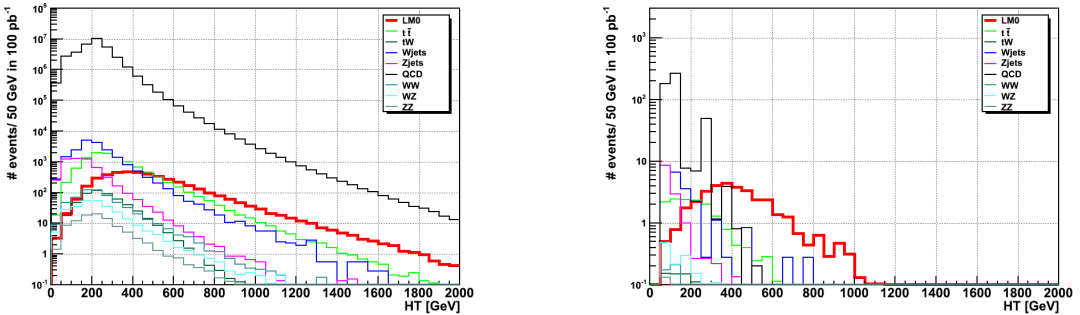


Figure 3.22:  $H_T$  after only the HLT requirement (left) and after all the cuts except the  $H_T$  cut (right).

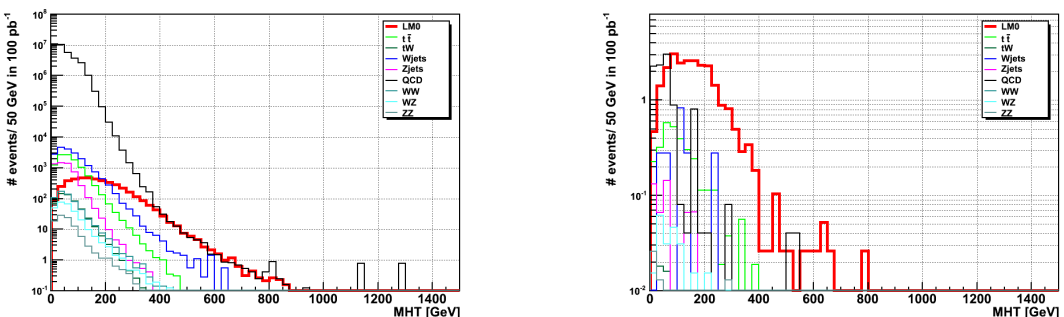


Figure 3.23:  $MH_T$  after only the HLT requirement (left) and after all the cuts except the  $MH_T$  cut (right).

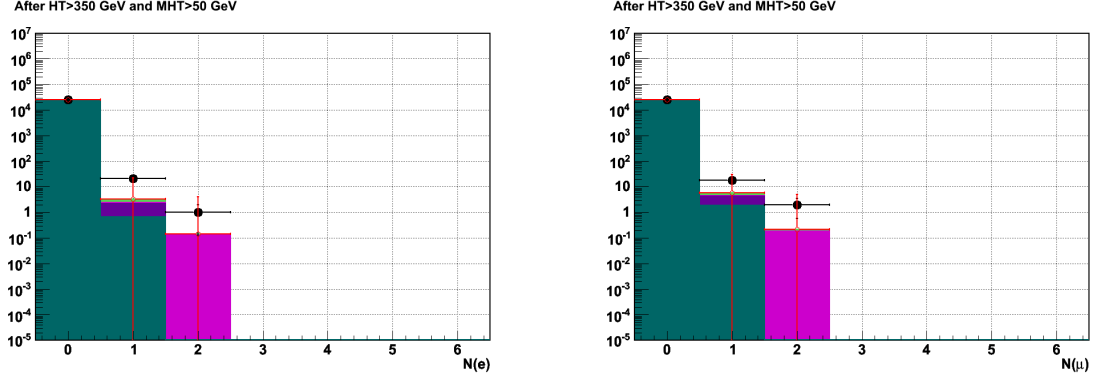


Figure 3.24: Data-MC comparison for the number of electrons (left) and muons (right) obtained after the  $H_T$  and  $MH_T$  selection. The colors assignment is in the legend of Fig.??.

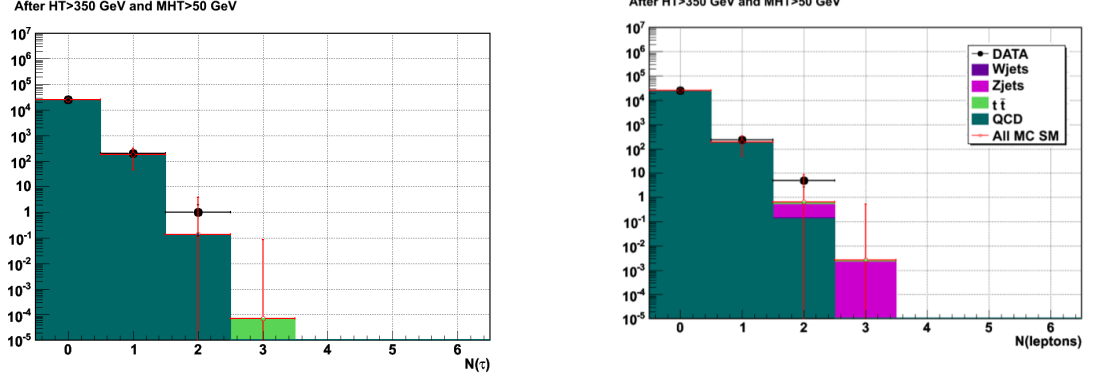


Figure 3.25: Data-MC comparison for the number of taus (left) and all the lepton flavors (right) obtained after the  $H_T$  and  $MH_T$  selection (right).

Tab.3.7 reports the selected event numbers for the  $LM0$  point and for the main background SM processes.

By using the mSugra scan samples listed in Tab.3.2, the efficiency of the selection for every point considered was computed. The signal is defined as the events with exactly two leptons with same charge. In Fig.3.26 the results are reported.

## 3.7 Background Estimation Methods

Tab.3.7 shows that the background contribution due to SM physics processes with same sign prompt leptons is negligible compared to other background sources. The main contribution comes from processes where at least one reconstructed lep-

	$ee$	$\mu\mu$	$\tau\tau$	$e\mu$	$e\tau$	$\mu\tau$	all
$LM0$	1.87	3.94	0.499	5.62	2.00	2.60	16.5
$t\bar{t}$	0.0233	0.0465	0.291	0.081	0.477	0.791	1.71
$tW$	0	0	0.00227	0	0.0205	0.0250	0.0478
$W_{jets}$	0.0	0.0	0.0	0.0	0.90	0.301	1.20
$Zee$	0.0	0.0	0.0	0.0	0.132	0.0	0.132
$Z\mu\mu$	0.0	0.0	0.0	0.0	0.0	0.0776	0.0776
$Z\tau\tau$	0.0	0.0	0.0	0.0	0.0	0.0675	0.0675
$WW$	0.0	0.0	0.0	0.0	0.0	0.0	0.0
$WZ$	0.0154	0.0462	0.0	0.0462	0.0308	0.0	0.139
$ZZ$	0.0	0.0	0.0	0.0	0.0	0.0130	0.0130
$QCD$	$1.00 \cdot 10^{-4}$	0.0	5.39	0	$3.02 \cdot 10^{-4}$	0.807	6.27
Total Bkg	0.0387	0.0927	5.68	0.127	1.58	2.11	9.62

Table 3.7: Number of selected events after the whole selection for the LM0 mSugra point and for the main background processes in  $100 \text{ pb}^{-1}$ .

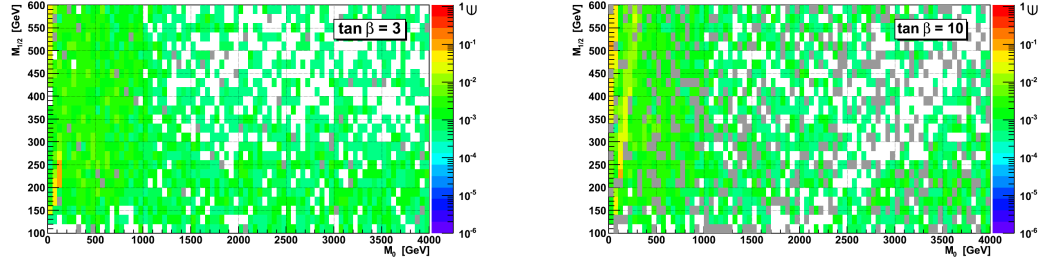


Figure 3.26: Signal (two same sign leptons) efficiency of the selection for the samples  $\tan\beta 3$  (left) and  $\tan\beta 10$  (right)

ton is a fake, or a real lepton but not isolated, they are indicated in the following as *non-prompt* leptons. Furthermore such background arises especially from the production of hadronic jets, which is regulated by the non perturbative QCD. For these reasons such sources deserve particular attention and a data driven method to estimate them is needed.

Another kind of background which needs care arises from mistaking in determine the lepton charge; in order to estimate it, a data driven method has been put in place.

### 3.7.1 Main Background Sources

#### Non-prompt Electrons

There exist several sources giving rise to non-prompt electrons which can be selected as prompt ones. The main sources are mentioned here. The fake electrons coming from photon conversion can have features consistent with the selection and pass it. Neutral pions can be produced by charge exchange of charged pions and the photons produced by the  $\pi^0$  decay, matched to the  $\pi^\pm$  track, can lead to an  $E/p$  and impact parameter consistent with the primary vertex. Real electrons coming from heavy flavor decay could pass the isolation requirements.

#### Non-prompt Muons

The sources of fake muons are here summarized. Charged pions and kaons can decay before they interact in the calorimeter producing muons. Hadronic showers originated by very high energetic jets could not be completely absorbed by the calorimeters and one of the produced particles could reach the muon system and identified as a muon. Muons can also come from cosmic rays and selected because they pass close to the primary vertex. Besides these fake sources there are also real muons which contribute to the background, they are the decay products of the mesons coming from the hadronization of the heavy flavor partons. The  $t\bar{t}$  process, since it (almost) always produces two b-jets, is the largest physics process giving rise to selected events where one lepton is a prompt one coming from  $W$  and the other is a not isolated muons coming from a  $b$  parton. Moreover the QCD production of  $b\bar{b}$ , given its huge cross section, can be an important source of selected events with two non isolated muons.

#### Non-prompt Taus

It is known that tau leptons decaying in hadrons present particular difficulty in their identification, since they give rise to hadronic jets which are hard to disentangle from QCD hadronic jets. Hence QCD jets are likely to be identified as hadronic taus.

### Physics processes background sources

The background contributions, for which data-driven methods have been implemented can be organized in groups depending on the number of the prompt leptons which are identified by the selection. The groups are here listed (just for convenience).

1. no prompt leptons: the purely dijets QCD events are the main sources.
2. one prompt lepton: they consist mainly of semileptonic  $t\bar{t}$  and  $W+jets$ ; also other processes, such as  $Z+jets$ , could be a source if one charged lepton is not identified.
3. two opposite sign leptons:  $Z+jets$ , dibosons, dileptonic  $t\bar{t}$  are the sources of background with two identified prompt leptons and a mismeasurement of the charge.
4. two same sign leptons: to this kind of background processes the next chapter is dedicated.

### 3.7.2 Method of the Estimation of Background from Non-Prompt Leptons

Before to explain in detail the methods used to estimate the background yield for each source in point 1 and 2 of the previous section, the general concepts are here resumed. The QCD background determination should be as data-driven as possible. Thought this is true for every background sources, for the QCD this statement apply more than other processes which rely on electroweak physics, which is satisfactory understood. For such reason the QCD background estimation in this analysis uses only information obtained from real data.

In the selected QCD events, the two higher  $p_T$  leptons are fake leptons or not isolated leptons. The general idea is to factorize a cut, or set of cuts, which better represents the lepton identification from the rest of selection. A *loose identification* is defined by eliminating such cut from the identification selection described in Sec.3.5 and is different for each kind of leptons.

After applying the whole set of cuts of the analysis selection, except for changing the lepton identification for the *loose* one, in real data, the remaining sample, named *loose sample*, will be constituted mostly of QCD events, given their large cross section. The selected events after the whole analysis selection will be given

essentially by the product of this number of events times the probability that the two leptons pass the identification cut. The background sources with only one prompt lepton, namely the point 1 background, can be estimated by the same method described for the QCD, except that one identified lepton is required in the loose sample and the other one is required to be loosely identified and not passing the tight selection. Also in this case, the fake rate is determined by using selected samples dominated by QCD processes.

The number of reconstructed leptons satisfying the complete analysis identification requirements will be indicated by  $N_{tight}$ ; the number of reconstructed leptons satisfying the loose identification requirement is indicated with  $N_{loose}$ .

The ratio  $N_{tight}/N_{loose}$  is mapped as a function of  $\eta$  and  $p_T$  of the lepton:

$$\epsilon_{T/L}(\eta_i, p_{T,i}) = \frac{N_{tight}(\eta_i, p_{T,i})}{N_{loose}(\eta_i, p_{T,i})} \quad (3.11)$$

Such quantity is determined by using data samples which are dominated by QCD events.

The other ingredient needed to compute the number of expected Standard Model event, is the number of loose leptons which should multiply the ratio above. Since the method is meant to use only data, the data samples used to compute the two factors should be uncorrelated. The selection of leptons satisfying the loose requirements but failing the analysis identification, named *looseNOTtight*, allows for picking out an orthogonal sample to the one used to compute  $\epsilon(\eta, p_T)$ . In order to take into account the fact that the sample does not contain all the loose leptons the estimated number is divided by the factor  $1 - \epsilon_{T/L}$ .

The number of events with 0 *prompt* lepton, as defined by the MC truth described in Sec.3.5.1 is indicated with  $N_{BKG}^{0prompt}$ ; the number of events with 1 *prompt* lepton, is indicated with  $N_{BKG}^{1prompt}(i)$  where the symbol  $i$  stands for the *non-prompt* lepton.

### Expressions for the Number of selected events with zero and one non-prompt leptons

The events, selected by the whole analysis selection, where both the leptons are non-prompt, indicated with  $i$  and  $j$  indexes, are here considered.

The absolute value of the pseudorapidity and transverse momentum of the non prompt leptons are indicated with:  $(\eta_i, p_{T,i})$  and  $(\eta_j, p_{T,j})$ . The number of events passing the *loose selection*, and not passing the *tight* lepton requirements for both

the leptons, is indicated with  $N_{L!T}(\eta_i, p_{Ti}; \eta_j, p_{Tj})$ .

The value  $N_{BKG}^{0prompt}(\eta_i, p_{Ti}; \eta_j, p_{Tj})$  is given by the expression:

$$N_{BKG}^{0prompt}(\eta_i, p_{Ti}; \eta_j, p_{Tj}) = \sum_i \sum_j N_{L!T}(\eta_i, p_{Ti}; \eta_j, p_{Tj}) \frac{\epsilon_{T/L}(\eta_i, p_{Ti})}{1 - \epsilon_{T/L}(\eta_i, p_{Ti})} \frac{\epsilon_{T/L}(\eta_j, p_{Tj})}{1 - \epsilon_{T/L}(\eta_j, p_{Tj})} \quad (3.12)$$

The number of events passing the *loose selection*, with one lepton passing the *tight* criteria, and the other one, indicated with  $i$ , not passing it, is indicated with  $N_{L!T}(\eta_i, p_{Ti})$ .

$$N_{BKG}^{1prompt}(\eta_i, p_{Ti}) = \sum_i N_{L!T}(\eta_i, p_{Ti}) \frac{\epsilon_{T/L}(\eta_i, p_{Ti})}{1 - \epsilon_{T/L}(\eta_i, p_{Ti})} \quad (3.13)$$

### 3.7.3 Determination of $\epsilon_{T/L}$ for Non-Prompt Leptons

The sample used to determine  $\epsilon_{T/L}$  has to be dominated by the QCD processes. On the other hand, the physics environment should be as similar as possible to the signal environment. These needs have driven the choice of the selection applied to the data sample:

- HLT path requiring at least a jet with uncorrected  $E_T > 50$  GeV.
- In order to reproduce the SUSY environment large hadronic activity is required by applying the cut:  $H_T > 300$  GeV.

#### Electrons

The set of requirements chosen to constitute the loose electron identification are essentially all the cuts in Sec.3.5.1 except for the  $\Delta\phi$ ,  $\Delta\eta$ ,  $\sigma_{i\eta i\eta}$  and  $H/E$  cuts. They are listed in Tab.3.8.

#### Muons

Since the muons from heavy flavor decays are the largest source of the non-prompt muons, the requirement which is applied to the tight identification and not the loose one has been chosen as the isolation.

The QCD di-jet  $b\bar{b}$  is the process chosen in order to determine  $\epsilon_{T/L}(\eta_i, p_{Ti})$ . The selection applied to the data sample requires at least one b-tagged, besides the HLT and the  $H_T$  requirement.

- At least one b-tagged jet
- In order to study the muon isolation without any bias introduced by the b-tagging requirement, a muon coming from the other  $b$ -jet is considered; this is achieved by looking for a muon far from the b-tagged jet requiring  $\Delta R(\mu, \text{b-tag}) > 1$

### Taus

The requirement eliminated from the tau identification chosen for the tau leptons is the highest level identification based on neural network algorithm described in Sec.3.5.2.

In order to select QCD dijet events, with no contamination from prompt leptons, an upper cut on the  $\cancel{E}_T$  has been applied; it is aimed to reject the  $W + \text{jet}$  events, the source of prompt leptons with largest cross section.

### Data-MC comparisons for $\epsilon_{T/L}(\eta_i, p_{Ti})$

The comparison between the data collected and the MC simulation are shown in this section.

As a reminder the Tab.3.8 summarizes the event selection and the definition of the loose identification for each lepton flavor in order to determine the  $\epsilon_{T/L}$  factor.

Fig.3.27 and 3.28 show  $\epsilon_{T/L}(\eta_i, p_{Ti})$  for several  $p_T$  intervals both for the barrel and for the endcap region.

Despite the low available statistics, a reasonable agreement is obtained, in particular no bias are evident.

The more copious statistics available for the taus selected by the loose identification, allowed for not only data-MC comparison, but also among several intervals of  $H_T$  in the collected data. Fig.3.29-3.31 show the good agreement among  $\epsilon_{T/L}(\eta, p_T)$  obtained from the samples with different  $H_T$  values and the MC QCD sample.

Such agreement assures that no bias is expected, in the predicted event number, due to potentially different environment of the selected samples.

	Electron	Muon	Hadronic Tau
event selection	HLT_Jet50 $H_T > 300 \text{ GeV}$	HLT_Jet50 $H_T > 300 \text{ GeV}$ $N(\text{b-tag jet}) > 0$ $\Delta R(\mu, \text{b-tag jet}) > 1$	HLT_Jet50 $H_T > 300 \text{ GeV}$
loose lepton identification	$d_0 < 0.02$ $N_{\text{missingHits}} = 0$ $\Delta \cot(\theta) < 0.02$ $Dist < 0.02 \text{ cm}$ $Q_{\text{GSF}} = Q_{\text{gen}} = Q_{\text{SC}}$ $Iso^{\text{PF} \text{comb}}$ cut	$d_0 < 0.02 \text{ cm}$ $N_{\text{trkHits}} > 10$ $\chi^2/\text{n.d.f.} < 10$ $N_{\text{validMuonHits}} > 0$	against $e$ against $\mu$

Table 3.8: List of the event selection and the loose identification for each lepton flavor.

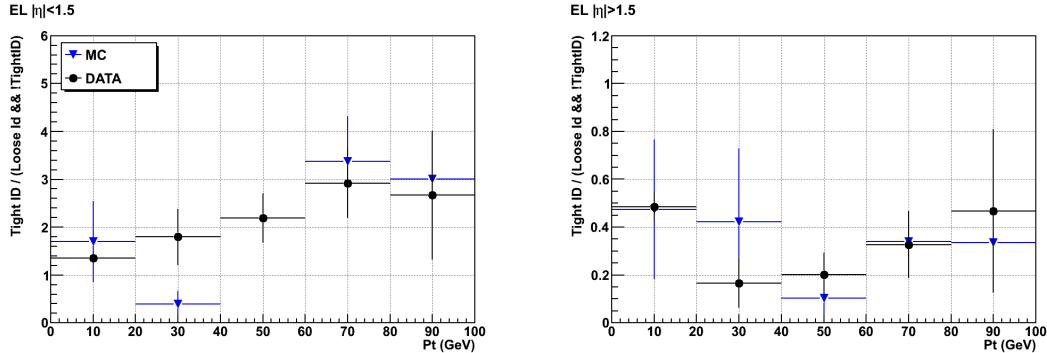


Figure 3.27: Comparison between data (black points) and MC simulation (blue triangles) for the electron  $\epsilon_{T/L}(\eta_i, p_{T,i})$  as a function of  $p_T$  in the barrel (left) and end-cap (right) region.

### 3.7.4 Number of selected events with two opposite sign leptons

Besides the background coming from the presence of non-prompt leptons, also Standard Model processes with two prompt opposite sign leptons can be recon-

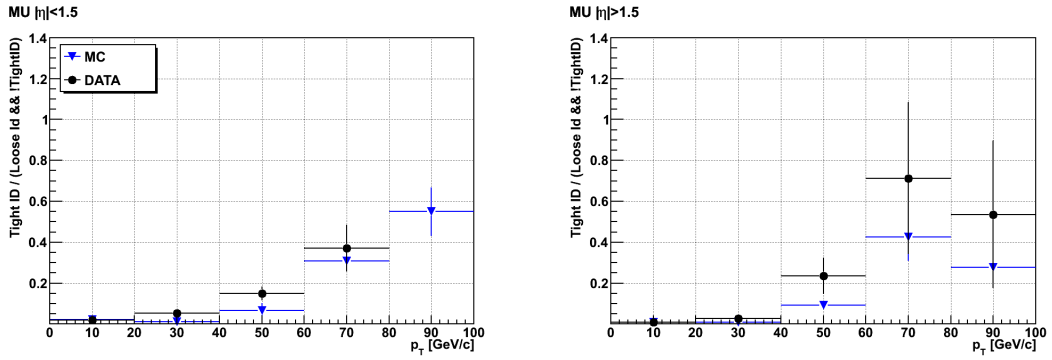


Figure 3.28: Comparison between data (black points) and MC simulation (blue triangles) for the muon  $\epsilon_{T/L}(\eta_i, p_{Ti})$  as a function of  $p_T$  in the barrel (left) and end-cap (right) regions.

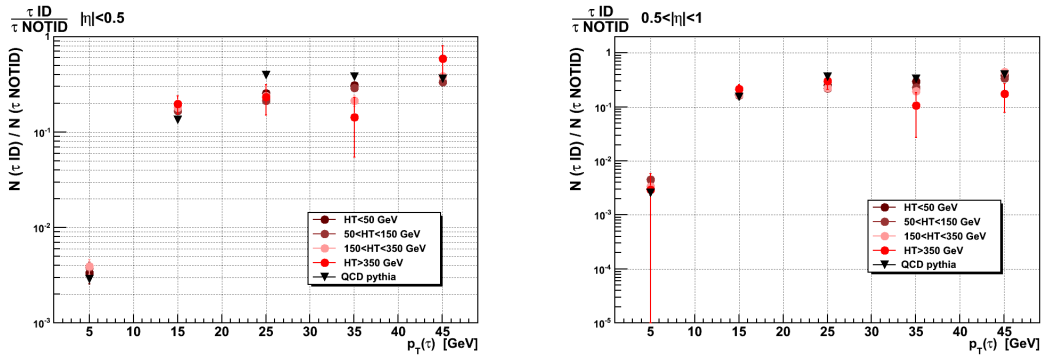


Figure 3.29: Comparison between data (points, see text for details) and MC simulation (black triangles) for the tau  $\epsilon_{T/L}(\eta_i, p_{Ti})$  as a function of  $p_T$  in  $0 < |\eta| < 0.5$  (left) and  $0.5 < |\eta| < 1$  (right) regions.

structed as same sign if a wrong charge is assigned to one lepton.

Such case is very unlikely for muons, instead a careful study is needed to estimate this kind of background for the electrons.

Indeed the photon originating from the bremsstrahlung radiation emitted by the electrons in the tracker volume, can convert and a track can be reconstructed with hits from one of the electrons originating from the conversion.

The most copious processes with two prompt opposite sign leptons are the Drell-Yan process ( $Z/\gamma^* + \text{jets}$ ) and the top quark pairs production.

The requirement on the compatibility of charge should reject most of the events of these processes; nevertheless given the importance of the same sign requirement

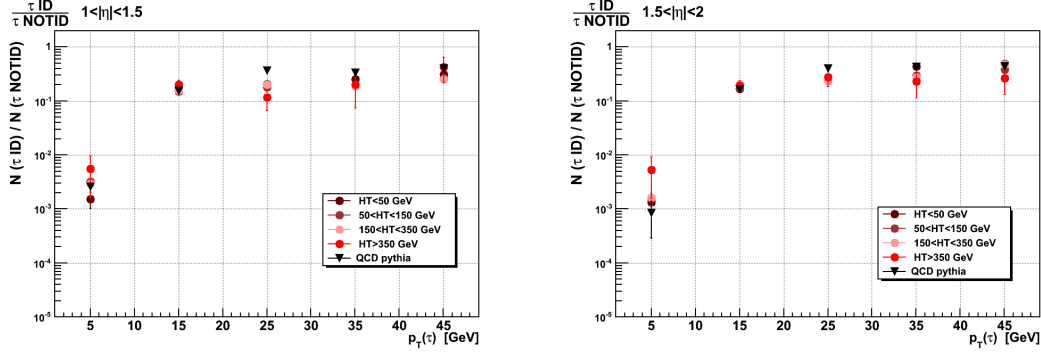


Figure 3.30: Comparison between data (points, see text for details) and MC simulation (black triangles) for the electron  $\epsilon_{T/L}(\eta_i, p_{Ti})$  as a function of  $p_T$  in  $1 < |\eta| < 1.5$  (left) and  $1.5 < |\eta| < 2$  (right) regions.

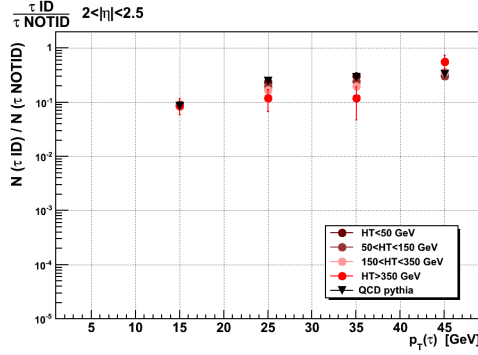


Figure 3.31: Comparison between data (points, see text for details) and MC simulation (black triangles) for the electron  $\epsilon_{T/L}(\eta_i, p_{Ti})$  as a function of  $p_T$  in  $2 < |\eta| < 2.5$  regions.

for this analysis, a data-driven method is needed to estimate the probability to have opposite sign leptons passing the whole analysis selection.

The data-driven method chosen in order to estimate this background makes use of data sample selected as events with  $Z$  boson production.

The  $\eta$  and  $p_T$  distributions of the electrons are considered.

For every interval of  $\eta$  and  $p_T$  the total number of electrons in the sample is indicated as  $N_{total}^e(\eta, p_T)$ , the number of electrons with mis assigned charge is defined as  $N_{wrongCh}^e(\eta, p_T)$  and the probability to assign a wrong charge to an

electron as a function of its  $\eta$  and  $p_T$ , is indicated with:

$$P_{\text{wrongCh}}(\eta, p_T) = \frac{N_{\text{wrongCh}}^e(\eta, p_T)}{N_{\text{total}}^e(\eta, p_T)} \quad (3.14)$$

One electron is selected by requiring very tight criteria, tighter than the analysis requests, such electrons are considered as *tag* electrons and indicated with  $e_{\text{Tag}}$ . Besides the analysis requests the  $e_{\text{Tag}}$  must be in the barrel region with  $|\eta| < 1$  and have a small fraction of Bremsstrahlung energy emitted. In the sample with at least one  $e_{\text{Tag}}$ , another electron is looked for, the so called *probe* electron; it has to satisfy the analysis requirements, and is indicated with  $e_{\text{Probe}}$ .

$e_{\text{Probe}}$	$e_{\text{Tag}}$
analysis selection	analysis selection $ \eta  < 1$ (barrel) $f_{\text{brem}} < 0.03$

Table 3.9: . Requirement to satisfied by the tag and probe electrons.

The data sample selected with the presence of one  $e_{\text{Tag}}$  and one  $e_{\text{Probe}}$  is supposed to be dominated by  $Z$  boson production, therefore opposite charge electrons are expected.

Fig.3.33 demonstrates that it is really the case, since the  $Z$  mass peak is well visible in the two lepton invariant mass.

The good outcome of this method, testified by the  $Z$  mass distribution, is possible because the transverse momentum resolution for electrons at such energy range is dominated by the ECAL resolution.

Since the probability to mis-assign the charge for both the two selected electrons can be neglected, the quantity  $P_{\text{wrongCh}}(\eta, p_T)$  is obtained by the ratio

$$P_{\text{wrongCh}}(\eta, p_T) = \frac{N_{\text{SS}}^e(\eta, p_T)}{N_{\text{total}}^e(\eta, p_T)} \quad (3.15)$$

where  $(\eta, p_T)$  are the  $e_{\text{Probe}}$  variables.

Such method allows for the estimation of  $P_{\text{wrongCh}}(\eta, p_T)$  only in the range of  $\eta$  and  $p_T$  covered by electrons coming from  $Z$  bosons. In order to extend such estimation in wider regions, the Monte Carlo simulation has to be used.

The  $P_{wrongCh}(\eta, p_T)$  value estimated with MC is compared with the one obtained by using data sample. If discrepancies will be visible, than a correction factor will be applied to the MC  $P_{wrongCh}(\eta, p_T)$  estimation in  $(\eta, p_T)$  region out of the  $Z$  peak range.

The check of the reliability of the method, by data-MC comparison, has been performed by comparing the  $P_{wrongCh}(\eta, p_T)$  obtained with different samples.

Fig.3.32 show the mis-charge rate as a function of the electron  $|\eta|$  and the transverse momentum in the interval  $40 < p_T < 70$  GeV, obtained by several methods: (i) by using a samples of generated single electrons (*particle gun*); the MC sample  $Z+jets$  was considered both (ii) by using the MC truth information to select the electrons from  $Z$  to determine the mis charge rate and (iii) by applying the tag and probe method exactly like for the data sample

The tag and probe method was applied also to the available data sample but no same sign electrons events were selected.

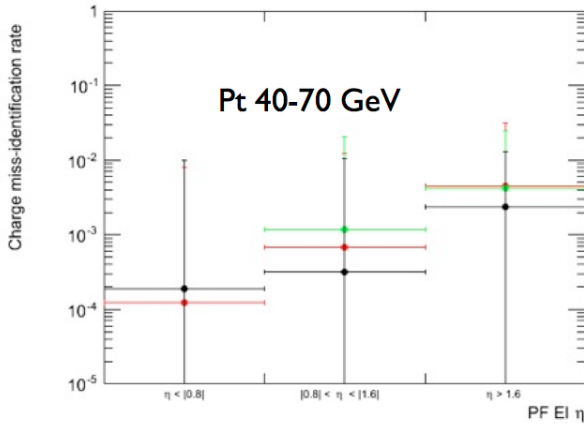


Figure 3.32: Mischarge rate as a function of  $|\eta|$  for  $40 < p_T < 70$  GeV determined with particle gun (black), MC truth in  $Z+jets$  sample (green) and the data-driven tag and probe method in  $Z+jets$  sample (red).

A good agreement among the  $P_{wrongCh}$  obtained with the three kind of selection in the MC samples.

Relaxed requirements on the charge of the two electrons have been applied: (i) both same sign and opposite sign pairs; (ii) same sign electrons as determined by the only *GSF* method for the probe electron; (iii) same sign electrons, with the probe charge determined by the two methods which give the same result, named

*majority* method.

Fig.3.33 shows the invariant mass of the two electrons for the four different electron selections; only the sample containing opposite sign pairs has acceptable statistics to pick out some shape and the peak around the  $Z$  mass value is well visible.

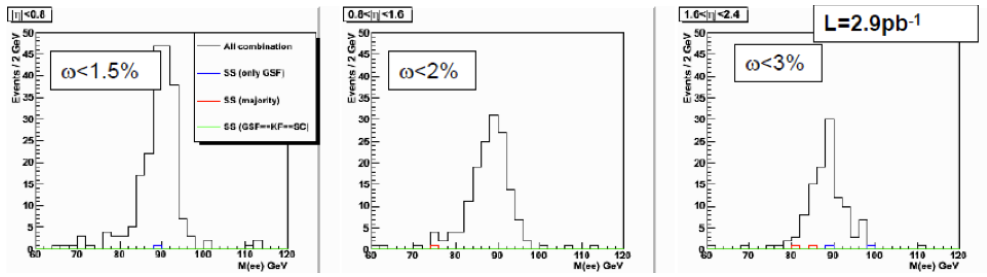


Figure 3.33: Invariant mass of two prompt leptons, opposite and same sign (black), requiring only same sign with *GSF* (blue), *majority* (red) and *GSF = GEN = SC* (green) method

### 3.7.5 Estimation of Background Yield

Given the values for  $\epsilon_{T/L}(\eta_i, p_{Ti})$ ,  $N_{L!T}(\eta_i, p_{Ti})$  and  $N_{L!T}(\eta_i, p_{Ti}; \eta_j, p_{Tj})$  obtained from real data as described in Sec.3.7.3, the total number of events for each flavor lepton channel can be estimated by summing the contributions of every source of non prompt leptons:

$$N_{BKG}^{tot}[lep_1, lep_2] = N_{BKG}^{0prompt}[lep_1, lep_2] + N_{BKG}^{1prompt}[lep_1, lep_2] + N_{BKG}^{OS}[lep_1, lep_2] \quad (3.16)$$

In the following the way the final number of events from background is estimated by data-driven methods is described. First MC samples are considered to perform a closure test aimed to validate the method. Furthermore it allows for the estimation of the uncertainty due to the contamination of a potential SUSY signal. Then the application to real data is described.

The following approximations are made.

- Tab.3.7 shows that for QCD background the probability to select non-prompt hadronic  $\tau$ s is larger than the probability to select non-prompt  $e$ s or  $\mu$ s. For

the background processes with one tight and one *looseNOTtight* lepton with a single hadronic  $\tau$ , the  $\tau$  is considered as non-prompt.

$$N_{BKG}^{process}[e, \tau] \sim N_{BKG}^{process}[e, \tau_{non-prompt}] \quad (3.17)$$

$$N_{BKG}^{process}[\mu, \tau] \sim N_{BKG}^{process}[\mu, \tau_{non-prompt}] \quad (3.18)$$

- $N_{BKG}^{OS}[lep_1, lep_2]$  is important only for the  $ee$  channel, for the reasons given in Sec.3.7.4, hence it is considered only in the di-electron final state and it is neglected in the other final states.
- $N_{BKG}^{0prompt}[\tau, \tau]$  is dominated by the QCD background, therefore, in the MC closure test the only physics process considered is  $process = QCD$ .

In the following the number of events predicted by the data-driven methods is, named *Predicted*, while the number of events obtained by performing the whole selection, is indicated with *Observed*.

### 3.7.6 Closure Test with Monte Carlo

One validation of the method is performed by using MC samples. The first check performed uses only background samples and is aimed to verify the agreement between the number of *Predicted* events, with the number of *Observed* events.

Tab3.10 and Fig.3.34 3.35 (left) show the agreement aimed.

Only Bkg	Observed	Predicted
$ee$	$0.014 \pm 0.01$	$0.131 \pm 0.093$
$\mu\mu$	$0.029 \pm 0.014$	$0.042 \pm 0.013$
$\tau\tau$	$5.6 \pm 2.0$	$12 \pm 12$
$e\mu$	$0.051 \pm 0.019$	$0.038 \pm 0.007$
$e\tau$	$1.03 \pm 0.042$	$0.54 \pm 0.16$
$\mu\tau$	$1.55 \pm 0.84$	$0.71 \pm 0.16$

Table 3.10: Comparison between the observed and predicted number of events (with statistical uncertainties) for each final state by considering only the MC background samples.

Another feature is needed in order to be able to estimate the background contribution in New Physics searches: the background yield predicted by data-driven method, should not be affected by the potential presence of signal.

In this analysis the possible presence of New Physics could spoil the method and as a consequence the sensitivity of the analysis, in the case the estimation of the number of *looseNOTtight* events,  $N_{L!T}$ , receives a not negligible contribution from the signal.

In order to obtain such a feature, care has been taken in the choice of the *loose* definition, nevertheless, a check of the wanted behavior is needed.

To this aim, the procedure above described, is repeated considering, not only the SM background events, but also the signal sample LM0. This simulates the performances and the effectiveness of the analysis in presence of new physics.

Fig.3.34 3.35 (right) highlights a considerable difference between the expected and the observed number of events, this shows that the analysis is able to pick out the existence of new physics with two same sign leptons.

Bkg + LM0	Observed	Predicted
$ee$	$1.35 \pm 0.16$	$0.42 \pm 0.33$
$\mu\mu$	$0.284 \pm 0.23$	$0.093 \pm 0.018$
$\tau\tau$	$5.9 \pm 2.0$	$12 \pm 12$
$e\mu$	$4.07 \pm 0.28$	$0.63 \pm 0.54$
$e\tau$	$2.45 \pm 0.45$	$0.98 \pm 0.24$
$\mu\tau$	$3.41 \pm 0.86$	$1.37 \pm 0.30$

Table 3.11: Comparison between the observed and predicted number of events (with statistical uncertainties) for each final state with background and signal (LM0) samples.

The excess of the observed number of events respect with the expected yield in different dilepton channels, indicates that this analysis is able to perform checks within its own framework.

For instance, in the case of an excess of events over the SM contributions observed in  $ee$  ( $\mu\mu$ ) channel but not in  $\mu\mu$  ( $ee$ ) channel, the systematics uncertainty on the background evaluation can be rethought. On the other hand, the claim of New Physics would be safer, if the excess is visible in all the  $e$  and  $\mu$  channels. Therefore,

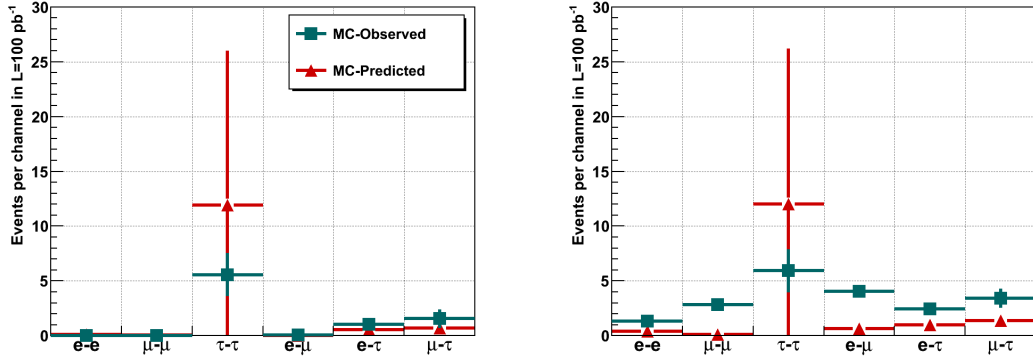


Figure 3.34: Comparison between the observed (green squares) and the predicted (red triangles) number of events by considering only background MC samples (left) and adding LM0 to the background samples (right).

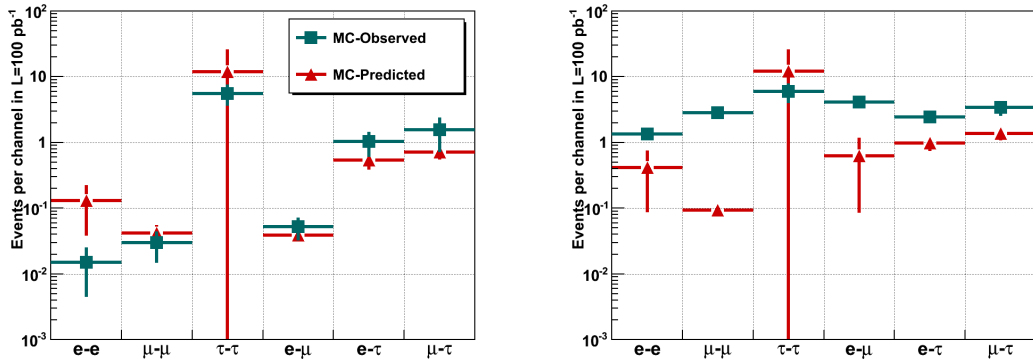


Figure 3.35: The same as Fig.3.34 but in logarithmic scale

with a proper treatment of the combination of the six final states the sensitivity of the analysis can be enhanced respect with a single final state analysis.

### 3.7.7 Possible sources of systematic uncertainties

One possible source of systematics is the choice of the loose identification.

In order to evaluate this potential systematic uncertainty, the requirements determining the tight selection have been slightly changed. No appreciable variations have been observed in the estimated number of events.

The method above described uses a sample dominated by some physics process, the QCD background, in order to estimate the  $\epsilon_{T/L}$  values and applies it to a sample selected by the SUSY analysis.

The two samples are orthogonal, therefore, one possible source of systematic uncertainty arises if the different kinematic region, and the consequent different environment, lead to different values of  $\epsilon_{T/L}$ .

In order to evaluate the entity of such systematics source, the  $\epsilon_{T/L}$  has been determined in several intervals of  $H_T$  and for each of them the expected number of events has been obtained.

Since  $H_T$  indicates the hadronic activity of the event, the stability of the result under variation of  $H_T$  guarantees the independence of the background estimation on the specific physics process.

Another quantity which can be taken as an indication of the physics environment, is the jet multiplicity.

This is important especially in the channels with  $\mu s$ , since the tag and probe method in  $b\bar{b}$  events could be affected by the angle between the two  $b$  partons, which is related to the total number of produced hard jets.

The number of predicted events is estimated by computing the  $\epsilon_{T/L}$  in the following conditions:

- **HT300:**  $H_T > 300$  GeV, all jet multiplicities;
- **HT50:**  $H_T > 50$  GeV, all jet multiplicities;
- **NJ2:**  $H_T > 300$  GeV and at most two hard jets for  $\mu\mu$  and  $e\mu$  channels;
- **NJ3:**  $H_T > 300$  GeV and at least three hard jets for  $\mu\mu$  and  $e\mu$  channels;

The resulting number of events is reported in the tables in the following section, along with the observed number of events.

The results for **HT300** are taken as the reference point, since the signal is expected to have high  $H_T$  values. The largest difference, between the reference point **HT300** and the other environment conditions for the  $\epsilon_{T/L}$  determination, has been considered as the systematics uncertainty on the number of events.

### 3.7.8 Background estimation in real data

The procedure described in the previous sections has been applied to the data sample collected. The results obtained for the number of observed and predicted events are reported in Tab.3.12 (left).

In order to evaluate the possible systematic uncertainty, the same procedure was repeated in different event conditions, as described above, to estimate the  $\epsilon_{T/L}$

factor. The results are reported in Tab.3.12 (right).

<i>data</i>	Obs.	Predicted	<i>NJ2</i>	<i>NJ3</i>	<i>HT50</i>
$ee$	0	$0.0001 \pm 0.0001$	$0.0001 \pm 0.0001$	$0.0001 \pm 0.0001$	$0.0001 \pm 0.0001$
$\mu\mu$	0	$0.023 \pm 0.021$	$0.029 \pm 0.028$	$0.020 \pm 0.019$	$0.039 \pm 0.026$
$\tau\tau$	0	$0.41 \pm 0.15$	$0.410 \pm 0.015$	$0.410 \pm 0.015$	$0.514 \pm 0.061$
$e\mu$	0	$0.0045 \pm 0.0036$	$0.0059 \pm 0.0054$	$0.0038 \pm 0.0033$	$0.015 \pm 0.011$
$e\tau$	0	$0.042 \pm 0.042$	$0.042 \pm 0.042$	$0.042 \pm 0.042$	$0.052 \pm 0.052$
$\mu\tau$	0	0	0	0	0

Table 3.12: Number of selected events for each final state with the statistical uncertainty. Left: comparison between the observed and predicted number of events. Right: predicted obtained with  $\epsilon_{T/L}$  determined in different event conditions for systematics study purpose.

No large departure from the reference point *HT300* results has been noticed. The resulting systematics uncertainty is symbolized in Fig. 3.36 3.37 with light blue rectangles

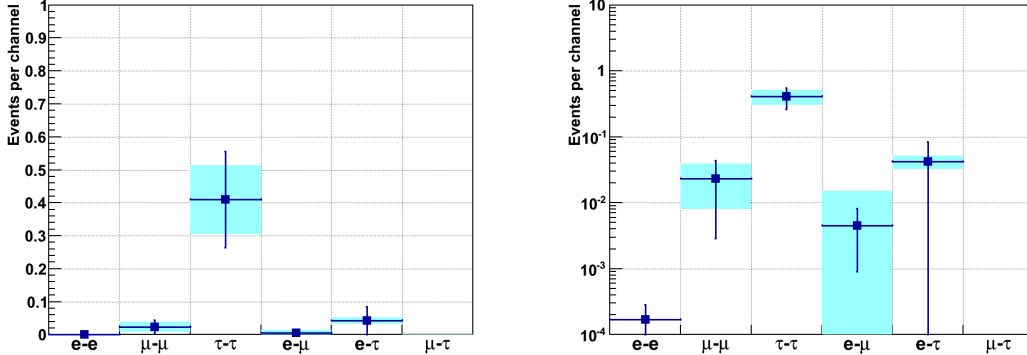


Figure 3.36: Comparison between the observed (black points) and predicted (blue squares) number of events in linear (left) and logarithmic (right) scale. The dashed rectangles represent the systematic uncertainty related to the estimation background method.

Tab.3.12 and Fig.3.36 show that no events were selected by the analysis cuts selection.

The predictions obtained with the adopted background evaluation method are compatible with the 0 observed events.

In order to have a first validation fo the methods with the data collected so far, the procedure was repeated by relaxing the analysis selection.

Non null number of events were obtained after requiring events with two same sign leptons identified as in the analysis, but changing the hadronic analysis selection with the following looser requirements:

- HLT: requires single jet with  $p_T > 50$  GeV;
- $H_T > 150$  GeV;
- No requirement on  $MH_T$  was applied.

<i>data</i>	Obs.	Predicted	<i>NJ2</i>	<i>NJ3</i>	<i>HT50</i>
$ee$	0	$0.001 \pm 0.0005$	$0.001 \pm 0.0005$	$0.001 \pm 0.0005$	$0.001 \pm 0.0005$
$\mu\mu$	0	$0.097 \pm 0.062$	$0.107 \pm 0.069$	$0.093 \pm 0.068$	$0.19 \pm 0.10$
$\tau\tau$	14	$17.3 \pm 5.3$	$17.3 \pm 5.3$	$17.3 \pm 5.3$	$20.73 \pm 0.72$
$e\mu$	1	$0.056 \pm 0.025$	$0.077 \pm 0.038$	$0.045 \pm 0.023$	$0.110 \pm 0.033$
$e\tau$	0	$0.30 \pm 0.12$	$0.30 \pm 0.12$	$0.30 \pm 0.12$	$0.33 \pm 0.13$
$\mu\tau$	2	$1.20 \pm 0.41$	$1.20 \pm 0.41$	$1.20 \pm 0.41$	$1.36 \pm 0.47$

Table 3.13: Number of events for each final state along with the statistical uncertainty, selected by the loose selection. Left: comparison between the observed and predicted number of events. Right: predicted obtained with  $\epsilon_{T/L}$  determined in different event conditions for systematics study purpose.

No large departure from the reference point  $HT300$  results has been noticed. The resulting systematics uncertainty is symbolized in Fig.3.37 with light blue rectangles

## 3.8 Sensitivity studies

A *statistical test* is a rule that states for which values of the observed number of events a given hypothesis should be rejected. In order to obtain such a test a critical value of  $n_{obs}$  has to be defined. Error of *first kind* are defined as the rejection of the hypothesis  $H_0$  when it is true. The probability for this eventuality is called  $\alpha$ , the *significance level* of the test. Error of *second type* are defined as the accepting  $H_0$  when it is false, the probability for this to happen is called  $\beta$  and the *power* of the test is defined as the quantity  $1 - \beta$ .

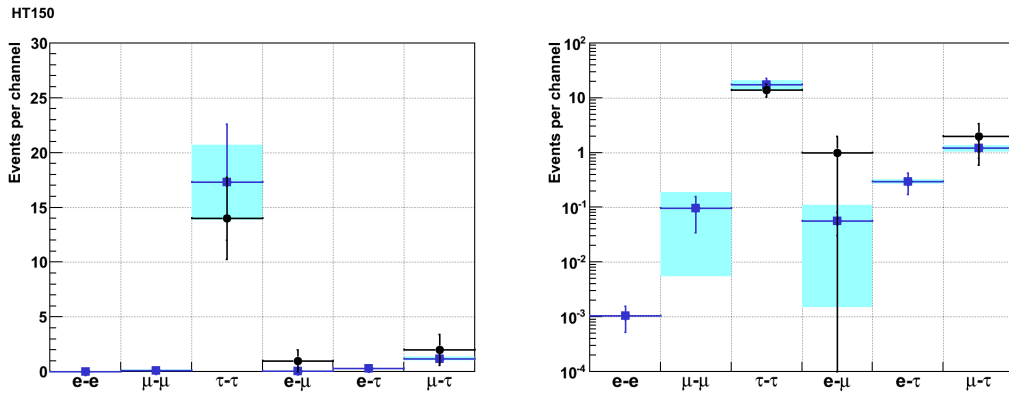


Figure 3.37: Comparison between the observed (black points) and predicted (blue squares) number of events in linear (left) and logarithmic (right) scale, after a looser selection than the analysis one. The dashed rectangles represent the systematic uncertainty related to the estimation background method.

In our case, as is usual in *Beyond Standard Model* searches, there exist only one hypothesis to be accepted or rejected, which is the presence of only Standard Model events, we call it  $H_0$ . The agreement between the data and the  $H_0$  can be quantified by defining a *test statistic*  $t$  which embodies the information from several variables.

The *p.d.f.* for such statistic in the  $H_0$  hypothesis is referred to as  $g(t|H_0)$  [68].

The term *over(under)coverage* is often used to indicate the ability of a method to claim a sensitivity worse (better) than the real one.

### 3.8.1 Sensitivity evaluation

Let us suppose we observe some data and call such statistics  $t_{obs}$ . The problem is to determine the significance of a discrepancy between the data and what is expected assuming the  $H_0$  hypothesis. This is usually obtained using the so called *p-value*, which is defined by:

$$p = \int_{t_{obs}}^{\infty} g(t|H_0) dt \quad (3.19)$$

It represents the probability to find  $t$  to be less compatible with  $H_0$  compared to the compatibility of the observed statistic  $t_{obs}$  with the same  $H_0$ .

Such *p-value* is a random variable, since it is function of data. In order to reject the  $H_0$  hypothesis, which in this and many contests leads to claim new physics,

the  $p$ -value should be low enough to respect the required level of significance. The significance related to a given  $p$ -value can be obtained by considering a Gaussian variable in certain sense corresponding to the data distribution. The equivalent significance is defined as the number of standard deviations that a Gaussian variable would fluctuate in one direction to give the observed  $p$ -value. Namely, by calling such a number  $Z$ , the upper tail area determined by requiring  $t > Z\sigma$  is equal to  $p$ . By calling  $\Phi$  the cumulative distribution of the Standard Gaussian and  $\Phi^{-1}$  its inverse,  $Z$  is defined as:

$$Z = \Phi^{-1}(1 - p) \quad \text{and} \quad \Phi(Z) = \frac{1 + \operatorname{erf}(Z/\sqrt{2})}{2}. \quad (3.20)$$

This analysis is a counting experiment with an estimated number of background events taken from subsidiary measurements described in Sec.3.7 and giving a number  $n_B$  obeying to the Poisson distribution. Such number is assumed to be the medium background estimation, referred to as  $\hat{\mu}_B$  and which is drawn from a Gaussian probability density function with a variance referred to as  $\hat{\sigma}_B$ .

The paper [69] investigates three different methods to obtain  $Z$  in some analysis differing for the way the  $\mu_B$  is estimated. For the case of this analysis the so called  $Z_{Bi}$  method is demonstrated to not undercover. The entity of the overcoverage depends on the yield of number of background events estimations and the uncertainty associated to it. Therefore the  $Z_{Bi}$  method was chosen in order to perform the sensitivity studies and it is briefly described in the following.

Ref. [69] states that a correspondence can be assumed between the statistical problem of this analysis and another kind of problem for which the  $Z_{Bi}$  method was originally developed, so that the terminology used is taken from such different analysis problem (known as the *on/off* problem in Gamma Ray Astronomy [70]).

$n_{on}$  is defined as the number of observed events in the signal region, and  $n_{off}$  the number of observed events in a region free from the signal, called *control region*.  $\tau$  is defined as  $\tau \equiv \mu_{off}/\mu_B$ , where  $\mu_{off}$  and  $\mu_B$  are the expected means of  $n_{off}$  and  $n_B$  in the  $H_0$  hypothesis.

The Ref. [71] and [69] report the demonstration that by considering  $n_{on}$  and  $n_{off}$  as Poisson distributed, the probability to obtain such two values is the probability to get  $n_{tot}$ , Poisson distributed, times the binomial probability to have it divided in  $n_{on}$  and  $n_{off}$  as in the observed values in data [72]. In this way all the dependence on ratio of Poisson means  $\tau$  is in the conditional binomial probability for the observed successes  $n_{on}$  given the observed total number of events  $n_{tot} = n_{on} + n_{off}$

[73].

Therefore the  $p$ -value is given by:

$$p_{Bi} = \sum_{j=n_{on}}^{n_{tot}} P(j|n_{tot}; \rho) \quad (3.21)$$

where  $\rho \equiv \mu_{on}/\mu_{off}$  and is  $\rho = 1/(1 - \tau)$  in the  $H_0$  hypothesis.

By using the Beta functions [74], the  $p_{Bi}$  can be written as the ratio of a truncate Beta function, also called incomplete Beta function  $Beta(\rho, n_{on}, 1 + n_{off})$ , to the complete one, with no dependence on  $\rho$ .

$$p_{Bi} = Beta(\rho, n_{on}, 1 + n_{off}) / Beta(n_{on}, 1 + n_{off}) \quad (3.22)$$

This ratio is often called the *incomplete Beta function*. The corresponding  $Z$  value is taken from Eq.3.20 and is referred to as  $Z_{Bi}$ .

For the sensitivity studies the input parameters are as in the following. The  $n_{on}$  term is taken as the number of events observed after the whole analysis selection (*signal region*);  $\hat{\mu}_B$  is taken as the number of events obtained in Sec.3.6;  $\tau$  is defined as the ratio of background means in the *signal region* and the one used to obtain the  $\mu_B$  value (*background region*), in our case it is taken to be equal to  $\frac{\hat{\mu}_B}{\sigma_B^2}$  given the correspondence demonstrated in [69];  $n_{off}$  is defined as the number of events observed in the *background region*,  $\tau \cdot \hat{\mu}_B$ , so in our case is taken to be equal to  $\frac{\hat{\mu}_B^2}{\sigma_B^2}$ .

This method was applied to the several points of the mSugra model available in the samples listed in Tab.3.2.

The input parameters related to the background estimation used are:  $\hat{\mu}_B = 10.16$  for  $100 \text{ pb}^{-1}$  and  $\sigma_B = k \cdot \sqrt{\hat{\mu}_B}$ . This form allows to parameterize the uncertainty on the number of background events as a function of the event yield, which is necessary to perform studies with changing the integrated luminosity.

The choice of the value for  $k$  is driven by the conservative approach to consider a relative uncertainty of about 50 % at  $L = 100 \text{ pb}^{-1}$ , so  $k = 1.5$ .

In case of very low  $p$ -values, the numerical methods used to calculate  $Z_{Bi}$  return  $Z_{Bi} = 0$ , while these cases would obtain a high significance. In order to get rid of these technical problems if  $p_{Bi} < 10^{-10}$  an approximate formula was used to get  $Z$ :

$$Z = \sqrt{u - \ln u} \quad \text{with} \quad u = -2\ln(p\sqrt{2\pi}) \quad (3.23)$$

This form is demonstrated to approximate the  $Z_{Bi}$  very accurately for relatively high significance [69].

In Fig.3.38 is shown the  $Z_{Bi}$  values for each  $(m_0, m_{1/2})$  point for  $\tan\beta = 3$  (top) and  $\tan\beta = 10$  (bottom), representing the sensitivity which can be reached after an integrated luminosity of  $100 \text{ pb}^{-1}$ .

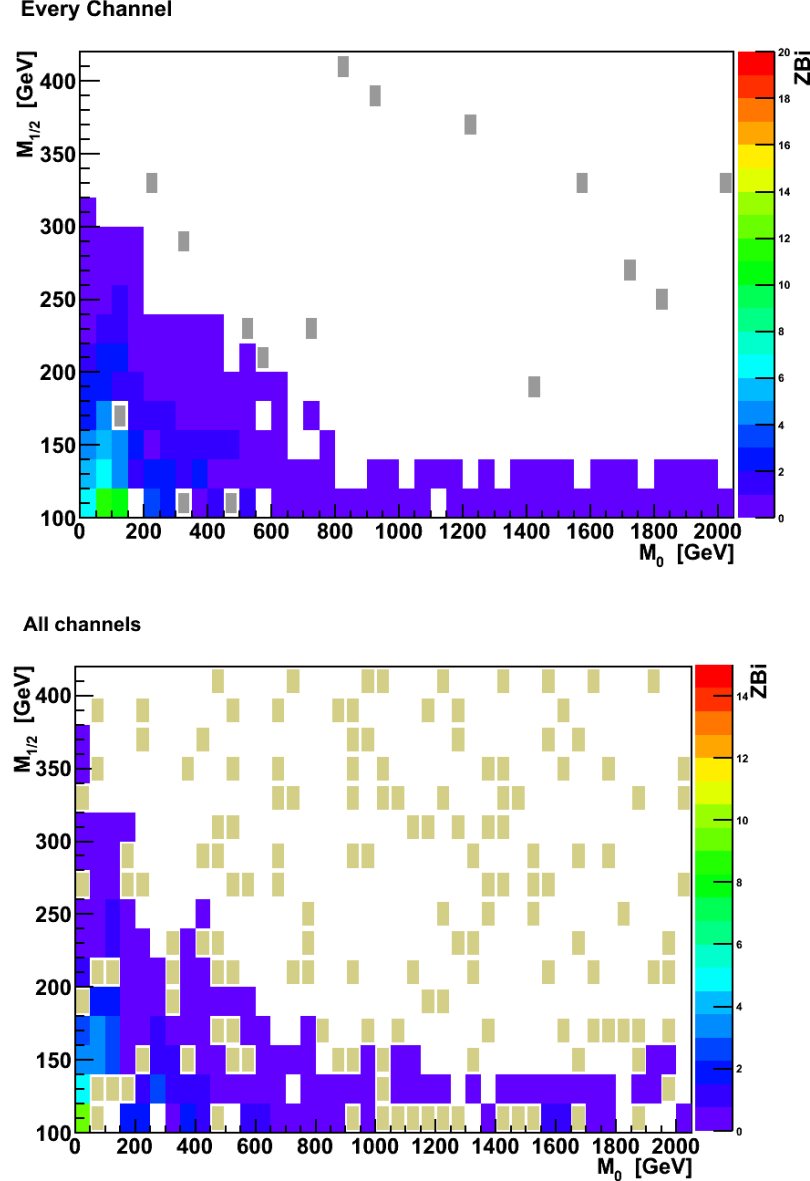


Figure 3.38:  $Z_{Bi}$  values which can be obtained in presence of mSugra signal with the parameters  $A_0 = 0$ ,  $sign\mu = +$  and  $\tan\beta=3$  (top) and  $\tan\beta=10$  (bottom), with  $L_{int} = 100 \text{ pb}^{-1}$ .

As is evident from Fig.3.38, a region of the  $(m_0, m_{1/2})$  plane can be covered by this analysis already with  $100 \text{ pb}^{-1}$ . From Tab.3.7 is clear that the channel  $\tau\tau$

is the one with the worst performances, therefore by excluding it, the significance could be enhanced. In order to verify it and quantify the improvement, the events which have two taus as the leptons with higher  $p_T$ , have been excluded and the corresponding  $Z_{Bi}$  is shown in Fig.3.39.

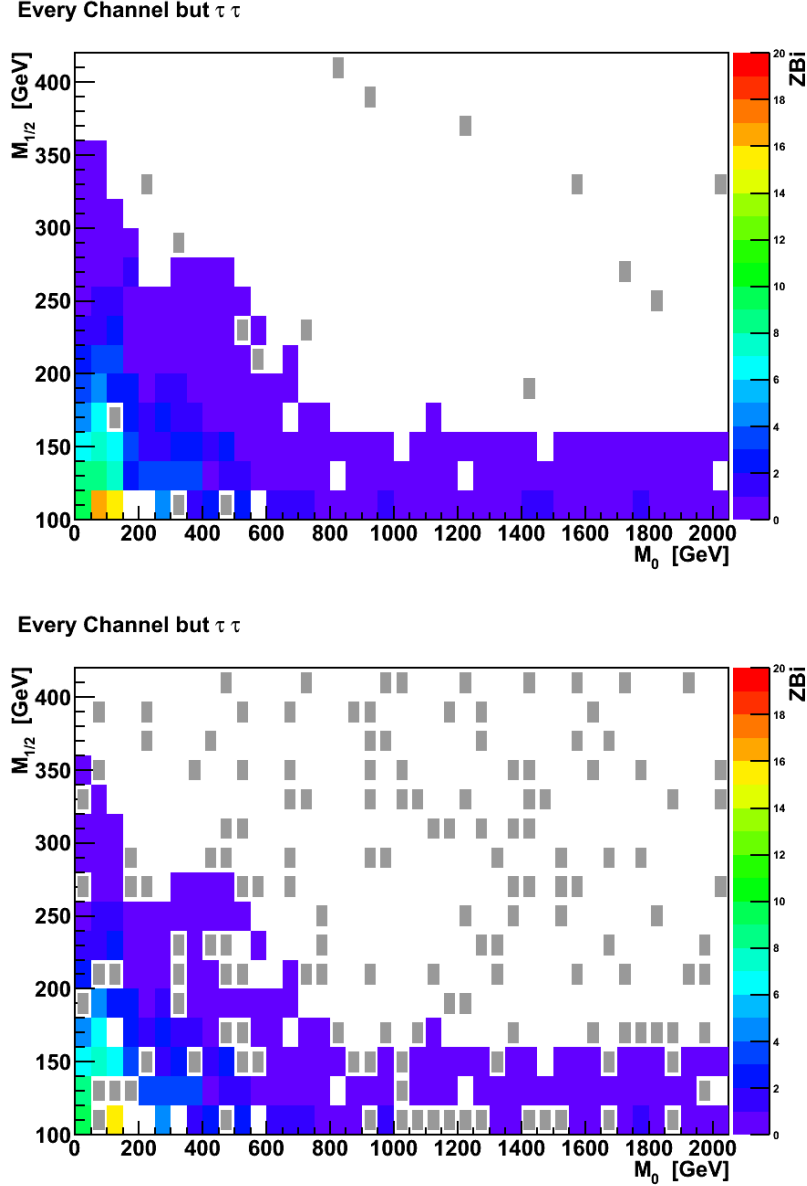


Figure 3.39:  $Z_{Bi}$  values which can be obtained in presence of mSugra signal with the parameters  $A_0 = 0$ ,  $sign\mu = +$  and  $\tan\beta=3$  (top) and  $\tan\beta=10$  (bottom), with  $L_{int} = 100\text{pb}^{-1}$  in all the channels but  $\tau\tau$ .

An investigation of which is the minimum integrated luminosity necessary to ob-

tain a  $Z_{Bi}$  greater than 5 was performed. Since the uncertainty on the background yield will lower for increasing integrated luminosity, a different parameterization for  $\sigma_B$  was chosen for  $L_{int} > 100 \text{ pb}^{-1}$ . The form  $\sigma_B = 1.5 \cdot \sqrt{\mu_B}$  allows for the  $\tau$  parameter to remain constant with the changing of  $L_{int}$ , as it is supposed to be in real *on/off* experiments.

In the next figures such integrated luminosity is shown for each point in the  $(m_0, m_{1/2})$  plane considered for  $\tan\beta = 3$  and  $\tan\beta = 10$ . The results for all the channels are shown in Fig.3.40 and the results obtained by excluding the  $\tau\tau$  channels are shown in Fig.3.41

### 3.8.2 Upper Limits

If after  $100 \text{ pb}^{-1}$  no evidence of SUSY signal is observed, an upper limit can be set for some models. An evaluation of the upper limits which will be possible to set with  $L_{int} = 100 \text{ pb}^{-1}$  for the mSugra points considered above has been performed with the procedure described in the following.

Confidence intervals for a parameter  $\theta$  can be found by defining a test of the hypothesized value  $\theta$ . Once a value  $\gamma$  is specified, confidence intervals for a parameter  $\theta$  values of the data that are disfavored by  $\theta$  (critical region) such that  $P(\text{data in critical region}) < \gamma$  confidence interval is the set of values of  $\theta$  which would not be rejected in a test of size (significance)  $\gamma$  and the confidence level associated to it is  $1 - \gamma$ . This means that the interval will cover the true value of  $\theta$  with probability  $> 1 - \gamma$ . If  $p_\theta < \gamma$  then  $\theta$  is rejected and the confidence interval at  $CL = 1 - \gamma$  consists of those values of  $\theta$  that are not rejected.

An upper limit on  $\theta$  is the greatest value for which  $p_\theta > \gamma$ .

$s$  is the expected number of signal events,  $b$  is the expected number of background events. The number of observed events is  $n$ , and it is distributed like a Poisson variable with median value  $s + b$ .

The study of upper limits for mSugra models with the same parameters used for the sensitivity evaluation have been performed by following the method described in [75] which uses a Bayesian approach. The number of observed events  $n$  is distributed as a Poisson with a median value  $s\epsilon + b$ ; where  $s$  is the signal yield,  $b$  the background yield and  $\epsilon$  a factor which embodies efficiencies, acceptance. The background yield and the acceptance are measured by subsidiary measurements. By using the Bayes' theorem the probability distribution function (*p.d.f.*) for

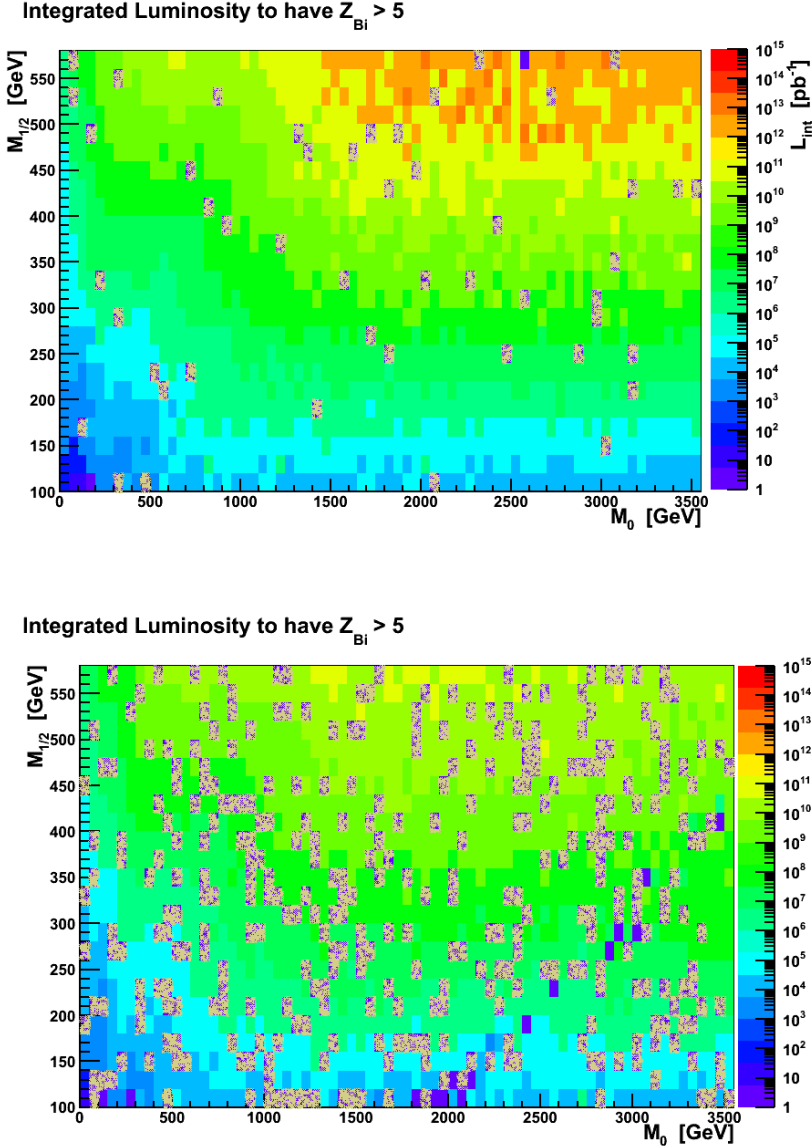


Figure 3.40: Minimal integrated luminosity needed to obtain a  $Z_{Bi} > 5$  for  $\tan\beta = 3$  (top) and  $\tan\beta = 10$  (bottom) considering all the six final states.

$s, b, \epsilon$ , given the observed value  $n$ , is derived from:

$$p(s, b, \epsilon | n) = \frac{\mathcal{L}(n|s, b, \epsilon) \pi(s) \pi(b) \pi(\epsilon)}{\int \int \int \mathcal{L}(n|s, b, \epsilon) \pi(s) \pi(b) \pi(\epsilon) ds db d\epsilon} \quad (3.24)$$

where  $\mathcal{L}$  is the *p.d.f.* to observe  $n$  events given a median value with specific  $s, b$  and  $\epsilon$  and  $\pi(s)$   $\pi(b)$  and  $\pi(\epsilon)$  are the priors for them. The prior for  $s$  is chosen to

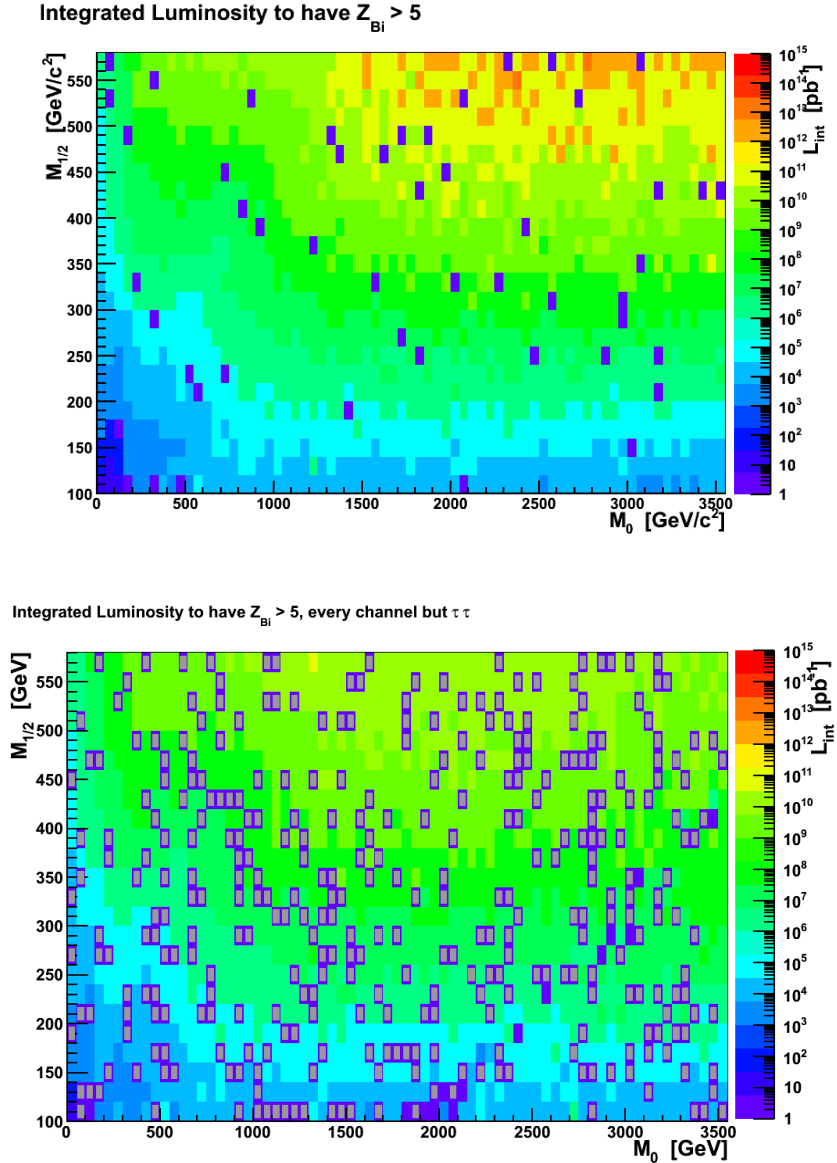


Figure 3.41: Minimal integrated luminosity needed to obtain a  $Z_{Bi} > 5$  for  $\tan\beta = 3$  (top) and  $\tan\beta = 10$  (bottom) excluding the  $\tau\tau$  final state.

be a non zero constant till some value and then zero, while for  $b$  and  $\epsilon$  it is taken to be a Gaussian:

$$\mathcal{L}(n|s, b, \epsilon) = \frac{1}{\sqrt{2\pi\sigma_b^2}} \frac{1}{\sqrt{2\pi\sigma_\epsilon^2}} \int_0^\infty \int_0^\infty \frac{\mu'^n e^{-\mu'}}{n!} e^{-\frac{(b'-b)^2}{2\sigma_b^2}} e^{-\frac{(\epsilon'-\epsilon)^2}{2\sigma_\epsilon^2}} db' d\epsilon' \quad (3.25)$$

where  $\mu$  is a function of the nuisance parameters  $b$  and  $\epsilon$ . The posterior *p.d.f* for

$s$  is obtained after the nuisances parameters have been integrated out.

$$p(s|n) = \int_0^\infty \int_0^\infty p(s, b, \epsilon|n) db' d\epsilon \quad (3.26)$$

and the upper limit  $s_{up}$  to the signal yield is derived from:

$$\int_0^{s_{up}} p(s|n) ds = 1 - \gamma \quad (3.27)$$

The code [76], uses the Bayesian method described in general terms in [75], and with nuisance parameters handled as in [77] in the non correlated case. Such code was used to obtain the results shown in the following. The input values used are  $b = n_{bkg} = 9.62$ ,  $\sigma_b = 0.5 \cdot b$  and a relative uncertainty on the acceptance  $\sigma_\epsilon/\epsilon = 0.15$ . A set of 100000 pseudo-experiments was performed using the values  $\sigma_b$  and  $\sigma_\epsilon/\epsilon$  to obtain the standard deviations of the Gaussian p.d.f. used as priors for the number of expected background events and the acceptance. The required confidence level is 95 % and the number of observed events has been set as the expected background events. The resulting expected upper limit to the selected number of events with  $L = 100\text{pb}^{-1}$  is 12.12. Such result is used to estimate which models in the mSUGRA plane can be excluded. The text in Fig.3.42 indicates the total number of events, both signal and background obtained after the selection.

The same procedure was repeated by excluding the  $\tau\tau$  final state. The input parameters are the same except for the expected number of background events, its uncertainty and the observed number of events were changed accordingly. The resulting upper limit is 9.102, and the mSugra points which can be excluded are shown in Fig.3.43.

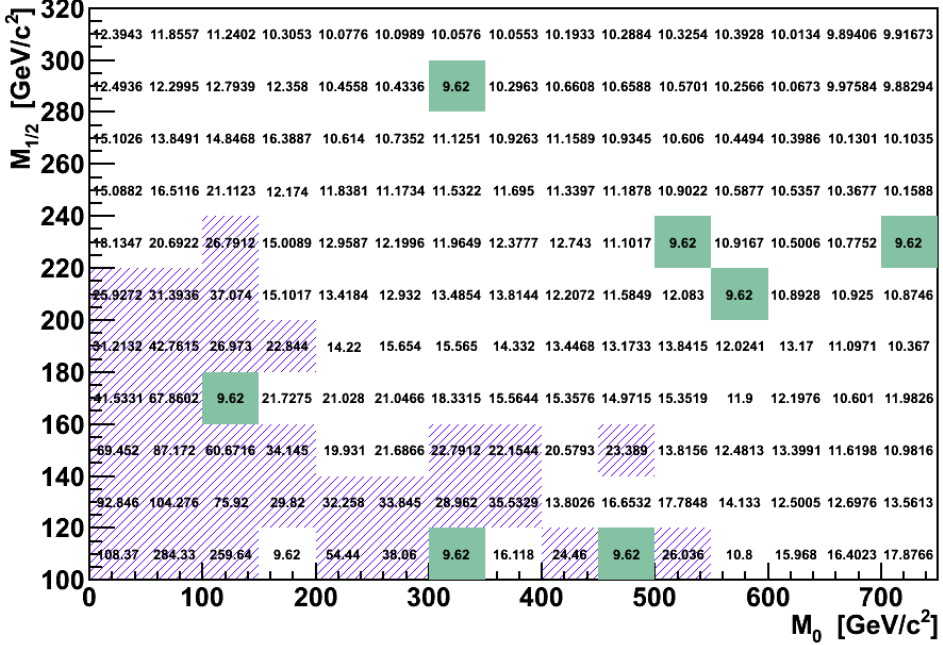


Figure 3.42: The numbers are the total number of events, the stripped region represents the points which can be excluded after  $100 \text{ pb}^{-1}$ . The green boxes indicate the mSugra points not available because of technical issues.

An evaluation of the exclusion reach was performed also for  $L = 1\text{fb}^{-1}$  and  $L = 30 \text{ pb}^{-1}$ , the corresponding exclusion plot, excluding the  $\tau\tau$  channel, is in Fig.3.44.

Fig.3.45 shows the regions excluded by DØ [78], CDF [79] and LEP [80] in the same plane investigated in this work. By comparing Fig.3.45 to Fig.3.44, is evident that, with only  $L = 30\text{pb}^{-1}$ , the integrated luminosity already delivered by LHC, is possible to overcome the current limits set by the Tevatron experiments with this analysis.

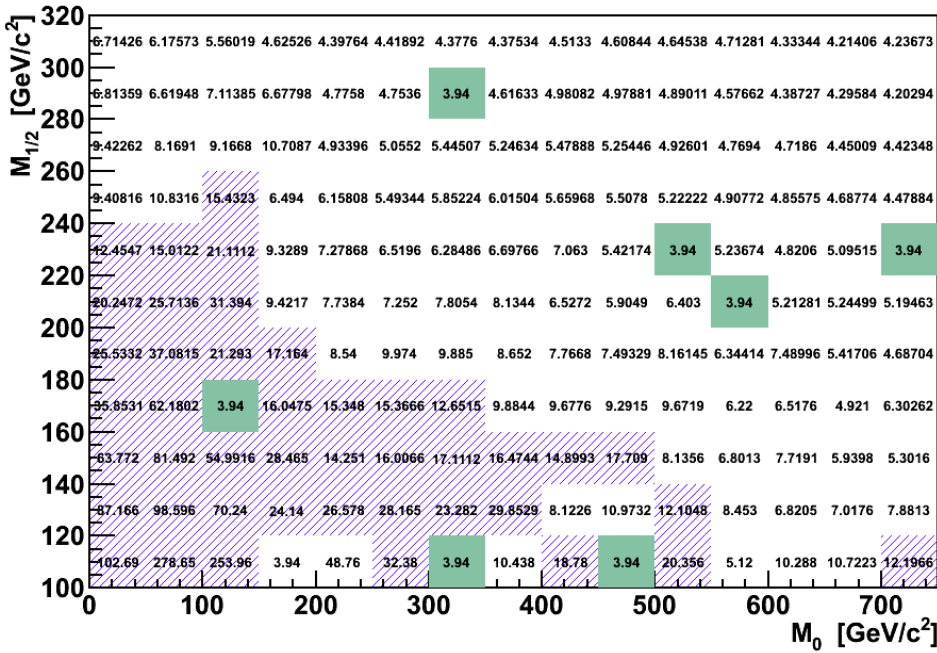
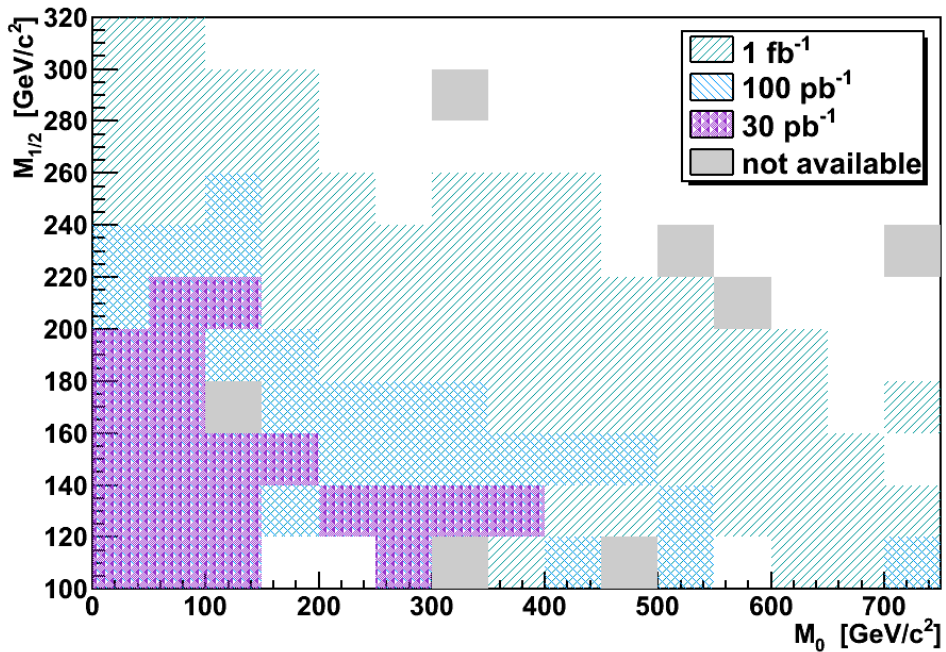
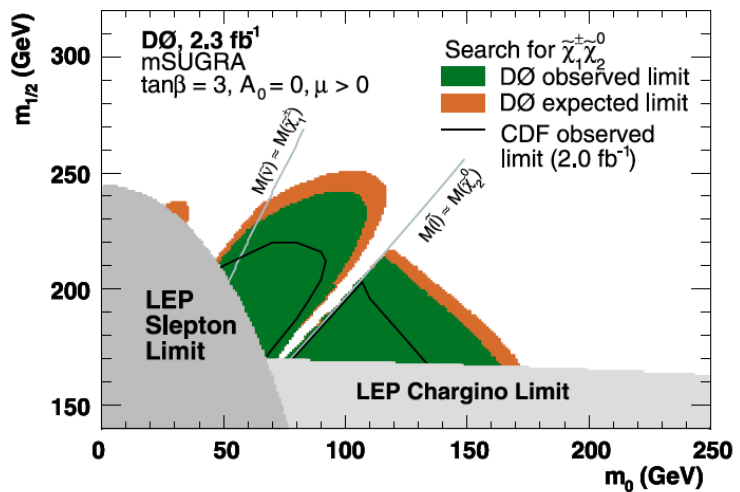


Figure 3.43: The numbers are the total number of events excluding the  $\tau\tau$  channel, the striped region represents the points which can be excluded after  $100 \text{ pb}^{-1}$ . The green boxes indicate the mSugra points not available because of technical issues.

Figure 3.44: Exclusion plot for all the channels but  $\tau\tau$ .Figure 3.45: Regions in the mSugra plane with  $\tan\beta=3$ ,  $\mu > 0$  and  $A_0 = 0$  excluded by the other experiments [78].



# Chapter 4

## Same Sign W pair production

*Coincidences, in general, are great stumbling blocks in the way of that class of thinkers who have been educated to know nothing of the theory of probabilities- that theory to which the most glorious objects of human research are indebted for the most glorious of illustration.*

Edgar Allan Poe – The Murders in the Rue Morgue

---

The production of same sign  $W$  bosons with both  $W$ s decaying in leptons, leads to final state of the SSDL SUSY analysis signal. This kind of processes can occur through two different mechanisms.

- **Single Parton Scattering (SPS).** In the framework of the Standard Model, one interaction between partons, namely Single Parton Scattering (SPS in the following) can lead to Same Sign  $W$  only at higher orders respect to the opposite sign  $W$  production.
- **Double Parton Scattering (DPS).** The other mechanism leading to same sign  $W$  is the occurring of two different parton interactions within the same

proton-proton collision. This is what is called *Double Parton Scattering* (*DPS* in the following ).

While the cross section of Same Sign W (SSW) production in the SPS is calculable using perturbative techniques in the range of the SM, the yield of the DPS production is a controversial issue.

The next Sections give a quick summary of the features of these two sources of Same Sign Ws pair.

## 4.1 Same Sign Ws production from Single Parton Scattering

The inclusive Same Sign W pairs production is a mixed strong-electroweak process with leading contributions of  $\mathcal{O}(\alpha_S^2 \alpha_W^2)$  and  $\mathcal{O}(\alpha_W^4)$ , while the  $W^+W^-$  occurs at  $\mathcal{O}(\alpha_W^2)$  [81], therefore it is about two orders of magnitude lower than the usual diboson production.

One characteristic feature of SSW coming from SPS is that the two Ws are always produced with two partons, so that the final state, is characterized by, besides the two same sign leptons, also by two hard jets.

## 4.2 Same Sign Ws production from Double Parton Scattering

The existence of Multiple Parton Interaction (MPI), is not only a natural assumption, but it has been also experimentally verified by several collaborations since time ago. The first observation of two hard scattering in the same hadron-hadron collision, was performed by AFS [82] in  $p$ - $p$  collisions at  $\sqrt{s} = 63$  GeV, then also UA2 [83], with  $p$ - $\bar{p}$  collisions at  $\sqrt{s} = 630$  GeV, and CDF [84], with  $p$ - $\bar{p}$  collisions at  $\sqrt{s} = 1.8$  TeV, get the evidence of DPS in the four jets final states.

The *DPS* received great interest in the last years for two main reasons.

- It can lead to final states which would be suppressed in the standard model considering only one particle interaction and thus considered golden channels in the Beyond SM searches; the analysis presented in this thesis is one exam-

ple of several others final states and new physics scenarios which potentially can suffer from DPS background.

- The other reason is that the mean number of parton interactions in one collision between two hadrons is strictly linked to the intrinsic structure of the hadron itself. A clear measurement of the cross section of double parton scattering thus would provide important information regarding the non perturbative nature of the strong interactions which confine the partons within one hadron.

### 4.2.1 Features determining the DPS cross section

Under the assumption of uncorrelated single interactions, when the minimum  $p_T$  considered is large enough the average number of interactions is small, thus one second hard interaction can be considered as a Poisson process. If  $\mathcal{P}_{12}$  is the probability to have two hard interactions labeled as 1 and 2 respectively, it can be written as  $\mathcal{P}_{12} = \frac{1}{m} \mathcal{P}_1 \mathcal{P}_2$ , with  $m = 2$  if the two processes are indistinguishable, otherwise  $m = 1$ . This leads to write the cross section for two hard scatterings in the form:

$$\sigma_D = \frac{1}{m} \frac{\sigma_1 \sigma_2}{\sigma_{eff}} \quad (4.1)$$

where the parameter  $\sigma_{eff}$  embodies all the deviations from the hypothesis with no correlations.

The possible sources of correlations, investigated in [85], are mentioned in the following:

#### **Impact Parameter:**

Each collision can have a different impact parameter  $b$  and this affects the probability to have more than one parton interaction.

From a physical and intuitive point of view, smaller  $b$  corresponds to a larger overlap between the two colliding hadrons, thus larger probability to have multiple interactions.

#### **$p_T$ ordering:**

The several interactions can be viewed as ordered in decrescent  $p_T$ , so that for one interaction, the correlation with the others can be mathematically expressed

by integrating out all the interactions with lower  $p_T$  lower. This corresponds to consider that the interactions with larger  $p_T$  can influence the ones with lower  $p_T$  and not vice-versa. In the case of two interactions with very different  $p_T$  (one hard and one soft) this is motivated also from a physical point of view, indeed it can be shown that it is equivalent to a time ordering [86].

All the calculations are based on this assumption and construct the Parton Density Function (PDF) of the  $i$ -th interaction by imposing the conservation of momentum and flavor taking into account the previous (in  $p_T$  order) interactions.

### **MPI Parton Density Functions:**

As for the calculation of the single parton scattering the PDF are needed, for the DPS, the multi-parton densities have to be defined. They give the joint probability to have  $n$  partons with momentum fractions  $x_i$ , and flavors  $f_i$  when probed by interactions at scales  $Q_i^2$ . Some sum rules should be satisfied in the computation of MPI PDF, they are based on the following topics.

- Total momentum conservation of the system represented by the hadron.
- Valence quarks: if a valence quark has been kicked-out in one interaction, the PDF for valence quark of its same flavor should change accordingly.
- Sea quarks and their companion: since in perturbative regime a quark and antiquarks origin from a gluon splitting, if one interaction kicks out a sea quark, because of the flavor conservation, its antiquark is left in the beam remnants.
- sea quarks and gluon density normalizations: unlike the valence quarks, the sea quarks and gluons have not a fixed multiplicities. This freedom can be used to fullfil the total momentum sum rule.

### **Primordial $k_T$ :**

Because of the Fermi motion inside the incoming hadrons, the partons should have also a non null  $k_T$ , the *primordial*  $k_T$ . By summing over all the partons inside the hadrons, the total  $k_T$  should be zero.

### **Color correlations:**

The time evolution of the system described by the formalism mentioned so far leads to a larger and larger distances among the partons. When the Fermi scale is approached, the description of the system in terms of perturbative QCD is not

valid and the partons should be considered to hadronize in color singlets.

The way the partons join in groups to be confined in hadrons depends both on their evolved momenta and on their color charge.

Therefore a complete and satisfactory description of the evolution of the DPS PDF, can not disregard the color correlations among the partons. So far the calculations of DPS have been performed by neglecting the color charge correlations and this should be kept in mind in interpreting the obtained results.

### 4.2.2 Existing calculations of the DPS cross section

Before observing the DPS, the first performed calculations of the cross section used the assumption that the multiple interactions in the same hadron collisions were uncorrelated except for the momentum conserving.

#### Generalities on MPI

In the works [87] the average number of partons with momentum fraction  $x$  and transverse coordinate  $\mathbf{b}$  was factorized in the effective parton distribution and the partonic matter distribution in the transverse space:

$$D(x; \mathbf{b}) = g_{eff}(x)f(\mathbf{b}). \quad (4.2)$$

The probability of a configuration with a certain number of partons and each one with longitudinal momentum fraction and impact parameter  $(x_i, \mathbf{b}_i)$  is:

$$\Gamma(x_1, \mathbf{b}_1, \dots, x_n, \mathbf{b}_n) = \frac{D(x_1, \mathbf{b}_1) \dots D(x_n, \mathbf{b}_n)}{n!} \exp\left(-\int D(x, \mathbf{b}) dx d^2 b\right) \quad (4.3)$$

Since such quantity is infra-red divergent, a lower cut-off is needed and the cross section obtained refers to the events with at least a hard (as defined by the cut off) partonic interaction, namely the hard cross section, referred to as  $\sigma_H$ . Therefore, by using the factorization 4.2 and indicating with  $\beta$  the impact parameter of the hadron collision:

$$\sigma_H = \int d^2 \beta \left[ 1 - e^{-\sigma_S F(\beta)} \right] = \sum_{n=1}^{\infty} \int d^2 \beta \frac{(\sigma_S F(\beta))^n}{n!} e^{-\sigma_S F(\beta)} \quad (4.4)$$

By introducing the average number of parton interactions  $\langle n \rangle$ , the cross section of one single interaction  $\sigma_S$  and for double interaction  $\sigma_D$  are:

$$\sigma_s = \langle n \rangle \sigma_H = \int d^2 \beta \sigma_S F(\beta) \quad \text{and} \quad \sigma_D = \frac{\langle n(n-1) \rangle}{2} \sigma_H = \frac{1}{2} \int d^2 \beta \sigma_S^2 F^2(\beta) \quad (4.5)$$

## Double Parton Scattering

By using the parameter  $\sigma_{eff}$  introduced Eq.4.1 ,  $\sigma_D$  can be expressed as:

$$\sigma_D = \frac{1}{2} \frac{\sigma_S^2}{\sigma_{eff}} \quad \text{so that} \quad \sigma_{eff} = \frac{1}{\int d^2\beta F^2(\beta)}. \quad (4.6)$$

Here  $\sigma_{eff}$  can be considered as the overlap of the partonic matter distribution of the two interacting hadrons so that the physical meaning of the Eq.4.6 is that, the probability of the second scattering depends on the flux of the other partons, which is inversely proportional to the proton transverse area. In this case, the simplest one, it is independent of the center of mass energy of the hadron collisions  $\sqrt{s}$  and the Infra-Red (IR) cut-off.

The measurement performed by CDF [88] by analyzing selected sample of  $\gamma+3$  jets made evident that the assumptions of the uncorrelated case cannot hold.

The Eqs.4.3, 4.4,4.1 lead to the following expression for the double interactions:

$$\begin{aligned} \sigma_{AB}^D = & \sum_{i,j,k,l} \int \Gamma_{ij}(x_1, x_2, b; t_1, t_2) \Gamma_{kl}(x'_1, x'_2, b; t_1, t_2) \\ & \hat{\sigma}_{ik}^A(x_1, x'_1) \hat{\sigma}_{jl}^B(x_2, x'_2) dx_1 dx_2 dx'_1 dx'_2 d^2b \end{aligned} \quad (4.7)$$

The  $\hat{\sigma}_S$  are the parton-level subprocess cross sections and  $\Gamma(x_1, x_2, b; t_1, t_2)$  are the generalized double distributions. In order to get the expression in Eq.4.6, several approximations have been imposed. Two of the main ones are the factorizations  $\Gamma(x_1, x_2, b; t_1, t_2) = D_h^{ij}(x_1, x_2; t_1, t_2) F_j^i(b)$  and  $D_h^{ij}(x_1, x_2; t_1, t_2) = D_h^i(x_1, t_1) D_h^j(x_2, t_2)$ , and  $F_j^i(b)$  is considered the same for every  $ij$  pair of partons inside the hadron.

The several kinds of correlations among the parton constituents of the colliding hadrons which relate the two subprocesses were summarized above. In general, they result in an enhancement of the DPS yield compared to the hypothesis of uncorrelated parton interactions.

In the following the existing models which describe the correlations among the parton interaction are mentioned.

### Inclusion of the correlations between valence and sea partons in transverse plane

In the article [87] the correlation between transverse size of the sea partons distributions to the configuration in transverse space of valence quarks is considered. The information about the distribution of the charged matter inside the hadron

is dominated by the valence quarks and is well modelled. On the contrary the distribution of the gluons is not known and in order to enhance the  $\sigma_D$  to the experimental value, it should be considered strongly related to the valence quark distribution.

In the calculations to obtain a value for the  $\sigma_D$  and thus  $\sigma_{eff}$  two groups of partons are considered, the valence and the sea and the correlation between the two groups is introduced in Eq.4.3. Some parameters have been fixed: the IR cut-off, the radius of the gluon and quark sea distributions. The chosen values allows for the result to be in agreement with the measurement by CDF [88]. Unlike the uncorrelated case, where there is no dependence of  $\sigma_{eff}$  from the  $\sqrt{s}$  and the IR cut-off, in this case a decrease with energy scale is found. Under the assumptions made in [87] the  $\sigma_{eff}$  depends only slightly from the hadron collision energy and the most of the  $\sigma_D$  enhancement is due to the dependence of  $\sigma_S$  from the collision energy. This would lead to think that once having a measurement of the  $\sigma_D$  at Tevatron we could estimate it at LHC energies using the same  $\sigma_{eff}$  value. Nevertheless, [87] considers only one of the possible kinds of correlations, another source of correlations is mentioned in the next section.

### **Inclusion of Correlations in longitudinal momentum**

Since the longitudinal parton momentum probed at the LHC energies is very small, the first approaches neglected at all the longitudinal momentum correlations.

Indeed the factorization

$$D_h^{ij}(x_1, x_2; t_1, t_2) = D_h^i(x_1, t_1) D_h^j(x_2, t_2) \quad (4.8)$$

is motivated by the large scale energies of the current hadron colliders.

Nevertheless, [89] has shown that the factorization in 4.8 leads to a scale violation. In such work, the equations describing the parton distribution function evolution with the scale were derived. They are called double Dokshitzer Gribov Lipatov Altarelli Parisi (dDGLAP) equations, since they are the analogue for the double interaction, of the Dokshitzer Gribov Lipatov Altarelli Parisi (DGLAP) equations [90] [91] [92]. If this factorization holds at a given scale, the evolution provided by the dDGLAP leads to violate it at any different scale [89] [93].

The amount of this violation is not known and it is difficult to estimate. In particular, there should exist some values for  $x_1$  and  $x_2$  such that, with the growth

of the energy scale, the correlation terms become dominant. In order to get such  $x_1$  and  $x_2$  values, numerical methods are needed.

Results in this context have been obtained in the article [94]. It describes a set of leading order DPS dDPFs satisfying the momentum and number sum rules at a given scale  $Q_0$ . The evolution of such dDPFs at different scales was performed by numerically integrating LO dDGLAP equations. The longitudinal momentum correlations, lead to a  $\sigma_{eff}$  depending more strongly on the  $\sqrt{s}$ . In order to test such models, the DPS cross section measurement at LHC is needed. In the meanwhile D0 had performed a measurement of  $\sigma_{eff}$  as a function of the second jet  $p_T$  and, although the statistical uncertainties are large and it is not a direct measurement as a function of  $\sqrt{s}$ , a trend decrescent with the energy scale is visible, as it has been interpreted in [95].

Even only from the above brief summary of the state of art of the theoretical studies on DPS, it is clear that our knowledge is far from a full understanding of the issue of how to take into account the several source of correlations. Experimental values of  $\sigma_{eff}$  at a different energy scale is needed in order to have a clearer indications of the correlations sources, which in turn would give information about the structure of the hadrons when they are very energetic.

The same sign Ws bosons production has been considered by several authors as the benchmark process for the DPS to be observed at LHC [96] [97].

In particular in [96] the authors used the dDPS evolution described in [95], in order to perform a study on same sign Ws.

The reason is that, in the early stages of LHC, when the SM behavior of the jets production and detection is not completely under control yet, measuring the DPS cross section from multi jets events would be difficult because of the troubles in discriminating the jets in DPS from the several processes with many jets in the final state, given the very high density environment of LHC.

On the contrary, the WW final state with two same sign leptons, although very rare, is clean, this is why the same sign W production is considered the “golden channel” for the measurement of DPS cross section.

Furthermore, given the large theoretical uncertainties on the yield of DPS at LHC energies, the SSDL SUSY analysis can not disregard the study of the same sign leptons coming from DPS.

### 4.3 Strategy to estimate the SSW contribution from the SM

Fig.4.1, taken from [96], shows the cross sections of processes producing W bosons as a function of the center of mass energy of  $p\text{-}p$  (and  $p\bar{p}$  in the energy range of Tevatron) collision.

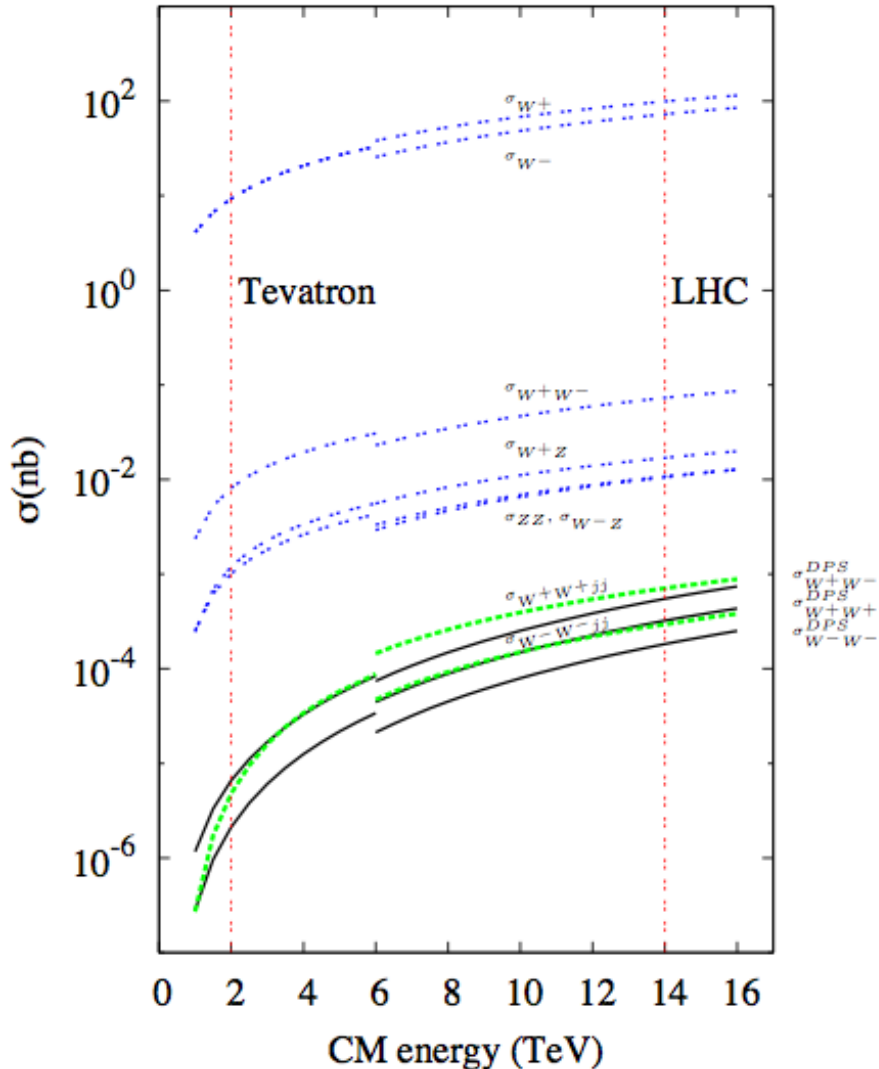


Figure 4.1: Cross section of several processes involving  $W$  boson(s) production as a function of the centre of mass energy at Tevatron and LHC. The solid (dotted) curves indicate the DPS (SPS) [96].

It is clear that the SSW production from SM SPS has a cross section too small to be observed with  $100 \text{ pb}^{-1}$ . Although the DPS WW cross section in Fig.4.1

is comparable with the SPS one, it is worth to emphasize that it is calculated by assuming for  $\sigma_{eff}$  the value measured at the Tevatron energies and thus, given the arguments in the previous section, it is not sure that the trend shown for the  $\sigma_{DPS}^{WW}$  is the right one.

Because of the charge conservation, the SSW production from SPS always occurs with two partons in the final state, resulting in the characteristic signature containing two hard jets besides the two same sign leptons. The SSW from DPS is a combination of two single parton interactions each one producing  $W+jets$  processes and is known that the cross section decreases with the jet multiplicity. Therefore a useful and effective way to discriminate the SPS from the DPS is to require the absence of hard jets in order to measure the SSW DPS cross section, as several works [96] [98] [97] suggest.

Such selection will allows for the measurement of DPS WW cross section where the two Ws are produced without additional jets, therefore it does not provide directly an estimation of the DPS SSW contribution to the SSDL SUSY analysis, since the cut on  $H_T$  would reject the Ws produced at rest without radiation. Nevertheless, the knowledge of the behavior of the jet multiplicity in SPS W production is helpful to get information about the behavior of the jet multiplicity in SSW DPS.

The subjects mentioned above led to plan the strategy to estimate the SSW contribution, which is here summarized.

1. Measurement of the cross section of DPS WW production where the W are produced without additional jets. This allows for the rejection of the SPS SSW and possible SUSY contributions.
2. Extrapolation of the DPS SSW yield at high  $H_T$  region by using information from  $W+jets$  events in order to get the shape of the DPS spectrum in  $H_T$ , and by taking normalization from the cross section estimated at point 1.
3. Once the SM contribution to the production of two same sign isolated leptons is under control, an evidence of the SSDL signal would imply the claim of the existence of new physics.

The next sections describe the feasibility study of the SSW production from DPS and some studies for the methods validation based on the use of real data.

## 4.4 MC Samples Used

The background samples are listed and described in Chapter 3. In the following the description of the MC samples for the Same Sign W processes is described.

### 4.4.1 Same sign W from Single Parton Scattering

The same sign  $W$  from Single Parton Scattering process have been generated with PYTHIA8.1 [99] interfaced with MadGraph [42] through the Les Houches Accord (LHA) [100] interface, including all the diagrams with the EW contributions up to order  $\alpha_{EW}^4$  and QCD contribution up to  $\alpha_s^2$ . There are 128 diagrams at  $\mathcal{O}(\alpha_{EW}^2 \alpha_s^2)$  and 668 diagrams at  $\mathcal{O}(\alpha_{EW}^4)$ . The larger number of diagrams involving only the EW coupling compared to that with QCD contribution, is balanced by the larger values of the strong coupling. The result is that the two sources contribute at the same extent to the SSW production.

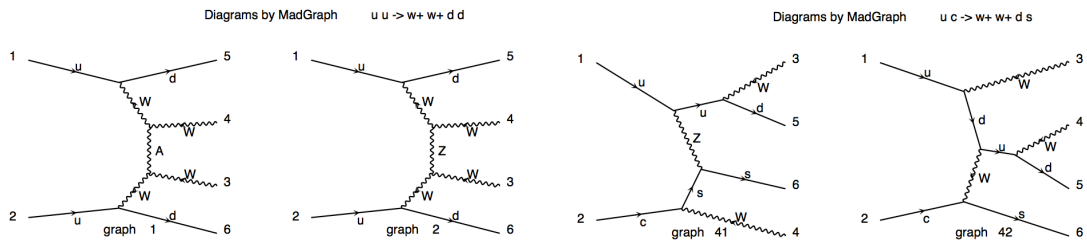


Figure 4.2: Examples of diagrams contributing to the SPS SS W production at  $\alpha_{EW}^4$  order and no  $\alpha_s$  vertices. Both neutral bosons ( $A \equiv$  photon and  $Z^0$ ) and charged boson ( $W$ ) exchange are illustrated.

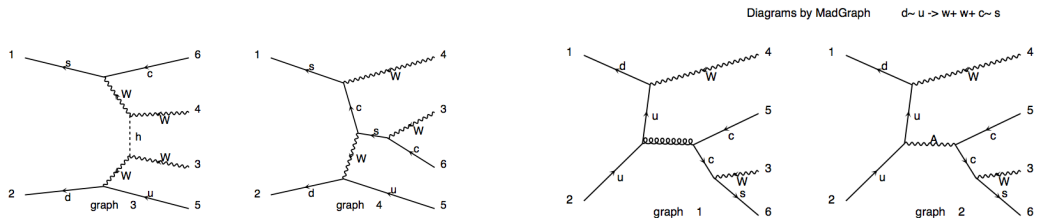


Figure 4.3: Examples of diagrams contributing to the SPS SS W production. For  $\alpha_{EW}^4$  order and zero  $\alpha_s$  order and at  $\alpha_{EW}^2 \alpha_s^2$  order.

These processes have the following features. The  $W^+W^+$  production cross section is expected to be larger than the  $W^-W^-$  one at LHC, due to the excess of  $u$  parton over  $d$  in the proton.

The most important feature for the aim the study here reported, is that, due to of the charge conservation, the two  $W$ s are always produced with associated two hard jets.

#### 4.4.2 DPS in Pythia8

The signal was generated by PYTHIA8.107<sup>1</sup> [101]. The PDF used are the so called CTEQ6L1 [102], which have all the parameters at Leading Order (LO). They are the same PDF sets used in other samples generated and used by the CMS Collaboration, in particular all the background samples used in this work.

Among the features of the CTEQ6L1, there is one particularly important for the MPI and DPS studies: the longitudinal momentum conservation, namely in the fits which produce the PDFs the integral over the momentum of the partons is constrained to be equal to the momentum of the proton, therefore the sum rule mentioned in Sec.4.2 is fulfilled.

### 4.5 DPS Same Sign W yield estimation

#### 4.5.1 Selection

Since in the SM processes the  $\tau$  leptons are produced with the same rate of muons and electrons, and since the identification of  $\tau$ s decaying in hadrons has a worse performances compared to  $e$  and  $\mu$  identification, the hadronic  $\tau$ s have not been considered in this study.

The requirements  $e$  and  $\mu$  must satisfy to be identified prompt are chosen to be the same as the identification criteria used in the SSDL analysis and described in Chapter 3.

This choice is driven by the will to make the two analyses consistent.

---

<sup>1</sup>with the tune which now is known as *Tune1*

A single lepton trigger path has been chosen for the HLT requirement, the following path were considered: HLT\_Mu9 which requires a muon reconstructed by both tracker and muon system with  $p_T > 9$  GeV and HLT\_Ele15\_LW\_L1R which requires an electron with  $p_T > 15$  GeV . The event is triggered if it passes at least one of such trigger bits.

In the following, the most meaningful distributions are shown. The left figures show the distributions for physics processes which can have a final state with exactly two leptons and with the same charge. Such distributions are shown normalized to their integral, since their shape is important to discriminate processes with uncertain cross sections. The right figures show the same distributions for all the other background processes, they are normalized to the statistics which will be reached with  $L = 100\text{pb}^{-1}$ , the cross section used are the same listed in Tab.3.1. Fig.4.4 and Fig.4.5 show the distribution of the transverse momentum for the two leptons with higher  $p_T$ .

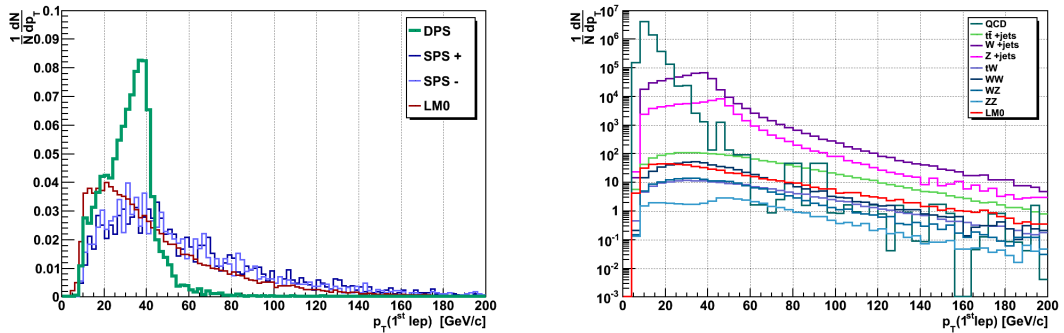


Figure 4.4:  $p_T$  distribution of the first lepton for the processes with same sign leptons normalized to unity (left) and for instrumental bakground sources normalized to  $100\text{ pb}^{-1}$  (right).

Since the leptons coming from  $W$ 's cannot have a low  $p_T$ , in order to reduce the QCD background, and to be consistent with other SM analyses in CMS, the threshold chosen for the leptons  $p_T$  is 20 GeV.

Fig.4.6 shows the  $p_T$  distribution for the jet with highest  $p_T$ .

It is evident that the presence of at least one high  $p_T$  jet has a very discriminant power in reducing the irreducible background.

The reason is that in the SPS SSW two partons are always produced together with the two  $W$ s, as already mentioned in Sec.4.4.1, and the SUSY events has a

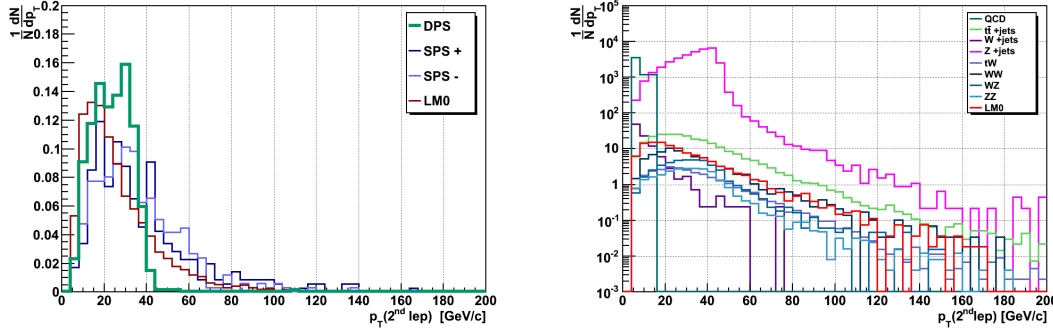


Figure 4.5:  $p_T$  distribution of the first lepton for the processes with same sign leptons normalized to unity (left) and for instrumental background sources normalized to  $100 \text{ pb}^{-1}$  (right).

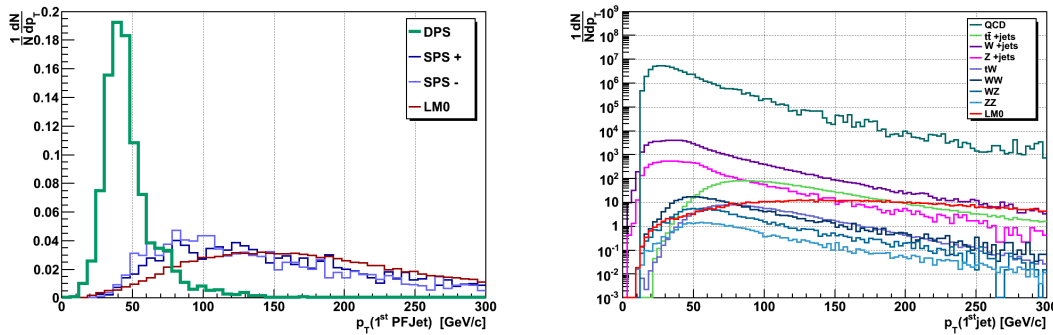


Figure 4.6:  $p_T$  distribution of the first jet for the processes with same sign leptons normalized to unity (left) and for instrumental background sources normalized to  $100 \text{ pb}^{-1}$  (right).

high hadronic activity. On the other hand the hard jet multiplicity in single  $W$  production decreases exponentially. For such reason a jet veto can be very effective and can represent the keyword of the selection.

A useful requirement aimed to reduce the diboson background is the absence of a third high  $p_T$  lepton. Fig.4.7 show that in the signal sample an extra lepton is rarely reconstructed.

A veto on the presence of an extra identified lepton with  $p_T > 10 \text{ GeV}$  has been chosen.

A requirement on missing energy is useful to reduce several background processes. The following topics led to the choice of the applied cut.

Since the two  $W$ s in the DPS are supposed to be produced with no kinematic correlations, distribution of the azimuthal angle between them has an uniform

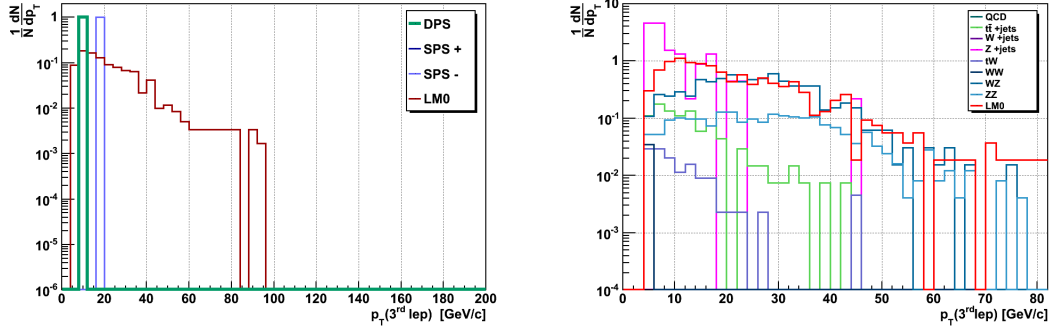


Figure 4.7:  $p_T$  distribution of the third lepton for the processes with same sign leptons normalized to unity (left) and for instrumental background sources normalized to  $100 \text{ pb}^{-1}$  (right).

distribution. This is shown in Fig.4.8, where the distribution of  $\Delta\phi(\text{lep1}, \text{lep2})$  for the DPS signal is compared to the distribution of other processes where the bosons produced are correlated each other since coming from the same parton interaction.

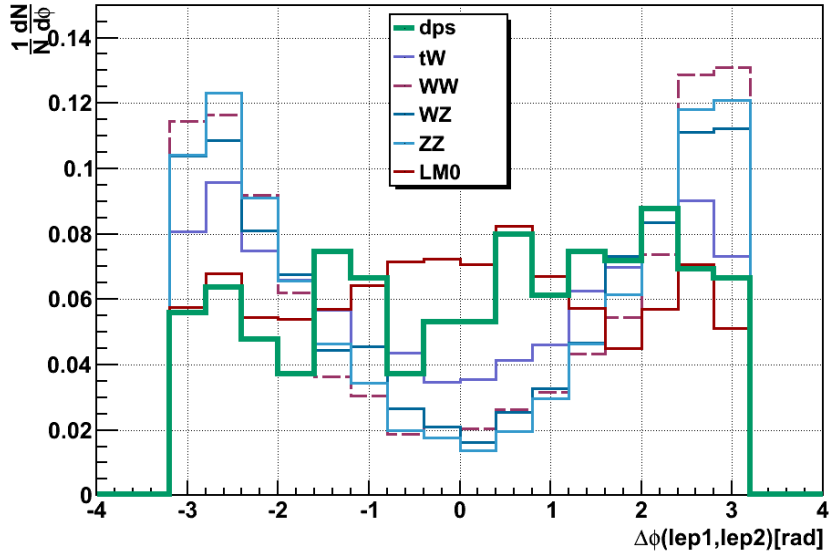


Figure 4.8:  $\Delta\phi(\text{lep1}, \text{lep2})$  for the DPS signal (teal) and the main background processes after the two identified lepton requirement.

The requirement of no production of hard jets, selects signal events with the  $W$  produced at rest. It is not possible to know the transverse direction of the two single neutrinos since the missing transverse energy represent their vectorial sum.

This makes applying a cut on the  $\cancel{E}_T$  not much effective, since it would reject signal events where the two neutrinos are produced with a large angle.

The vectorial sum of the  $p_T$  of the two leptons, indicated with  $\vec{p}_T^{lepPair}$ , should have same module and opposite verse of the missing transverse energy  $\cancel{E}_T$ :

$$\vec{p}_T^{lepPair} \equiv \vec{p}_T(\text{lep1}) + \vec{p}_T(\text{lep2}) = -\vec{\cancel{E}}_T \quad (4.9)$$

Therefore, the difference  $|\vec{\cancel{E}}_T| - |\vec{p}_T^{lepPair}|$ , essentially corresponding to the hadronic activity in the signal, should be compatible with 0.

This is not true for the background processes involving the  $Z$ , therefore a cut on this variable is effective in reducing the main irreducible background, the  $WZ$  production. This is visible in the scatter plot of the  $\cancel{E}_T$  and  $\vec{p}_T^{lepPair}$  variables in Fig.4.9 and in the distribution of  $|\vec{\cancel{E}}_T| - |\vec{p}_T^{lepPair}|$  in Fig.4.10.

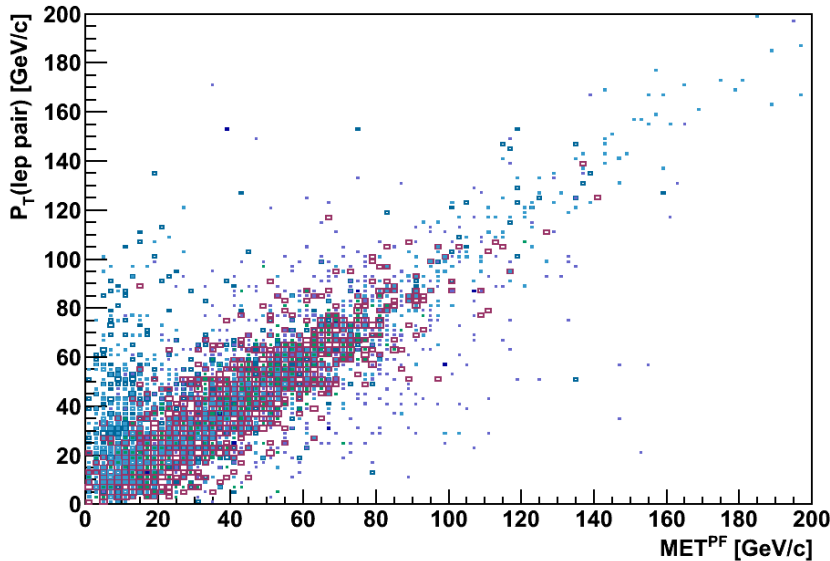


Figure 4.9: Scatter plot of  $\vec{p}_T^{lepPair}$  vs  $\cancel{E}_T$ . The color code is in the legend of Fig.4.8

- **HLT:** HLT\_Mu9 OR HLT\_Ele15\_LW\_L1R;
- **ID2lep:** At least 2 identified leptons ( $e, \mu$ ) with  $p_T > 20$  GeV and  $|\eta(e/\mu)| < 2.5/2.4$  ;
- **jetVeto:** Hard jet veto: reject events with at least one jet with  $p_T > 50$  GeV;

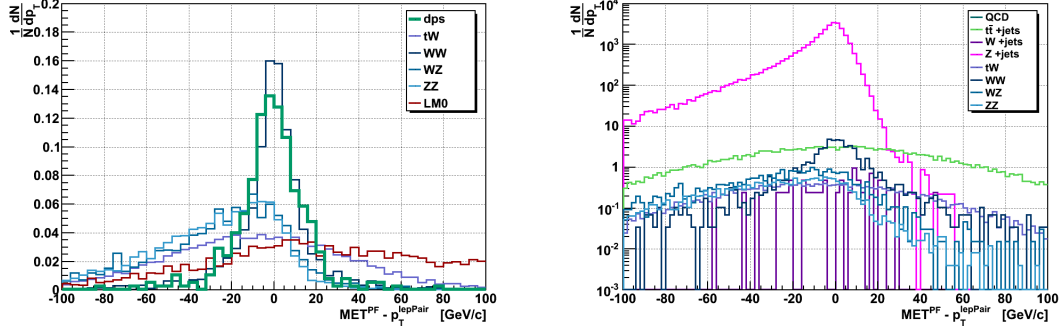


Figure 4.10:  $\vec{E}_T - \vec{p}_T^{leptonPair}$  for the processes with same sign leptons (left) and for instrumental background sources.

- **extraLepVeto:** No extra leptons with  $p_T > 10$  GeV;
- **ΔMET:**  $|\vec{E}_T| - |\vec{p}_T^{leptonPair}| > - 20$  GeV and  $\vec{E}_T > 10$  GeV;
- **ZVeto:** in the same lepton flavor channels  $ee$  and  $\mu\mu$   $|M((lep1, lep2) - M_Z)| > 15$   $GeV/c^2$ .

#### 4.5.2 Strategy for an inclusive DPS SSW cross section measurement

The CMS Collaboration has planned a measurement of the cross section of two opposite sign W production, referred to as *OSWW* in the following.

It can arise at  $\mathcal{O}(\alpha^2)$ , therefore is much more copious than the same sign W production through both SPS and DPS.

Hence the OSWW cross section will be measured earlier than the SSWW processes can constitute an issue for the analyses aimed to SUSY search.

One strategy to measure the DPS SSW cross section,  $\sigma^{SS}$ , is to use the normalization to the OSWW cross section,  $\sigma^{OS}$ , value. In order to properly use this method, the OSWW selection must be applied exactly, changing only the requirement of same charge leptons, instead of opposite sign.

The selection developed in CMS, aimed to measure  $\sigma^{OS}$ , foresees a jet veto in order to reduce the  $t\bar{t}$  and QCD background, this fits with our purposes to reject most of SPS SSW and possible SUSY events.

Therefore using the expression

$$\sigma_{DPS}^{SS} = \frac{N^{SS}}{N^{OS}} \cdot \sigma^{OS} \quad (4.10)$$

the DPS SSW cross section can be obtained avoiding to estimate the efficiencies. Nevertheless, in such approach care should be taken in assuming the same efficiencies for the OS WW and SS WW from DPS.

### Lepton acceptance and jet veto corrections

While there is no reason to think that the lepton identification should differ in OSWW respect with SSWW, the geometrical acceptance could be different. Indeed diboson opposite sign W production needs high  $p_T$  transfer, so its Ws are more central than the DPS Ws.

This is evident from Fig.4.11, where the  $\eta$  distributions of leptons from Ws at generator level are shown for DPS and diboson OSW processes.

This issue leads to modify the Eq.4.10 by introducing a factor, the ratio of the acceptances of the two processes  $\frac{a_{OS}}{a_{SS}}$ . The acceptance for the leptons from OS WW is estimated in the dedicated analysis. By assuming the two hard interactions in DPS WW are uncorrelated, the leptons produced have the same distribution of leptons originating from W decays in single W production. The systematic uncertainty on the acceptance in  $W+jets$  events, has been estimated in CMS for the measurement of the  $W$  production cross section [103], by comparing the acceptance estimation using several generators, both at LO and higher orders. The relative uncertainty is estimated to be 2%.

Fig.4.11 shows that the lepton  $\eta$  distribution in DPS WW is compatible with the one for the single  $W$  production. Instead the leptons in opposite sign WW production are produced more centrally.

Tab.4.1 quantifies the above statements.

The effect of the different acceptance in  $W^+W^-$  and DPS WW processes is translated in a scale factor in the normalization procedure. In order to take into account the two leptons, such factor is represented by square of the ratio  $R_a \equiv [a(DPS)/a(W^+W^-)]^2$ .

	$W^+W^-$	DPS WW	$W+jets$
acceptance( $e/\mu$ )	0.83	0.73	0.72
$R_a \equiv \left(\frac{a_{DPS}}{a_{OSWW}}\right)^2$		$0.774 \pm 0.039$	

Table 4.1: Lepton acceptance and  $R_a$  factor.

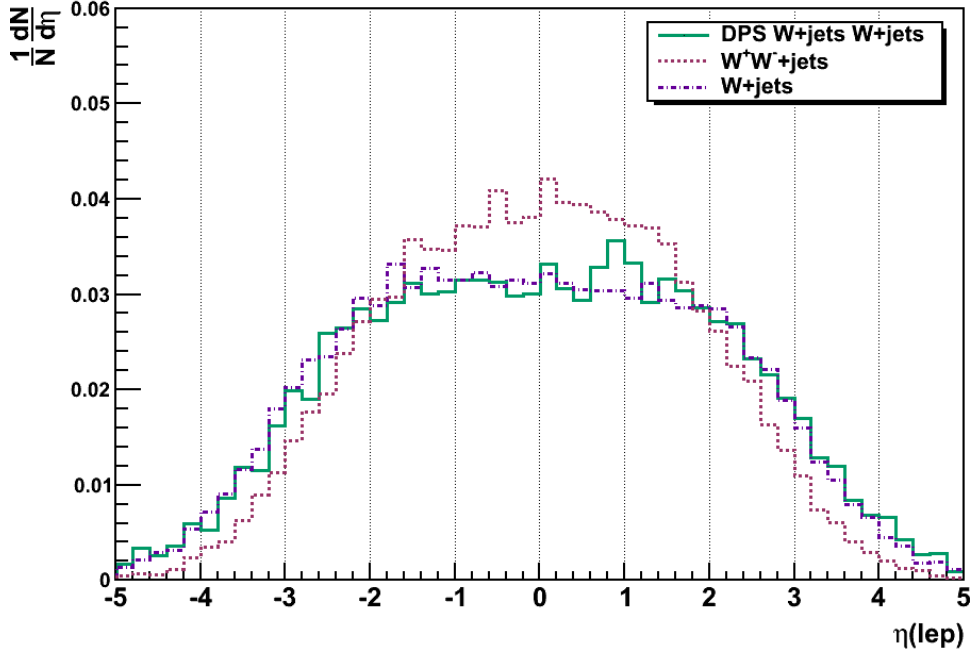


Figure 4.11:  $\eta$  distribution of the lepton coming from  $W$  decays at generator level normalized to area.

Like the lepton acceptance, also the jet veto is expected to have a different efficiency for  $W^+W^-$  process compared with DPS WW.

The jet veto efficiency has been measured in events selected as  $Z+\text{jets}$  as a function of the threshold on the jet  $p_T$ . Since the jet emission in a single parton interaction is regulated by the same physics mechanism, the  $W^+W^-$ ,  $W$  and  $Z$  production should have the same jet veto efficiency. The behavior of  $Z$  production events is well modelled by MadGraph generator, therefore the Montecarlo simulation is expected to be reliable also for  $W+\text{jets}$  and  $W^+W^-$  processes.

The jet veto efficiency for DPS WW production is  $\epsilon_{jetVeto}(\text{DPS}) = \epsilon_{jetVeto}^2(\text{SPS})$ , therefore the correction factor is  $R_{jetVeto} = \epsilon_{jetVeto}(\text{SPS})$ .

### 4.5.3 Selection Results

The cut flow of the selected number of events is reported in Tab.4.2 for the considered SM background processes. The values correspond to an integrated luminosity of  $L = 100\text{pb}^{-1}$ .

The efficiency obtained for the opposite sign diboson  $WW$  sample, after having

*Number of Events with  $L=100 \text{ pb}^{-1}$*

	$QCD$	$W\text{jets}$	$Z\text{jets}$	$t\bar{t}$	$tW$	$WW$	$WZ$	$ZZ$
$\mathbf{N_{in}}$	$8.73 \cdot 10^{10}$	$3.02 \cdot 10^6$	444600	15010	1060	4300	1820	590
HLT	$4.93 \cdot 10^7$	609797	127158	4440	272	687	228	59.9
ID2lep	-	10.8	42873	287	21.1	59.8	30.1	18.9
Vetos	-	9.03	40821	46.6	7.78	52.8	18.4	10.5
$\Delta\text{MET}$	-	7.83	8046	32.7	5.36	46.4	8.27	4.77
ZVeto	-	7.53	968.3	29.5	4.89	41.78	3.28	0.609
<b>SS</b>	-	1.51	1.27	0.187	0.0114	0.0350	1.46	0.0731
<b>OS</b>	-	6.02	0.967	29.3	4.88	41.8	1.82	0.536

Table 4.2: Cut flow of the selected number of events in  $100 \text{ pb}^{-1}$  for the background processes

applied the corrections for the lepton acceptance and jet veto, and requiring two opposite sign leptons is  $\epsilon_{OS}(W^+W^-) = 0.0072$ . The efficiency for the production of same sign W bosons from DPS of same selection but changing the charge requirement in same sign is  $\epsilon_{SS}(SSWDPS) = 0.0074$ .

The compatibility of the efficiency for the DPS requiring the SS leptons and the one for  $W^+W^-$  after the OS requirement justifies the strategy of the normalization to the  $W^+W^-$  cross section. Tab.4.2 shows that the largest background processes are expected to be the production of one vector boson. The background evaluation can be performed using the same general data driven methods described in 3.7, the only difference is the lepton  $p_T$  threshold.

The uncertainties on the background evaluation are expected to be 50%.

## 4.6 Extrapolation of SSW DPS contribution at high HT

By considering the DPS SSW process as a background to the SSDL SUSY analysis, it is crucial to estimate the DPS contribution in the region selected by the SUSY

analysis. The estimation of the number of events from DPS WW process requires only the estimation of the background contribution. Given the jet veto in the selection the measured value will be the number of events DPS SSW with no production of hard jets (defined with  $p_T > 50$  GeV in the study here performed).

With the data sample collected so far it was possible to estimate the ratio of events coming from DPS  $WW$  with  $H_T$  greater than a given value to the number of events with  $H_T = 0$ .

$$R_{H_Tcut} = \frac{N(H_T > H_T^{cut})}{N(H_T = 0)} \quad (4.11)$$

#### 4.6.1 Strategy

With the assumption that the two hard interactions are uncorrelated, the kinematic of the WW DPS process can be approximated to the kinematic of resulting from two single  $W$  boson production.

This approximation allows for a method to estimate the trend of the  $H_T$  distribution for WW DPS, already in the time being, when the integrated luminosity is not enough to observe the DPS, yet.

Under such assumption the  $H_T$  value for a WW DPS event,  $H_T[DPS]$ , is the sum of the  $H_T$  of two events with single  $W$  production taken at random,  $Wjets_1$  and  $Wjets_2$ :

$$H_T[DPS] = H_T[Wjets_1] + H_T[Wjets_2] \quad (4.12)$$

The distribution of  $H_T$  normalized to unity is taken in consideration.

The value assumed by the  $H_T[DPS]$  distribution,  $f(H_T[DPS])$ , namely the probability to get the value  $H_T[DPS]$ , can be expressed as the sum of all the probabilities to get two  $H_T$  values in  $W+jets$ , such that their sum is  $H_T[DPS]$ . In practice, this can be obtained by considering an histogram of the  $H_T$  variable for  $W+jets$  and the discrete version of the above arguments can be written as:

$$f\left(H_T[DPS]\right) = \sum_i \sum_j f\left(H_T[Wjets](i)\right) f\left(H_T[Wjets](j)\right) \quad (4.13)$$

where the indices  $i$  and  $j$  run over the bins of the histogram and  $H_T[DPS]$ ,  $H_T[Wjets](i)$  and  $H_T[Wjets](j)$  are such that:

$$H_T[DPS](j) = H_T[Wjets](i) + H_T[Wjets](j) \quad (4.14)$$

Such constrain allows for the elimination of a variable, by expressing  $H_T[Wjets](j)$  as a function of  $H_T[DPS](j)$  and  $H_T[Wjets](i)$  the  $H_T[DPS](j)$  distribution is

given by:

$$f\left(H_T[DPS]\right) = \sum_i f\left(H_T[Wjets](i)\right) f\left(H_T[DPS] - H_T[Wjets](i)\right) \quad (4.15)$$

The above arguments are nothing else but the explicite deduction of the expected result: the  $H_T$  distribution of WW DPS can be approximated as the the  $H_T$  distribution for  $W+jets$  events convolved with itself. Such convolution is in the following indicated as  $\mathcal{C}(H_T)$ .

The  $W+jets$  events are easily selected from real data by requiring an identified and high  $p_T$  lepton along with missing transverse energy.

#### 4.6.2 Validation with real data

The large cross section of the  $W$  production at LHC, made possible to validate the method above described at this first stage of data taking.

The lepton identification criteria are the same as in the SSDL and SSW selection. The  $H_T$  variable is computed with the jets having a  $p_T > 50$  GeV, this allows for consistency with the SSDL SUSY analysis and the jet veto in the SSW selection. Additionally a low  $p_T$  threshold would make the soft activity (underlying event, contribution from secondary  $p$ - $p$  interaction) counted twice. For the data and the  $Wjet$  sample at least one lepton is required, while for the DPS the number of leptons should be at least two. The selection applied is here summarized:

- $e/\mu$  identified by the criteria in Sec.3.5.1 and  $p_T(e/\mu) > 20$  GeV;
- $\cancel{E}_T > 20$  GeV;
- $N_{lep} > 0$  (1) in data and  $Wjet$  (DPS WW).

Fig4.12 shows the  $H_T$  distribution for the selected data and compares it to the selected **Wjets** sample.

The good agreement between data and the MC  $W+jets$  sample demonstrates that in the selected events the contribution of processes other than  $W+jets$  is negligible. The distribution of convolution described in Sec.4.6.1 is shown in Fig.4.13 for the data sample and the **Wjets** and is compared to the  $H_T$  distribution of the DPS WW sample.

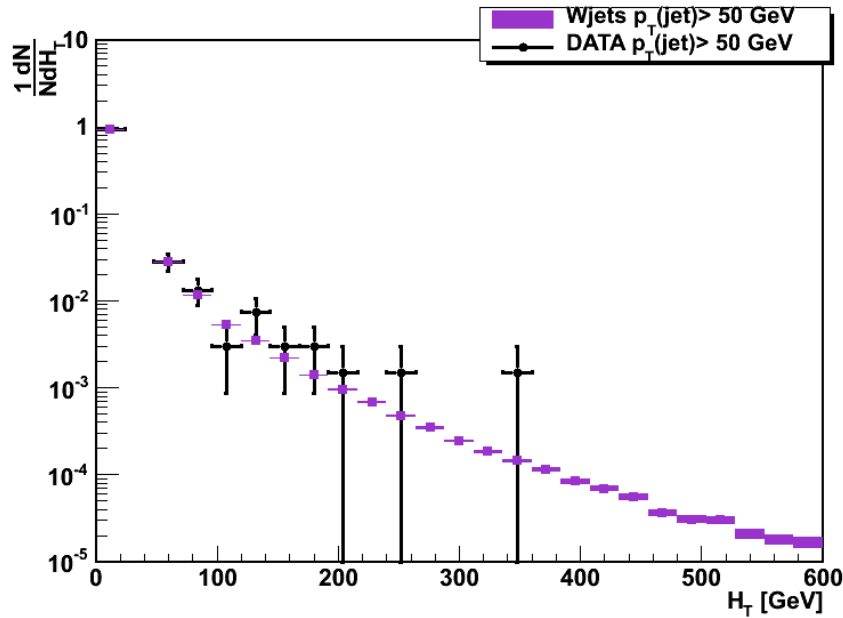


Figure 4.12: Distribution of  $H_T$  (for DPS WW) and  $H_T$  convolution (for data and  $W_{jets}$  samples) computed with  $p_T(jet) > 50$  GeV (left) and  $p_T(jet) > 25$  GeV (right).

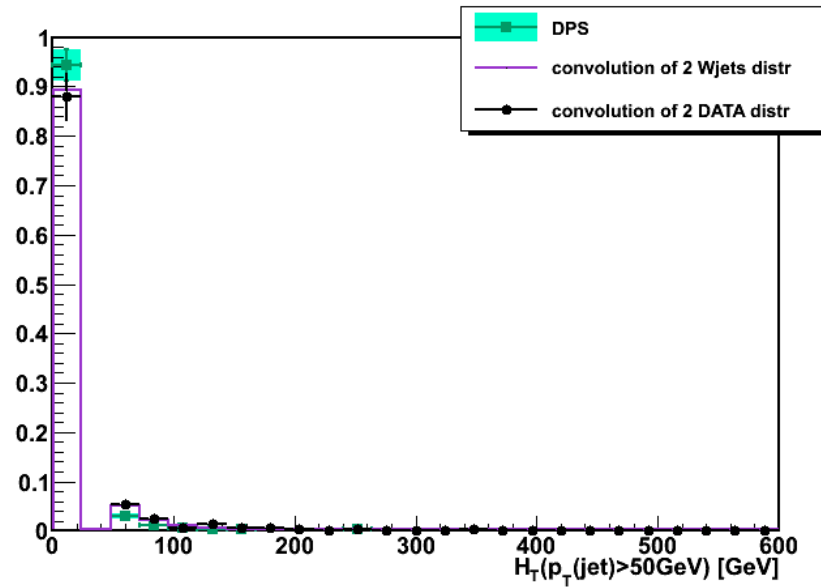


Figure 4.13: Distribution of  $H_T$  (for DPS WW) and  $H_T$  convolution (for data and  $W_{jets}$  samples) computed with  $p_T(jet) > 50$  GeV

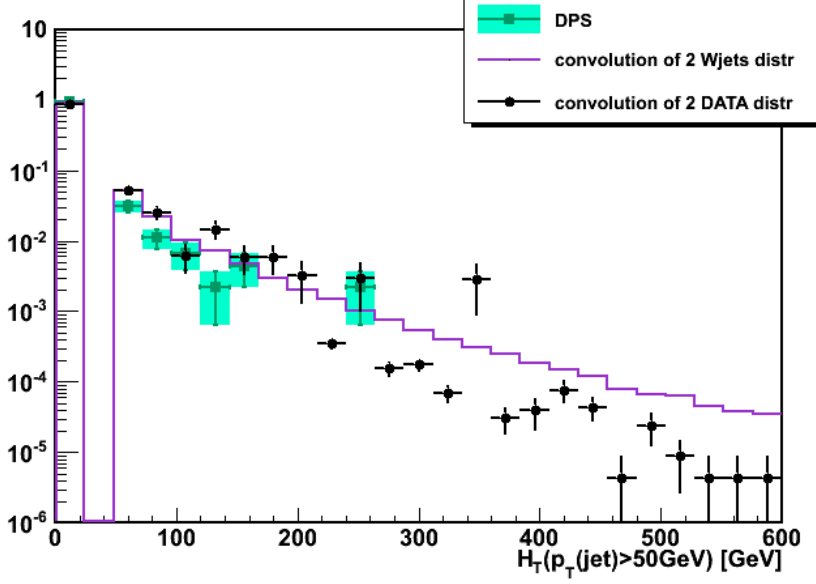


Figure 4.14: As in Fig.4.13 but in logarithmic scale

The apparent several contributions to the convolution distribution of data are due to the low statistics available, as can be observed by looking at the  $H_T$  distribution (see Fig.4.12). The normalization will be performed by considering the DPS SSW cross section, or its yield for  $H_T = 0$ , when they will be measured.

### 4.6.3 Contribution to SSDL SUSY Background

The number of events from DPS SSW with  $H_T = 0$  will be estimated from data when large statistics will be available. It will represent the normalization factor to the ratio  $R_{H_Tcut}$  defined in Eq.4.11.

$$N_{DPS}^{SSW}(H_T > H_T^{cut}) = N_{SS} \cdot R_{H_Tcut} \quad (4.16)$$

The fraction of DPS WW events with  $H_T > 350$  GeV, has been estimated by counting the events with  $\mathcal{C}(H_T) > 350$  GeV in the data sample. It results to be

$$R_{350} = (3.446 \pm 0.092) \cdot 10^{-3} \quad (4.17)$$

A systematic uncertainty could arise from the assumption that the two parton interactions are uncorrelated, which is the basis of the convolution expression in Eq.4.15. The extent of the departure from the uncorrelated case can be evaluated through the cross section measurement of the DPS processes. In particular, when

this method will be applied, the normalization factor, namely the cross section or the  $N(H_T = 0)$ , is measured.

By assuming for the effective cross section, the value measured by the Tevatron experiments  $\sigma_{eff} = 14\text{mb}$ , the expected inclusive cross section of  $W$  pairs production through double parton scattering is 343 fb. From this value the produced number of events having  $H_T > 350 \text{ GeV}$  with  $L = 100\text{pb}^{-1}$  is  $1.2 \cdot 10^{-3}$ .



# Conclusions

In this work an analysis aimed to search for SUSY in the final state with two like sign leptons has been presented. Like sign leptons final state is rare in the Standard Model scenario, while it is a typical SUSY signature. The main features of the analysis developed are here summarized. Supersymmetric theories are founded on some common bases, but the subtle theoretical framework leads to the necessity to make assumptions. Moreover SUSY events often generate long decay cascades, and the spread of final states can be very variegated.

It is clear that analyses optimized for specific models are ineffective until SUSY is not discovered. On the contrary the common features of SUSY models have been considered in the choice of the selection requirements. The aim of the analysis is to highlight an excess of events over the expected SM background, after the selection. The selection here presented is as simple as possible, it applies requirements only on variables with a well understood behavior:  $H_T$  and  $MH_T$  and the presence of two like sign prompt leptons. The lepton identifications, the most important requirements, are based on methods validated by many analyses which were able to perform measurements confirming the SM predictions and in agreement with previous experiments.

These characteristics of the few requirements constituting the whole selection, make the analysis *only feebly affected by systematic errors and efficient for all SUSY models*.

The peculiarity of the analysis here presented is its contentiousness: an approach as inclusive as possible has been adopted. The good performances of the CMS detector, accurately tested in this first year of data taking, allowed to put into practice such inclusiveness while keeping the results trustable.

The inclusion of low  $p_T$  leptons enable the search to be *sensitive to SUSY models with a small mass splitting between the Chargino and the lightest SUSY particle*.

The heaviness of the  $\tau$  makes it a special lepton respect to the electron and the

muon. The Charginos and Neutralinos prefer to decay in  $\tau$ , due to its larger Yukawa coupling, compared to  $e$  and  $\mu$ . The branching ratio  $\mathcal{B}(\chi \rightarrow \tau + X)$  can overcome the  $\mathcal{B}(\chi \rightarrow e/\mu + X)$ , the extent of the overtaking depends on the model and can reach high values especially in models with large  $\tan\beta$ .

The difficulty in reconstructing tau leptons decaying in hadron, and distinguishing them from QCD jets, led other analyses to ignore final states with  $\tau$ s. This conservative approach could lead to miss the possible presence of new physics.

On the contrary, in the analysis here presented tau leptons decaying in hadrons are identified and the ***final states with taus are included and handled like the other final states.***

Additionally the common approach to every final state allows for internal checks within the same analysis framework.

After the robust and simple selection, the remaining background processes have a low yield, but, in order to be able to claim or exclude new physics, an accurate knowledge of every source of SM contribution is mandatory. ***Data driven methods to estimate the SM contribution*** to the final sample has been developed.

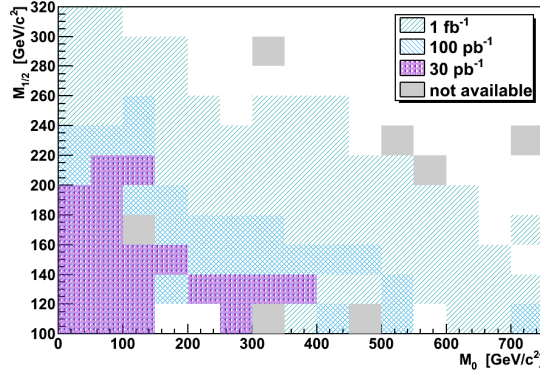
The number of SM events *predicted* by the data driven methods agrees with the the one *observed* by counting the events after the whole selection:

<i>MC-Predicted in <math>L=100 \text{ pb}^{-1}</math></i>	<i>MC-Observed in <math>L=100 \text{ pb}^{-1}</math></i>
$N(ee) = 0.131 \pm 0.093$	$N(ee) = 0.71 \pm 0.16$
$N(\mu\mu) = 0.042 \pm 0.013$	$N(\mu\mu) = 0.029 \pm 0.014$
$N(\tau\tau) = 12 \pm 12$	$N(\tau\tau) = 5.6 \pm 2.0$
$N(e\mu) = 0.038 \pm 0.007$	$N(e\mu) = 0.051 \pm 0.019$
$N(e\tau) = 0.54 \pm 0.16$	$N(e\tau) = 1.03 \pm 0.042$
$N(\mu\tau) = 0.71 \pm 0.16$	$N(\mu\tau) = 1.55 \pm 0.84$

The ***real data sample*** corresponding to  $L = 3\text{pb}^{-1}$  has been considered. No events were selected by the SSDL selection, in agreement with the prediction from the data driven methods. Furthermore, in order to test with real data the background evaluation the selection was relaxed and the observed event numbers have been compared to the predicted ones assuming only SM processes:

<i>relaxed selection</i>	
<i>DATA-Predicted</i>	<i>DATA-Observed</i>
$N(ee) = 0.001 \pm 0.0005 \pm 0.00$	$N(ee) = 0$
$N(\mu\mu) = 0.097 \pm 0.062 \pm 0.091$	$N(\mu\mu) = 0$
$N(\tau\tau) = 17.3 \pm 5.3 \pm 3.4$	$N(\tau\tau) = 14$
$N(e\mu) = 0.056 \pm 0.025 \pm 0.054$	$N(e\mu) = 1$
$N(e\tau) = 0.030 \pm 0.12 \pm 0.029$	$N(e\tau) = 0$
$N(\mu\tau) = 1.20 \pm 0.41 \pm 0.16$	$N(\mu\tau) = 2$

A sensitivity study on the mSuGra plane was performed. By using an integrated luminosity of  $30\text{pb}^{-1}$  it is possible to exclude the models which cover a wide range of the mSUGRA plane, overcoming the existent limits set by the Tevatron experiments.



There exist some SM physics processes with same sign leptons in the final state. In the SUSY SSDL study for  $L = 100\text{pb}^{-1}$  such processes were not taken into account in the background evaluation, due to their small cross section. At higher integrated luminosity such rare SM processes will deserve attention, since they are an irreducible background to the SUSY analyses.

**For the first time the same sign Ws boson production has been considered.**

Understanding the Double Parton Scattering incidence to the analysis aimed to search for New Physics is mandatory at LHC.

Indeed the probability to have two hard parton interactions within the same proton-proton collision, suffers from large theoretical uncertainties due to the non-perturbative nature of the hadron structure, furthermore the latter could depends on the hadron energy. These topics state that it would be unwise relying LHC analysis on the cross sections measurements performed at Tevatron. Moreover an evaluation of the DPS yield, could provide information about the hadron structure, hence the autonomous importance of DPS.

A *strategy to measure its cross section* has been planned and a *method to extrapolate its contribution to the SSDL SUSY analysis* has been put in place.

The requirement of absence of hard jets in the event, allows to disentangle the Double Parton Scattering production from the SPS SSWW and from the potential SUSY processes. A MC feasibility study has been performed. The integrated luminosity collected so far, did not allow to perform the DPS WW cross section measurement.

Based on the assumption of two uncorrelated interaction, a strategy to evaluate the contribution to the SSDL SUSY background has been developed and tested with the initial data.

*The fraction of events coming from DPS WW with  $H_T$  satisfying the SSDL SUSY analysis requirements has been estimated by using the data collected so far.* The value obtained is:

$$\frac{N(H_T > 350\text{GeV})}{N(H_T = 0)} = (3.446 \pm 0.092) \cdot 10^{-3}$$

By assuming for  $\sigma_{eff}$  the value measured by Tevatron experiments, the expected number of events selected by the SSDL analysis in  $100\text{pb}^{-1}$  is about  $1.2 \cdot 10^{-3}$ .



# Acronyms

<b>LHC</b>	Large Hadron Collider .....	1
<b>TeV</b>	Tera electronVolt .....	1
<b>SM</b>	Standard Model .....	1
<b>QCD</b>	Quantum Chromo Dynamic .....	2
<b>EW</b>	ElectroWeak .....	2
<b>SUSY</b>	SUperSYmmtry .....	9
<b>WIMPs</b>	Weak Interacting Massive Particles .....	7
<b>VEV</b>	Vacuum Expectation Value .....	3
<b>UV</b>	UltraViolet .....	6
<b>PMSB</b>	Plank Mediated Supersymmetry Breaking .....	13
<b>GMSB</b>	Gauge Mediated Supersymmetry Breaking .....	13
<b>SSB</b>	Spontaneous Symmetry Braking .....	13
<b>MSSM</b>	Minimal Supersymmetric Standard Model .....	14
<b>CMSSM</b>	Constrained Minimal Supersymmetric Standard Model .....	22
<b>LSP</b>	Lightest Supersymmetric Particle .....	16
<b>NLSP</b>	Next to Lightest Supersymmetric Particle .....	29
<b>RGE</b>	Renormalization Group Evolution .....	23
<b>FCNC</b>	Flavor Changing Neutral Current .....	21
<b>OSDL</b>	Opposite Sign Di-Lepton .....	38
<b>SSDL</b>	Same Sign Di-Lepton .....	38
<b>LINAC2</b>	LINEar ACcelerator 2 .....	44
<b>PSB</b>	Proton Synchrotron Booster .....	45

<b>ECAL</b>	Electromagnetic CALorimeter .....	51
<b>HCAL</b>	Hadronic CALorimeter .....	51
<b>DT</b>	Drift tube .....	59
<b>CSC</b>	Cathode Strip Chambers .....	59
<b>RPC</b>	Resistive Plate Chambers .....	59
<b>BX</b>	bunch crossing.....	60
<b>L1</b>	Level-1 .....	62
<b>HLT</b>	High Level Trigger.....	62
<b>TPG</b>	Trigger Primitive Generators.....	62
<b>RCT</b>	Regional Calorimeter Trigger .....	63
<b>GMT</b>	Global Muon Trigger .....	64
<b>FED</b>	Front-End Driver .....	64
<b>DAQ</b>	Data Acquisition .....	64
<b>DQM</b>	Data Quality Monitoring .....	65
<b>LCG</b>	LHC Computing Grid .....	66
<b>CRAB</b>	CMS Remote Analysis Builder .....	66
<b>PF</b>	Particle Flow .....	74
<b>KF</b>	Kalman Filter .....	76
<b>GSF</b>	Gaussian Sum Filter .....	76
<b>BDT</b>	Boost Decision Trees .....	77
<b>TaNC</b>	Tau Neural Classifier .....	93
<b>SSW</b>	Same Sign W .....	132
<b>SPS</b>	Single Parton Scattering.....	131
<b>DPS</b>	Double Parton Scattering.....	131
<b>MPI</b>	Multiple Parton Interaction.....	132
<b>DGLAP</b>	Dokshitzer Gribov Lipatov Altarelli Parisi .....	137
<b>dDGLAP</b>	double Dokshitzer Gribov Lipatov Altarelli Parisi .....	137
<b>PDF</b>	Parton Density Function.....	134

# Bibliography

- [1] C. Yang and R. Mills, Phys. Rev. **96**, 191 (1954).
- [2] J. Goldstone, Nuovo Cimento **19**, 154 (1961).
- [3] P. Higgs, Phys. Rev. Lett **13**, 508 (1964).
- [4] F. Mandl and G. Saw, *Quantum Field Theory* (John Wiley and Sons, 1984).
- [5] S. P. Martin, hep-ph/9709356v5 (1997).
- [6] The Supernova Cosmology Project, R. Knop *et al.*, Astrophys.J. **598** (2003), astro-ph/0309368.
- [7] G. Jungman, M. Kamionkowski, and K. Griest, Phys.Rept. , 195 (1996), hep-ph/9506380.
- [8] E. Kolb and M. Turner, *The Early Universe* (Front. Phys. 69, 1, 1990).
- [9] WMAP Collaboration, Astrophys.J. Suppl. **180**, 306 (2009).
- [10] D. Hooper, (TASI 2008), arXiv:0901.4090.
- [11] A. D. Sakharov, JETP Lett. **6** (1967).
- [12] J. Wess and B. Zumino, Nucl. Phys. **B70** (1974).
- [13] S. Coleman, *Aspects of symmetry* (Cambridge Univ. Press, 1985).
- [14] M. Drees, R. Godbole, and P. Roy, *Theory and Phenomenology of Sparticles* (World Scientific, 2004).
- [15] C. Itzykson and J. B. Zuber, *Quantum Field Theory* (MacGrawHill, 1980).
- [16] G.D'Ambrosio, G. Giudice, G. Isidori, and A. Strumia, Nucl. Phys **B645**, 155 (2002).

- [17] Particle Data Group, C. Amsler *et al.*, Physics Letters **B667** (2008).
- [18] Heavy Flavor Averaging Group, E. Barberio *et al.*, p. arXiv:0808.1297 (2009).
- [19] M. Blanke *et al.*, JHEP , 003 (2006), arXiv:hep-ph/0605214.
- [20] CDF Collaboration, Aaltonen *et al.*, p. CDF Note 3697 (2004).
- [21] J. K. Mizukoshi, X. Tata, and Y. Wang, Phys.Rev. **D66**, 115003 (2002).
- [22] Muon G-2 Collaboration, G. W. Bennett *et al.*, Phys. Rev. **D73** (2006), hep-ex/0602035.
- [23] CMD-2 Collaboration, R. R. Akhmetshin *et al.*, Phys. Lett. **B648**, 28 (2007).
- [24] SND Collaboration, M. N. Achasov *et al.*, JETP Lett. **103**, 380 (2006).
- [25] KLOE Collaboration, F. Aloisio *et al.*, Phys. Lett. **B606** (2005).
- [26] BABAR Collaboration, B. Aubert *et al.*, Phys. Rev. Lett. **103**, 231801 (2009), arXiv:0908.3589.
- [27] K. Hagiwara *et al.*, Phys. Lett. B **B606**, 173 (2007).
- [28] UA2 Collaboration, J. Alitti *et al.*, Phys. Lett. **B**, 363 (1990).
- [29] LEP Collaboration, Eur. Phys. J. **C47** (2006), hep-ex/0602042.
- [30] H. B. X. Tata, *Weak scale supersymmetry:from superfields to scattering events* (Cambridge, 2006).
- [31] L. Randall and D. Tucker-Smith, Phys.Rev.Lett. **101**, 101803 (2008).
- [32] M. Nojiri and Y. Yamada, Phys.Rev. **D**, 015006 (1999).
- [33] G. Bachy *et al.*, CERN/LEP-DI-IM-RF (1989).
- [34] L. Evans and P. Bryant, JINST **3** (2008).
- [35] CERN AB Division, <http://accel-general.web.cern.ch/accel%2Dgeneral/> (2008).
- [36] CMS Collaboration, CERN-LHCC-2006-001 , <http://cdsweb.cern.ch/record/922757> (2006).

- [37] CMS Collaboration, JINST **0803** (2008).
- [38] CMS Collaboration, Phys.Rev.Lett **105**, 022002 (2010).
- [39] CMS Collaboration, CMS NOTE-2009/012 .
- [40] The LCG TDR Editorial Board, p. CERN/LHCC 2005 (2005).
- [41] D. Spiga *et al.*, 14th Int. Conf. on High Performance Computing , 580 (HiPC 2007).
- [42] J. Alwall *et al.*, JHEP , 028 (2007), arXiv:0706.2334.
- [43] T. Sjostrand, S. Mrenna, and P. Skands, JHEP (2006), hep-ph/0603175.
- [44] S. Jadach *et al.*, Comput.Phys.Commun. , 275 (1990).
- [45] B. Allanach, Comput.Phys.Commun. , 305 (2002), hep-ph/0104145.
- [46] A. Djouadi *et al.*, ActaPhys.Polon. **B**, 635 (2007).
- [47] W. Beenakker, R. Hoepker, and M. Spira, hep-ph/9611232.
- [48] CMS Collaboration, CMS-PAS-SUS-08-038 .
- [49] CMS Collaboration, CMS-PAS-SUS-09-002 .
- [50] CDF Collaboration, T. Aaltonen *et al.*, Phys. Rev. Lett. **101** (2008).
- [51] H. Baer *et al.*, Phys.Rev. **D59**, 055014 (1999).
- [52] CMS Collaboration, CMS-PAS-PFT-09-001 ,  
<http://cdsweb.cern.ch/record/1194487?ln=en>.
- [53] CMS Collaboration, CMS-PAS-PFT-10-002 ,  
<http://cdsweb.cern.ch/record/1279341?ln=en>.
- [54] CMS Collaboration, CMS-PAS-PFT-10-003 ,  
<http://cdsweb.cern.ch/record/1279341?ln=en>.
- [55] CMS Collaboration, CMS-PAS-TRK-10-005 ,  
<http://cdsweb.cern.ch/record/1279383?ln=en>.
- [56] CMS Collaboration, CMS-PAS-MUO-10-002 ,  
<http://cdsweb.cern.ch/record/1279140?ln=en>.

- [57] R. E. Kalman, (Transaction of the ASME-Journal of Basic Engineering, March, 1960).
- [58] R. Frühwirth, (Nucl. Instrum. Meth., A 262, 1987).
- [59] W. Adam *et al.*, J.Phys.G Nucl.Part.Phys **31** (2005).
- [60] CMS Collaboration, CMS-PAS-PFT-10-003 .
- [61] L. Breiman *et al.*, *Classification and Regression Trees* (Waldsworth International, 1984).
- [62] M. Cacciari, G. Salam, and G. Soyez, JHEP **0804:063**, arXiv:0802.1189.
- [63] CMS Collaboration, CMS-PAS-PFT-08-001 ,  
<http://cdsweb.cern.ch/record/1279358?ln=en> (2008).
- [64] CMS Collaboration, D. Barge *et al.*, CMS AN-2009/159.
- [65] CMS Collaboration, CMS-PAS-EGM-10-004 .
- [66] CMS Collaboration, A. Bryer *et al.*, CMS AN-2010/224 .
- [67] CMS Collaboration, CMS-PAS-PFT-10-004 ,  
<http://cdsweb.cern.ch/record/1198228?ln=en>.
- [68] Particle Data Group, C. Amsler *et al.*, Physics Letters **B667** (2008).
- [69] R. Cousins, J. Limmemann, and J. Tucker, arXiv:physics/0702156.
- [70] T. Li and Y. Ma, Astrophysical Journal **272**, 317 (1983).
- [71] R. Cousins, K. Hymes, and J. Tucker, arXiv:0905.3831.
- [72] F. James and M. Roos, Nuclear Physics **B172**, 475 (1980).
- [73] N. Reid, Stat. Sci. **10**, 138 (1995).
- [74] W. Press *et al.*, Cambridge (1992).
- [75] J. Heinrich *et al.*, arXiv:physics/0409129.
- [76] J. Conway, (<http://www-cdf.fnal.gov/physics/statistics/code/bayes.f>).
- [77] J. Conway, CDF/PUB/STATISTICS/PUBLIC/6428 (2005).

- [78] D0 Collaboration, Abazov *et al.*, Phys.Lett **B**, 34 (2009).
- [79] CDF Collaboration, Aaltonen *et al.*, Phys.Rev.Lett , 251801 (2008).
- [80] LEPSUSY Working Group, p. <http://lepsusy.web.cern.ch/lepsusy>Welcome.html> (2004).
- [81] A. Kulesza and W. Stirling, Phys.Lett. **B**, 168 (2000).
- [82] AFS Collaboration, Z.Phys.C **34**, 163 (1987).
- [83] UA2 Collaboration, Phys. Lett. B **268**, 145 (1991).
- [84] CDF Collaboration, Phys. Rev. D **47**, 4857 (1993).
- [85] T. Sjostrand and P. Skands, arXiv:hep-ph/0402078 (2004).
- [86] Y. Dokshitzer *et al.*, *Basics of Perturbative QCD* (Editions Frontieres, 1991).
- [87] G. Calucci and D. Treleani, Phys.Rev. **D60**, 054023 (1999).
- [88] CDF Collaboration, Phys. Rev. D **56**, 3811 (1997).
- [89] A. Snigirev, Phys.Rev. **D**, 114012 (2003).
- [90] V. Gribov and L. Lipatov, Sov.J.Nucl.Phys. **15**, 438 (1972).
- [91] G. Altarelli and G. Parisi, Nucl.Phys.B **126** (1977).
- [92] Dokshitzer, Nucl.Phys.B **126** (1977).
- [93] V. Shelest, A. Snigirev, and G. Zinovjev, Phys.Lett. **B**, 325 (1982).
- [94] J. Gaunt and W. Stirling, JHEP **1003** (2010), arXiv:0910.4347 (hep-ph).
- [95] A. Snigirev, Phys.Rev. **D**, 065014, arXiv:1001.0104 (2010).
- [96] J. Gaunt, C. Kom, A. Kulesza, and W. Stirling, EPJ **C** (2010).
- [97] Braidot *et al.*, Proceedings of MPI 08 , 55 (2008).
- [98] E. Maina, arXiv:0909.1586.
- [99] T. Sjostrand, S. Mrenna, and P. Skands, arXiv:0710.3820.

- [100] E. Boos *et al.*, in proceedings of the Workshop on Physics at TeV Colliders (21 May – 1 June 2001), hep-ph/0204316.
- [101] R. Corke, (2009), arXiv:0901.2852v1.
- [102] J. Pumplin *et al.*, hep-ph/0201195v3.
- [103] CMS Collaboration, CMS-PAS-EWK-10-002 ,  
<http://cdsweb.cern.ch/record/1279615?ln=en> (2010).

# Acknowledgment

The person to whom I've been <sup>2</sup> grateful the most during this period, is Dr. Michele Pioppi, who supervised my work since the beginning of my PhD studies and... had the courage (or naivety <sup>3</sup> ?) to go on till the end. His most precious teaching was the concreteness, without his continuous calls to be pragmatic this thesis would be for the most made of suspension points.... Surely also his knowledge of detectors and physics and his initiative were valuable to my work. A thank also to Dr. Attilio Santocchia who introduced me in CMS and Dr. Daniele Spiga (DanieleS), with both I shared my first work in CMS.

I would like to thank the Imperial College & Friends SUSY (ICFSUSY) group for the useful analysis framework, it makes focusing on Physics easier. I am particularly grateful to the other SSDL ICFSUSY guys: Arlo Guneratne Bryer, Alberto Ocampo and Marc Weinberg.

A thank to Dr. Paolo Bartalini who generated the same sign W samples. Thanks to the readers: Dr. Mirco Cannoni for having read the first chapter, this made me a bit more relaxed, since I could be sure that no absurdities are in it, and Prof. Marisa Valdata who has read the rest of the thesis, providing useful advices.

I would like to take this chance also to thank (with a four years delay) my laurea thesis supervisor, Dr. Paolo Gauzzi, who gave me the opportunity to take part to a real whole data analysis as an undergraduate student in KLOE.

For the non-work thank-list I start with Andrea (e poi dicono che ti tratto male!...), my companion in misfortune for all this period, the other, besides me, *disgraziato* (cit.) of the pg family: the lot fell to him hearing all my monologues... I want to thank all the CSM ...hops! sorry I mean CMS PG group, especially the young people: DanieleS, DanieleB, Roberto, Hassen, Michele, Livio (do you mind if I put you in the *young* group?), Andrea, Filippo, Mattia, Benedetta, and the

---

<sup>2</sup>the tense is not by accident  $\odot$  ;oP

<sup>3</sup>“..assomiglia all' ingenuità la saggezza, ma non ora, non qui...” G.L.Ferretti ;oP

new entry in PG Silvia, I enjoyed the short but intense (for me) time with you. A special thank goes to DanieleS and Hassen, for their moral support during the (first and last respectively) period of this experience. Now reread the last sentence with the change moral→CRAB (maybe CRABbers are used to support people in any sense....).

Thanks to all the people I often saw in the last period, in canteen, diners out of CERN, and every kind of “social life”... A thank to all the PG phd students of the last three years of both the offices, especially Bozzo&Co (Matteo, Nicola, Antonio, Roberto,...).

Outside the Physics world, first of all thanks to people who attended my transition from one “craziness” to another one (“dalla padella alla brace”...? time will tell..). Christian (or do you prefer Kristijan?), despite his long disappearances, when *c’è c’è* and knows how to comfort me. Claudia, who can listen me to say strong sentences without get scandalized, and an additional thank for hosting me in her great flat every time I pass by way of Rome. Both of them get closer to me since I’m far, who knows why?... ;o)

Thanks also to some people I met during my life and (even if unconsciously) made me understand something: Iohannes, Michele (*lo scriteriato*), Lina, Enrique, Piera.... and all the regular customers of the several canteens I attended in the last ten years.

I thank my grandparents and my parents Innocenza and Filippo who left me free in the everyday and life choices since as a child, always supporting them. Thanks to my brother Daniele, his wife Eva and all his new Guatemalan family, who made me aunt of the wonderful Camila!

I wish to thank all the people I met who, only with their existences made me aware of the truth of some commonplace. My thanks are sincere since it makes me feel a bit more alive and part of the human kind.

A great thank to all the people who, in their own work do more than simply apply rules, and knows how to deal with statistics... especially in human sciences, also the distributions tails deserve attention... ;o)

Finally a comprehensive thank to the writers I loved in my adolescence without knowing the reason.

# List of Figures

1.1	Top and stop loops corrections to the lightest Higgs mass. . . . .	19
1.2	RG evolution of the $\alpha^{-1}(Q)$ in the Standard Model (dashed lines) and the MSSM (solid lines). In the MSSM case, the sparticle mass thresholds are varied between 250 GeV and 1 TeV, and $\alpha^3(m_Z)$ between 0.113 and 0.123. Two-loop effects are included. [5]. . . . .	23
1.3	Example of the running of a specific model parameters [5]. . . . .	24
1.4	Indicative mass spectrum for the LM0 point in mSUGRA model. .	26
1.5	Up: the fermionic and scalar loops to the Higgs field. Down: the vertices of the Yukawa interactions of the scalar-fermion-fermion vertex, its conjugate, and the quartic scalar interactions. . . . .	27
1.6	Leading order loops contribution to $b \rightarrow s\gamma$ in susy. . . . .	30
1.7	Contribution diagrams to $B_d \rightarrow \tau^+\tau^-$ in the Standard Model contest	30
1.8	[21]Contours in the $m_0$ - $m_{1/2}$ plane of the mSUGRA model with $A_0 = 0$ where the branching fraction for $B_s \rightarrow \mu^+\mu^-$ ( $B_s \rightarrow \tau^+\tau^-$ ) is $10^{-7}$ ( $10^{-6}$ ) for several values of $\tan\beta$ . In the striped region the $\chi_1^0$ is not the LSP and the dark-shaded region in the b) figure is excluded by theoretical constraints on EWSB. . . . .	31
1.9	Comparison among several sparticles production at LHC assuming a particular model [30]. . . . .	34
1.10	Gluino pairs production at LHC from strong gluon-gluon fusion (up) and quark-antiquark (down) interactions [5]. . . . .	39
1.11	Squark Gluino production at LHC from strong gluon-quark fusion [5]. . . . .	39

1.12 Example of decay chain which can origin from $\tilde{g}\tilde{q}$ production in the contest of LM0 point in mSUGRA scenario. The red (violet) arrows indicate a possible decay chain starting from a gluino (squark). The green dashed arrows represent the lepton emissions. The light violet thick arrows illustrate the produced missing energy and the light violet thin arrows illustrate all the other SM particles emission . . . . .	40
2.1 The LHC ring with the already existing LEP structures (in grey) and the new structures appositely built for LHC (in red). . . . .	44
2.2 The acceleration compound committed to the several acceleration stages to prepare the protons bunches to the admittance to the LHC [35]. . . . .	45
2.3 The way LHC ring is divided in sectors and octants. The position of the four main experiments is also shown [34]. . . . .	46
2.4 Left: maximum value of the instantaneous luminosity reached per day. Right: integrated luminosity per day. . . . .	49
2.5 Integrated Luminosity collected since March till November 2010 in linear (left) and logarithmic (right) scale. . . . .	49
2.6 A perspective view of the CMS detector [37]. . . . .	52
2.7 z-r section of the inner tracking system [37]. . . . .	53
2.8 Left: a perspective of the Pixel subdetector structure. Right: a quarter of the $r-z$ section, showing the position of the Pixels layers.	53
2.9 Views of the four silicon strip tracker system. Left: schematic drawing of TIB and TID with the margherita disk. Right: a schematic drawing of the TEC system [37] . . . . .	55
2.10 Left: Layout of the CMS electromagnetic calorimeter showing the arrangement of the crystal modules, supermoduls and end caps. Right: layout drawing of the EB mechanism [37] . . . . .	56
2.11 Drawing of the $r-\phi$ section illustrating the division in wedges of the HB (left). drawing showing the HE position in the CMS apparatus in the $r-\phi$ section (middle) and $r-z$ section (right). [37] . . . . .	57
2.12 Left: a schematic drawing showing the HO modules positions and their layered structure. Right: the tower structure of the HB, HE and HO subsystems [37] . . . . .	57
2.13 Layout of the CMS barrel muon DT chambers in one of the 5 wheels [37] . . . . .	60

2.14 A quarter of the $r$ - $z$ section of the CMS detector, with the position of every subdetector, in particular the CSC muon chambers are visible [37] . . . . .	61
2.15 Drawing of a quarter of the $r$ - $z$ CMS section showing the division in trigger towers of the calorimeters. . . . .	63
2.16 Schematic view of the L1 Trigger system. . . . .	65
3.1 Top (Bottom) $B(\chi^\pm \rightarrow \tau)/B(\chi^\pm \rightarrow e(\mu))$ at generator level for the sample with $\tan\beta=3$ . The grey boxes indicate some technical failure. . . . .	72
3.2 Top (Bottom): $B(\chi^\pm \rightarrow \tau)/B(\chi^\pm \rightarrow e(\mu))$ at generator level for the sample with $\tan\beta=10$ . The grey boxes indicate some technical failure. . . . .	73
3.3 Charged-hadron tracks (lines with squares, representing the hits measured in the tracker and the various extrapolation positions to the ECAL and HCAL) each linked to one or two ECAL clusters (left) and an HCAL cluster (right) which are indicated with dots. Each square represents a calorimeter cell. The grey area is proportional to the logarithm of the energy measured in each cell. The clusters represented by a star are linked to neither of the two tracks, and are therefore photon candidates. . . . .	75
3.4 Basic jet properties in di-jet events: Distributions of (a) jet transverse momentum; (b) jet invariant mass; (c) the ratio of jet momentum to jet invariant mass; (d) jet pseudorapidity; (e) jet azimuth; and (f) number of particle constituents in a jet [53]. . . . .	78
3.5 Definition of the Tau isolation annulus [63]. . . . .	79
3.6 Resolution of $\cancel{E}_T$ for particle based (solid symbols) and calorimeter based (hollow symbols) reconstruction in data (circles) and simulation (squares) as a function of $\sum E_T$ . . . . .	80
3.7 HLT efficiency of the paths $HLT\_HT200$ (top) and $HLT\_DiJetAve70$ (bottom) as a function of the transverse $p_T$ of the less energetic lepton, for different final states. . . . .	82
3.8 Offline reconstructed $H_T$ variable before and after applying the $HLT\_HT200$ trigger (based on $H_T^{HLT}$ ). . . . .	83
3.9 From left to right: track of an electron originating from the primary vertex; tracks from photon conversion; definition of the $Dist$ variable: the distance between the $B1$ and $B2$ points in the $x$ - $y$ plane, when the two tracks overlap $Dist$ is defined to be negative. . . . .	86

3.10 Mva output variable . . . . .	89
3.11 $H/E$ in the barrel (left) and in the End Caps (right). . . . .	89
3.12 $Iso_{rel}^{comb}$ variable for prompt (left), heavy flavor (middle) and fake (right) electrons . . . . .	90
3.13 $Iso_{rel}^{comb}$ variable for prompt (left), heavy flavor (middle) and fake (right) muons. . . . .	90
3.14 Particle Flow Combined Relative Isolation as a function of $p_T$ for prompt (left) and Heavy Flavor (right) electrons. . . . .	91
3.15 Particle Flow Combined Relative Isolation as a function of $p_T$ for prompt (left) and Heavy Flavor (right) muons. . . . .	91
3.16 $Cut_{PF}^{eff09}$ as a function of the lepton $p_T$ , for the electrons (left) and the muons (right). . . . .	92
3.17 Left: Probabilities for quark/gluon jets to pass the tau candidate selection criteria for several tau identification algorithms as function of $p_T$ as measured from data. Right: efficiencies of several algorithms to reconstruct the hadronic decays of tau lepton in simulated $Z \rightarrow \tau^+ \tau^-$ events. [63]. . . . .	95
3.18 Data-MC comparison of probabilities for quark/gluon jets to pass the tau candidate selection criteria of the TaNC tau identification algorithms as function of $\eta$ [63]. . . . .	95
3.19 Reconstructed $p_T$ of the identified muons(left) and electrons (right). . . . .	97
3.20 Reconstructed $p_T$ of the identified taus (right). . . . .	97
3.21 Number of reconstructed and identified leptons after only the HLT requirement (left) and after the $H_T$ and $MH_T$ (right). . . . .	98
3.22 $H_T$ after only the HLT requirement (left) and after all the cuts except the $H_T$ cut (right). . . . .	98
3.23 $MH_T$ after only the HLT requirement (left) and after all the cuts except the $MH_T$ cut (right). . . . .	98
3.24 Data-MC comparison for the number of electrons (left) and muons (right) obtained after the $H_T$ and $MH_T$ selection. The colors assignment is in the legend of Fig.???. . . . .	99
3.25 Data-MC comparison for the number of taus (left) and all the lepton flavors (right) obtained after the $H_T$ and $MH_T$ selection (right). . . . .	99
3.26 Signal (two same sign leptons) efficiency of the selection for the samples $\tan\beta 3$ (left) and $\tan\beta 10$ (right) . . . . .	100

3.27 Comparison between data (black points) and MC simulation (blue triangles) for the electron $\epsilon_{T/L}(\eta_i, p_{Ti})$ as a function of $p_T$ in the barrel (left) and end-cap (right) region. . . . .	106
3.28 Comparison between data (black points) and MC simulation (blue triangles) for the muon $\epsilon_{T/L}(\eta_i, p_{Ti})$ as a function of $p_T$ in the barrel (left) and end-cap (right) regions. . . . .	107
3.29 Comparison between data (points, see text for details) and MC simulation (black triangles) for the tau $\epsilon_{T/L}(\eta_i, p_{Ti})$ as a function of $p_T$ in $0 <  \eta  < 0.5$ (left) and $0.5 <  \eta  < 1$ (right) regions. . . . .	107
3.30 Comparison between data (points, see text for details) and MC simulation (black triangles) for the electron $\epsilon_{T/L}(\eta_i, p_{Ti})$ as a function of $p_T$ in $1 <  \eta  < 1.5$ (left) and $1.5 <  \eta  < 2$ (right) regions. . . . .	108
3.31 Comparison between data (points, see text for details) and MC simulation (black triangles) for the electron $\epsilon_{T/L}(\eta_i, p_{Ti})$ as a function of $p_T$ in $2 <  \eta  < 2.5$ regions. . . . .	108
3.32 Mischarge rate as a function of $ \eta $ for $40 < p_T < 70$ GeV determined with particle gun (black), MC truth in $Z+jets$ sample (green) and the data-driven tag and probe method in $Z+jets$ sample (red). . . . .	110
3.33 Invariant mass of two prompt leptons, opposite and same sign (black), requiring only same sign with $GSF$ (blue), $majority$ (red) and $GSF = GEN = SC$ (green) method . . . . .	111
3.34 Comparison between the observed (green squares) and the predicted (red triangles) number of events by considering only background MC samples (left) and adding LM0 to the background samples (right). . . . .	114
3.35 The same as Fig.3.34 but in logarithmic scale . . . . .	114
3.36 Comparison between the observed (black points) and predicted (blue squares) number of events in linear (left) and logarithmic (right) scale. The dashed rectangles represent the systematic uncertainty related to the estimation background method. . . . .	116
3.37 Comparison between the observed (black points) and predicted (blue squares) number of events in linear (left) and logarithmic (right) scale, after a looser selection than the analysis one. The dashed rectangles represent the systematic uncertainty related to the estimation background method. . . . .	118

3.38 $Z_{Bi}$ values which can be obtained in presence of mSugra signal with the parameters $A_0 = 0$ , $sign\mu = +$ and $\tan\beta=3$ (top) and $\tan\beta=10$ (bottom), with $L_{int} = 100\text{pb}^{-1}$ . . . . .	121
3.39 $Z_{Bi}$ values which can be obtained in presence of mSugra signal with the parameters $A_0 = 0$ , $sign\mu = +$ and $\tan\beta=3$ (top) and $\tan\beta=10$ (bottom), with $L_{int} = 100\text{pb}^{-1}$ in all the channels but $\tau\tau$ . . . . .	122
3.40 Minimal integrated luminosity needed to obtain a $Z_{Bi} > 5$ for $\tan\beta = 3$ (top) and $\tan\beta = 10$ (bottom) considering all the six final states. . . . .	124
3.41 Minimal integrated luminosity needed to obtain a $Z_{Bi} > 5$ for $\tan\beta = 3$ (top) and $\tan\beta = 10$ (bottom) excluding the $\tau\tau$ final state. . . . .	125
3.42 The numbers are the total number of events, the stripped region represents the points which can be excluded after $100 \text{ pb}^{-1}$ . The green boxes indicate the mSugra points not available because of technical issues. . . . .	127
3.43 The numbers are the total number of events excluding the $\tau\tau$ channel, the stripped region represents the points which can be excluded after $100 \text{ pb}^{-1}$ . The green boxes indicate the mSugra points not available because of technical issues. . . . .	128
3.44 Exclusion plot for all the channels but $\tau\tau$ . . . . .	129
3.45 Regions in the mSugra plane with $\tan\beta=3$ , $\mu > 0$ and $A_0 = 0$ excluded by the other experiments [78]. . . . .	129
 4.1 Cross section of several processes involving $W$ boson(s) production as a function of the centre of mass energy at Tevatron and LHC. The solid (dotted) curves indicate the DPS (SPS) [96]. . . . .	139
4.2 Examples of diagrams contributing to the SPS SS $W$ production at $\alpha_{EW}^4$ order and no $\alpha_s$ vertices. Both neutral bosons ( $A \equiv \text{photon}$ and $Z^0$ ) and charged boson ( $W$ ) exchange are illustrated. . . . .	141
4.3 Examples of diagrams contributing to the SPS SS $W$ production. For $\alpha_{EW}^4$ order and zero $\alpha_s$ order and at $\alpha_{EW}^2\alpha_s^2$ order. . . . .	141
4.4 $p_T$ distribution of the first lepton for the processes with same sign leptons normalized to unity (left) and for instrumental background sources normalized to $100 \text{ pb}^{-1}$ (right). . . . .	143

4.5	$p_T$ distribution of the first lepton for the processes with same sign leptons normalized to unity (left) and for instrumental background sources normalized to $100 \text{ pb}^{-1}$ (right). . . . .	144
4.6	$p_T$ distribution of the first jet for the processes with same sign leptons normalized to unity (left) and for instrumental background sources normalized to $100 \text{ pb}^{-1}$ (right). . . . .	144
4.7	$p_T$ distribution of the third lepton for the processes with same sign leptons normalized to unity (left) and for instrumental background sources normalized to $100 \text{ pb}^{-1}$ (right). . . . .	145
4.8	$\Delta\phi(\text{lep1}, \text{lep2})$ for the DPS signal (teal) and the main background processes after the two identified lepton requirement. . . . .	145
4.9	Scatter plot of $\vec{p}_T^{\text{leppair}}$ vs $\cancel{E}_T$ . The color code is in the legend of Fig.4.8 . . . . .	146
4.10	$\cancel{E}_T - p_T^{\text{leppair}}$ for the processes with same sign leptons (left) and for instrumental background sources. . . . .	147
4.11	$\eta$ distribution of the lepton coming from $W$ decays at generator level normalized to area. . . . .	149
4.12	Distribution of $H_T$ (for DPS WW) and $H_T$ convolution (for data and $W\text{jets}$ samples) computed with $p_T(\text{jet}) > 50 \text{ GeV}$ (left) and $p_T(\text{jet}) > 25 \text{ GeV}$ (right). . . . .	153
4.13	Distribution of $H_T$ (for DPS WW) and $H_T$ convolution (for data and $W\text{jets}$ samples) computed with $p_T(\text{jet}) > 50 \text{ GeV}$ . . . . .	153
4.14	As in Fig.4.13 but in logarithmic scale . . . . .	154



# List of Tables

1.1	Observed elementary particles in Standard Model. . . . .	4
1.2	Higgs bosons and sparticles in the MSSM with their partners. . . . .	16
1.3	Sparticles in MSSM, both gauge eigenstates and mass eigenstates (when different from the gauge eigenstates) are reported. . . . .	20
2.1	Beam parameters for the nominal LHC design. . . . .	47
2.2	Luminosity parameters for the nominal LHC design. . . . .	48
3.1	List of the MC background samples used in this analysis. The cross sections listed are those used in this work. . . . .	70
3.2	List of the MC signal samples used in this analysis. The LM0 cross section is at NLO with a k-factor as calculated by Prospino [47]. . .	71
3.3	Electron identification cuts. . . . .	87
3.4	Details of the five hadronic tau decays considered by the TaNC algorithm. . . . .	93
3.5	Summary of the electron selection. . . . .	96
3.6	Summary of the muon selection. . . . .	96
3.7	Number of selected events after the whole selection for the LM0 mSugra point and for the main background processes in $100 \text{ pb}^{-1}$ . .	100
3.8	List of the event selection and the loose identification for each lepton flavor. . . . .	106
3.9	Requirement to satisfied by the tag and probe electrons. . . . .	109
3.10	Comparison between the observed and predicted number of events (with statistical uncertainties) for each final state by considering only the MC background samples. . . . .	112
3.11	Comparison between the observed and predicted number of events (with statistical uncertainties) for each final state with background and signal (LM0) samples. . . . .	113

3.12	Number of selected events for each final state with the statistical uncertainty. Left: comparison between the observed and predicted number of events. Right: predicted obtained with $\epsilon_{T/L}$ determined in different event conditions for systematics study purpose. . . . .	116
3.13	Number of events for each final state along with the statistical uncertainty, selected by the loose selection. Left: comparison between the observed and predicted number of events. Right: predicted obtained with $\epsilon_{T/L}$ determined in different event conditions for systematics study purpose. . . . .	117
4.1	Lepton acceptance and $R_a$ factor. . . . .	148
4.2	Cut flow of the selected number of events in $100 \text{ pb}^{-1}$ for the background processes . . . . .	150



At leisure is the Soul  
That gets a Staggering Blow -  
The Width of Life - before it spreads  
Without a thing to do -  
It begs you give it Work -  
But just the placing Pins -  
Or humblest Patchwork - Children do -  
To still it's noisy Hands -

Emily Dickinson